Role of Magnesium in the Production of Nodular Graphite Cast Iron

An Assessment on Reaction Mechanism and Sustainable Substitute

Von der Fakultät für Ingenieurwissenschaften,
Abteilung Maschinenbau und Verfahrenstechnik der
Universität Duisburg-Essen

zur Erlangung des akademischen Grades
eines
Doktors der Ingenieurwissenschaften
Dr.-Ing.

genehmigte Dissertation

von

Ida Bagus Gede Sumbranang Adhiwiguna
aus
Denpasar, Indonesien

Erster Gutachter : Univ.-Prof. Dr.-Ing. Rüdiger Deike
Zweiter Gutachter : Univ.-Prof. Dr.-Ing. habil. Karl-Heinz Spitzer

Tag der mündlichen Prüfung: 12.12.2024

DOI: 10.17185/duepublico/82823
URN: urn:nbn:de:hbz:465-20250106-075154-5

Authorship Declaration

I declare that I am the sole author of this dissertation, entitled "Role of Magnesium in the Production of Nodular Graphite Cast Iron – An Assessment on Reaction Mechanism and Sustainable Substitute," submitted as a fulfillment of the requirement for the degree of Doktor der Ingenieurswissenschaften (Dr.-Ing.) at Universität Duisburg-Essen, Germany.

I confirm and certify that:

(1) This dissertation is my original work and has not been submitted in whole or in part for any other degree or diploma at any other institution.
(2) The content of this dissertation is a result of my original research, investigations, and experiments, except where due acknowledgment is made.
(3) All external sources of information, including data, images, and literature, have been appropriately cited within the dissertation.

I guarantee this is a true copy of my dissertation, including any final revisions approved by my thesis committee at Universität Duisburg-Essen, Germany.

Duisburg, 12.12.2024
Ida Bagus Gede Sumbranang Adhiwiguna
Matrikel Nr. 3063118

Preface

Recognizing that independently addressing every question and overcoming all obstacles in research is impossible, this dissertation owes its completion to the invaluable support, guidance, and encouragement of numerous individuals and institutions, to whom I extend my heartfelt gratitude.

I sincerely thank my supervisor, Univ.-Prof. Dr.-Ing. Rüdiger Deike, and my co-supervisor, Univ.-Prof. Dr.-Ing. habil. Karl-Heinz Spitzer, for their invaluable guidance, constructive feedback, and unwavering support throughout my research journey. Their expertise and insightful mentorship have been crucial in shaping the direction and quality of this work.

I am equally indebted to my colleagues at the Chair of Metallurgy and Metal Forming, Institut für Technologien der Metalle, at the University of Duisburg-Essen, for their collaboration, insightful discussions, and unwavering camaraderie. My sincere appreciation also goes to the industrial mentors whose practical perspectives and critical feedback greatly enriched the applicability and impact of this research.

On a personal note, I am deeply grateful to my family, friends, and especially my wife, Ida Ayu Putu Trisna Andayani, for her enduring patience, unconditional support, and endless encouragement. Her steadfast belief in me has been an invaluable source of strength throughout this journey.

Finally, I hope this dissertation makes a meaningful contribution to advancing knowledge in ductile iron production and provides valuable insights for reducing reliance on magnesium in this critical industrial process.

"Durch unser Wissen unterscheiden wir uns nur wenig, in unserer grenzenlosen Unwissenheit aber sind wir alle gleich"

Sir Karl R. Popper (1902 – 1994)

Kurzfassung

Trotz seiner Bedeutung für die Herstellung von Gusseisen mit Vermicular- und Kugelgrafit gibt es aus der Perspektive der Nachhaltigkeit mindestens zwei Gründe, den Status quo beim Magnesiumeinsatz infrage zu stellen. Einerseits ist der Produktionsprozess energie- und emissionsintensiv und andererseits ist Magnesium nach der Definition der EU ein kritischer Rohstoff. Aus den Entwicklungen der globalen Rohstoffmärkte in den letzten zwei Jahrzehnten lassen sich die Abhängigkeiten in der Versorgung mit Magnesiumprodukten identifizieren. Vor diesem Hintergrund hat sich in der jüngsten Vergangenheit gezeigt, dass Unsicherheiten in den Lieferketten Verluste bei der Wettbewerbsfähigkeit zur Folge haben. Daher konzentriert sich diese Arbeit auf die Bewertung der Rolle von Magnesium in der Produktion von Gusseisen mit Kugelgrafit, mit dem Ziel Magnesium zu substituieren und mögliche nachhaltige Alternativen zu identifizieren.

Durch den Einsatz des Kokillenguss-Verfahrens können die Hochtemperaturreaktionen zwischen Magnesium und Gusseisen unbeeinflusst von möglichen Formstoffreaktionen beobachtet werden. Die Ergebnisse zeigen, eine schnelle Auflösung, Desoxidation und Entschwefelung bevor die Verdampfung des Magnesiums beginnt. Mit der Bildung von festem MgO und MgS werden Überhitzungszustände an der Grenzfläche erzeugt, die je nach Überhitzungsgrad Siedemechanismen begünstigen, die zu einer Flüssigkeitsfragmentierung oder zu physikalisch-chemischen Reaktionen an den Rissen in den bereits vorhandenen festen Reaktionsprodukten führen.

In Anbetracht des Verhaltens von Magnesium während der Entschwefelung wurde Kalk als Alternative untersucht. Sowohl Labor- als auch Industrieversuche wurden durchgeführt und zeigen, dass Kalk ein zuverlässiges Entschwefelungsmittel für die Gusseisenindustrie ist. Darüber hinaus wurde der Reaktionsmechanismus untersucht, um den Prozess optimal steuern zu können. Die Ergebnisse zeigen, dass Aluminium, Silizium und Eisen an dem Prozess beteiligt sind, wodurch ein spezifisches flüssiges Schlackensystem entsteht, das den Entschwefelungsprozess begünstigt. Allerdings spielen im weiteren Verlauf der Reaktion, die sich verändernde Löslichkeiten der Elemente eine Rolle und es kommt zur Ausscheidung von festem Calciumsilikat wodurch die Reaktion zwischen Kalk und Schwefel zwar gehemmt wird, aber dennoch zeigen die Ergebnisse, dass die Entschwefelung weiter stattfindet, so dass die angestrebten geringeren Schwefelgehalte erreicht werden. Zusätzlich lassen sich wirtschaftliche und ökologische Vorteile feststellen.

Ein weiterer Effekt des Magnesiums ist die Veränderung der Grafitausscheidung. Durch die Untersuchung des Wiederauflösens von Kugelgrafit beim erneuten Einschmelzen von Schrott wird bestätigt, dass zwei Faktoren notwendig sind, um Kugelgrafit zu etablieren: Niedrige Schwefel- und Sauerstoffkonzentrationen sowie ein ausreichender Gehalt an gelöstem Magnesium. Es ist erwähnenswert, dass die Rolle des Magnesiums nicht nur darin besteht, mit oberflächenaktiven Elementen zu reagieren, sondern dass Magnesium auch die Kohlenstoffaktivität im flüssigen Eisen erhöht und somit die Grafitkristallisation im Verlauf der Erstarrung fördert.

Abstract

Despite its significance in ensuring that compacted and ductile cast iron can consistently be manufactured, there are at least two reasons from the sustainability perspective that it is necessary to challenge the status quo in utilizing magnesium. Besides its energy and emission-intensive production process that builds up the whole carbon footprint of the cast iron product, magnesium is classified as a critical raw material by the EU. In this instance, developments in global raw material markets over the past two decades have revealed dependencies in the supply of magnesium products. Consequently, it has recently become evident that supply chain uncertainties result in competitiveness losses. Hence, this work will mainly focus on assessing the role of magnesium in ductile cast iron production, particularly during desulfurization and nodularization, before eventually identifying any possible sustainable alternative.

By employing a chill casting approach, high-temperature interaction between magnesium and molten cast iron with different sulfur content can be observed without interference from possible mold material reactions. The results indicate that rapid dissolution, deoxidation, and desulfurization sequentially take place and are complete before the notable boiling process begins. As the reaction progresses, a superheating state at the interface could be expected due to further heat transfer and exothermic reactions related to solid MgO and MgS formation. Depending on the degree of superheating, the distinct mechanism of boiling will be favored, resulting in either liquid fragmentation or physical-chemical reactions at the crack on the pre-existing solid reaction products.

Considering the behavior of magnesium during desulfurization, lime was investigated as an alternative that provides a similar result to cast iron. Both laboratory and industrial trials were conducted, concluding that lime is a reliable desulfurization agent for the cast iron industry. Moreover, the reaction mechanism was also explored to control the process optimally. The results indicate that aluminum, silicon, and iron are involved in establishing specific liquid slag systems that favor desulfurization. However, as the reaction continues, the solubility dynamic comes into play, and precipitation of solid calcium silicate is anticipated, thus retarding the further interaction between lime and sulfur. Nonetheless, the results demonstrate that desulfurization continues, allowing the required end-sulfur content to be achieved, in addition to competitive economic and ecological advantages.

Another effect of magnesium incorporation associated with nodularization is the change in the graphite precipitation. By examining the development of graphite during the remelting of cast iron scrap with nodular graphite, it is confirmed that two factors are necessary to establish nodular graphite: low sulfur and oxygen concentrations, as well as a sufficient level of dissolved magnesium. It is worth mentioning that the role of irreplaceable magnesium is not only to react with surface-active elements but also to increase carbon activity in the liquid iron, thereby promoting graphite crystallization during solidification.

Table of Contents

Authorship Declaration ..... **I**
Preface ..... **II**
Kurzfassung ..... **V**
Abstract ..... **VI**
Table of Contents ..... **VII**
List of Figures ..... **XI**
List of Tables ..... **XVII**

PART I Commencement **1**
Chapter 1 Introduction **3**
1.1. Research Background **3**
1.2. Purpose of Study **5**
1.3. Research Structure **5**
Chapter 2 Current Research Status **7**
2.1. Magnesium Interaction with Molten Iron **7**
2.2. Lime as a Desulfurization Agent for Molten Iron **9**
2.3. Nucleation of Spheroidal Graphite in Ductile Iron **11**

PART II Initial Identification **17**
Chapter 3 Interaction between Magnesium and Molten Cast Iron **19**
3.1. Methodology **19**
3.2. Experimental Results **20**
3.2.1. Reaction Layer between Magnesium and Cast Iron (ERP) 20
3.2.2. Round Structures in the Reaction Zone (RRP) 24
3.2.3. Round Structures in the Thermal Center (HRP) 27
3.2.4. Graphite Layers on Nonmetallic Reaction Products 28
3.2.5. Effect of Dissolved Magnesium on Graphite and Matrix Structure 30
3.3. Analysis and Discussion **32**
3.3.1. Reaction Mechanism of Magnesium in Molten Cast Iron 32
3.3.2. Spherical Magnesium-containing Reaction Products 35
3.3.3. Possible Magnesium-induced Segregation and Precipitation 37
3.4. Summary of Magnesium and Cast Iron Interaction **41**

PART III Desulfurization **43**
Chapter 4 Lime as Desulfurization Agent for Molten Cast Iron **45**
4.1. Methodology **45**
4.2. Experimental Results **46**
4.2.1. ON-AD: Lime Desulfurization by Surface Addition 46
4.2.2. IN-AD: Lime Desulfurization by Injection Process 48
4.2.3. Reaction Layer between CaO and Cast Iron 49

4.3. Analysis and Discussion 51
4.3.1. Role of Deoxidation in Desulfurization Results 51
4.3.2. Role of Liquid Slag in Desulfurization Results 53
4.3.3. Possible Scaled-up Implementation on the Industrial Scale 58
4.4. Summary of Lime Applicability as Desulfurization Agent 58
Chapter 5 Reaction Mechanism of Lime and Molten Cast Iron 59
5.1. Methodology 59
5.2. Results and Discussion 60
5.2.1. BO-AD: Observation of the Desulfurization in Inert Atmosphere 60
5.2.2. ON-AD: Observation of the Desulfurization in Open Atmosphere 62
5.2.3. Involvement Indication of MnS and FeS during Desulfurization 64
5.2.4. Analysis of Reaction Mechanism during Cast Iron Desulfurization 66
5.3. Summary of Lime-based Desulfurization Mechanism 73
Chapter 6 Ecotechnological Study on Lime-based Desulfurization 75
6.1. Materials and Methods 75
6.1.1. Technological Trial in Industrial Lime-based Desulfurization 75
6.1.2. Ecological Examination in Industrial Lime-based Desulfurization 76
6.2. Results and Discussion 79
6.2.1. Lime-based Desulfurization Results by Injection Process 79
6.2.2. Ecological Impact Assessment in Comparative CO_2eq 81
6.2.3. Comparative Discussion on Ecotechnological Advantages 83
6.3. Summary of Industrial Lime-based Desulfurization 86

PART IV Nodularization 87
Chapter 7 Graphite Nucleation during Recycling of Ductile Iron 89
7.1. Materials and Methods 89
7.1.1. Cooling Curve Analysis 89
7.1.2. Copper Mold Chill Casting 89
7.1.3. Extended Cooling Curve Analysis and Chill Casting Experiments 90
7.2. Experimental Results 90
7.2.1. Temperature Profile during Cooling Curve Analysis without Holding 90
7.2.2. Microstructure Development due to Chill Casting without Holding 92
7.2.3. Formation of Graphite Cluster at the Thermal Center after Chill Casting 93
7.3. Analysis and Discussion 99
7.3.1. Effect of Superheating on the Solidification of Cast Iron upon Remelting 99
7.3.2. Solidification of Deteriorated Graphite upon Remelting of LS-CI 101
7.4. Summary of Graphite Structure upon Ductile Iron Recycling 103
Chapter 8 Dissolution Behavior of Spheroidal Graphite 105
8.1. Materials and Methods 105
8.1.1. MH-Exp: High-Temperature Molten Metal Holding Trials 105
8.1.2. ET-Exp: Dissolution Behavior of Nodular Graphite Experiments 105

8.2. Experimental Results 106
8.2.1. Changes in Concentration of Carbon and Silicon during MH-Exp 106
8.2.2. Matrix Development and Graphite Structure after ET-Exp 107
8.2.3. Observation of the Residual Graphite Structure after ET-Exp 110
8.3. Analysis and Discussion 110
8.3.1. Discussion on Carbon and Silicon Depletions during MH-Exp.....110
8.3.2. Description of Nodular Graphite Dissolution Mechanism 112
8.3.3. Correlation of Homogenization and Oxidation to Fading 114
8.4. Summary of Graphite Dissolution in Ductile Cast Iron 115
Chapter 9 Relation of Magnesium and Heterogeneous Nucleation 117
9.1. Materials and Methods 117
9.1.1. Observation of the Nuclei of Nodular Graphite (Controlled Melting) 117
9.1.2. Effect of Treatment Agents on Graphite Nucleation (In-mold Treatment) 117
9.2. Experimental Results 118
9.2.1. Chemical Composition of the Nuclei in the Residual Graphite Structure.....118
9.2.2. Effect of the In-mold Treatment Agent on Graphite Nucleation.....124
9.2.3. Effect of Nonmetallic Inclusion on the Graphite Structure.....126
9.3. Analysis and Discussion..... 128
9.3.1. The Interplay between Inclusions, Composition, and Graphite Structure.....128
9.3.2. The Importance of Inclusion and Magnesium to the Nodular Graphite.....130
9.3.3. Theoretical Dynamics in the Nucleation and Growth of Nodular Graphites 131
9.4. Summary of Relation between Magnesium and Nodular Graphite 132

PART V Denouement..... 133
Chapter 10 Conclusion and Outlook..... 135
10.1. Conclusion..... 135
10.2. Outlook..... 135
Bibliography..... 137
Publications 157

List of Figures

Figure 3.1. Experimental setup for high-temperature interaction between magnesium and molten cast iron. 19
Figure 3.2. Sample preparation after high-temperature interaction between magnesium and molten cast iron. 20
Figure 3.3. Typical reaction interfaces between magnesium and (**a**) HS-CI and (**b**) LS-CI under a light microscope at all studied casting temperatures. 20
Figure 3.4. SEM images of typical reaction layer of (**a**) HS-CI and (**b**) LS-CI. 21
Figure 3.5. Chemical analysis results of the reaction layers indicated in (**a**) **Figure 3.4a** and (**b**) **Figure 3.4b**. 21
Figure 3.6. Evolving fluid under (**a**) light microscope and (**b**) SEM observation in addition to (**c**) detailed AES observation points on the reaction layer listed in **Table 3.2**. 22
Figure 3.7. Alternative reaction layer morphology with minimal unreacted magnesium. 23
Figure 3.8. Round reaction product near the edge reaction product between magnesium and cast iron**.** 24
Figure 3.9. Different configurations of the round reaction products – (**a**) only the reaction product, (**b**) both the reaction product and the heterogeneous matrix structure, and (**c**) only the heterogeneous matrix structure. 25
Figure 3.10. Element mapping analysis result for the round reaction product indicating the reaction product and the heterogeneous matrix structure. 25
Figure 3.11. Line scan results for boundary layer of round reaction product for (**a**) HS-CI and (**b**) LS-CI. 26
Figure 3.12. Element mapping result of the hollow reaction product in HS-CI. 27
Figure 3.13. The wall structure of the hollow reaction product in **Figure 3.12**. 28
Figure 3.14. Graphite flake on round reaction products in (**a**) HS-CI and (**b**) LS-CI samples. 29
Figure 3.15. Detailed graphite flake structure located on the edge reaction product between magnesium and cast iron. 30
Figure 3.16. Matrix structure in the Nital-etched condition (**a**) away from and (**b**) near to the rest of the magnesium and reaction products. 31
Figure 3.17. Cast iron matrix of HS-CI with the coexistence of lamellar and nodular graphite structures. 32
Figure 3.18. Dispersed Mg-containing particles in the vicinity of (**a**) edge and (**b**) round reaction products. 33
Figure 3.19. Trace of liquid fragmentation upon high-temperature interaction between cast iron and magnesium. 35
Figure 3.20. Equilibrium reaction products depend on the magnesium supply at higher temperatures. 37
Figure 3.21. Equilibrium reaction products depend on the magnesium supply at lower temperatures. 38

Figure 3.22. Matrix variances (Nital-etched condition) of (**a**) HS-CI and (**b**) LS-CI with high dissolved magnesium concentrations. 41
Figure 4.1. Illustration of the lime-based desulfurization process for molten cast iron using the surface addition method. 46
Figure 4.2. Illustration of the lime-based desulfurization process for molten cast iron using injection method. 46
Figure 4.3. Average normalized concentrations of (**a**) sulfur and (**b**) carbon in molten cast iron during desulfurization using CaO and a mixture of CaO-carbon. 47
Figure 4.4. Average normalized concentrations of (**a**) sulfur and (**b**) carbon in molten cast iron during desulfurization using CaO-carbon with Si-containing additives. 48
Figure 4.5. Average normalized concentrations of sulfur in cast iron during desulfurization involving the addition of aluminum (**a**) with and (**b**) without carbon. 48
Figure 4.6. Changes in the sulfur content in molten cast iron for surface addition and injection desulfurization methods. 49
Figure 4.7. Reaction layer between the desulfurization agent and molten cast iron under (**a**) light microscope and using (**b**) scanning electron microscope. 49
Figure 4.8. Elemental mapping results of the reaction layer as provided in **Figure 4.7b**. 50
Figure 4.9. Selected measurement points on the reaction layer as provided in **Figure 4.7b**. 51
Figure 4.10. Modified isothermal section of the ternary system SiO_2-CaO-Al_2O_3 at 1500°C calculated on FactSage. 55
Figure 5.1. Illustration of lime-based desulfurization process for cast iron at open atmospheric conditions. 60
Figure 5.2. Typical structure of reaction layer between lime and cast iron under a light microscope – the depicted contrast is typical for all observations under the light microscope during further analysis. 60
Figure 5.3. Element mapping result of the reaction layer captured in **Figure 5.2**. 61
Figure 5.4. Sample of reaction layer under (**a**) light microscope and detailed (red circle) under (**b**) SEM observation concentrated to the slag/iron interface. 61
Figure 5.5. Elemental mapping result of red-circled area (interface) in **Figure 5.4**. 62
Figure 5.6. Sample of transition on reaction layer under (**a**) light microscope and detailed (red circle) under (**b**) SEM observation between rest lime and slag system. 63
Figure 5.7. Sample of transition on reaction layer under (**a**) light microscope and detailed (red circle) in (**b**) SEM observation between indication of CaS and slag system. 64
Figure 5.8. Sample of reaction layer under (**a**) light microscope and (**b**) SEM observation involving detection of possible manganese-sulfide segregation. 65
Figure 5.9. The elemental mapping result of the reaction layer in **Figure 5.8**. 65

Figure 5.10. Sample of reaction layer under (**a**) light microscope and (**b**) SEM observation involving detection of possible iron-sulfide segregation (red circle and arrow). 65
Figure 5.11. The elemental mapping result of the reaction layer in **Figure 5.10**. 66
Figure 5.12. General morphology of reaction layer between lime powder and molten cast iron during desulfurization. 67
Figure 5.13. Isothermal ternary phase diagram SiO_2-Al_2O_3-CaO calculated on FactSage. 67
Figure 5.14. Isothermal ternary phase diagram of SiO_2-FeO-CaO calculated on FactSage. 69
Figure 5.15. Phase development correlated with sulfur segregation at the interface calculated on FactSage 71
Figure 5.16. Isothermal ternary phase diagram of CaS-FeS-MnS calculated on FactSage. 72
Figure 6.1. Construction of an automatic injection machine for lime-based desulfurization of cast iron [128, 160] 76
Figure 6.2. Material flow diagrams of the current magnesium-based desulfurization. 77
Figure 6.3. Material flow diagrams of the alternative lime-based desulfurization. 77
Figure 6.4. Sulfur content before (initial) and after (final) desulfurization process. 79
Figure 6.5. Effect of different lance design and desulfurization mixtures on the final sulfur content. 80
Figure 6.6. Graphite structure of CGI products made from (**a**) magnesium- and (**b**) lime-based desulfurized cast iron. 81
Figure 6.7. Summary of comparative carbon footprint potential (CO_2eq) for magnesium-based and lime-based desulfurization process in cast iron. 85
Figure 7.1. Experimental setup and sample preparation for the chill casting experiment 90
Figure 7.2. Cooling curves analysis results of (**a**) HS-CI and (**b**) LS-CI with different superheating temperatures. 91
Figure 7.3. The microstructure of the solidified cast iron sample removed from the double-chamber crucible for the cooling curve analysis experiment for the LS-CI sample at (**a**) 1300°C and (**b**) 1400°C 91
Figure 7.4. Detailed microstructure on the sample in **Figure 7.3b** (LS-CI at 1400°C without holding) at the interface to the crucible indicating (**a**) vermicular structure and (**b**) ledeburite matrix after Nital-etching 92
Figure 7.5. Microstructure of as-polished (**a1**, **b1**, and **c1**) and Nital-etched (**a2**, **b2**, and **c2**) of cast iron samples before chill casting for HS-CI (**a1** and **a2**) and LS-CI (**b1** and **b2**) compared with the typical microstructure after chill casting (**c1** and **c2**) – microstructure after the chill casting experiments is essentially similar for both HS-CI and LS-CI regardless of the superheating temperatures. 92
Figure 7.6. Sample of (**a**) Mn-S-enriched inclusions in chill-casted HS-CI (found at all studied temperatures) and (**b**) rest graphite in chill-casted LS-CI (detected at low superheating of 1300°C and 1400°C). 93

Figure 7.7. Typical representation of graphite cluster structure captured at the thermal center of chill-casted HS-CI in (**a**) as-polished and (b) Nital-etched conditions. 94
Figure 7.8. Graphite cluster in HS-CI sample after chill casting at (**a**) 1300°C, (**b**) 1400°C, and (**c**) 1500°C. 94
Figure 7.9. Typical representation of graphite cluster structure captured at the thermal center of chill-casted LS-CI in (**a**) as-polished and (**b**) Nital-etched conditions. 95
Figure 7.10. Graphite cluster morphology in chill-casted (**a**) HS-CI and (**b**) LS-CI observed under SEM after deep-etching process: (**1**) lamellar graphite, (**2**) pearlite matrix in HS-CI, (**3**) vermicular graphite, (**4**) spheroidal graphite, (**5**) ferrite matrix in LS-CI, and (**6**) pearlite matrix in LS-CI. 95
Figure 7.11. Graphite cluster in LS-CI sample after chill casting at (**a**) 1300°C, (**b**) 1400°C, and (**c**) 1500°C without a holding procedure. 96
Figure 7.12. Graphite cluster in LS-CI after chill casting at (**a**) 1300°C and (**b**) 1400°C with a three-minute holding procedure. 97
Figure 7.13. The microstructure of the solidified LS-CI removed from the double-chamber crucible for cooling curve analysis involving the three-minute holding procedure at 1400°C in (**a**) as-polished and (**b**) Nital-etched conditions. 98
Figure 7.14. Graphite cluster in LS-CI after chill casting involving the three-minute holding procedure at 1500°C (**a**) without and (**b**) with the addition of aluminum metal. 98
Figure 8.1. The average change in the carbon content during the high-temperature holding of (**a**) HS-CI and (**b**) LS-CI – additional sample LS-CI 1400°C* was melted in an alumina-based crucible. 106
Figure 8.2. The average development in the carbon and silicon contents in (**a**) HS-CI and (**b**) LS-CI during holding at a temperature of 1300°C. 107
Figure 8.3. The average development in the carbon and silicon contents in (**a**) HS-CI and (**b**) LS-CI during holding at a temperature of 1500°C. 107
Figure 8.4. Microstructure of Nital-etched LS-CI (**a**) before and (**b**) after ET-Exp (1200°C for 10 min) – transforming (**1**) nodular graphite in a matrix system of (**2**) pearlite and (**3**) ferrite into (**4**) residual graphite in a matrix system of (**5**) ledeburite and (**6**) martensite. 108
Figure 8.5. Microstructure development LS-CI after being held at 1200°C followed by water quenching for (**a1**) 5, (**b1**) 10, and (**c1**) 15 min in as-polished condition as well as for (**a2**) 5, (**b2**) 10, and (**c2**) 15 min in Nital-etched condition. 108
Figure 8.6. Microstructure of the Nital-etched LS-CI after 15 min of holding at 1200°C followed by water quenching indicating (**a**) residual graphite in red circle detailed in (**b**): (**1**) graphite, (**2**) martensite, and (**3**) ledeburite. 109
Figure 8.7. Microstructure of the Nital-etched LS-CI after 15 min of holding at (**a**) 1100°C, (**b**) 1200°C, and (**c**) 1300°C followed by water quenching – the detailed red arrow of G pointing at residual graphite. 109

Figure 8.8. Structure of (**a**) residual nodular graphite and (**b**) detail of its nonmetallic nucleus in the LS-CI sample.....110
Figure 8.9. FactSage calculation results for HS-CI and LS-CI oxidation processes at all explored temperatures.....112
Figure 9.1. Experimental setup of in-mold treatment of molten cast iron. 118
Figure 9.2. As-received microstructure of LS-CI in (**a**) as-polished and (**b**) Nital-etched conditions.....118
Figure 9.3. Spectrum of graphite nodules in different regions in LS-CI after controlled melting at <1200°C. 119
Figure 9.4. Nonmetallic inclusion detected within residual nodular graphites after a controlled melting trial. 120
Figure 9.5. Elemental mapping result of the commercial treatment agent FeSiMg6 in cast iron production.....120
Figure 9.6. Structure of (**a**) residual graphite nodule with a trace of (**b**) oxide nucleus.....121
Figure 9.7. Structure of residual graphite with a trace of oxy-sulfide nuclei.....121
Figure 9.8. Structure of residual graphite with a trace of oxy-sulfide nuclei coexisting with (carbo-) nitride.....122
Figure 9.9. Structure of residual graphite nodules with a trace of (**a**) carbide and (**b**) nitride nuclei.....122
Figure 9.10. Structure of (**a**) residual graphite nodule with a trace of (**b**) nitride nucleus [236]. 123
Figure 9.11. Structure of (**a**) residual graphite nodules with a trace of (**b**) staged nucleus.....124
Figure 9.12. Structure of (**a**) residual graphite nodule with a trace of (**b**) complex nucleus.....124
Figure 9.13. Graphite structures of (**a**) LS-CI, (**b**) HS-CI, and (**c**) AS-CI without involving treatment agents.....124
Figure 9.14. Graphite structures of LS-CI with (**a**) 10, (**b**) 5, and (**c**) 2.5 g FeSiMg6 as the treatment agent. 125
Figure 9.15. Graphite structures of HS-CI containing (**a**) 0.002, (**b**) 0.04, and (**c**) 0.1 wt.% S with 10 g FeSiMg6 as the treatment agent.....125
Figure 9.16. Graphite structures of AS-CI with 5 g (**a**) Mg-AlSn, (**b**) NiMg15, and (**c**) FeSi-CeLa as treatment agents. 125
Figure 9.17. Graphite structures of (**a**) LS-CI, (**b**) HS-CI, and (**c**) AS-CI with 5 g CaSi as the treatment agent. 126
Figure 9.18. Graphite structures of (**a**) LS-CI, (**b**) HS-CI, and (**c**) AS-CI with 10 g FeSi75 as the treatment agent. 126
Figure 9.19. Mg-modified inclusions as heterogeneous nucleation sites for lamellar graphite structures captured in (**a**) untreated LS-CI in **Figure 9.13a** and (**b**) HS-CI with 0.1 wt.% S in **Figure 9.15c**.....127
Figure 9.20. Mg-containing inclusions in the center of graphite nodules in HS-CI with 0.04 wt.% S in **Figure 9.15b**. 127
Figure 9.21. Al-containing oxide inclusions as possible heterogeneous nuclei of graphite structures in HS-CI with 0.04 wt.% S in **Figure 9.15b**. 128

Figure 9.22. Matrix configuration in Nital-etched conditions of AS-CI with 5 g of (**a**) Mg-AlSn, (**b**) NiMg15, and (**c**) FeSi-CeLa as treatment agents. 130

List of Tables

Table 3.1. Initial chemical composition (wt.%) of cast iron samples. 19
Table 3.2. AES analysis results (wt.%) of the boundary between the reaction layer and cast iron indicated in **Figure 3.6c**..... 22
Table 3.3. Chemical analysis (wt.%) of the extensive reacted layer indicated in **Figure 3.7**..... 23
Table 3.4. Chemical analysis (wt.%) of the spherical cavity indicated in **Figure 3.13**..... 28
Table 3.5. Chemical analysis (wt.%) of the graphite flake on edge reaction product indicated in **Figure 3.15**..... 30
Table 3.6. Chemical analysis (wt.%) on the cast iron matrix with the graphite structures indicated in **Figure 3.17**..... 31
Table 3.7. The chemical composition (wt.%) of the cast iron sample considered in the thermodynamic calculations using FactSage..... 37
Table 4.1. Initial chemical composition (wt.%) of cast iron before desulfurization. 45
Table 4.2. Chemical composition (wt.%) of measurement points indicated in **Figure 4.9**..... 50
Table 4.3. Changes in the Gibbs Free Energy for the possible formation reaction of calcium silicates during the lime-based desulfurization of molten cast iron at 1500°C calculated on FactSage..... 54
Table 4.4. Changes in the Gibbs Free Energy concerning the formation of liquid slag during the desulfurization of cast iron involving the formation of calcium silicates at 1500°C calculated on FactSage..... 54
Table 5.1. Initial chemical composition (wt.%) of cast iron before desulfurization. 59
Table 5.2. Chemical composition (wt.%) of analysis points indicated in **Figure 5.6b**..... 63
Table 5.3. Chemical composition (wt.%) of analysis points indicated in **Figure 5.7b**..... 64
Table 5.4. Phase configuration along the increasing ratio of Fe_2SiO_4 to Ca_2SiO_4. 70
Table 6.1. Initial chemical composition (wt.%) of cast iron before desulfurization. 75
Table 6.2. List of estimated specific emissions for utilized materials in magnesium-based desulfurization process..... 78
Table 6.3. List of estimated specific emissions for utilized materials in lime-based desulfurization process..... 78
Table 6.4. Effect of different desulfurization agent mixtures on the landfill classes of the desulfurization slag..... 80
Table 6.5. Average mechanical properties of CGI products made from magnesium- and lime-based desulfurized cast iron..... 81
Table 6.6. Comparative impact assessment (estimated CO_2eq) for desulfurization process of cast iron..... 82
Table 6.7. Cost estimation for the desulfurization process of cast iron (including possible slag disposal)..... 83

Table 7.1. Initial chemical composition (wt.%) of cast iron samples. 89
Table 7.2. Chemical composition (wt.%) of nonmetallic inclusions detected after chill casting as provided in **Figure 7.6**. 93
Table 7.3. Chemical composition (wt.%) of LS-CI after chill casting without and with three-minute holding. 96
Table 8.1. Initial chemical composition (wt.%) of cast iron samples. 105
Table 8.2. The chemical composition (wt.%) of the nonmetallic graphite nucleus provided in **Figure 8.8b**. 110
Table 9.1. Initial chemical composition (wt.%) of cast iron samples. 117
Table 9.2. Chemical composition (wt.%) of inclusions in residual graphite structures pointed out in **Figure 9.4**. 119
Table 9.3. Chemical composition (wt.%) of oxy-sulfide-based nuclei in residual graphite structures. 121
Table 9.4. Chemical composition (wt.%) of carbide- and nitride-based nuclei in residual graphite structures. 122
Table 9.5. Chemical composition (wt.%) of the compounding nuclei in the residual graphite structures. 123
Table 9.6. Chemical composition (wt.%) of Mg-modified nitride as a nucleation site for lamellar graphite. 126
Table 9.7. Chemical composition (wt.%) of Mg-modified sulfide as a nucleation site for lamellar graphite. 127
Table 9.8. Chemical composition (wt.%) of Mg-containing nuclei in graphite nodules pointed out in **Figure 9.20**. 127

PART I
Commencement

Chapter 1
Introduction

1.1. Research Background

Iron and steel casting has been a pivotal sector within the metallurgical industry for years due to its reliability in various industrial applications. A recent report by the European Foundry Association (CAEF) [1] indicates that iron and steel casting production in Europe reached around 10.7 million tons in 2021, of which approximately 3.2 million tons originated from Germany as one of the leading producers worldwide. Remarkably, among other diverse ranges of iron and steel casting products, a noticeable upward trend in the production of ductile cast iron (SGI) has been recorded [2], driven by its superior mechanical properties and versatility advantages. Reflected in Europe, SGI products constitute a significant portion of the total casting production. According to the abovementioned CAEF report, around 4.7 million tons of SGI were produced by CAEF members in 2021, and at least 20% originated from Germany.

Nevertheless, despite its industrial significance and long-standing circular practice through a recycling approach, as one energy-intensive operation related to a high-temperature process, the cast iron foundries registered in the European Pollutant Release and Transfer Register (PRTR) System are also responsible for approximately 0.2 million tons CO_2 emissions in Germany in 2021 [3]. Given that small and medium-sized enterprises dominate the cast iron foundries, the issue of emission reduction gains relatively less priority than in the iron and steel industries. According to Trianni et al. [4], the main reasons are strongly associated with the insufficiency of available resources followed by the more demanding urgency to sustain the business, which is entirely understandable from the perspective of industrial practice.

Based on the investigation conducted by Zhu et al. [5], three factors significantly contribute to the specific emission in the cast iron production process. The first factor is the production of initial charge materials. From this perspective, the increase in the emissions of cast iron production correlates to pig iron utilization [6, 7]. However, increasing the proportion of steel scrap to foundry-grade pig iron is not without limits. Excessive scrap consumption requires further adjustments, such as introducing a certain number of different ferroalloys and carburizers to maintain the standardized chemical composition of cast iron. Interestingly, based on the comprehensive life cycle analysis, this practice tends to be counterproductive, as previously investigated by Abdelshafy et al. [8].

The second factor is the melting operation to prepare the liquid metal. As further amplified by Mitterpach et al. [9], higher negative environmental impact is expected to be primarily influenced by the melting operation, specifically by the melting furnace used. This argument supports the finding of Finkewirth et al. [10], who suggest the employment of an induction furnace can deliver a reduced amount of specific emission compared to the cupola furnace. However, it is worth noting that induction furnaces highly depend on power generation. Therefore, unless the considered grid emission factor can be controlled to a specific limit as

described in [5, 11], induction furnaces are not always more eco-friendly than efficient cupola furnaces, as reported by Torielli et al. [12]. Since these factors could strongly influence the justifications of the life cycle analysis [13], any contextual consideration should also be carefully and impartially evaluated. Moreover, shifting the melting technology tends to be the highest possible barrier for the cast iron industry, making it unlikely to be a short-term strategy for small to medium-sized foundries.

Given the challenges connected to the other two factors, the treatment process of molten cast iron should be the starting point as the third factor mentioned in [5]. Particularly during the production of SGI and vermicular cast iron (CGI), it is known that a precise combination of various materials and treatment parameters is utterly necessary. One of those essential requirements is maintaining the required low sulfur content, where a desulfurization process is mandatory if a similar base iron possessing a higher sulfur concentration intended for lamellar cast iron (LGI) will be utilized. In this regard, magnesium or magnesium-containing alloys would be commonly used as desulfurization agents. A similar approach has also been conducted in the iron and steel industry, in which magnesium co-injection coupled with other substances into the molten pig iron has been transformed into a standard practice among steelmakers worldwide [14, 15]. This proven success rationally should have driven an adjustable adaptation for the cast iron industry, yet currently remains overlooked.

In addition to its contribution during the desulfurization process, magnesium-containing alloys have also been industrially practiced as nodularization agents to produce SGI. Despite its reliability and continuous advancements since its initial discovery in 1938 [16], the discourse surrounding the spheroidal graphite's nucleation, including its growth process, remains without a consensus. Following the subsequent patent in 1949 by treating the molten cast iron using cerium [17] or magnesium [18], this lack of clarity regarding the fundamental reason for the role of magnesium as a nodularization agent in establishing nodular graphite in SGI signifies the necessity for comprehensive elucidations. The fact that magnesium is seemingly irreplaceable in the process yet founded on an insecure explanation should have triggered continuous comprehensives.

Concurrently, given the increasing awareness of carbon emissions, employing magnesium presents at least two sustainability challenges that counterbalance its effectiveness in supporting SGI production. From an ecological perspective and comprehensive life cycle, the production of magnesium itself is related to unneglectable environmental risks that indirectly affect the carbon footprint of SGI-based cast iron products [19, 20]. Furthermore, high dependency due to a limited number of global primary magnesium suppliers raises concerns regarding supply chain reliability and market competitiveness [21, 22]. Therefore, it is rationally critical to challenge the status quo of utilizing magnesium by comprehensively addressing its unsettled roles during the desulfurization and nodularization processes before exploring technological alternatives to ensure both economic and ecological sustainability for the future of the cast iron industry.

1.2. Purpose of Study

Based on the previously provided research background that challenges the status quo of utilizing magnesium in the cast iron industry, this study addresses the following aspects:

(1) Identify the high-temperature interaction dynamics between magnesium and molten cast iron during desulfurization and nodularization.
(2) Examine the applicability of lime as a sustainable alternative desulfurization agent for molten cast iron.
(3) Explore the nearly irreplaceable role of magnesium during the nucleation process of spheroidal graphite structure in ductile iron.

1.3. Research Structure

Correspond to the above-defined purposes, this present research is comprehensively constructed into five different parts as follows:

(1) Part I (commencement) underscores the urgency of this study, defines its purposes, and describes the research structure. Moreover, this part also comprises a review of current developments relevant to the aspects addressed in this research.
(2) Part II (initial identification) supplies exclusively the exploration of the interaction dynamics between magnesium and molten cast iron at high temperatures, mirroring both desulfurization and nodularization processes.
(3) Part III (desulfurization) provides a comprehensive analysis of lime applicability as a reliable alternative desulfurization agent for molten cast iron. This part also assesses the reaction mechanism of lime and molten cast iron, followed by an ecotechnological analysis for the industrial implementation of lime-based technology.
(4) Part IV (nodularization) challenges the feasibility of magnesium-free production of ductile iron by exploring the graphite development during the recycling of ductile iron, identifying the heterogeneous nucleation of nodular graphite through observation of its dissolution behavior, and eventually explaining the irreplaceable role of magnesium in the production process of commercial ductile iron.
(5) Part V (denouement) is the final part of this present study, which comprises the general conclusion drawn from all results, including an outlook for further research.

Chapter 2
Current Research Status

2.1. Magnesium Interaction with Molten Iron

Compared to a similar application from the cast iron perspective, research regarding the high-temperature interaction between magnesium and molten iron was predominantly conducted in the desulfurization circumstances of pig iron during the steelmaking process. One of the pioneering studies related to this metallurgical aspect was published by Irons and Guthrie [23, 24, 25] by employing magnesium vapor. Based on their report, the dissolution of magnesium into the bulk of molten metal was essentially recorded. However, if no further reactions are considered, the dissolved magnesium is expected to re-evaporate following a prolonged high-temperature holding.

Based on the abovementioned studies, magnesium dissolution is regarded as a prerequisite of desulfurization, as the direct reaction between magnesium and sulfur at the bubble interface accounts for only one to ten percent of the whole chemical interaction. This argument is supported by observations indicating the magnesium influx from the bubble into molten iron was significantly larger than sulfur toward the interface. Consequently, the chemical reaction between magnesium and sulfur occurred predominantly within the bulk of molten iron, where their reaction products nucleate on the existing MgS particles. In this context, the pre-existing MgS inclusions are connected to the reaction products from the direct reaction at the bubble interface, which are stripped along the upward transport of the magnesium bubbles or other mechanical agitations experienced by the molten metal.

The concept of MgS heterogeneous nucleation related to desulfurization was also proposed by Lindström et al. [26], who conducted empirical examinations under laboratory conditions. Their study employed rapid cooling and comprehensive analysis to observe the interaction between solid magnesium and pig iron during desulfurization. It was found that no single MgS particles were observed as reaction products; instead, they were attached to the MgO particles. This investigation enhanced the results from Irons and Guthrie, even though the magnesium dissolution was not observable due to the batch addition technique of solid magnesium particles instead of continuous injection of magnesium vapor.

The interchange between the interfacial reaction and dissolution process of magnesium was further investigated by Yang et al. [27, 28] by employing magnesium vapor through in-situ aluminothermic reduction of magnesium oxide. Based on their observation, the mass transfer of magnesium and sulfur determines which mechanism will be preferable. Specifically, in the context of high sulfur concentration, a higher mass transfer of sulfur toward the interface is expected, thus inducing the interface reaction. On the contrary, magnesium dissolution could dominate the process during the initial stage of magnesium vapor introduction. The higher rate of magnesium dissolution was proposed to be correlated with the partial pressure in the bubble, which decreases over time as the bubble rises toward the molten metal surface and becomes the rate-controlling step.

Nonetheless, as amplified by investigation from Yang et al. [29] using in-situ carbothermic reduction of magnesium oxide, the rate gap of mass transfer between magnesium and sulfur during the initial stage of interaction is not necessarily significant; hence, both mechanisms should be considered. Since the partial pressure of magnesium during the upward transport gradually decreases, the proportion of interfacial reaction becomes preferable over time. Consequently, desulfurization on the surface of the magnesium bubbles was appraised as the primary mechanism countering the previous conclusion from Irons and Guthrie.

Amplifying the argument that magnesium-based desulfurization should take place on the surface of magnesium bubbles was recently reported by Su et al. [30] by employing a bottom injection of magnesium vapor coupled with a mechanical agitation apparatus. Their results indicated that the mass transfer process controls the desulfurization, but the effect of magnesium dissolution on the molten metal desulfurization can be neglected. Supplementary to their results, they argued that the dissolution mechanism proposed by Irons and Guthrie cannot explain the correlation between the magnesium bubble size and the desulfurization result, as provided by the same authors yet published in a separate report [31].

In addition to its response to the dissolved sulfur concentration, the behavior of magnesium in the molten iron is also determined by the dissolved oxygen concentration level. As reported by Yang et al. [32], the deoxidation reaction involving magnesium is much more preferable than desulfurization at specific oxygen concentrations. As a result, desulfurization cannot be exclusively determined by the equilibrium between magnesium and sulfur. To this extent, the dissolution level of magnesium will also be strongly affected. Based on their exploration, the dissolved magnesium level in molten iron will be significantly reduced, thus promoting the interfacial desulfurization reaction on the surface of magnesium bubbles.

Since the mechanism of magnesium interaction with molten iron is far from consensus, it triggered a further investigation by Sun et al. [33] using a simulation approach. Their study proposed that three stages would be involved in the entire process. In the initial stage, the magnesium concentration in the molten iron is insignificant; hence, the dissolution is more likely to proceed. As the concentration increases due to the continuous supply of magnesium vapor, deoxidation and desulfurization will start to overtake, yet it will still be coupled with a certain degree of dissolution. Eventually, during the final stage, a sharp increase in magnesium vapor is foreseen as low oxygen and sulfur levels are attained. Although dissolution can still be expected, the availability of free magnesium in the molten iron is vulnerable to evaporation, leading to a decreasing tendency of magnesium content.

Considering the research conducted in the iron and steel industry, an equivalent trial from a cast iron perspective was introduced by Deike et al. [34], who used a chill casting approach. Their results suggest an interchange phenomenon between MgO and MgS during the process dependent on oxygen and sulfur concentration, as Lindström et al. [26] mentioned to explain results reported by Visser and Boom [35]. Furthermore, their analysis also indicates that magnesium is anticipated to react initially with oxygen ahead of sulfur. Although cast iron possesses more alloying elements, their results resonate well with steelmaking examination, indicating a possible contextual interchange in process observation outcomes.

2.2. Lime as a Desulfurization Agent for Molten Iron

The lime-based desulfurization process could be a promising sustainable alternative to substitute or partially reduce magnesium consumption. In contrast to the cast iron industry, this approach has been practiced for years in iron and steelmaking operations, where co-injection with magnesium into molten pig iron is considered a standard procedure and technologically preferable. Besides directly reducing sulfur concentration through a chemical reaction, the lime (CaO) addition can avoid the resulfurization phenomenon since it forms a more stable calcium sulfide (CaS) than magnesium (MgS) [36, 37]. Nevertheless, the sole utilization of CaO is skeptically considered during steelmaking, as explicitly reported by Manachin and Shevchenko [38]. According to their industrial study, a single injection of high-quality lime for the desulfurization process of pig iron was appraised as reliable but followed by several challenges. These drawbacks comprise significant reagent consumption, decreased molten iron temperature, a notable prolonged process duration, and a substantial amount of generated slag, including iron loss.

However, given the supply chain, cost stability, and emissions advantages of CaO compared to magnesium, extensive research has been conducted to optimize the CaO proportion as a desulfurization agent. Oeters et al. [39] showed that the limitation during CaO utilization could be associated with the formation of solid reaction products. In their trials using a lime rod, a solid CaS-layer as a reaction product is expected to form in a silicon-free molten iron. If silicon was present, an additional dicalcium silicate layer (Ca_2SiO_4 or C2S) was detected between the CaO and CaS layers. Nonetheless, in both cases, those solid reaction products were observed to cover the unreacted CaO, thus hindering further desulfurization reaction as it entirely depends on rate-limiting solid-diffusion processes. Kawai et al. [40] also reported an equivalent result despite employing a different melting setup using a lime-based crucible instead of a lime rod.

The formation of CaS and C2S proposed by Oeters et al. was recently confirmed by Lee and Min [41] using a similar melting setup but was conducted in an inert atmosphere. Based on their observation, the formation of C2S is induced by the lime-based desulfurization process since no reaction layer on the surface of CaO can be observed in the absence of sulfur in the molten metal. The thickness of the formed C2S layer is also suggested to correlate with the presence of carbon. Specifically, a thicker C2S layer can be detected in the case of carbon-free molten iron considered in the experiment. This phenomenon is appraised to be related to higher oxygen partial pressure that promotes oxidation of dissolved silicon, indicating the crucial role of oxygen activity in sustaining the desulfurization process.

A different perspective for explaining comparable results was proposed by Boyd et al. [42], who suggested the possible involvement of a gas phase between the CaO-bearing materials and molten metal. According to their results, the development of the CaS layer on the surface of CaO does not necessarily require immersion into the molten metal as long as the sulfur can be transported to the interface. This concept was further amplified by Fruehan [43], who argued that forming C2S as a determining product of lime-based desulfurization is slow and requires gas intermediates. Based on their trials, SiS and S-containing gas were anticipated to evolve as vapor species from the molten metal. Accordingly, since establishing a continuous

under-pressure atmosphere would be challenging industrially, both research proposed the gas-injection method as a practical CaO-introduction approach to the molten iron.

The establishment of C2S as an associate product of the lime-based desulfurization process has also been proven to correlate with the size of lime particles. As reported by Lindström and Sichen [44] in their laboratory experiment comparing the performance of several commercial desulfurization agents, it is observed that fine CaO (<50 μm) particles did not exhibit the formation of the C2S layer. In this case, the fine CaO particles were detected to transform entirely into CaS. Accordingly, they argued that the fine CaO particles, if uniformly distributed, cannot build a local high oxygen concentration, which was pointed out by Lee and Min [41] as a crucial factor in forming the C2S layer. Interestingly, under the boundary of their study, it was also indicated that a certain quality of CaO can deliver a comparable desulfurization degree to a magnesium-based process.

As substantiated repeatedly in the abovementioned studies, the lime-based desulfurization process should complementarily be coupled with deoxidation to reduce the oxygen activity in molten iron. However, not every incorporation of a deoxidation agent effectively increased the desulfurization result. As later provided by Niedringhaus and Fruehan [45] and supported by Oktay and Fruehan [46], it is elucidated that adding aluminum improves desulfurization results but not zirconium (Zr), which theoretically possesses higher oxygen affinity. It was shown that the zirconium involvement only increases the initial desulfurization rate and indicates the role of low oxygen activity induced by deoxidation as the driving force at the starting point of the desulfurization process, as also reported by Nakai et al. [47].

Nevertheless, the effect of aluminum is also limited once the desulfurization temperature is set lower than the eutectic of the $CaO\text{-}Al_2O_3$ system. On the contrary, using CaF_2 and pre-melted $CaO\text{-}Al_2O_3$ has been proven to be more impactful, indicating the existence of a liquid phase is more necessary for sustaining the desulfurization process. The results in [45, 46] magnify the previous observation proposed by Mitsuo et al. [48], as they comprehensively observed the reaction layer between molten iron with and without the addition of aluminum during lime-based desulfurization. Based on their trials, in addition to reducing the oxygen activity, the role of aluminum is primarily promoting the formation of liquid slag during desulfurization. This liquid phase formation is associated with decelerating the involvement of passive layers C2S and the tricalcium silicate (Ca_3SiO_5 or C3S). Their report also proposes the existence of iron oxide ($FeO\text{-}Fe_2O_3$) and the $CaO\text{-}Al_2O_3$ as a ternary system, constructing the reaction layer between CaO and molten metal.

The sulfide capacity is another factor that determines the performance of the lime-based slag system in facilitating desulfurization [49]. Although the utilization of CaF_2 in [45, 46] as an additive in the lime-based desulfurization agent has decreased the melting point of molten slag, an excessive involvement of CaF_2 is considered counterproductive. This effect can be worsened if the lime-based slag has already been enhanced by adding Na_2O to improve its sulfide capacity, as once proposed by Vargas-Ramirez et al. [50]. Niekerk and Dippenaar [51] also reported that the CaF_2 in a $CaO\text{-}SiO_2\text{-}Na_2O\text{-}CaF_2$ slag system did not participate in the desulfurization and decreased the sulfide capacity upon further elevated proportion. Thus,

increasing the proportion of CaO/SiO_2 is, in a particular context, a preferable approach to improving the sulfide capacity, as suggested by Choi et al. [52].

The significance of increasing liquid slag and CaO-driven sulfide capacity in facilitating the lime-based desulfurization process is further amplified by Takahashi et al. [53]. Using a lime rod immersion approach, they revealed that the desulfurization rate was notably low if liquid slag was not considered in the processing system. Furthermore, it was also suggested that no sulfur detected from the molten metal could penetrate the CaO rod; thus, the role of CaO is primarily to supply and maintain the sulfide capacity of liquid slag. This argument aligns contextually with Boyd et al. [42], who proposed that the CaO is a sulfur getter and the reaction only occurs at the interface. To this extent, any penetration to solid CaO is only possible if the liquid slag is involved in the system, as once signified by Tanaka et al. [54]. Consequently, any significant existence of solid reaction products will obstruct and decelerate CaO availability before eventually scaling down the desulfurization process.

2.3. Nucleation of Spheroidal Graphite in Ductile Iron

In addition to the desulfurization operation, magnesium is commonly employed during the nodularization process to produce SGI and CGI. Nonetheless, particularly in the case of SGI, the necessity and role of magnesium in influencing the nucleation of nodular graphite are still under ongoing discussion. It is founded on the primary polarization in two arguments centered around the two classical primary theories of nucleation processes, namely the homogeneous nucleation concept based on the original work of Volmer and Weber [55] and the heterogeneous nucleation approach developed initially by Volmer [56].

From the perspective of homogeneous nucleation, it is proposed that magnesium does not directly contribute to the construction of nodular graphite nucleation. Despite being intriguingly debatable due to a significant undercooling of around 200-230°C [57, 58, 59] will be required, some studies suggest that the availability of carbon crystalline (C_n cluster) might provide effective nuclei for the nodular graphite. This idea was founded on the formation indication of a carbon-rich region, given the state of molten cast iron can be approached as a colloidal system [58, 59]. It is based on the early report from Krieger and Trenkler [60], who demonstrated an increasing tendency in viscosity associated with an elevated carbon concentration in molten iron.

Although a direct correlation between the carbon-rich region and nucleation of nodular graphite was not explicitly mentioned, its establishment driven by the addition of graphite or carbide into the molten iron has been proven to enhance the nucleation process of graphite structure. Loper et al. [61] reported that adding a graphite-bearing additive could act as an inoculant for flake graphite during LGI production. This result was further confirmed by Frost and Stefanescu [62] by introducing a preconditioning process involving the addition of graphite or SiC, which also proved to increase nodule count for SGI and the number of eutectic cells in LGI. In addition, as recently indicated by Stefanescu et al. [63], a possible C_n or $(Fe_3C)_n$ cluster was also experimentally detected and confirmed the possibility that such a cluster could serve as homogeneous nuclei for graphite. To a certain extent, it is also reported

that the formation of a carbon-rich region can be observed during the solidification process due to carbon rejection associated with primary austenite formation. Followed by a notable carbon segregation around the development of the austenite dendrite, eutectic graphite is expected to nucleate, representing a conceivable homogeneous nucleation process.

An indication of a possible direct connection between carbon-rich regions and the nucleation of graphite nodules involving carbon segregation was contextually reported in a review by Fredriksson [64]. His study was founded on observing inoculant dissolution behavior, which contains carbide or carbide-forming compounds. According to the set of studies provided, during the dissolution process of the inoculant, a certain degree of inhomogeneity in composition was established within the molten iron. This deviation in chemical composition was observed to favor homogeneous nucleation of graphite structure, including nodular graphite. One of his highlights was the correlation between local silicon enrichment in molten cast iron (segregation) that directly influences carbon activity. This perspective was enhanced further by the observation from Stefanescu et al. [63] and later confirmed by Semleit et al. [65] for SiC dissolution behavior in cast iron.

Furthermore, the indirect contribution of magnesium to the formation of nodular graphite nuclei and an indication of possible homogeneous graphite nucleation was demonstrated by Hara et al. [66], employing a combination of focused ion beam (FIB) milling for sample production and cross-sectional transmission electron microscopy (X-TEM) method for investigation. Based on their result, it is elucidated that magnesium is necessary to produce ductile iron. However, after carefully observing the nodular graphite structure, they argued that no magnesium-containing particles were found constructing the nuclei, and no other substance was seen as a core except the graphite structure itself.

A formation of nodular graphite without any addition of magnesium was once reported by Dhindaw and Verhoeven [67], relying on the solidification observation of synthetic cast iron melted and cast under vacuum. It is demonstrated that the production of nodular graphite is possible only if a sufficiently high cooling rate coupled with superheating can be guaranteed. Nevertheless, maintaining a high cooling rate was not the only determining factor since it is impossible to establish a comparable structure if low superheating and excessive high-purity melts were considered during the experiment. Conclusively, despite supporting the idea of the unnecessity of magnesium during nodular graphite nucleation, this research promotes the nucleation process on carbide substance and a heterogeneous approach instead of a homogeneous system, as supported later by the same authors in a different report [68]. Based on both studies, it is elucidated that no graphite nodule can be detected if ultra-pure charge material is employed unless nucleated with silicon (Si), calcium (Ca), or aluminum (Al).

Regardless of the unsettled debate on the possibility of any homogeneous nucleation, a pure iron-carbon-silicon (Fe-C-Si) alloy will rarely be considered in actual industrial operations. In practical scenarios, left alone with the various alloying elements, a certain degree of trace elements and impurities are always present in the molten cast iron. Therefore, the prevailing arguments favor the heterogeneous mechanism. However, this debate remains unresolved since two significant streams of ideas are also involved in this long-term discourse.

The first proposed theory is the magnesium gas bubble theory, which argues that nodular graphite nucleates at the interface of magnesium gas bubble and molten cast iron. One of the first reports supporting this perspective was published by Yamamoto et al. [69], who observed a magnesium treatment process of synthetic cast iron under different pressurized atmospheres. Their examinations indicated that nodular graphite does not nucleate if the atmospheric pressure exceeds the critical vapor pressure of magnesium. Furthermore, it is also elucidated that less magnesium was measured inside the graphite nodules than in the matrix, and magnesium-based compounds were not always detected inside the nodules. Conclusively, they proposed that both phenomena could only be explained using the gas bubble theory, where carbon in the supersaturated molten cast iron will precipitate into gas bubbles suspended in molten metal, thus forming spherical graphite nodules.

Despite being relatively unpopular, this theory recently gained support from Itofuji [70], who utilized an industrial trial approach followed by rapid cooling in a metal mold. The main idea relied on comparable reasoning that since the magnesium solubility in iron is low, a suspension between magnesium vapor and molten cast iron should be formed. Based on their observation, voids with enriched magnesium content associated with the magnesium bubbles were detected on the rapidly cooled sample if magnesium treatment was conducted. In this instance, it is also suggested that a trace of graphite was associated with those voids, thus indicating that graphite grows inward from the surface of the magnesium bubble. Non-metallic nucleations, including Mg-Si-Al-N and Mg-S, were also detected in the studied sample. Yet, their existence did not necessarily attach to graphite structure, thus becoming an enhancing argument that non-metallic inclusion is not always necessary.

As also highlighted earlier, the counterargument of the above gas bubble theory is the non-metallic inclusion theory, which suggests that nodular graphite nucleation takes place at the interface between non-metallic inclusion and molten metal. Interestingly, if there is one conclusive argument between these two ideas, that would be there is no definitive assertion that all nodular graphite has a non-metallic inclusion in its core, as Alonso et al. [71] suggested after a meticulous observation of a massive number of graphite samples. Nonetheless, compared to the previously mentioned theory, this view has garnered more significant support from various researchers utilizing diverse examination methods.

One of the earliest studies supporting the non-metallic inclusion theory was published by Jacobs et al. [72], who revealed that the nodular graphite nucleates at a duplex non-metallic inclusion related to the melt treatment. According to their report, the duplex structure is constructed by a sulfide core (Ca-Mg or Sr-Ca-Mg sulfide) and a spinel structure outer shell of Mg-Al-Si-Ti oxide before the graphite eventually grows epitaxially. As an enhancing point, their study also substantiated that a higher silicon level in the melt induces higher nodule density related to increased carbon supersaturation and favorable conditions for nodular graphite formation. Supplemented by another study published by Francis [73], it is proposed that the non-metallic inclusions have a dimension approximately 2 to 5 μm in diameter yet are primarily constructed by oxides (Ce-Fe-Mg-Si) coupled with a co-detection of particular sulfide composition. Furthermore, it is also pointed out that sulfur and oxygen content are detrimental in promoting nodular graphite nucleation, and their removal correlated with the

addition of Mg and cerium (Ce), as also mentioned by Jacobs et al. [72]. However, instead of focusing on their additional role as sulfide formation, Francis highlighted that adding Mg and Ce might increase the span of favorable solidification circumstances for the nodular graphite related to undercooling following a still-unknown mechanism.

In this particular context of sulfur concentration, Nakae and Igarashi [74] revealed that any disparities in sulfur content in molten ductile iron determine the composition of non-metallic inclusions found in the center of graphite nodules. Their comprehensive experiments involving synthetic cast iron containing various levels of sulfur and subsequently treated with multiple amounts of nodulizer showed that if the sulfur content in the base melt of ductile iron is less than 0.0022 wt.%, the rectangular nucleus of Mg-Si-Al-nitride is detected. On the other hand, if the sulfur content is higher than 0.005 wt.% but less than 0.084 wt.%, the spherical MgS will be observed as the nucleus in the nodular graphite structure.

In addition to identifying the exact chemical compositions in the single system of sulfide or nitride particles as demonstrated by Nakae and Igarashi [74], a supplementary contribution was put forward by Tartera et al. [75] and recently by Stefanescu et al. [76]. Based on their observations, a complex mixture and staged configurations can also be detected inside the nodular graphite hand in hand with the single system, contrasting a coexistence with the results provided by Jacobs et al. [72]. To this extent, instead of relying on a complex of various components, some investigations indeed highlighted the non-metallic configurations found as nodular graphite cores, as once demonstrated by Celis et al. [77]. Supplementing a separate publication by Jacobs et al. [78], their results in heavy-section nodular cast iron indicated that a duplex structure of MgS core containing CaS surrounded by MgO shell can be found inside a primary nodular graphite. On the other hand, a single system based on a mixture of MgS and MgO is measured inside a secondary nodular graphite instead.

Furthermore, in contrast to the abovementioned duplex approach, a triple-stage was once proposed by Skaland et al. [79] as a further possible modification, particularly at the oxide shell of the non-metallic inclusions. Based on their observation, inclusions found within the nodular graphite generally possess a sulfide core (MgS and CaS). This sulfide core is then surrounded by a configuration of an oxide shell typically made of $MgO.SiO_2$ or $2MgO.SiO_2$. During the inoculation process, the outer surface of this pre-existing oxide shell is expected to undergo chemical modifications. Specifically, the transformation from magnesium silicate configuration into either $XO.SiO_2$ or $XO.Al_2O_3.SiO_2$ was suggested, where X represents Ca, strontium (Sr), or barium (Ba) originating from the inoculant.

Since then, following numerous convincing early investigations, various supporting recent studies have been conducted with amplifying outcomes. Focus on a study observing the effect of Ca and lanthanum (La) in ductile cast iron production using the scanning electron microscopy (SEM) technique, Conhard et al. [80] reported that two main types of nuclei for nodular graphite exist, namely Mg-Si-based rectangular nuclei with traces of Ca, Al, La, and sulfur in comparison with Mg-Ca-La-sulfide spherical nuclei. In addition, by employing additional characterization techniques, including SEM, TEM, electron probe microanalyzer (EPMA), and auger electron spectroscopy (AES), Igarashi and Okada [81] confirmed the

existence of a round MgS particle with a diameter around 1 to 2 μm as a nucleus of nodular graphite. Based on their report, it is also substantiated that Mg-Si-Al-nitride and MgO were attached to the MgS particle beside the graphite structure.

The abovementioned observation results from Igarashi and Okada [81] are further amplified by a recent report from Qing et al. [82] employing TEM and FIB methods. However, instead of stating MgS as solely a nucleation site for MgO and Mg-Si-Al-nitride, they indicated that the nuclei of nodular graphite are complex compounds constructed by those components, although the formation of nitride components might take place later during solidification. This indication of nitride compound involvement during nucleation of nodular graphite was also investigated by Solberg and Onsøien [83] using SEM and TEM methods. Based on their observation, it is elucidated that an Al-Mg-Si-nitride-based particle can also function as an effective nucleus for the nucleation of nodular graphite.

Furthermore, distinct carbide and carbo-nitride substances were also detected in the core of the graphite nodule coexistence with nitride compounds. This phenomenon was reported by the results from Laffont et al. [84], who employed the scanning transmission electron microscopy (STEM) observation technique. They concluded that an iron-rich structure constructs the non-metallic core of nodular graphite structure. This iron-containing structure originated from the base material of the inoculant and covered by a magnesium-rich sulfide. Furthermore, a titanium carbo-nitride (Ti-CN) was reported to grow on the MgS structure before an Al-Mg-Si-nitride compound precipitated, surrounding or attaching to the Ti-CN compound. Their observation results align well with a recent study by Michels et al. [85], despite reporting more complex carbo-nitride containing Zr-Ti-Nb. Nonetheless, as demonstrated by trial results from Alonso et al. [86] by employing interrupted solidification experiments, it is also revealed that TiC alone can act as an effective nucleus for the early solidification of nodular graphite structure.

In addition to those sulfide, oxide, carbide, and nitride compounds, some investigations also reported phosphorous-bearing particles as a core of nodular graphite. This possible detection of phosphide is associated with Mg-La-Ce and attached to typical duplex structure MgS and oxides of Mg-Ca, as substantiated by Stefanescu et al. [87] and supported by Deike et al. [34]. In addition, a comparable phosphide is also suggested by Michels et al. [88], although it was appraised to coexist with oxides of Mg-La-Ce.

PART II
Initial Identification

Chapter 3

Interaction between Magnesium and Molten Cast Iron

Before aiming to assess and develop any possible alternatives for magnesium, it is necessary to comprehensively understand the reaction process during the high-temperature interaction between magnesium and cast iron, specifically during the desulfurization and nodularization processes. Detailed experimentation involving an interrupted reaction process employing a chill casting approach in a copper mold is developed to observe the reaction layer between magnesium and cast iron. Accordingly, this chapter demonstrated that rapid deoxidation and desulfurization reactions of cast iron involving liquid magnesium might occur following a specific dynamic mechanism before the magnesium ignition begins.

3.1. Methodology

This chapter included two types of cast iron, as delineated in **Table 3.1**. The first sample (designated HS-CI) comprised the cast iron produced by the cupola furnace. In contrast, the second sample (coded as LS-CI) pertained to a circulated nodular cast iron.

Table 3.1. Initial chemical composition (wt.%) of cast iron samples.

	C	Si	S	P	Mn	Fe
HS-CI	3.4 – 3.5	1.6 – 1.7	0.10 – 0.12	0.06 – 0.07	0.5 – 0.6	93 – 94
LS-CI	3.4 – 3.6	2.2 – 2.3	< 0.005	0.02 – 0.03	0.10 – 0.15	93 – 94

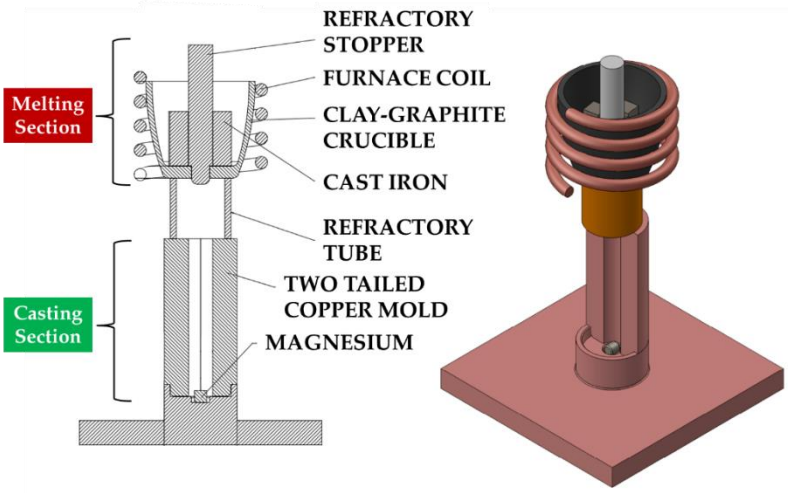

Figure 3.1. Experimental setup for high-temperature interaction between magnesium and molten cast iron.

A dedicated experimental configuration was developed to facilitate the high-temperature reaction and incorporate a rapid cooling mechanism to interrupt any subsequent continuous reaction between magnesium and molten cast iron. As represented in **Figure 3.1**, the experimental arrangement encompasses two discrete components: the melting and casting sections. The melting section is designed to prepare approximately 400 g of molten cast iron in a clay-graphite crucible. The crucible is equipped with a base opening yet initially secured

by a refractory-based stopper during the melting process. On the other hand, the casting section integrates a two-tailed copper mold (casting cavity of Ø25x130 mm) in which 1 g of pure magnesium metal (3N5) is positioned at the bottom of the mold.

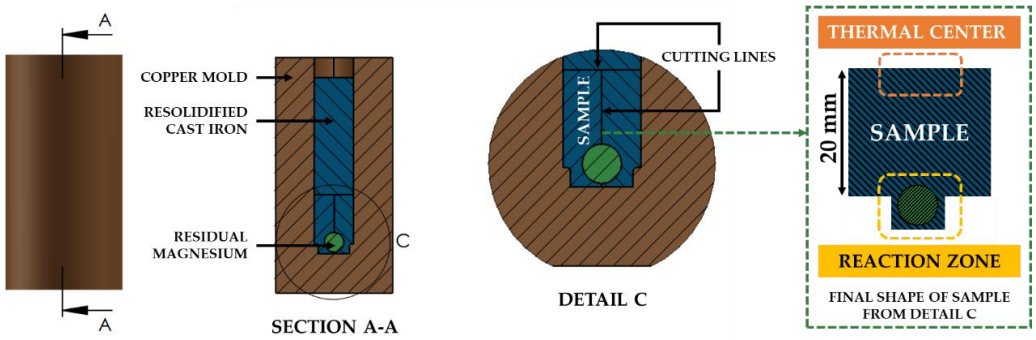

Figure 3.2. Sample preparation after high-temperature interaction between magnesium and molten cast iron.

The experiment started by positioning the stopper to close the base opening and containing the cast iron sample in the crucible. The system was then heated in an induction furnace under atmospheric conditions. Once the set casting temperature is reached, the stopper is retracted, allowing the molten cast iron to flow through the opening at the crucible base. The studied casting temperatures included 1300°C, 1400°C, and 1500°C were measured by a type-S thermocouple. As the molten cast iron flows through the casting section, it rapidly interacts with the solid magnesium. After cooling, each sample was extracted from the mold and cut, as highlighted in **Figure 3.2**. All the samples were subsequently metallographically prepared before being analyzed using light microscopy, scanning electron microscopy with energy-dispersive X-ray spectroscopy (SEM/EDS), and auger electron spectroscopy (AES).

3.2. Experimental Results

3.2.1. Reaction Layer between Magnesium and Cast Iron (ERP)

As shown in **Figure 3.3**, it is substantiated that the experimental configuration effectively interrupted the ongoing high-temperature reaction between molten cast iron and magnesium, as proven by captured residual unreacted solid magnesium (red box).

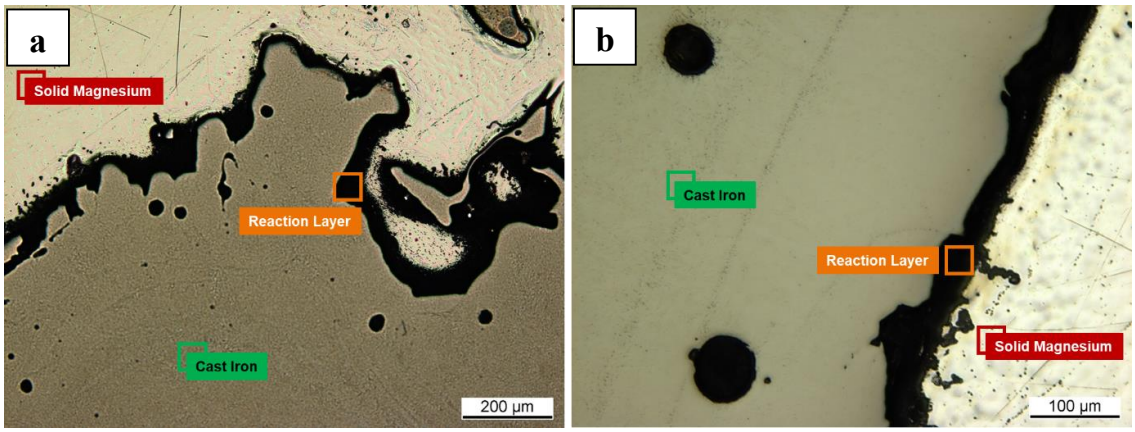

Figure 3.3. Typical reaction interfaces between magnesium and (**a**) HS-CI and (**b**) LS-CI under a light microscope at all studied casting temperatures.

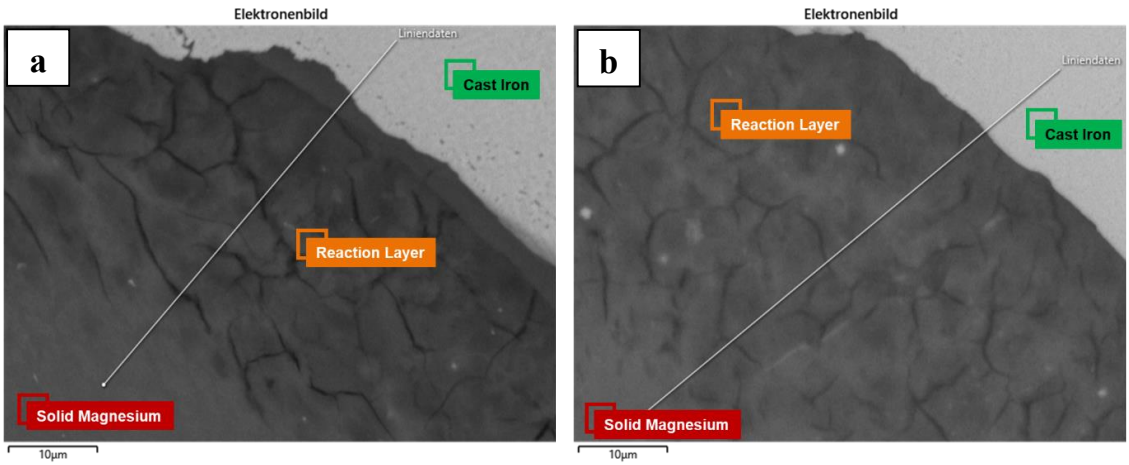

Figure 3.4. SEM images of typical reaction layer of (**a**) HS-CI and (**b**) LS-CI.

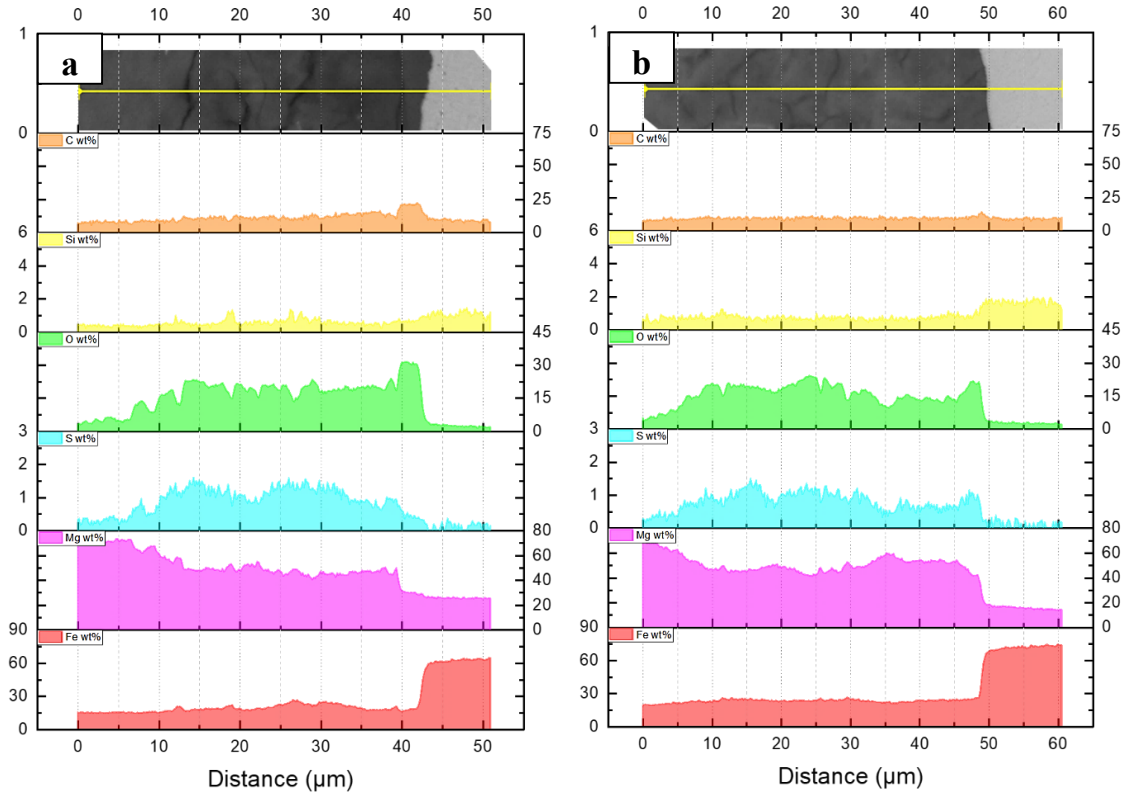

Figure 3.5. Chemical analysis results of the reaction layers indicated in (**a**) **Figure 3.4a** and (**b**) **Figure 3.4b**.

Notably, the interruption was not highly instantaneous enough to exclude all reactions; instead, the cooling rate was sufficient to successfully allow the molten cast iron (green box) to interact with the magnesium and form an observable reaction layer (orange box). According to these observations, irrespective of the explored melting temperatures, both HS-CI and LS-CI produced similar morphologies of the reaction layer, further denoted as edge reaction products (ERP).

As documented in **Figure 3.4**, the ERP is commonly detected as a solid phase accompanied by several notable cracks. In addition to the SEM observations, the initial EDS line-scan results revealed a consistent trend for both cast iron samples. Based on these analysis results, the ERP is indicated to be primarily composed of iron (Fe) and magnesium (Mg), followed by oxygen (O) and sulfur (S), represented by the red, magenta, green, and cyan colors in **Figure 3.5**, respectively.

Table 3.2. AES analysis results (wt.%) of the boundary between the reaction layer and cast iron indicated in **Figure 3.6c**.

Nr.	C	O	Mg	S	Fe
Sp. 1	2.3	41.4	46.5	0.4	9.4
Sp. 2	2.7	39.7	48.4	0.6	8.8
Sp. 3	11.1	24.2	12.6	0.8	51.3
Sp. 4	12.3	14.0	4.7	1.1	68.0
Sp. 5	12.3	3.1	1.5	0.3	82.8
Sp. 6	13.2	5.3	2.2	0.3	79.0
Sp. 7	17.5	12.7	5.9	0.7	63.3
Sp. 8	13.3	2.4	0.9	0.2	83.2

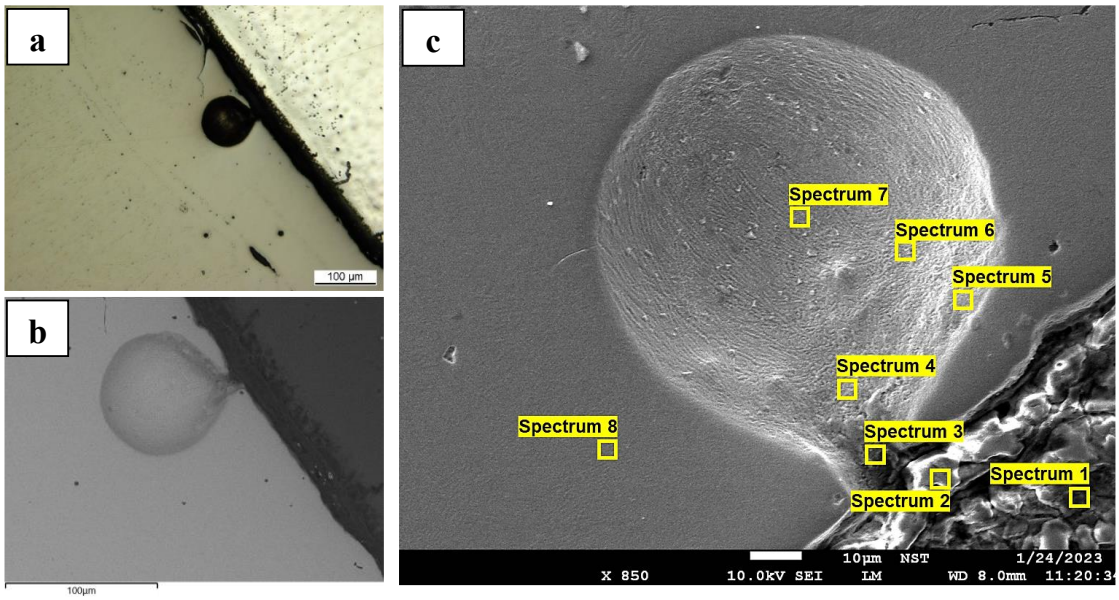

Figure 3.6. Evolving fluid under (**a**) light microscope and (**b**) SEM observation in addition to (**c**) detailed AES observation points on the reaction layer listed in **Table 3.2**.

Further analytical procedures were subsequently carried out to understand the interchange of the Mg-O-S system on the ERP. The first approach involved surface analysis of the barrier between the cast iron and the ERP using AES. As indicated in **Figure 3.6** and the analysis results in **Table 3.2** at spectrum (Sp.) 1 to 4, a sulfur enrichment in the region of cast iron (Sp.4) is detected compared with the ERP, which possesses a higher oxygen content (Sp.1). Another interesting observation is the emergence of an evolving fluid manifested as a round structure escaping the ERP. Based on its wall structure indicating a rough surface, this round structure is expected to represent a trace of a liquid phase. However, given its construction,

the possibility of a gas phase cannot be disclosed entirely. Therefore, both possibilities will be explored in detail in the discussion section. In addition, this AES measurement also revealed a high concentration of Mg-O-S in the center of this round structure compared with its outward regions (Sp.7 to Sp.5), indicating its relation to the reaction product.

Table 3.3. Chemical analysis (wt.%) of the extensive reacted layer indicated in **Figure 3.7**.

Nr.	C	O	Mg	Si	S	Fe
Sp. 1	20.3	18.9	35.0	12.4	4.6	8.8
Sp. 2	22.2	37.4	27.4	5.3	2.7	5.9
Sp. 3	23.7	27.7	29.3	11.7	3.9	3.8
Sp. 4	17.0	34.9	34.4	7.9	3.0	2.7
Sp. 5	30.0	40.3	17.4	7.7	0.7	3.9
Sp. 6	37.3	33.3	16.6	5.3	0.2	7.3
Sp. 7	40.9	39.0	11.9	5.8	0.5	2.0
Sp. 8	38.1	37.8	12.4	8.0	0.3	3.3
Sp. 9	4.8	10.0	40.6	5.1	2.5	37.0
Sp. 10	89.5	7.0	2.0	1.0	0.1	0.5

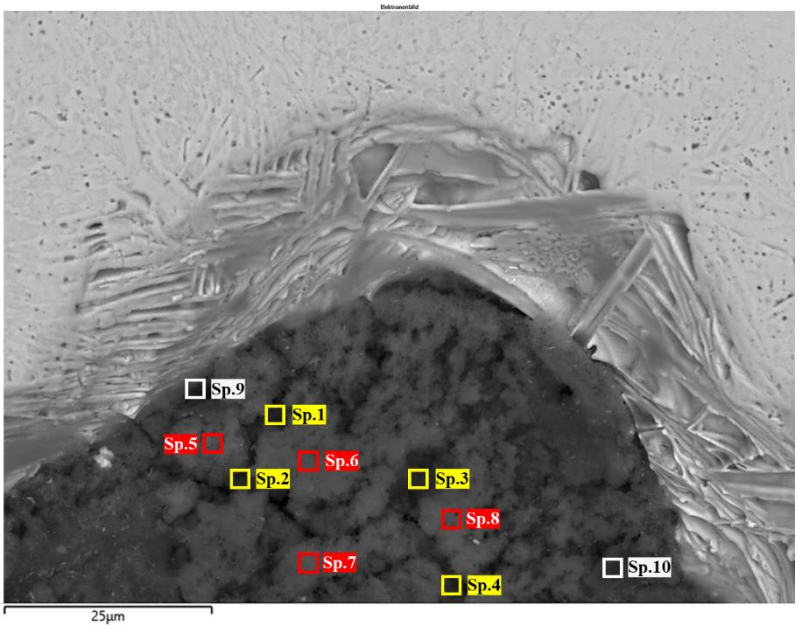

Figure 3.7. Alternative reaction layer morphology with minimal unreacted magnesium.

EDS was also employed as a second approach to explore the cracks at the ERP as possible inhomogeneity. In contrast to **Figure 3.4**, another ERP coupled with the expected significant high-temperature interaction was considered. As represented in **Figure 3.7**, the observable disintegration of the foremost region associated with the heterogeneity in the matrix structure of cast iron suggests that further reactions might be captured. It is necessary to mention that different morphologies of ERPs can coexist; hence, the disparity only indicates a different alignment with the cutting orientation. As anticipated, following the analysis in **Table 3.3**, the concentration differences within the ERP become apparent. This observation is highlighted by the yellow square in **Figure 3.7** (Sp.1 to 4), where higher sulfur

and magnesium contents are detected in contrast to the measurement regions indicated by the red square (Sp.5 to 8). Moreover, a negative correlation is also evident between silicon and oxygen in this crack region; meanwhile, the silicon itself is not necessarily correlated with the iron content. **Table 3.3** at Sp.10 represents even a significant high carbon content, indicating possible graphite precipitation.

3.2.2. Round Structures in the Reaction Zone (RRP)

Specific separated round structures are also detected while observing the reaction layer, as represented in **Figure 3.8**. Based on the SEM investigation, these structures exhibit a similar morphological appearance as the ERP, albeit with a different configuration. There are generally three observable appearances, as comparatively documented in **Figure 3.9**. However, this variation is practically only constructed by two systems: the round reaction product (coded as RRP) and the matrix heterogeneity denoting the boundary between the RRP and the cast iron matrix. In the case of matrix heterogeneity, its structure is also comparable to its ERP counterpart, as indicated in **Figure 3.7**. Still related to the ERP, the variance in **Figure 3.9** also coexists and thus should only be related to the cutting alignment. Nonetheless, it is worth noting that the representation in **Figure 3.9** might demonstrate specific processes that will be explored in the discussion.

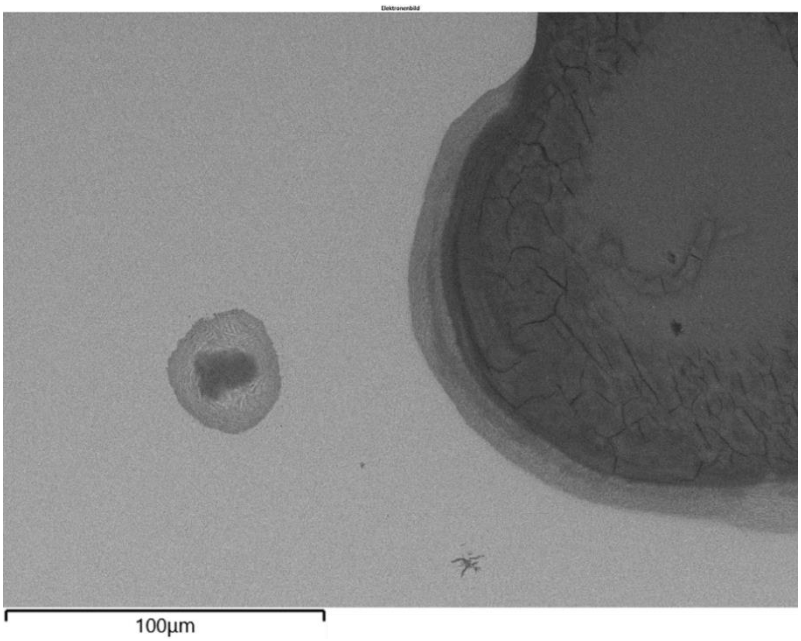

Figure 3.8. Round reaction product near the edge reaction product between magnesium and cast iron**.**

Their relatively comparable chemical compositions can also substantiate the morphological similarity of the RRP and the ERP. This assertion is emphasized by the elemental mapping result displayed in **Figure 3.10**, where the analysis reveals that the composition of the RRP also includes a blend of Mg-O-S components. Based on this element mapping results, the concentration profile of magnesium (magenta) has a relatively equivalent pattern to the oxygen (green) concentration. Considering the sulfur (cyan) content, the profile is tendentially influenced by the coexistence of oxygen. Specifically, it is indicated that an

oxygen-enriched region possesses a lower sulfur content. Moreover, intriguing silicon enrichment (yellow) within the matrix heterogeneity can also be observed in this instance.

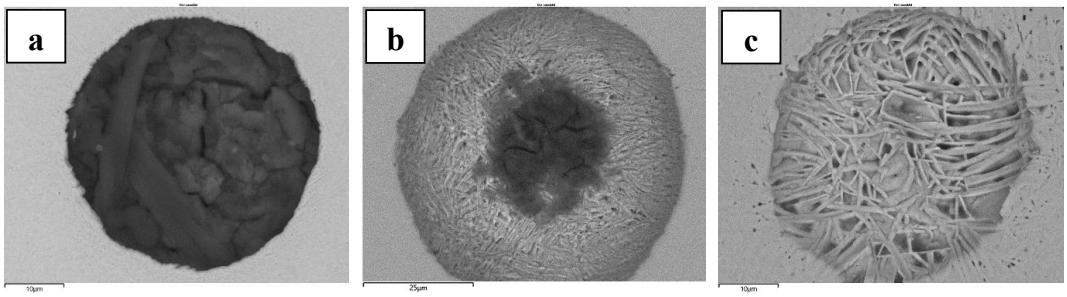

Figure 3.9. Different configurations of the round reaction products – (**a**) only the reaction product, (**b**) both the reaction product and the heterogeneous matrix structure, and (**c**) only the heterogeneous matrix structure.

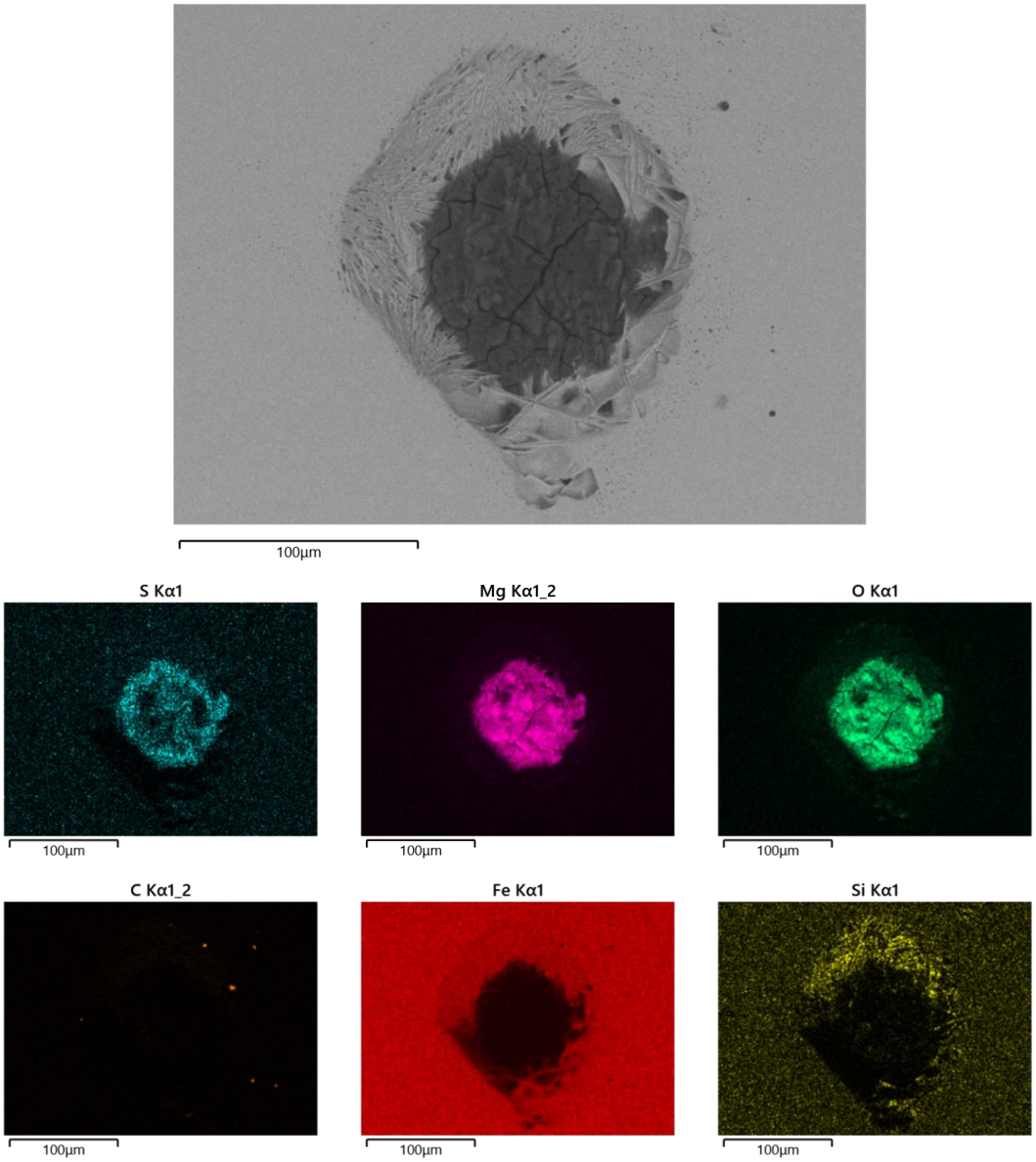

Figure 3.10. Element mapping analysis result for the round reaction product indicating the reaction product and the heterogeneous matrix structure.

Based on the element mapping results in **Figure 3.10**, a supplementary exploration was carried out to intensify the possible silicon segregation by analyzing the RRP boundary to the cast iron represented by the matrix heterogeneity, as detailed in **Figure 3.11**. Based on these analysis results, some increasing peaks of silicon content can also be substantiated without a direct correlation with the cast iron matrix, enhancing the previous analysis. In this case, according to the line scan results of both samples, the development of measured silicon (yellow) does not always match the iron concentration profile (red). It is also interesting to observe that the studied structure represents a bowl-like shape, where its heterogeneity indicates an intercrossing construction as if something were coming in between its channel.

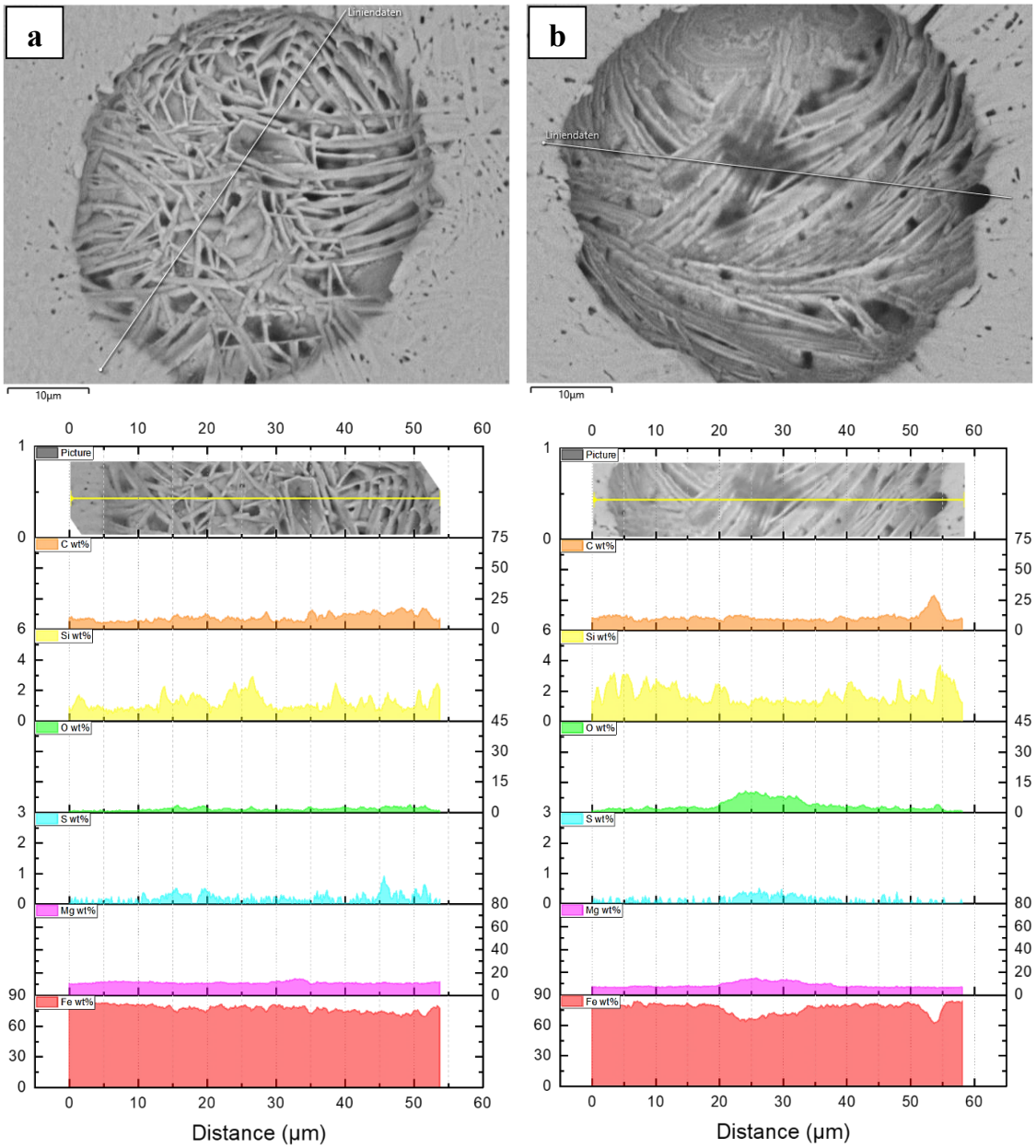

Figure 3.11. Line scan results for boundary layer of round reaction product for (**a**) HS-CI and (**b**) LS-CI.

3.2.3. Round Structures in the Thermal Center (HRP)

Considering the rapid cooling process involved in these experiments, in addition to the RRP typically found in the reaction zone (as indicated in **Figure 3.2**), another round object containing notable magnesium concentration was also detected near the thermal center, which was more common in the upper part of the studied sample. These round cavities, further named hollow reaction products (HRP), possess a spherical shape and tendentially have similar chemical compositions to those of the RRP. As documented in **Figure 3.12**, the chemical analysis indicated a substantial Mg-O-S concentration within the HRP, along with Fe-Mn-Si detection. It is worth mentioning that the dark area in the element mapping result is related to the EDS detector position, which indicates that this structure is indeed another bowl-like shape. However, in contrast to the previously explored compound Mg-O-S in RRP, although it possesses similar components in chemical analysis, this configuration hardly manifests the characteristics of the reaction layer.

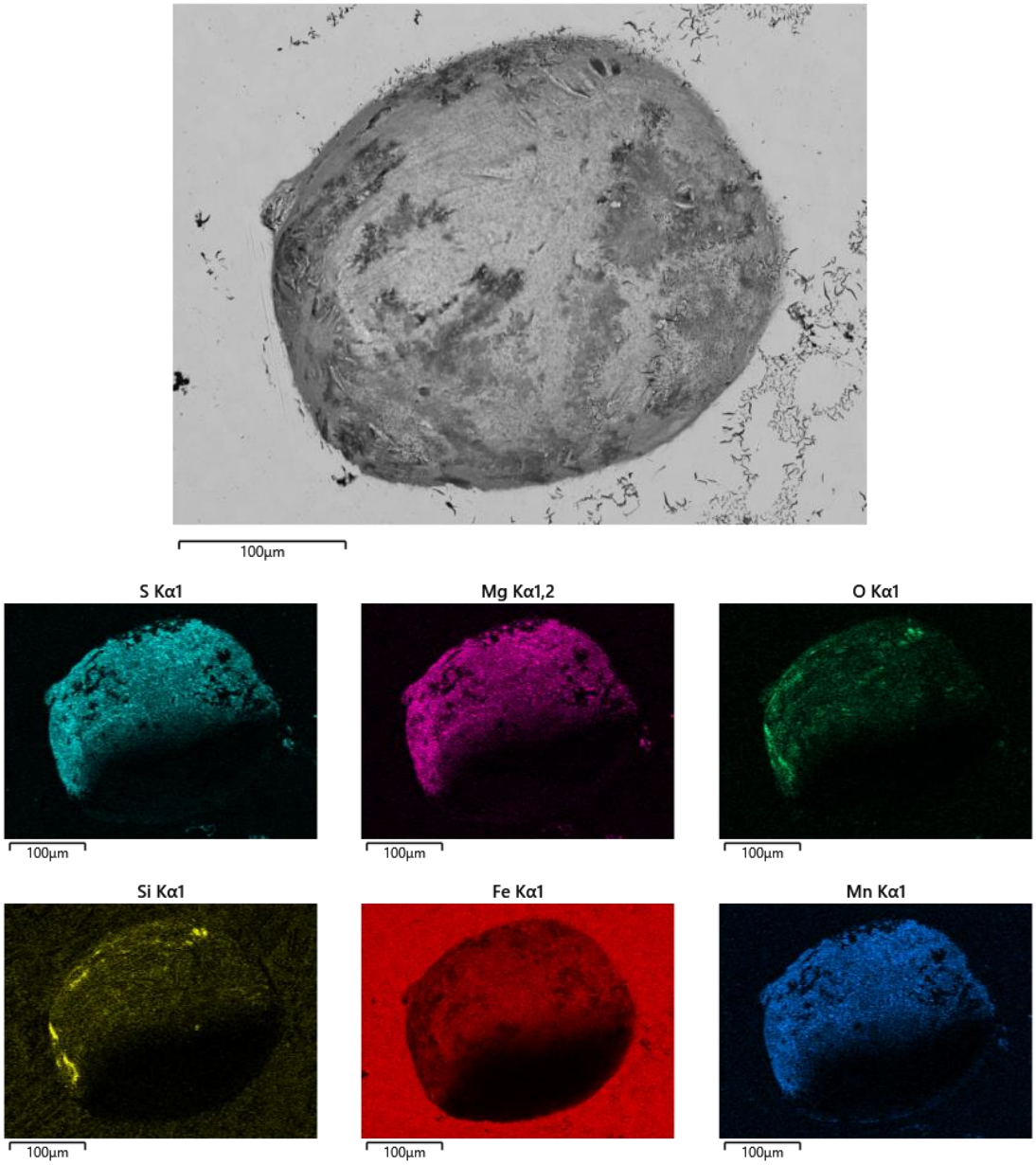

Figure 3.12. Element mapping result of the hollow reaction product in HS-CI.

A detailed observation of the wall structure demonstrated the disparity between this HRP and the RRP. As provided in **Figure 3.13**, the structure of the HRP reveals a solid matrix of cast iron with a well-distributed dotted structure instead of a cracked nonmetallic reaction product or heterogeneous matrix structure, as typically discovered in the RRP and ERP. According to the chemical analysis summarized in **Table 3.4**, the segregation of Mn-S-Mg generally covers the whole cavity. A notable concentration of Mn and S accompanied by Mg is detected on each darker spot; meanwhile, the matrix contains a more proportional fraction of Mn-S-Mg. Interestingly, some graphite structures can also be observed surrounding the structure, indicating late solidification. These differences suggest that this HRP might represent an entrapped ascended magnesium bubble.

Table 3.4. Chemical analysis (wt.%) of the spherical cavity indicated in **Figure 3.13**.

Nr.	C	O	Mg	Si	S	Mn	Fe
Sp.1	9.2	1.8	7.8	0.7	13.1	13.4	54.0
Sp.2	11.0	2.3	8.4	0.8	15.3	15.9	46.4
Sp.3	13.2	6.2	7.1	3.0	13.8	14.4	42.3
Sp.4	11.2	3.3	7.5	0.9	15.4	17.0	44.7
Sp.5	12.6	3.9	4.0	1.4	5.1	5.1	68.0
Sp.6	12.0	7.7	4.2	3.1	5.5	5.2	62.4
Sp.7	12.4	4.8	3.7	1.5	4.8	4.8	68.1
Sp.8	10.0	4.2	4.1	1.5	5.7	6.1	68.5

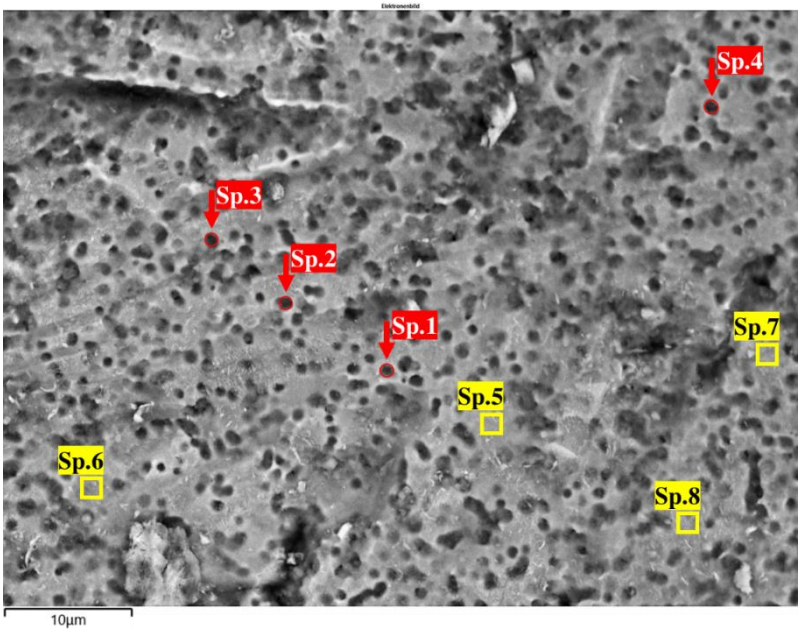

Figure 3.13. The wall structure of the hollow reaction product in **Figure 3.12**.

3.2.4. Graphite Layers on Nonmetallic Reaction Products

Another unique discovery from this experiment is the emergence of graphite flakes or stripes on the reaction product in the studied cast iron samples of HS-CI and LS-CI. Such sizeable graphite flakes are frequently observable on the RRP and only occasionally on the ERP, as captured in **Figure 3.14** and **Figure 3.15**, respectively. Furthermore, as documented

in **Figure 3.14**, the graphite structure grows connected to the cast iron matrix. Importantly, such a structure is not always found in all reaction products (RRP or ERP) but only in definite configurations following specific solute element segregation, dissimilar to typical chemical analysis results. According to the analysis provided in **Figure 3.14**, the graphite (orange) flake, to a certain extent, is followed by a significant enrichment in the sulfur content (cyan) and is occasionally coupled with a surge in the silicon (yellow) concentration.

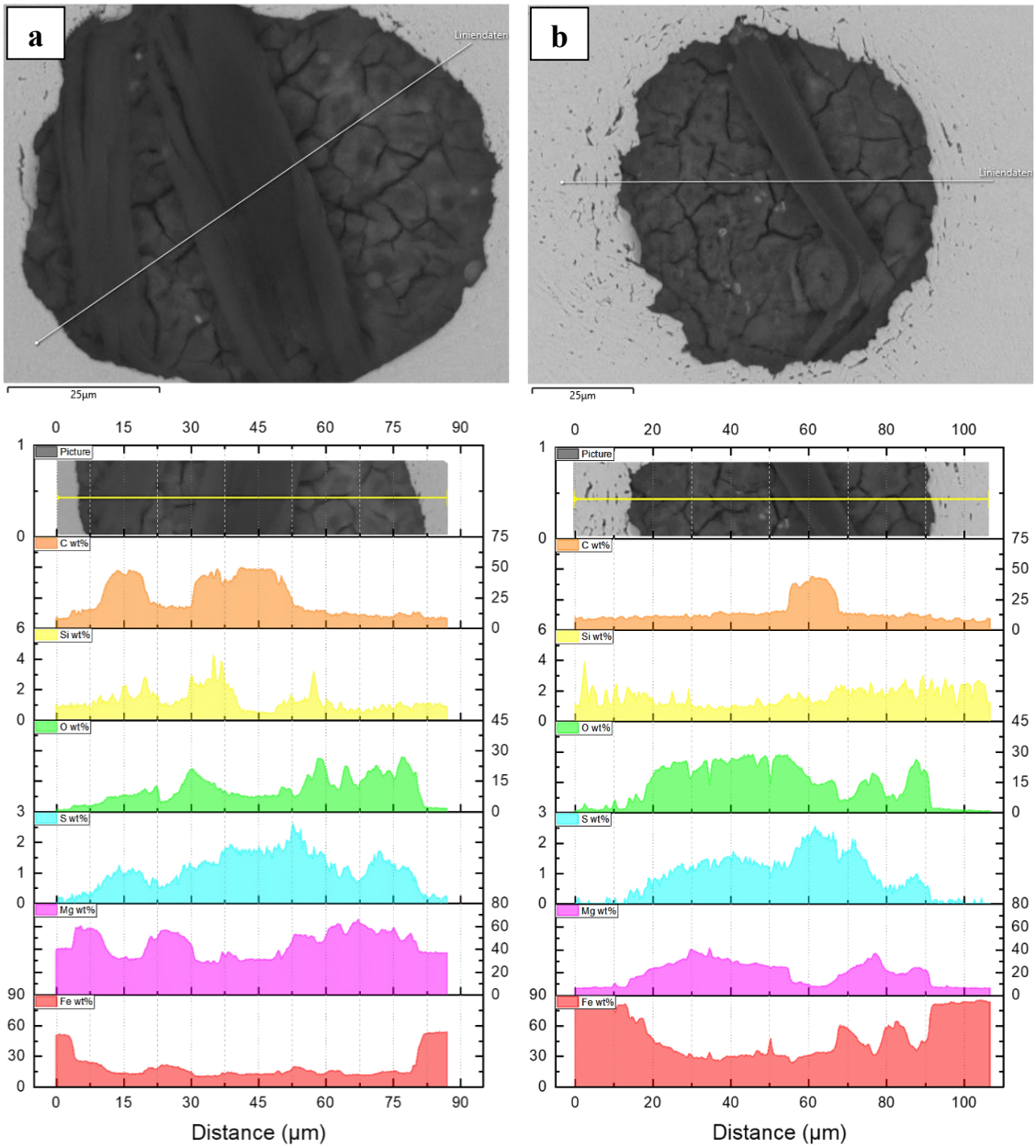

Figure 3.14. Graphite flake on round reaction products in (**a**) HS-CI and (**b**) LS-CI samples.

In addition to the analysis in **Figure 3.14**, measurements were systematically conducted on the surrounding graphite structure identified on the ERP, as documented in **Figure 3.15**. The results summarized in **Table 3.5** (Sp.2 and 3) also demonstrated that fluctuations in the concentrations of silicon and iron were measured. As previously highlighted in **Table 3.3**, an interchange between silicon and oxygen is also detectable, as presented by the similar

spectra in **Table 3.5**. Despite those measurements concurrently exhibiting a high iron content and comparable to the fluctuation in **Figure 3.14**, it should be emphasized that the correlation between silicon and iron might not solely refer to the matrix effect. As the detected iron content indicates, the mismatch between the measured silicon and the iron concentration profile might originate from independent, distinct phase systems and reaction mechanisms. The analysis in **Table 3.5** also suggested a negative correlation between the sulfur and oxygen concentrations at the measurement points relatively close to the graphite flake in **Figure 3.15**, supporting the previous results provided in **Figure 3.14**.

Table 3.5. Chemical analysis (wt.%) of the graphite flake on edge reaction product indicated in **Figure 3.15**.

Nr.	C	O	Mg	Si	S	Mn	Fe
Sp.1	13.9	30.0	51.2	1.0	2.2	-	1.8
Sp.2	18.8	10.0	17.8	9.6	7.3	-	36.5
Sp.3	20.6	4.6	17.6	18.2	10.4	-	28.6
Sp.4	70.4	27.0	1.4	0.8	-	-	0.5
Sp.5	71.8	27.8	0.1	0.1	-	-	0.3
Sp.6	68.1	30.3	-	1.4	-	-	0.3
Sp.7	65.2	32.5	0.1	1.7	-	-	0.7
Sp.8	38.1	40.0	14.3	5.6	0.3	-	1.8
Sp.9	28.3	34.2	10.7	5.6	0.3	-	20.9
Sp.10	6.7	-	0.4	1.3	-	0.6	91.1
Sp.11	7.8	-	-	1.4	0.1	0.6	90.2

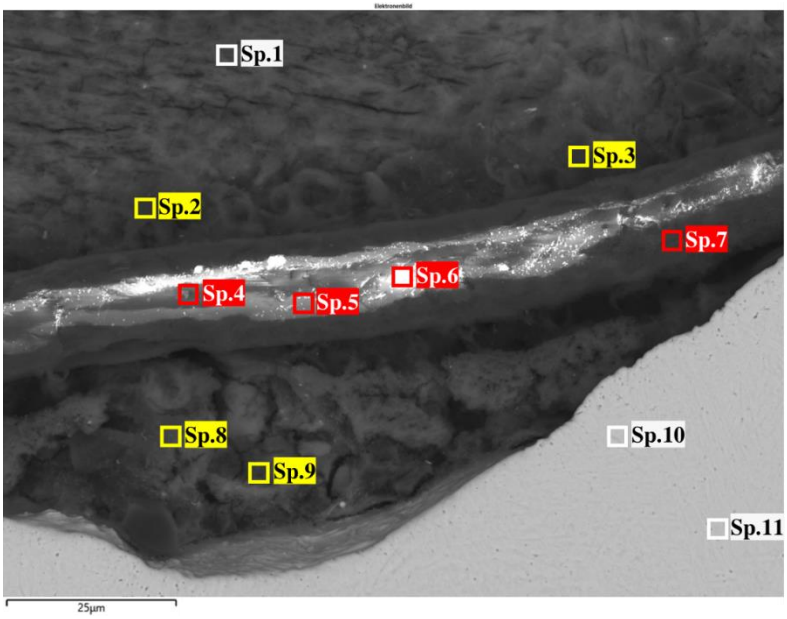

Figure 3.15. Detailed graphite flake structure located on the edge reaction product between magnesium and cast iron.

3.2.5. Effect of Dissolved Magnesium on Graphite and Matrix Structure

Notable variations in the matrix structure of the cast iron can also be observed during this set of experiments, which are correlated with the presence of the remaining magnesium.

As captured in **Figure 3.16b**, a random needle-like structure characterizes the cast iron matrix adjacent to the magnesium-rich area in the reaction zone, in contrast to the conventional ledeburite structure related to rapid cooling, as provided in **Figure 3.16a**. Supplementarily, identifying primary austenite dendrites is considerably rare in the matrix vicinity near residual magnesium and magnesium-containing reaction products.

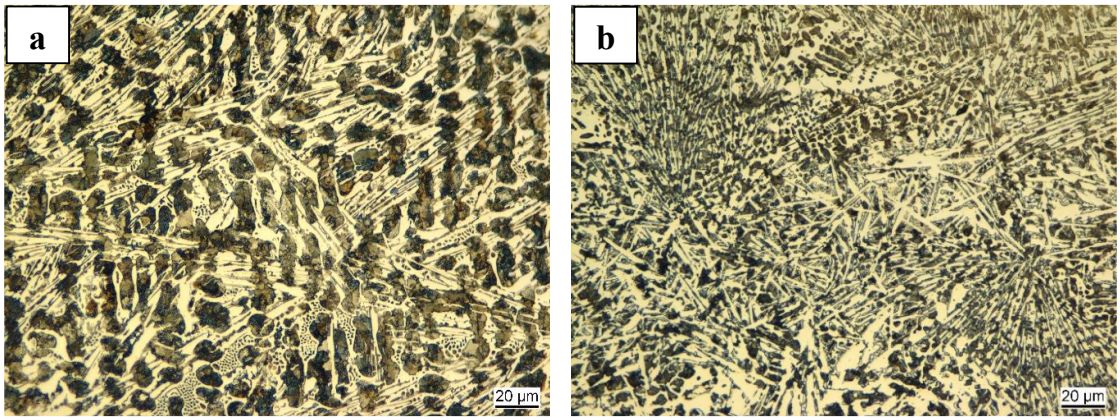

Figure 3.16. Matrix structure in the Nital-etched condition (**a**) away from and (**b**) near to the rest of the magnesium and reaction products.

Table 3.6. Chemical analysis (wt.%) on the cast iron matrix with the graphite structures indicated in **Figure 3.17**.

Nr.	C	Mg	Si	S	Mn	Fe
Sp.1	8.80	1.23	1.17	-	-	88.79
Sp.2	8.54	1.43	1.26	-	0.66	88.10
Sp.3	8.78	1.77	1.29	-	0.68	87.48
Sp.4	8.28	1.38	1.47	-	-	88.87
Sp.5	8.89	1.61	1.49	-	0.68	87.33
Sp.6	62.53	0.88	0.46	-	-	36.13
Sp.7	61.07	0.99	0.44	-	-	37.50
Sp.8	63.44	1.15	0.41	0.18	-	34.81
Sp.9	50.95	1.06	0.59	-	-	47.41

Following the modification in the matrix structure, as previously indicated in **Figure 3.16**, lamellar and nodular graphite coexistence can also be observed in the HS-CI sample near the magnesium-rich region. According to the EDS results summarized in **Table 3.6**, referring to the measurement points in **Figure 3.17**, a significant magnesium concentration can be measured on the cast iron matrix and the graphite structure despite having slightly different concentration degrees. However, given the size of the examined graphite structures, the measured magnesium should also be circumstantially influenced by the cast iron matrix except for Sp.8, which indicates the involvement of Mg-S particles. Since the sample studied was HS-CI, these nodular graphites nucleated during the process.

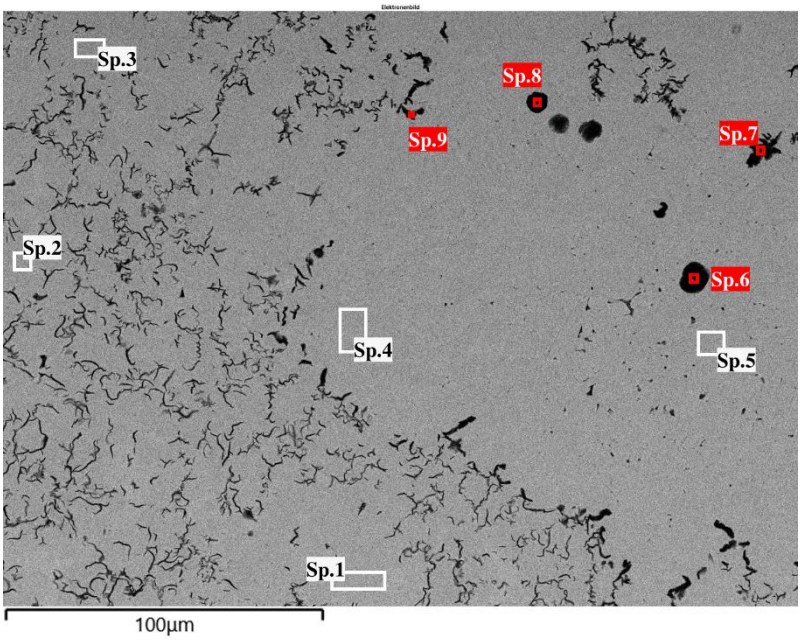

Figure 3.17. Cast iron matrix of HS-CI with the coexistence of lamellar and nodular graphite structures.

3.3. Analysis and Discussion

3.3.1. Reaction Mechanism of Magnesium in Molten Cast Iron

Based on the results of the present chapter, especially in **Figure 3.5**, the coexistence of Mg-O and Mg-S systems in ERP is highly anticipated. This result indicates that the developed reaction layers are a reaction product between magnesium and cast iron instead of being induced only by high-temperature oxidation, given that the experiments were conducted in an open atmosphere. This coexistence also suggests that both desulfurization and deoxidation are interconnected and determined by the diffusion and equilibrium of dissolved magnesium [Mg], oxygen [O], and sulfur [S] at the interface, as indicated by the following observations:

(1) The reaction products in the Mg-O-S configuration are detected adhering to the residual magnesium (**Figure 3.3** and **Figure 3.4**), thus implying that both reactions occurred at the magnesium-rich section and required adequate diffusion of dissolved oxygen and sulfur in cast iron.

(2) A significant magnesium concentration can be measured in the cast iron matrix near the reaction product (**Figure 3.5**). This suggests a sustained magnesium supply to the interface between magnesium and molten cast iron.

(3) A minor quantity of dispersed Mg-O-S particles (provided in **Figure 3.7**, more detail in **Figure 3.18**) can be detected in the bulk of the cast iron matrix at a certain distance from the interface and tends to surround only the reaction products, both detached or attached on the residual magnesium.

Conclusively, a continuous supply of magnesium is indeed anticipated. Nevertheless, its bulk diffusion rate into the molten iron was limited and could be overtaken by the transport rate of [O] and [S] to the magnesium-rich regions. As the reaction progressed, the diffused [O] could no longer balance the excessive magnesium supply. Hence, a subsequent reaction with

diffused [S] will be initiated interchangeably, resulting in solid MgO and MgS coexisting as reaction products. Notably, the sequence in which deoxidation first occurs is elucidated by the concentration gradient summarized in **Table 3.2**, which manifests early-stage interactions and aligns well with the proposed observation results reported in [32, 34].

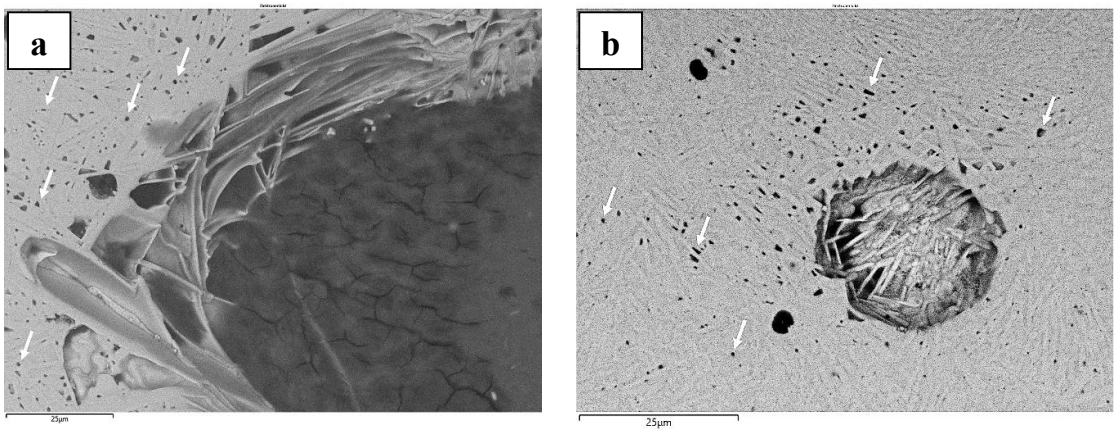

Figure 3.18. Dispersed Mg-containing particles found surround the (**a**) edge and (**b**) round reaction products.

Considering its high affinity for oxygen, magnesium naturally develops an oxide layer on its surface following atmospheric oxidation involving chemisorption, nucleation, and growth sequences [89]. This protective layer has an initial thickness of around 2 to 5 nm [90, 91] yet can decelerate further oxidation and any circumstantial evaporation until a temperature limit of 450°C [92, 93]. Above 450°C, the established oxide layer starts to crack and transform into a nonprotective porous layer, which is correlated with several factors, including the diffusion of vacancies during oxide thickening at lower temperatures [91], the development of internal stress due to a low Pilling-Bedworth ratio [94], the disparity in thermal expansion coefficients [93] and pressure at the metal/oxide interface at higher temperatures [95]. Eventually, these pores and cracks act as transport channels, initiating further and violent oxidation. Since oxidation is an exothermic reaction that releases heat, an even further temperature increase is expected, thus triggering the ignition of magnesium.

In his study, Czerwinski [96] introduced the term oxide nodules, which aligns with the oxidation mechanism mentioned above. The nodules are expected to grow at the oxide ridges, corresponding to nonprotective oxidation. Practically, this growth is associated with the interaction between the escape of magnesium and the penetration of oxygen at the established cracks on the oxide layer. According to his morphological observations, a comparative structure can also be visually identified between the proposed oxide nodules and the reaction products revealed in the present chapter, albeit with distinguishable chemical compositions. Hence, based on this possible resonance, investigating the reaction mechanism of magnesium in molten iron by incorporating the well-established concept of magnesium oxidation is practicable.

Nonetheless, besides considering nonprotective oxidation, the evaporation of magnesium should also be expected. However, the involvement of magnesium bubbles during the reactions should lead to a more complex mechanism based on the following contradictions:

(1) A trace amount should be measurable if the magnesium interaction depends only on magnesium bubbles [23]. However, no notable indication can be detected in the matrix.
(2) If the bubble growth were significant, rapid escape would instead be expected [26] because of the high vapor pressure of magnesium, which would retard dissolution.
(3) Conversely, an escaping fluid (in **Figure 3.6**) cannot be expected to arise from a liquid phase alone, given the tension between immiscible liquids [97]. This suggests that a certain pressure is available, preferably related to the magnesium vapor [98].

Consequently, it is difficult to presume that a single phase of magnesium engaged in the reactions. Therefore, the concept in [96] amplified by Takeno and Yuasa [99] in describing magnesium oxidation could be utilized, where a heterogeneous structure made of a mixture of magnesium liquid/vapor and solid magnesium oxide constructs the nonprotective layer on solid magnesium. Specifically, an interconnected porous oxide structure was suggested, where the liquid and vaporized magnesium squeezed through as they utilized the pores as transport channels. Based on those proposals, a comparable approach for describing the magnesium reaction with molten cast iron should also be plausible. **Table 3.3** shows that a higher magnesium concentration can be measured at the cracks (spectrum in yellow) compared to the surrounding area (spectrum in red) in **Figure 3.7**. Additionally, the sulfur concentration at those similar cracks is relatively high. Considering the early sequence of deoxidation ahead of desulfurization, as manifested in **Table 3.2**, it is indicated that any reaction that occurred at the cracks was a subsequent chain of reaction sequences.

The case in which significant chemical reactions have already occurred in the vicinity of cracks indicates that the evaporation degree had to be partially balanced by the physical interaction (dissolution) and chemical reaction (desulfurization and deoxidation) rates. This argument is based on the typical boiling curve first reported by Nukiyama [100], where liquid superheating (ΔT) is required to overcome the surface tension to develop and sustain bubble growth. As a result, chemical reactions at a specific number of initial cycles between magnesium and molten iron were expected to complete a tick before significant liquid superheating was achieved. However, as the reaction progresses, a local temperature increase driven by further high-temperature interactions and the formation of MgO and MgS can be anticipated. These two exothermic reactions, in particular, could also increase the temperature and induce local evaporation, resulting in a blowing channel to the cast iron matrix (**Figure 3.7** and **Figure 3.18**). This mechanism also circumstantially explains the existence of magnesium-containing particles in the gaps within the heterogeneous matrix structure, as indicated by the white arrows in **Figure 3.18**. Nonetheless, the degree of local temperature increase (value of ΔT) cannot be expected to have a one-constant number. Therefore, considering the dynamics in this high-temperature interaction, different boiling mechanisms could be involved, as explored in the next section.

3.3.2. Spherical Magnesium-containing Reaction Products

Although all experiments were conducted under atmospheric conditions, direct sublimation of magnesium (the triple point at ca.350 Pa [101]) is unlikely. As documented in **Figure 3.3** that indicate residual unreacted magnesium is present; hence, a phase transition (solid-liquid-gas) of magnesium during the early stage of interaction with molten iron can be characterized as follows:

(1) At the boundary of this experiment, as the molten cast iron interacts with the solid magnesium, the forefront of the magnesium at the interface transforms into a liquid phase. However, due to the high heat conductivity of the copper mold, the magnesium remains solid at a position significantly further from the interface.

(2) At the interface, the established liquid magnesium reacts first with oxygen to MgO and subsequently with sulfur to MgS. As mentioned earlier, both reactions are exothermic and can locally enhance the temperature increase of the magnesium liquid.

(3) Considering that ΔT represents a temperature gap between the superheated interface (iron/magnesium) and the bulk of magnesium, this local increase in temperature could be highly significant. In other words, a higher ΔT can be anticipated, shifting the boiling mechanism from nucleate to transition and eventually to film boiling.

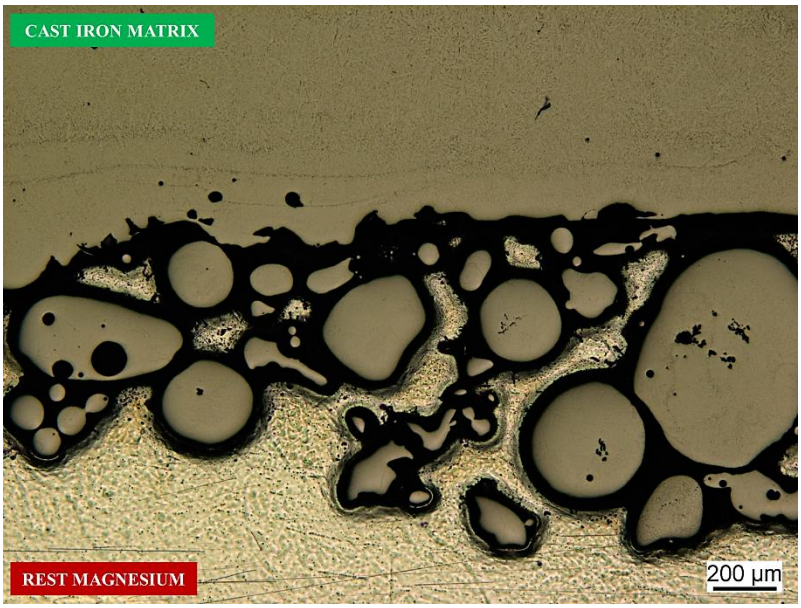

Figure 3.19. Trace of liquid fragmentation upon high-temperature interaction between cast iron and magnesium.

Based on the theories of vapor explosion, if a significant value of ΔT is considered, the interaction is expected to initiate liquid fragmentation following different approaches, as reviewed in [102]. In short, the interacting liquids are involved in dispersion dynamics, produce numerous tiny beads [103], and are eventually responsible for igniting uncontrolled vapor explosions [104]. In this chapter, a visual indication of liquid fragmentation was also recorded. As shown in **Figure 3.19**, a random dispersion of iron droplets within the magnesium (approaching the interface) should be correlated with the discussed phenomenon. A similar dispersion effect can also be examined in the cast iron matrix, revealed by the existence of RRP (**Figure 3.8** to **Figure 3.10**) and particle dispersion

originating from the reaction products (**Figure 3.18**). However, no two morphologically identical interaction points were recorded. This fact indicated that the interaction result is sensitive to several determining factors: concentration and temperature gradients, growth and morphology of reaction products, and heat transfer from molten iron, including exothermic reactions.

Compared with ERP, which adheres to residual solid magnesium, RRP is highly likely to reflect the fraction of liquid magnesium dispersed away from the interface. As indicated by its spherical structure provided in **Figure 3.9**, a homogenous liquid as a fragmentation product with a lower temperature gradient is foreseen. As fragmentation occurred, this dispersed liquid could also probably contain a certain proportion of solid MgO and MgS. Subsequently, a further reaction will occur on the crack at the solid reaction product. In this instance, a uniform temperature distribution could not always be ensured following a similar mechanism involving exothermic reactions producing MgO and MgS. Once a locally elevated temperature is reached, evaporation is enhanced, thus establishing a similar blowing channel that results in a distorted heterogeneous structure in the cast iron matrix (**Figure 3.11**).

In another case of round reaction product in addition to the RRP, considering the typical morphology of gas entrapment in cast metals, the best candidate for providing insight into magnesium bubbles is shown in **Figure 3.12** as a round and hollow (HRP) magnesium-rich structure. This is supported by the significant oxygen and sulfur concentrations that align with the involvement of surface reactions at the gas/liquid interface, as suggested in [29, 33]. Additionally, analysis of the wall structure of this HRP (**Figure 3.13**) in **Table 3.4** revealed that two distinct regions with different proportions in composition indicate the possible coexistence of MgS and MnS. This occurrence suggests that the availability of magnesium to react with surface-active elements of [O] and [S] was insufficient at the interface, thus triggering a dynamic between chemical reactions and a solubility limit.

Since this structure was successfully captured, it is rational to assume that the temperature of molten iron might be relatively low and that bubble movement was relatively slow. Based on these observations, the reaction mechanism involving HRP can be explained as follows:

(1) According to the mechanism explored in the previous sections, a reaction to MgO will be initiated at the early stage of interaction. Dissolved manganese [Mn], in this case, is not expected to play a role since the [O] concentration in molten iron (in the absence of magnesium) is preferably controlled by dissolved silicon or carbon [105, 106].
(2) Under a low level of [O], desulfurization begins. However, the magnesium supply is inadequate after a particular reaction time because of the formation of solid MgO and MgS. Therefore, the formation of MnS was induced by sulfur segregation, as reported previously in [107]. The existence of MgO and MgS can even enhance the formation of MnS by providing optimal nucleation sites, given their crystallography match [108]. In this stage, MnS can also be dissolved in MgS, constructing MgS-$_{MnS}$.
(3) During the continuous cooling process, the sulfur solubility is also reduced, amplified by the high concentrations of [C] and [Si] in the cast iron [109]. This interplay increased the sulfur activity, and the solubility limit of MnS might be reached. In this stage, secondary MnS nucleated [110], yet varied the morphology typically found in HS-CI

(angular type III [111]). This shift might correlate with the co-reaction of magnesium, although the MgS could also be dissolved in MnS, forming MnS_{-MgS}.

Given the wall structure of HRP, the first two stages are supposedly driven by chemical reactions, thus yielding a covering product at the interface. In contrast, the final stage involves nucleation actuated by decreasing solubility, establishing dispersed segregation. Moreover, MgS_{-MnS} and MnS_{-MgS} are calculated to compound a homogeneous mixture; hence, both terms are only introduced to indicate the dominant fraction [112, 113]. In industrial practice, such a significant temperature drop during the desulfurization of cast iron is less anticipated. Therefore, MnS establishment is less expected, but the upward travel duration would restrain the gas/liquid chemical reactions.

3.3.3. Possible Magnesium-induced Segregation and Precipitation

In addition to theoretical analysis, equilibrium calculations employing the thermodynamic software FactSage® were conducted to strengthen the provided discussion in describing the high-temperature interaction of magnesium and molten cast iron. Since the configurations of both reaction products in HS-CI and LS-CI are comparable, cast iron (further named FS-CI), with the chemical composition listed in **Table 3.7**, was considered to react virtually with magnesium. The FS-CI composition tends to follow the HS-CI sample to cover the involvement of manganese; meanwhile, high concentrations of [O] and [S] are intended to approach the segregation at the interface as surface-active elements. Calculating the different [O] and [S] values is unnecessary since it will only change the mass proportion, yet the reaction sequence remains constant. As variables, this section explored four interaction temperatures and six fractions (wt.%) of magnesium addition relative to a 100 g FS-CI sample. Additionally, only major solid and gaseous products are captured, as provided in **Figure 3.20** and **Figure 3.21**.

Table 3.7. The chemical composition (wt.%) of the cast iron sample considered in the thermodynamic calculations using FactSage.

	C	Si	S	O	Mn	Fe
FS-CI	3.5	1.7	0.2	0.1	0.5	94.0

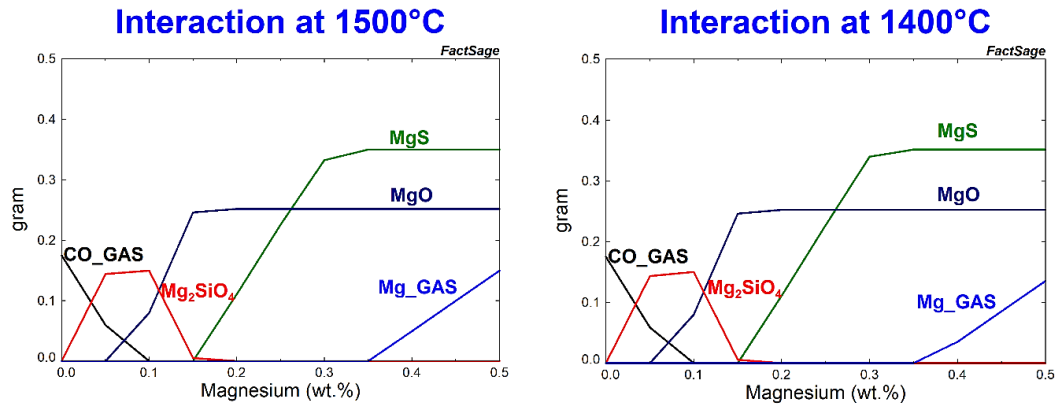

Figure 3.20. Equilibrium reaction products depend on the magnesium supply at higher temperatures.

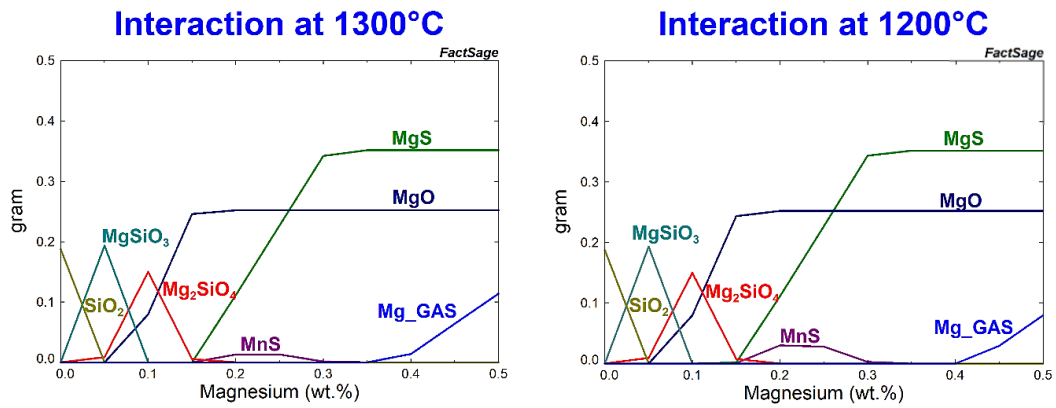

Figure 3.21. Equilibrium reaction products depend on the magnesium supply at lower temperatures.

Numerous ideas explored in the previous sections could be further confirmed based on the calculation results. If no magnesium was involved (wt.% = 0) during the interaction, the deoxidation process of molten cast iron would be dependent on [C] and [Si], as also described in [114]. As the wt.% magnesium content increases, independent of the temperature, the deoxidation process starts before desulfurization, as indicated in **Table 3.3** and **Figure 3.7**. Interestingly, at a wt.% of 0.15 - 0.20, the coexistence of both reactions is predicted, which is also practically considered in this chapter. By extending the region to a wt.% of 0.30 at lower temperatures (**Figure 3.21**), the nucleation of MnS is projected to follow the concentration of [S]. Since the sulfur content is correlated with magnesium addition, this MnS nucleation should also be related to the supply of magnesium, which was utilized to describe the reaction mechanism of HRP, referring to the provided results in **Table 3.4** and **Figure 3.13**. Eventually, it is also foreseen that less magnesium gas evolves at lower temperatures. This result implies that capturing a bubble at a lower temperature would be more probable since the pressure resultant can still be maintained by a lower vapor pressure (internal) and a higher viscosity of molten iron (external), which is also considered in explaining the HRP.

According to the observations in the present chapter, different elements are also observed to segregate in the vicinity of the magnesium-rich region, especially in the reaction zone. One is silicon [Si], an alloying element in both cast iron samples. Although its detection can be traced back to the matrix effect, it is not rare to have a measured silicon concentration with no direct correlation with the iron profile. In this case, its possible segregation is predicted to correlate with the establishment of magnesium silicate. This oxide is expected to be stable at a high concentration of [O] at the interface but with a limited magnesium supply (wt.% up to 0.20), independent of the reaction temperature. To this extent, the calculation also suggests that forsterite (Mg_2SiO_4) formation is preferable to the carbothermic reduction of SiO_2.

The presence of magnesium silicate might have been captured in **Figure 3.10**. Based on this element mapping, a certain enrichment level of silicon (yellow) was measured, covering the examined RRP. Following the silicon content, concentrated levels of magnesium (magenta) and oxygen (green) were also detected in that region, thus suggesting the possible existence of oxides made of the Mg-Si-O system. This configuration surrounding the RRP indicates

that the magnesium supply needed to balance further oxygen influx was inadequate, which can also be explained by the thermodynamic calculation results.

Consider a continuous influx of [O] and [S] from the bulk of the cast iron with decreasing magnesium supply (e.g., from 0.30 to 0.10 wt.%); the reaction product transforms from the MgO-MgS system into the MgO-Mg_2SiO_4 format. Following the reaction mechanism between magnesium and cast iron, in addition to the characteristic of the RRP as a predominantly liquid phase, as magnesium escapes through the pores toward the interface, the existing reaction products shrink due to similar factors that cause cracks on the former protective oxide layer. This sequence explains the configuration observed in **Figure 3.10** (as well as in the general ERP and RRP), where the Mg-O-S system can be detected in the center of the reaction product covered by the possible configuration of the Mg-Si-O system.

Another possible detection of silicon segregation compounding certain phases is evident in the unexpected presence of graphite flakes, as depicted in **Figure 3.15**. Based on the corresponding chemical analysis in **Table 3.5**, the measured region proximal to the graphite structure (sp.2-3) found at the ERP has noteworthy silicon, sulfur, and iron concentrations. A similar tendency is also substantiated in the comparable structure on the RRP, indicated by the line scan results in **Figure 3.14**, where the sulfur concentrations are undoubtedly high exactly on the measuring line where the graphite is located. These results for the sulfur content are critically significant for two reasons:

(1) The measured sulfur content is higher than typical reaction products, given that the detection is a background effect and the LS-CI possesses an initial low [S].
(2) The measured sulfur does not fluctuate following the oxygen profile, which is often the case for typical reaction products, indicating an intensive sulfur enrichment.

The possible relationship between high sulfur concentrations and the reaction products can also be seen in **Figure 3.7** and its corresponding analysis in **Table 3.3**. In this particular result, high carbon content is detected at almost every measurement point, where an indication of a graphite flake has even been revealed at Sp.10. Nevertheless, to the best of the author's knowledge, there is limited research on this specific phenomenon. A possible relation between sulfur and graphite formation was once reported by Moszynki et al. [115] for the case of surface carburized iron. However, relevant observations involving graphite precipitation during desulfurization were not available until reported by Schrama et al. [116]. According to their results, graphite flakes precipitate at the layer between the desulfurization slag containing MgS and the carbon-saturated iron. Adopting the equation that predicts the graphite solubility limit in molten iron developed by Neumann et al. [117], they argued that graphite precipitation was dominated by a low-temperature effect on the slag/metal interface rather than solute elements in iron.

Applying this perspective to the present observation results, if only the temperature governed the graphite precipitation, a graphite flake should be expected and could also be found on other common reaction products. The case in which the discussed graphite precipitated only at an atypical sulfur profile suggests that the role of solute elements and their possible segregation are practically unneglectable at the boundary of this chapter. Given the chemical

analysis near the graphite flakes and rapid cooling process, carbon supersaturation should be expected and associated with the behavior of solute elements at the interface. Specifically, since a notably high concentration of sulfur was observed, a significant increase in carbon activity and decreasing solubility could be expected [118, 119]. This occurrence of sulfur segregation might also explain the high iron content reported in **Table 3.5**. In addition to the possibility of direct FeS formation, interchange with MgS could also be expected, as reported in [34]. In addition to sulfur, this effect is enhanced by silicon segregation, as supplementarily indicated in **Figure 3.4**, which is also known to affect the solubility of carbon in cast iron [65, 120].

The intriguing dynamic in solubility also extends to [Mg], considering its expected possible limit in molten iron spans from 0.023 to 0.059 wt.% at 1600°C [121, 122]. The range was proposed by assuming the introduction method of magnesium vapor instead of being in a molten state. However, according to Trojan and Flinn [123], that number could be optimized if physical boiling could be avoided, which is the explored possibility in this chapter. Furthermore, based on their results, increasing [C] and [Si] affects the maximum level of [Mg] to a value of 2 wt.% (for 3.5 wt.% carbon), depending on the temperature. Considering the method employed in this chapter, a comparable level of [Mg] might be recorded in the EDS results in **Table 3.6** (EDS) and AES results in **Table 3.2**. This alignment is substantiated by the possibility that boiling might have been partially controlled, as indicated by the observed structure in **Figure 3.9** to **Figure 3.11**. The premise is also supported by their wall structure, which represents a random heterogeneous configuration comparable to the interface captured in [24] between magnesium bubbles and molten iron.

This interplay between [Mg] and [C] could be an additional principal factor in graphite precipitation where exceptional supersaturation is involved. Since carbon is not a surface-active element, its crystallization at the interface should result from other influencing solute components following the earlier interaction mechanism. The abovementioned local extreme carbon saturation could be approached circumstantially by adopting the equation proposed by Neumann et al. [117] as provided in **Equation (1)**. According to this equation, the maximum carbon solubility in molten iron represented by the liquidus line at the hypereutectic region should be affected by the concentration of other solute elements by considering a specific interaction value named the solubility factor (m'). Generally, if an alloying element has a negative value of m', it negatively correlates with carbon solubility.

$$\%\mathrm{C}_{\mathrm{max}}^{(\mathrm{Si,Mn,X})} = 1.3 + 2.57 \times 10^{-3} \cdot \mathrm{T} + \mathrm{m}'_{\mathrm{Si}} \cdot \%\mathrm{Si} + \mathrm{m}'_{\mathrm{Mn}} \cdot \%\mathrm{Mn} + \mathrm{m}'_{\mathrm{X}} \cdot \%\mathrm{X} \qquad \textbf{(1)}$$

Compared with silicon, magnesium was predicted (no experimental value available) to have a negative value of m'. This factor implies that the higher the concentration of [Mg] is, the more significant the expected increase in carbon supersaturation; thus, the chance of carbon precipitation intensifies. Furthermore, as also shown in [117], if the carbon solubility limit continues to decrease because a significant concentration of alloying elements possesses a negative value of m', a deviation of the hypereutectic liquidus line is theoretically possible. Enhanced by the tendency of alloying elements with a negative value of m' to have an

additive effect on the value of the carbon equivalent (e.g., Si), a shift from hypoeutectic to hypereutectic could be inevitable.

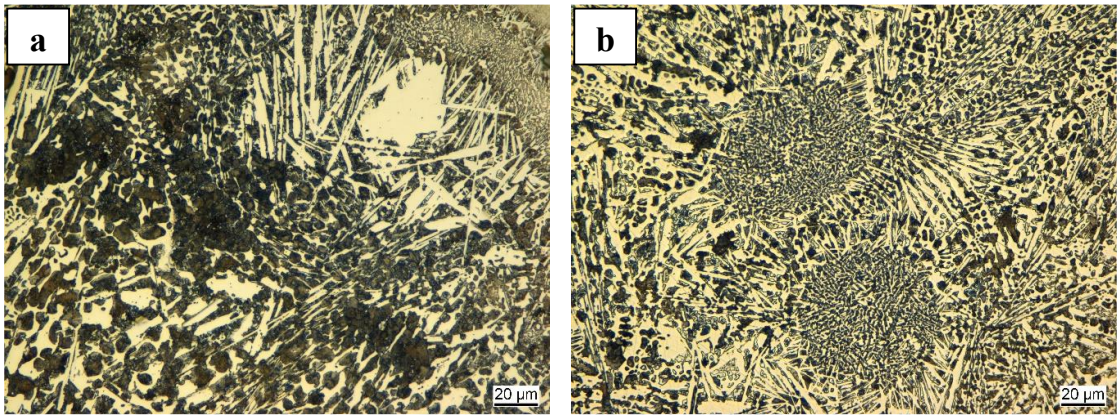

Figure 3.22. Matrix variances (Nital-etched condition) of (**a**) HS-CI and (**b**) LS-CI with high dissolved magnesium concentrations.

This effect is also evident and substantiated by the shift in the matrix structure at the reaction zone, as provided in **Figure 3.16** and detailed in **Figure 3.22**. These results show several disparities, including a lower proportion of primary austenite, increased eutectic solidifications, and even a primary cementite that starts to nucleate. Such an adjustment is only possible if the equilibrium has been remarkably changed and not only due to the Scheil-cooling effect [124]. A similar argument was reported by several researchers [125, 126, 127], who suggested that [Mg] cannot be neglected as a significant factor in the carbon equivalent despite further research still being highly demanded.

3.4. Summary of Magnesium and Cast Iron Interaction

Based on the observation results of this chapter, in which the reaction of solid magnesium with molten cast iron was examined at temperatures ranging from 1300°C to 1500°C, the following findings could be drawn:

(1) The investigation results revealed that liquid magnesium formed on the surface of the solid magnesium during the initial phase. The established liquid magnesium is expected to react sequentially with dissolved oxygen and sulfur at the interface.

(2) As the high-temperature interaction continues, further reactions occur at the crack established in the preexisting solid reaction product (MgO or MgS). In this instance, a certain degree of superheating could be established depending on heat transfer and enhanced by the exothermic reactions of the formation of MgO and MgS.

(3) Depending on the degree of superheating, a boiling mechanism can be initiated. Nucleate boiling is expected to dominate the local low-temperature gradient. This mechanism is observed as a blowing channel escaping the reaction product, explaining the Mg-containing particle filling the gap within the heterogeneous matrix.

(4) In an alternative case, potential liquid fragmentation related to a certain degree of film boiling is anticipated at high superheating. Consequently, fractions of liquid magnesium with or without preexisting solid products are dispersed into the iron

matrix, establishing magnesium droplets that eventually follow a similar reaction sequence.

(5) Considering that magnesium vapor escapes from the interface, ascending magnesium bubbles are expected. In this instance, surface reactions to MgO or MgS could be anticipated depending on the travel time before reaching the open atmosphere.

(6) In addition to the reaction mechanism, an intriguing carbon precipitation is observed at a specific configuration of a reaction product. This reaction product is characterized by an atypical significant sulfur concentration coupled with silicon segregation.

(7) In terms of carbon solubility, this research demonstrated that a shift in cast iron solidification is plausible with a certain amount of dissolved magnesium.

PART III
Desulfurization

Chapter 4

Lime as Desulfurization Agent for Molten Cast Iron

After comprehensively describing the role of magnesium during the desulfurization of cast iron in the previous chapter, this present chapter examines the prospective application of lime as a sustainable desulfurization agent for the cast iron industry. The investigation encompasses laboratory experiments that explore two methods for introducing lime powder onto and into molten cast iron using surface addition and gas injection techniques. Based on the findings of this chapter, lime could technically be a reliable cast iron desulfurization agent by reaching an end-sulfur concentration of <0.015 wt.%, thus providing an opportunity for a sustainable alternative for the foundry industry.

Publication Note:
During the manuscript preparation until the final submission of this dissertation, this chapter is a part of a published research article in Steel Research International [128].

4.1. Methodology

In the first experimental setup using a surface addition method (coded ON-AD), 1 kg of cast iron with the chemical composition listed in **Table 4.1** was melted in an alumina-based crucible using an induction furnace under atmospheric conditions, as illustrated in **Figure 4.1**. This crucible is selected based on test results provided in separate reports [129], considering the future application of this lime-based desulfurization in the cast iron industry. The trial ran for 40 minutes, in which the desulfurization agent was introduced three times: immediately after melting, after 10 minutes, and after 25 minutes, which eventually comprehends the total amount of 40 g CaO-powder (Fels 94.8% CaO and a particle size of <100 μm) excluding the additive (C, Al, Si) addition. Metal sampling was conducted every five minutes to monitor the change in the sulfur content, and slag collection was performed at the end of every trial.

Table 4.1. Initial chemical composition (wt.%) of cast iron before desulfurization.

C	Si	S	P	Mn	Fe
3.4 – 3.5	1.6 – 1.7	0.09 – 0.12	0.06 – 0.07	0.5 – 0.6	93 – 94

In the second experiment using an injection method (named IN-AD), a lime injection test was conducted employing an apparatus that could introduce 20 g desulfurization agent (CaO and pure carbon powder excluding Al) into 1 kg of molten iron using nitrogen as the transport medium, as shown in **Figure 4.2**. A venturi nozzle was used as the core equipment in the apparatus, where the pressure of nitrogen was utilized to carry the powder stored in a separate container equipped with a screw conveyor to maintain a constant supply.

In this instance, the cast iron in **Table 4.1** was melted (in circumstances similar to ON-AD) at 1500°C and measured continuously by a type-S thermocouple. The desulfurization agent was uninterruptedly injected for 3 minutes at a constant nitrogen flow rate (0.9 Nm^3/h at 1.5

bar) into the molten iron using a refractory-coated metal lance. Comparable to the ON-AD setup, a metal sample was also taken before and after the lime-powder injection process to contrast the change in the sulfur content associated with the desulfurization process. After the injection, the lance was retracted from the molten cast iron, and the emerging slag on the surface of the molten iron was subsequently removed and collected for further analysis.

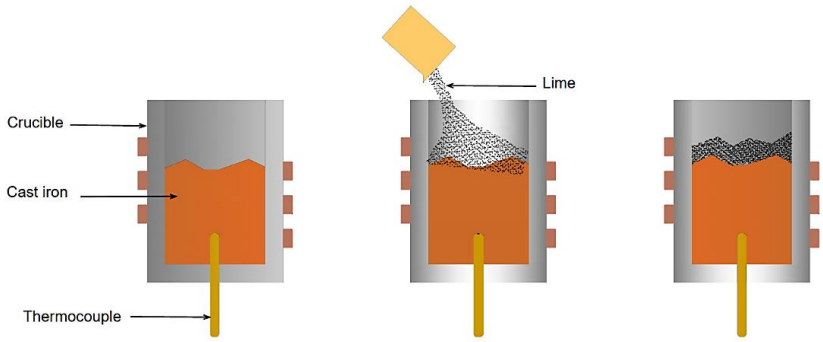

Figure 4.1. Illustration of the lime-based desulfurization process for molten cast iron using the surface addition method.

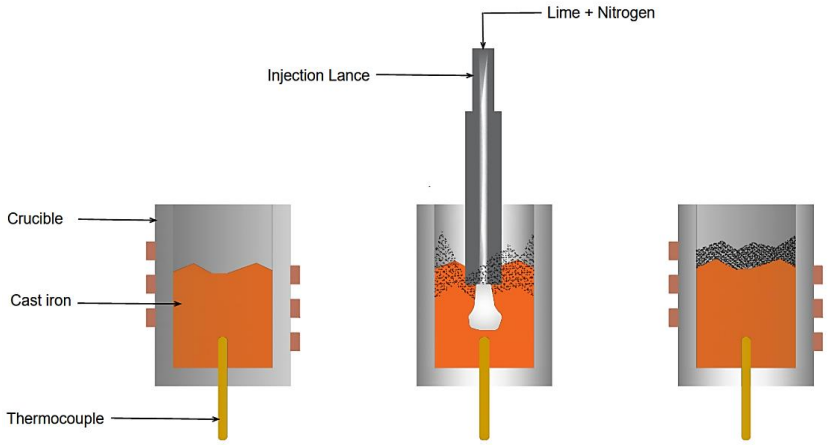

Figure 4.2. Illustration of the lime-based desulfurization process for molten cast iron using injection method.

Eventually, the chemical compositions of all the metal samples from ON-AD and IN-AD, primarily the carbon and sulfur contents, were analyzed using an optical emission spectrometer (OES) and confirmed by a combustion carbon-sulfur (CS) analyzer. In addition, slag samples were prepared and subjected to metallography analysis using a light microscope and scanning electron microscope with energy-dispersive X-ray spectroscopy (SEM/EDS). It is important to note that the slag preparation involved a water-free process, and the analysis was conducted immediately after preparation to avoid any possible hydration of unreacted CaO.

4.2. Experimental Results

4.2.1. ON-AD: Lime Desulfurization by Surface Addition

The ON-AD setup primarily examines the effects of different lime-based desulfurization mixtures on the degree of desulfurization. Within the research boundary, the applicability of lime for desulfurizing cast iron is successfully demonstrated, as shown in

Figure 4.3a in a normalized representation of the initial analysis. In addition to this experiment, lime was mixed with carbon at a mass proportion of two to one wt.% (CaO to carbon) to compensate for the decarbonization documented in **Figure 4.3b** during the 40-minute-long desulfurization treatment. The results reveal that an increase in temperature facilitates a faster desulfurization process and eventually leads to a greater desulfurization degree. Moreover, a desulfurization degree of 90% can reliably be achieved at a treatment temperature of around 1500°C, roughly representing the tapping temperature of molten iron from the cupola furnace.

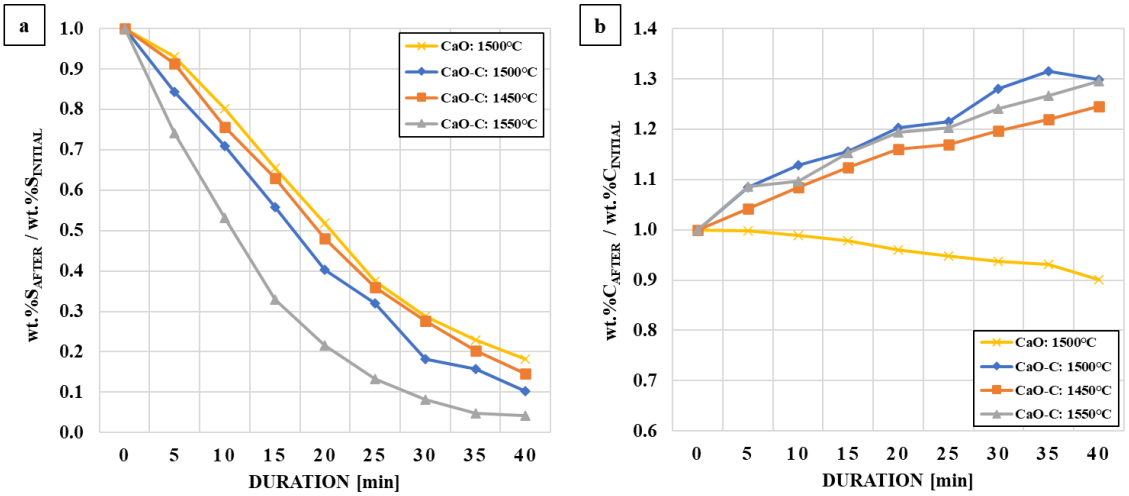

Figure 4.3. Average normalized concentrations of (**a**) sulfur and (**b**) carbon in molten cast iron during desulfurization using CaO and a mixture of CaO-carbon.

As represented in **Figure 4.4** and **Figure 4.5**, the desulfurization degree can be increased by incorporating a deoxidator while maintaining the temperature. Specific amounts of silicon (Si) and aluminum (Al) were introduced in this chapter to explore potential improvements as proposed in various reports on the steelmaking process [43]. In this instance, SiC (65 wt.% Si) and FeSi75 (75 wt.% Si) were selected as Si-bearing materials. The results in **Figure 4.4a** show that even with a higher concentration of Si, it can only moderately enhance the desulfurization result. It is worth mentioning that SiC requires more time before the improvement effect becomes apparent than FeSi75. Despite a better result, the desulfurization degree remains relatively comparable to the experiment without Si addition but at a higher temperature of 1550°C (gray line). Conversely, introducing excessive silicon content results in a lower carburization performance until there is no effect (decarburization instead) for FeSi75 at 1550°C (yellow line), as presented in **Figure 4.4b**.

Compared with Si-bearing materials, a substantial improvement is observed with the introduction of aluminum metal. The results in **Figure 4.5a** indicate that an increase in the aluminum content in the mixture of desulfurization agents could improve the desulfurization process, which is consistent with the results of previous studies [38, 45]. Even though the final sulfur content after 40 minutes of treatment will reach relatively similar values, the addition of 0.5 wt.% Al (relative to the mass of iron) to each charge of the desulfurization agent mixture could result in a faster process where a desulfurization degree of 90% can be attained within a treatment duration of 10-15 minutes, coupled with a lower total amount of

desulfurization agent. As shown in **Figure 4.5b**, desulfurization can also be improved if only aluminum without any carbon is integrated into the desulfurization agent mixture despite a lower process rate. However, this enhancing effect of Al addition is proven limited by treatment temperature, where no improvement could even be demonstrated at 1300°C.

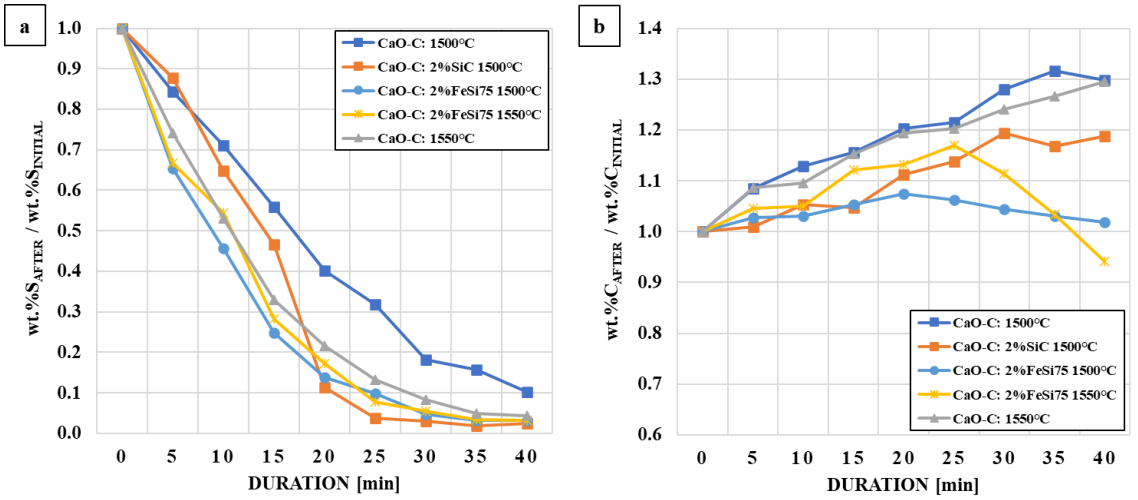

Figure 4.4. Average normalized concentrations of (**a**) sulfur and (**b**) carbon in molten cast iron during desulfurization using CaO-carbon with Si-containing additives.

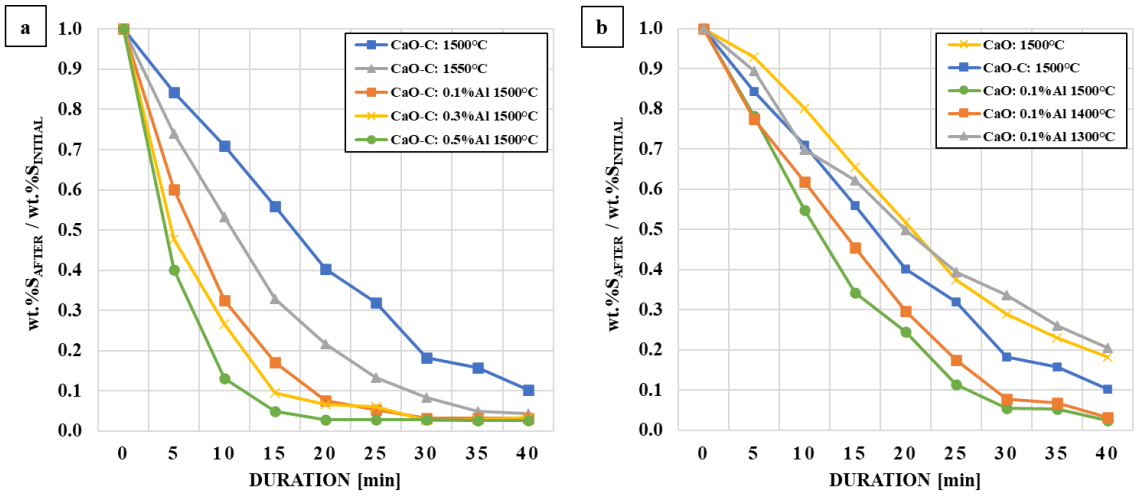

Figure 4.5. Average normalized concentrations of sulfur in cast iron during desulfurization involving the addition of aluminum (**a**) with and (**b**) without carbon.

4.2.2. IN-AD: Lime Desulfurization by Injection Process

The IN-AD experiment setup was conducted to enhance the lime efficiency and optimize the process duration. The results were subsequently compared with the ON-AD method, which was limited to a comparable amount of desulfurization agent (20 g of CaO-C mixture). As documented in **Figure 4.6**, it is evident that introducing a mixture of lime-based desulfurization agents through gas injection, which generates a higher stirring effect in molten metal than the inductive method, leads to a more effective process. Specifically, the findings indicate that the IN-AD method outperforms the ON-AD in desulfurization, as represented by lower end-sulfur concentration and a higher desulfurization degree. Additionally, as suggested in the previous studies reported in [45, 49], a decline in the

desulfurization degree was noticed in responding to an excessive addition of aluminum during the injection process.

Figure 4.6. Changes in the sulfur content in molten cast iron for surface addition and injection desulfurization methods.

4.2.3. Reaction Layer between CaO and Cast Iron

The interaction between CaO and cast iron was investigated by examining the slag from the optimum desulfurization process (CaO-C with 0.1 wt.% Al at 1500°C). The analysis focused on potential reaction layers by employing metallography analysis. A typical interaction region can be uniquely identified by searching the trace of the desulfurization agent, characterized by distinct greenish structures embedded with the metallic phase of iron, as captured in **Figure 4.7a** under the light microscope. Subsequently, supplemented by an elemental mapping analysis in **Figure 4.8** referring to the SEM image in **Figure 4.7b**, it is revealed that distinct regions representing various phases construct the reaction layer at the interface. It is worth noting that a similar reaction layer configuration is always found regardless of the experimental setup.

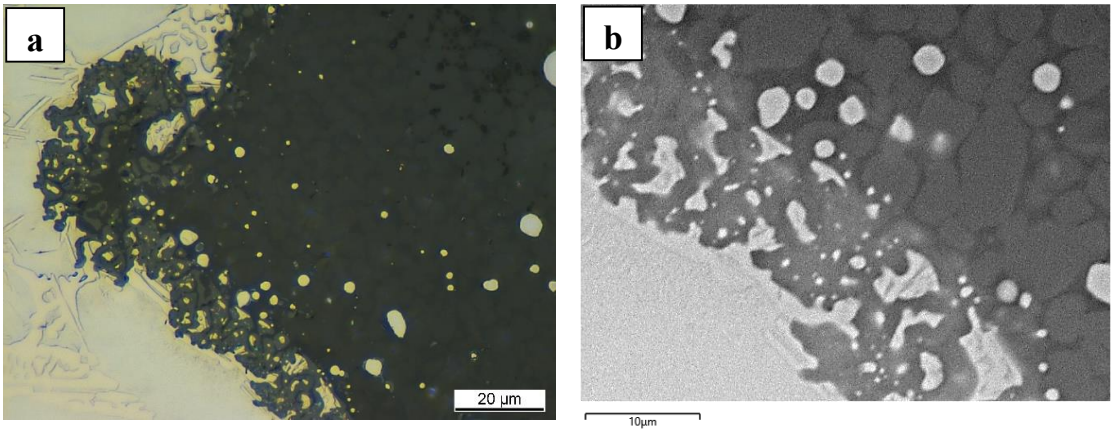

Figure 4.7. Reaction layer between the desulfurization agent and molten cast iron under (**a**) light microscope and using (**b**) scanning electron microscope.

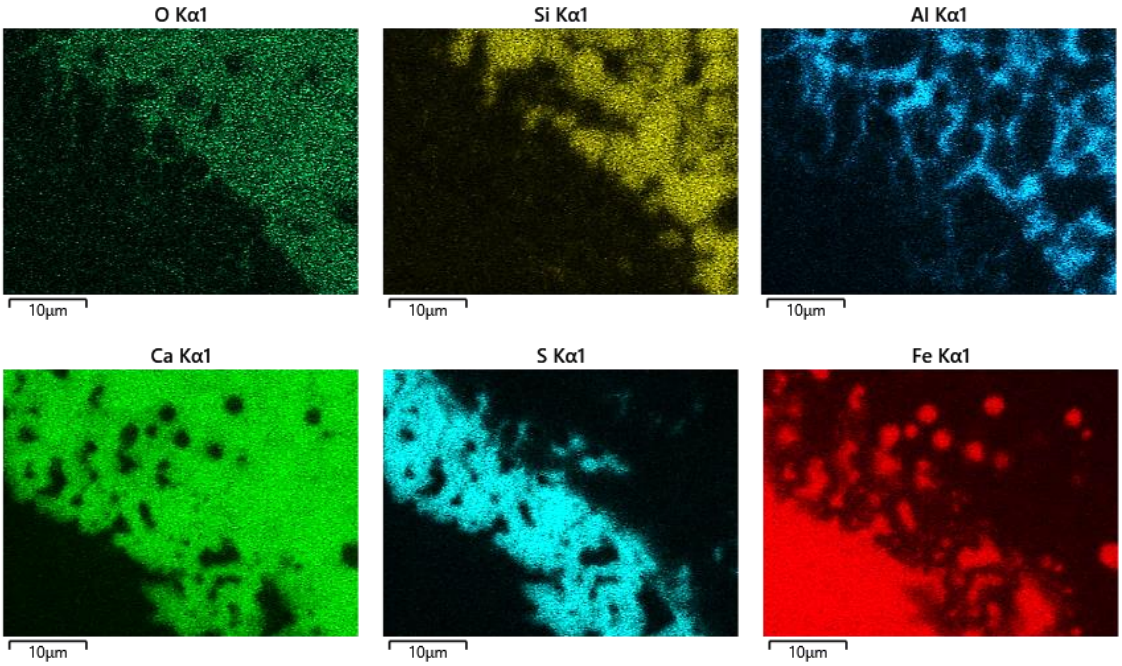

Figure 4.8. Elemental mapping results of the reaction layer as provided in **Figure 4.7b**.

The element mapping analysis in **Figure 4.8** revealed that aluminum (Al) is associated with silicon (Si), calcium (Ca), and oxygen (O), which indicates the possible formation of a slag system. This slag system might include relatively lower sulfur (S) content than the region covering it from direct attachment with cast iron (Fe). This covering region has a significant content of S associated with Ca, which suggests the formation of CaS as the desulfurization product. It is important to note that even though no sulfur indication is recorded in the Fe-rich and slag regions, it does not necessarily mean zero sulfur in the iron matrix; hence, it does not also demonstrate zero Fe in the slag system.

Table 4.2. Chemical composition (wt.%) of measurement points indicated in **Figure 4.9**.

		C	O	Al	Si	S	Ca	Mn	Fe
Sp.1	System A	4.8	1.7	1.9	2.1	1.3	4.2		84.0
Sp.2		5.2	2.4	2.0	2.3	2.9	7.2		78.0
Sp.3		5.5	2.8	2.3	2.4	2.6	7.3		77.1
Sp.4	System B	5.7	11.8	1.9	2.8	18.6	29.4		29.7
Sp.5		5.9	7.7	3.3	2.0	18.7	29.5	0.8	32.1
Sp.6		5.9	5.1	2.2	1.6	19.4	28.4	0.7	36.7
Sp.7	System C	4.6	21.1	2.6	11.3	2.1	33.9		24.4
Sp.8		4.5	21.5	2.9	11.6	1.7	34.1		23.6
Sp.9		4.6	21.8	2.3	12.3	1.4	34.7		22.9
Sp.10	System D	4.8	19.3	13.1	4.0	4.0	28.0		26.8
Sp.11		4.8	20.2	10.9	3.9	3.8	28.6		27.9
Sp.12		4.8	21.4	11.9	6.3	2.1	29.9		23.6

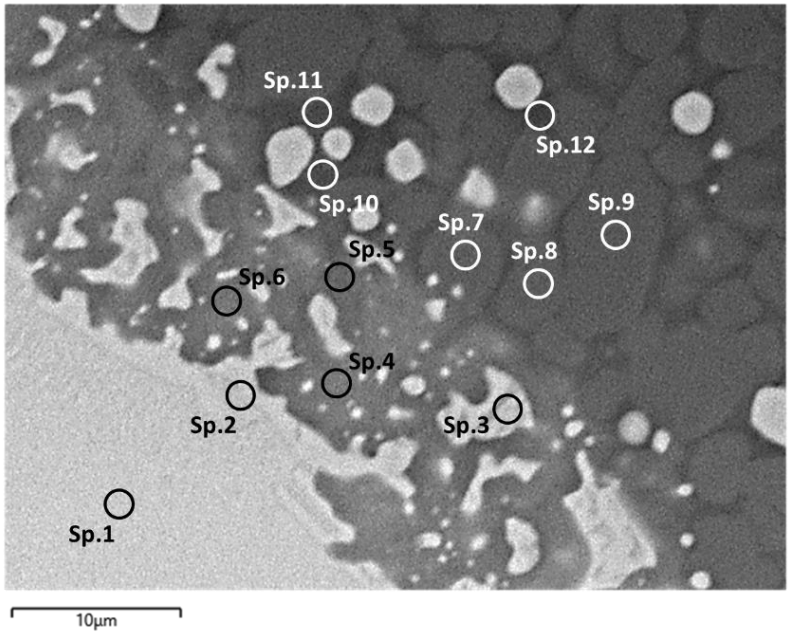

Figure 4.9. Selected measurement points on the reaction layer as provided in **Figure 4.7b**.

In addition to elemental mapping, a point analysis was carried out on the reaction layer provided in **Figure 4.7b** to identify the composition of the established reaction layer between the desulfurization agent and the cast iron, followed by detailed measurement points in **Figure 4.9**. In this case, the analysis results in **Table 4.2** indicate that the slag system consists of two sections: the bright-gray area (system C) represents enrichment in Ca-Si-O, and the dark-gray area (system D) shows segregation in Ca-Al-O. Furthermore, as previously indicated in **Figure 4.8**, this slag system is covered by a sulfur-rich region (system B) coupled with a high concentration of Ca, representing the CaS system interconnected with the cast iron matrix (system A).

4.3. Analysis and Discussion

4.3.1. Role of Deoxidation in Desulfurization Results

In alignment with previous investigations, this chapter also suggests that dissolved oxygen [O] might play a role in sustaining the reaction between lime and dissolved sulfur [S] in cast iron following the reaction in **Equation (2)**. According to the equation, the equilibrium shifts rightward when the concentration of [O] in the molten metal decreases. Consequently, the liberated oxygen should be subsequently followed by specific deoxidation reactions, which might be thermodynamically preferable either by carbon [C], silicon [Si], or aluminum [Al], as in **Equation (3)**, **(4)**, and **(5)**, respectively.

$$\mathrm{CaO} + [\mathrm{S}] \leftrightarrow (\mathrm{CaS}) + [\mathrm{O}] \quad (2)$$

$$[\mathrm{C}] + [\mathrm{O}] \leftrightarrow \{\mathrm{CO}\} \quad (3)$$

$$[\mathrm{Si}] + 2[\mathrm{O}] \leftrightarrow (\mathrm{SiO_2}) \quad (4)$$

$$2[\mathrm{Al}] + 3[\mathrm{O}] \leftrightarrow (\mathrm{Al_2O_3}) \quad (5)$$

$$(\mathrm{SiO_2}) + 2[\mathrm{C}] \leftrightarrow [\mathrm{Si}] + 2\{\mathrm{CO}\} \quad (6)$$

( ) in Slag [ ] in Solution { } in Gas

Considering the typical treatment of molten cast iron, the presence of [O] is influenced by the [C] and [Si] concentrations, which interact with the molten metal temperature [105, 130]. As also reviewed by Grachev [106], this interchange is characterized by the [O] concentration being primarily controlled by [Si], which reacts to produce (SiO_2) following **Equation (4)**. This SiO_2 is relatively stable as long as the temperature of molten iron is lower than the specific equilibrium temperature following the reaction in **Equation (6)**; otherwise, the carbothermic reduction of the formed (SiO_2) will proceed. Considering the cast iron sample investigated in this chapter (3.5% C and 1.7% Si), the anticipated equilibrium temperature is approximately 1410°C. Hence, because the studied desulfurization temperature was 1500°C, carbon depletion in **Figure 4.3b** is expected.

Given its role as the main component in the cast iron composition, incorporating carbon into the desulfurization agent was primarily conducted to compensate for the abovementioned depletion. Interestingly, this approach also yielded a modest improvement in desulfurization, as recorded in **Figure 4.3a**. In addition to the well-established correlation between higher carbon and oxygen activity [131, 132], other possible explanations could also be attributed to the role of carbon in this particular circumstance.

First, the increase in [C] in this regard can potentially shift the equilibrium temperature of **Equation (6)** to a lower level. Upon examination of the development of the [C] concentration during the desulfurization process in **Figure 4.3b**, the equilibrium temperature can be anticipated to be as low as 1390°C, leading to a higher overheating. According to Orths and Weis [114], such a level of overheating could favorably result in reduced oxygen solubility in the molten cast iron, thereby enhancing the desulfurization result. Second, the involvement of carbon in the dynamics of lime-based desulfurization can also be expected considering the chemical reactions provided in **Equations (2)** and **(3)**, as previously reported in [42, 133] and recently substantiated by Lee and Min [41]. Moreover, the positive involvement of carbon could also be indicated in the observation of **Figure 4.5**, where desulfurization by adding aluminum is enhanced if carbon is present in the mixture. This effect could be associated with the correlation between high [C] and increasing sulfur activity, which could become the third factor, as also known in the steel industry [118, 119].

Furthermore, it is known that at a constant temperature of molten metal, the increase of the silicon content is correlated with a lower level of [O]. This observation was amplified by Shibaev et al. [134], who showed that the oxygen solubility is progressively reduced by increasing the silicon content by up to 10 wt.%. Their report aligns with the results provided in **Figure 4.4a**, which shows that enhancing the [Si] by introducing FeSi75 and SiC (despite a slower dissolution rate [65]) yields improved desulfurization outcomes. Nonetheless, the increased [Si] in the cast iron could induce a greater degree of decarburization [114], which is associated with decreased carbon solubility and increased carbon activity [120]. This phenomenon is substantiated in **Figure 4.4b**, which shows that despite introducing a similar carbon quantity into the desulfurization agents, utilizing FeSi75 leads to a notably lower final carbon concentration than a similar process without FeSi75.

Compared with the addition of FeSi75 and SiC, the results in **Figure 4.5** proved that adding aluminum resulted in a more substantial improvement. An enhanced performance was observed regarding the final sulfur content achieved with a similar amount of desulfurization agent and the rate at which a specific end-sulfur level can be attained. As mentioned in several previous studies, this superior effectiveness can also be attributed to the higher affinity of aluminum for oxygen and its greater efficacy in reducing the concentration of [O] in molten iron, as reported by Matousek [135]. Their study indicated a strong negative correlation between [Al] and [O] in the molten iron, thus creating favorable conditions (following **Equations (2)** and **(5)**) for the lime-based desulfurization process. However, this effect also has specific observable limits, namely, the amount of aluminum involved (**Figure 4.6**) and the temperature (**Figure 4.5b**), which will be explored in the next section.

4.3.2. Role of Liquid Slag in Desulfurization Results

According to the results of the present chapter, reducing the concentration of [O] in molten metal might not be the only determining factor in sustaining lime-based desulfurization. These three observations support the following argument:

(1) The introduction of FeSi75 and SiC resulted in a comparable outcome to the trial without Si addition but was treated at a temperature of 1550°C (**Figure 4.4a**).
(2) The IN-AD results in **Figure 4.6** revealed that further addition did not correspond to a higher degree of desulfurization after surpassing certain limits of aluminum addition.
(3) The addition of aluminum delivered relatively comparable results to those without aluminum (and carbon) if the temperature was changed to 1300°C (**Figure 4.5b**).

Based on the abovementioned results, a certain degree of elevated temperature is necessary to sustain desulfurization. This high temperature also increases the proportion of the liquid phase in the system, thus indirectly indicating the role of the liquid phase in the lime-based desulfurization process, which is supported by the morphology of the reaction layer captured in **Figure 4.7**. Specifically, based on the analysis in **Figure 4.8**, a possible liquid slag system can be attributed to the irregular morphology of the potential indicator of CaS as a reaction product attached to a specific complex oxide configuration. Given that the focus of this exploration is solely on the contrasting involvement of liquid slag in sustaining the desulfurization process, the analysis will be limited to the role of Si and Al because both of them were adjusted parameters in the previous section and possess noticeably high contrast in the elemental mapping provided in **Figure 4.8** and enrichment in **Table 4.2**. Any involvement of other elements and a detailed analysis of the reaction mechanism during the process will not be comprehended but will be provided in the next chapter.

The analysis could be started by considering only the binary CaO-SiO_2 system. Upon the interaction of CaO with the molten cast iron at a high temperature, [S] diffuses toward the interface and reacts with the outermost surface of CaO following **Equation (2)**. Accordingly, oxygen is released, dissolves at the interface, and reacts with [Si] following **Equation (4)**. Nevertheless, as indicated by the elemental analysis in **Figure 4.8**, an overlap between Ca-Si-O concentrations is shown; thus, a calcium-silicate configuration should be anticipated. In such circumstances, instead of a two-step reaction process (**Equation (2)** followed by **(4)**), the formation of calcium silicate should coincide with the desulfurization

process; in other words, the lime-based desulfurization process induces its formation. Although SiO_2 is somehow available in the molten iron, such a solid-solid reaction CaO-SiO_2 will presumably be less accelerated because of kinetic limitations.

In the boundary of the CaO-SiO_2 binary system, four calcium silicate compositions should be considered: Ca_3SiO_5 (C3S), Ca_2SiO_4 (C2S), $Ca_3Si_2O_7$ (C3S2), and $CaSiO_3$ (CS) during desulfurization following the reactions in **Equations (7)** to **(10)** for one mol of CaO. The assumption of a constant amount of CaO is based on the surficial reaction behavior [53], where the reacted amount of CaO (surface exposed to the molten metal) is presumed to be constant. On the other hand, the diffused [S] and [Si] toward the interface could vary depending on the projected reaction products (CaS and possibly calcium silicates).

$$\mathrm{CaO} + 0.40 \cdot [\mathrm{S}] + 0.20 \cdot [\mathrm{Si}] \quad \leftrightarrow \quad 0.20 \cdot \mathrm{C3S} + 0.40 \cdot \mathrm{CaS} \tag{7}$$
$$\mathrm{CaO} + 0.50 \cdot [\mathrm{S}] + 0.25 \cdot [\mathrm{Si}] \quad \leftrightarrow \quad 0.25 \cdot \mathrm{C2S} + 0.50 \cdot \mathrm{CaS} \tag{8}$$
$$\mathrm{CaO} + 0.57 \cdot [\mathrm{S}] + 0.29 \cdot [\mathrm{Si}] \quad \leftrightarrow \quad 0.14 \cdot \mathrm{C3S2} + 0.57 \cdot \mathrm{CaS} \tag{9}$$
$$\mathrm{CaO} + 0.67 \cdot [\mathrm{S}] + 0.33 \cdot [\mathrm{Si}] \quad \leftrightarrow \quad 0.33 \cdot \mathrm{CS} + 0.67 \cdot \mathrm{CaS} \tag{10}$$

Table 4.3. Changes in the Gibbs Free Energy for the possible formation reaction of calcium silicates during the lime-based desulfurization of molten cast iron at 1500°C calculated on FactSage.

Reactions	$\Delta G_R^\circ \left[\mathrm{J\ mol_{CaO}^{-1}}\right]$	$\Delta G_R \left[\mathrm{J\ mol_{CaO}^{-1}}\right]$
(7)	-134470.3	-35200.3
(8)	-167999.0	-43911.5
(9)	-183524.3	-41406.7
(10)	-204483.0	-38863.5

Table 4.4. Changes in the Gibbs Free Energy concerning the formation of liquid slag during the desulfurization of cast iron involving the formation of calcium silicates at 1500°C calculated on FactSage.

Reaction Products	$\Delta G_R^\circ \left[\mathrm{J\ mol_{CaO}^{-1}}\right]$	$\Delta G_R \left[\mathrm{J\ mol_{CaO}^{-1}}\right]$
(7): $0.20 \cdot \mathrm{C3S} + 0.4 \cdot \mathrm{CaS}$	-134470.3	-35200.3
(8): $0.25 \cdot \mathrm{C2S} + 0.5 \cdot \mathrm{CaS}$	-167999.0	-43911.5
(9)*: $0.68 \cdot (\mathrm{LS}) + 0.03 \cdot \mathrm{C2S} + 0.51 \cdot \mathrm{CaS}$	-136369.5	-41874.2
(10)*: $0.75 \cdot (\mathrm{LS}) + 0.59 \cdot \mathrm{CaS}$	-154144.4	-38606.1

NOTE: * → modification from the designated reaction products in **Table 4.3**.

Referring to those reaction configurations, the determination of the preferable composition of the resulting calcium silicate at 1500°C can be approached through the examination of the change in Gibbs Free Energy under certain additional assumptions that a solid lime particle is involved (a_{CaO}=1) and that the reaction product at the reaction boundary between CaO and cast iron is also a pure substance with an activity equal to 1. Following those circumstances, the first calculation results, which were obtained by employing a thermodynamic database on FactSage, are listed in **Table 4.3**. According to the results of this calculation, the reaction involving the formation of C2S (**Reaction (8)**) is

thermodynamically favorable. The calculation results also revealed that the designated products for **Reactions (9)** and **(10)** are not necessarily expected. In contrast, liquid slag (LS) formation is anticipated and possesses a different chemical configuration. The calculation was accordingly rerun by considering the liquid slag, including the activity of its components. Based on the calculation results listed in **Table 4.4**, the formation of C2S is reaffirmed even when the standard conditions are considered.

Since C2S is a solid reaction product, its formation potentially retards the further interaction of lime and the molten metal, mainly if the formed C2S completely covers the unreacted CaO, thus reducing the utilization degree of CaO. To this extent, it is consequently suggested that the observed improvement in desulfurization degree by incorporating FeSi75 and SiC in **Figure 4.4a** is predominantly driven by the reduced dissolved oxygen level in the molten iron. A similar effect can also be expected if the degree of superheating is increased, thus explaining the comparable desulfurization degree between Si addition and the absence of Si yet conducted at higher melting temperatures. Unless other elements are involved in affecting the solid C2S, the reaction of lime-based desulfurization would be surficial limited, thus explaining why finer lime particles perform better in terms of lime utilization than coarser particles do [26] and the possibility of C3S formation when C2S interacts with unreacted CaO cores for coarser particles at high temperatures, as reported by Mitsuo et al. [48].

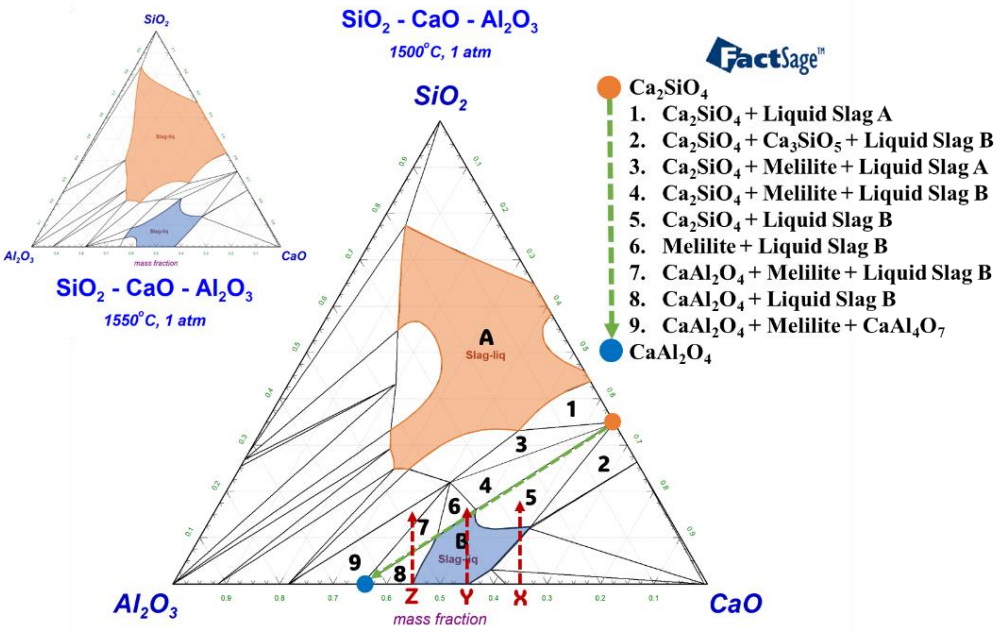

Figure 4.10. Modified isothermal section of the ternary system SiO_2-CaO-Al_2O_3 at 1500°C calculated on FactSage.

One of those elements considered to be able to influence C2S is aluminum, which is expected to construct a ternary system of CaO-Al_2O_3-SiO_2, as provided in **Figure 4.10**. According to this diagram, C2S is composed of approximately 35 wt.% SiO_2 and even a minor addition of Al_2O_3 shifts the equilibrium system into a multiphase region involving a specific portion of (LS), as indicated by the green dashed line connecting Ca_2SiO_4 and $CaAl_2O_4$ in **Figure 4.10**. The selection of those points is based on the thermodynamic calculation conducted in this

chapter that either silicon or aluminum dominates the deoxidation process, which aligns with the reaction sequence that was once proposed by Fruehan [43]. Based on the diagram and given the process's dynamic, the (LS) can even be contained at certain occurrences in the system of $CaO\text{-}SiO_2$, as highlighted by No.1 following **Reaction (9)*** as the second favorable reaction product thermodynamically at 1500°C (**Table 4.4**). In fact, a comparable $CaO\text{-}SiO_2$ system has been used as a configuration to sustain desulfurization. However, it might be limited by the CaO/SiO_2 ratio and their proportion compared to the C2S [136, 137]. To this extent, as the treatment temperature increases from 1500°C to 1550°C and the proportion of (LS) is expected to expand (**Figure 4.10**), the possibility of (LS) facilitating the further diffusion of [S] and reacting with (CaO) is positively magnified, which consequently improves the desulfurization outcome, as reported in **Figure 4.3a**.

As indicated earlier, enhancing the share of (LS) could also be carried out by introducing Al_2O_3 into the binary system of $CaO\text{-}SiO_2$ by incorporating a controlled amount of Al; thus, the **Reaction (5)** could thermodynamically participate during desulfurization. The effect can be observed in the results in **Figure 4.5**, and the chemical analysis results in **Figure 4.8** and **Table 4.2** can approach the reaction mechanism. Since aluminum has higher oxygen affinity, deoxidation coupled with the desulfurization process is expected to involve aluminum ahead of silicon. Hence, the effect of aluminum on the lime-based desulfurization process does not modify C2S but primarily forms a specific (liquid) slag composition. This availability of enough (LS) eases the diffusion of [S] to react with (CaO). However, despite its higher oxygen affinity, aluminum could only be some ticks in advance than silicon in responding to the deoxidation reaction because of its lower concentration in cast iron. In this first reaction sequence, a liquid $CaO\text{-}SiO_2\text{-}Al_2O_3$ ternary slag system is anticipated and contains a certain amount of the dissolved desulfurization product (CaS).

Once the availability of aluminum is limited, the dissolved silicon will entirely overtake the deoxidation reaction, thus increasing the SiO_2 proportion in the composition of the available liquid slag system. As the reaction progresses, the solubility of SiO_2 is surpassed, and C2S precipitates, which explains the smooth round morphology of the high silicon domain with a low aluminum content in **Figure 4.9**. This argument is supported by the chemical analysis results in **Table 4.2**, where enrichment of Ca-Si-O is observed in system C, representing a potential nucleated C2S surrounded by a Ca-Al-O system with a trace of Si (system D).

According to Hino et al. [138], this C2S-saturated lime-based liquid slag has a lower sulfide capacity. Aggravated by the growth of solid fraction, both dissolution and diffusion are retarded. Particularly at the cast iron interface, the (CaO) in (LS) would be disproportionately consumed by (CaS) formation. Once the solubility limit is reached due to a lack of CaO supply, the solid CaS will start to precipitate, as reported by Ban-Ya et al. [139], but for the $CaO\text{-}Al_2O_3$ system. This interchange rationalizes the irregular appearance of the CaS layer separating the (LS) from the molten iron at the interface, which eventually affects the desulfurization performance.

The involvement of C2S precipitation, as also foreseen in **Table 4.3** and **Table 4.4** calculations, can be further elucidated using a ternary diagram in **Figure 4.10**. Unlike in the

binary system of CaO-SiO_2, the involvement of Al_2O_3 can be explained by following the behavior of three red dashed arrows (labeled as X, Y, Z), which also suggests the importance of keeping the amount of Al_2O_3 below a specific limit regardless of its origin. Considering the availability of [Al], the released oxygen following the desulfurization reaction will mainly react with [Al] and first construct a binary system of CaO-Al_2O_3. As indicated at point X at approximately 35 wt.% Al_2O_3, the ability of aluminum to provide a liquid slag system is considered insufficient. In this case, unreacted CaO is still anticipated, and a specific amount of SiO_2 is necessary to establish liquid slag before further enrichment of SiO_2 will eventually surpass the solubility limit and reach composition No. 5, which comprises C2S and liquid slag B, as also indicated in **Table 4.2**.

A complete molten calcium aluminate slag can be anticipated if the aluminum addition is carefully increased to achieve a Y composition with approximately 45 wt.% Al_2O_3. This condition could be the starting point of the optimal aluminum addition level since further silicon involvement would not directly initiate solid product precipitation and is kinetically favorable for the desulfurization process. Nevertheless, this effect will not remain consistent for the unlimited introduction of aluminum. Starting from point Z for approximately 55 wt.% Al_2O_3, the solid fraction is expected to be involved in the calcium aluminate configuration, which actually or might be more undesired than the previous composition in point X. In this case, further addition of SiO_2 to the slag system will increase the solid fraction until composition No. 9 in **Figure 4.10** for 100% solid product, thus making it unfavorable for the desulfurization reaction.

Furthermore, increasing aluminum addition beyond point Z shifts the point near the higher proportion of Al_2O_3 to CaO, thus worsening the desulfurization result. Following a similar calculation approach used for the CaO-SiO_2 system in **Table 4.3** and **Table 4.4**, it is suggested that the formation of solid $CaAl_4O_7$ is the most thermodynamically favorable for an excessive amount of aluminum. As mentioned earlier, establishing and increasing the proportion of a solid reaction product will reduce the desulfurization outcome and could be contextually associated with the result in **Figure 4.6**.

Since the aluminum content in commercial cast iron is limited to 0.1 wt.% [140], excess addition during the desulfurization process would practically never occur, considering the tight process control in the foundry. In this case, an insufficient molten metal temperature could be the limiting factor for the enhancing effect of Al addition during the desulfurization process. **Figure 4.5b** shows a significant reduction in desulfurization degree that can be observed once the temperature is decreased to 1300°C. Since the eutectic point in the system of CaO-Al_2O_3 and the lowest liquidus temperature in the CaO-rich CaO-SiO_2-Al_2O_3 system are higher than 1300°C, a solid reaction product is therefore expected during the desulfurization reaction involving Al addition. This phenomenon explains why the result is comparable to the case of CaO utilization only, which further enhances the significance of liquid slag in sustaining the lime-based desulfurization process.

4.3.3. Possible Scaled-up Implementation on the Industrial Scale

Based on the results of this present chapter, adopting a lime-based desulfurization process in the cast iron foundry should be considered as highly possible. The injection method should be viewed as the first alternative for introducing lime into molten cast iron, as previously substantiated in **Figure 4.6**. Considering that this method aligns well with the standard operation in the steelmaking process, the barrier in industrial implementation should be expected to be significantly lower. However, given the ladle size in the foundry industry, which is one hundred times smaller than that in the steel industry, developing a particular lance design coupled with a modified automatic injection apparatus is required. In this context, transferring the 20 g of desulfurization agent is consumed for 1 kg of molten cast iron; the developed machine should be able to transport an approximate amount of 50 kg of CaO-C powder into molten cast iron in one treatment ladle with a capacity of 2500 kg. Nonetheless, given the circumstances in industrial practice compared with laboratory, fluctuations are highly expected.

Further considerations in the industrial implementation of this lime-based desulfurization process are the molten cast iron temperature and the amount of generated slag. Precisely, as described in the experimental setup ON-AD and IN-AD, the molten metal temperature is continuously measured and kept at a constant value, which is not the case from an industrial perspective. Consequently, a different injection parameter and system are required to ensure a more efficient process to minimize the temperature drop. Moreover, an alternative valorization method should be prepared to manage the increased slag volume from the lime-based process compared with the conventional magnesium-based method. Nonetheless, in addition to the comparable performance in ensuring the low end-sulfur concentration in the molten cast iron, the advantages of lime from both economic and ecological perspectives should become an enhancing factor in transforming the concept into an industrial practice. As a response, together with all the technical challenges in implementing lime-based desulfurization in an integrated cast iron production process, the balancing effect on financial and environmental sustainability factors should be further assessed, as provided in the next dedicated chapter [141].

4.4. Summary of Lime Applicability as Desulfurization Agent

Based on the experimental results and thermodynamic calculations, the following findings can be drawn from the present chapter:

(1) Despite possessing a higher silicon content (approximately 1.7 wt.%) compared to pig iron, the lime-based desulfurization process for molten cast iron is practicable for reaching a low end-sulfur content (<0.015 wt.%).
(2) The outcome of lime-based desulfurization is determined by the interplay between the dissolved oxygen in molten iron and the proportion of the liquid slag in the developed reaction product as the desulfurization reaction proceeds.
(3) Adding aluminum could improve desulfurization by promoting low dissolved oxygen levels and providing a sizable proportion of liquid slag. However, the additional amount of aluminum should be controlled to be <0.1 wt.% and treatment temperatures must be maintained above 1400°C to avoid counterproductive effects.

Chapter 5

Reaction Mechanism of Lime and Molten Cast Iron

Following the results of the previous chapter, which states that the establishment of liquid slag has a critical role in sustaining lime-based desulfurization, this chapter comprehensively investigates the reaction mechanism between lime powder and molten cast iron. The primary purpose is to understand the interplay of alloying elements during the process sequence by focusing the observation on the reaction layer. Accordingly, this chapter elucidates that distinguishable structures construct the interface between lime powder and molten cast iron. It is carefully identified that the slag systems contain a distinct proportion of calcium, silicon, aluminum, iron, and sulfur, establishing a foundation for promoting a deeper understanding of these fundamental mechanisms in steelmaking and cast iron foundry.

5.1. Methodology

The first experiment (coded as BO-AD) offers a reference for justifying the slag analysis, particularly when identifying the reaction layer between lime and cast iron. In this setup, cast iron with the chemical composition listed in **Table 5.1** was melted under a vacuum induction furnace covered under an argon atmosphere (1 atm) to avoid any involvement of additional oxygen. Instead of lime powder, 5 g of coarse CaO particles (ca. 2 mm) were employed and positioned at the base of the pure graphite crucible (Ø35x50 mm). Furthermore, 150 g of cast iron was rested on top of the CaO particles before being heated until a temperature of 1500°C followed by a holding duration of around five minutes. Upon melting and holding at a high temperature, the system was allowed to cool down and solidify in the crucible; meanwhile, the atmosphere was maintained inert. The generated slag sample (contact point between CaO and cast iron) was subsequently prepared (mounting, grinding, and polishing) before being directly subjected to metallography analysis.

Table 5.1. Initial chemical composition (wt.%) of cast iron before desulfurization.

C	Si	S	P	Mn	Al	Fe
3.4 – 3.5	1.6 – 1.7	0.10 – 0.12	0.06 – 0.07	0.5 – 0.6	0.01 – 0.03	93 – 94

In the second trial (designated as ON-AD), a 1 kg sample of cast iron in **Table 5.1** was placed in a clay-graphite crucible (Ø70x90 mm) before being heated up and melted at a temperature of 1500°C, as illustrated in **Figure 5.1**. The trial was carried out under open atmospheric conditions mirroring the practical circumstances. Furthermore, the temperature was controlled using an S-type thermocouple protected by an alumina-based tube, which was inserted (and subsequently sealed) through the bottom of the crucible. The experiment ran for a total duration of 40 minutes following a surface addition technique, in which 25 g of CaO (particle size of <100 μm) and 1 g of aluminum were added together three times: right after melting, 10 minutes, and 25 minutes. The generated slag was collected and prepared using a procedure similar to that mentioned in BO-AD before being analyzed under a light microscope and scanning electron microscope with energy-dispersive X-ray spectroscopy (SEM/EDS). It is important to note that all sample preparation involved a water-free

process, and the analysis was conducted immediately to avoid any possible hydration of unreacted CaO.

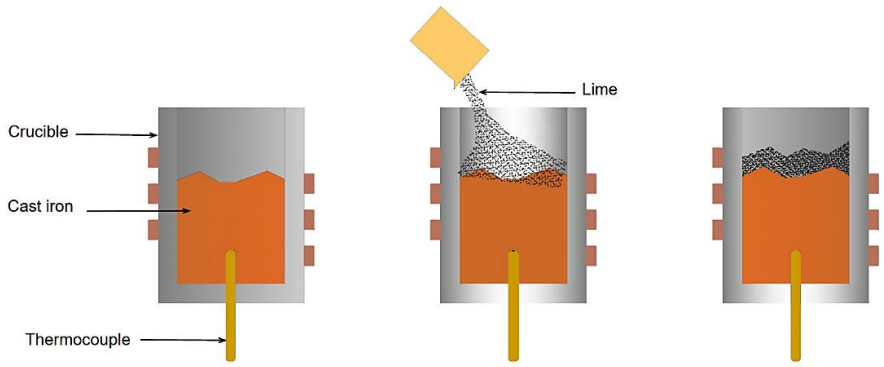

Figure 5.1. Illustration of lime-based desulfurization process for cast iron at open atmospheric conditions.

5.2. Results and Discussion

5.2.1. BO-AD: Observation of the Desulfurization in Inert Atmosphere

The typical reaction layer structure between lime and cast iron under a light microscope is documented in **Figure 5.2**, where the residual lime-based desulfurization agent is characterized by greenish structures embedded with the metallic phase of cast iron (brighter contrast on the upper right). The lamellar graphite (black circle) can also be observed on the cast iron structure, arising from a slow cooling during the trial process; meanwhile, three distinct structures are captured to construct the residual lime-based desulfurization agent. It is worth mentioning that those categorized systems do not mean an utterly separated composition but rather a transition under specific configurations. Following **Figure 5.2**, the red circle indicates the segregation of the CaS system as the direct reaction product, the yellow circles for the segregation of oxide systems as the byproducts, and the green circle highlights the segregation of unreacted CaO.

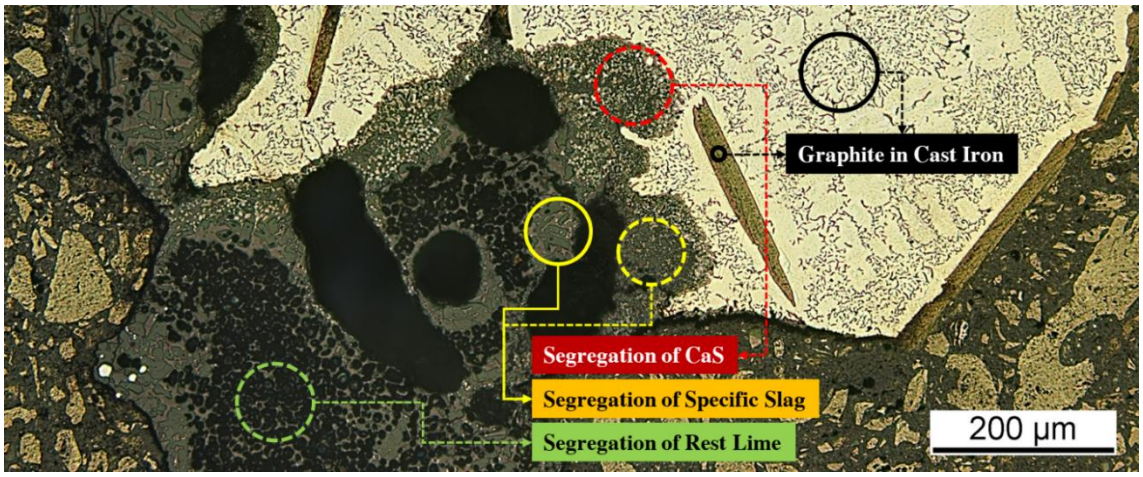

Figure 5.2. Typical structure of reaction layer between lime and cast iron under a light microscope – the depicted contrast is typical for all observations under the light microscope during further analysis.

This initial identification is supported by the elemental mapping in **Figure 5.3**, where a high contrast of sulfur (S) and calcium (Ca) are attached to the cast iron (Fe), indicating segregation of possible CaS system. Conversely, the highest Ca coupled with oxygen (O) concentration is detected in the area marked as segregation of rest lime in **Figure 5.2**, representing a possible unreacted CaO. Lastly, the segregation of the possible slag system is revealed by the appreciable contrast of oxide components in **Figure 5.3**, including Ca, aluminum (Al), and silicon (Si).

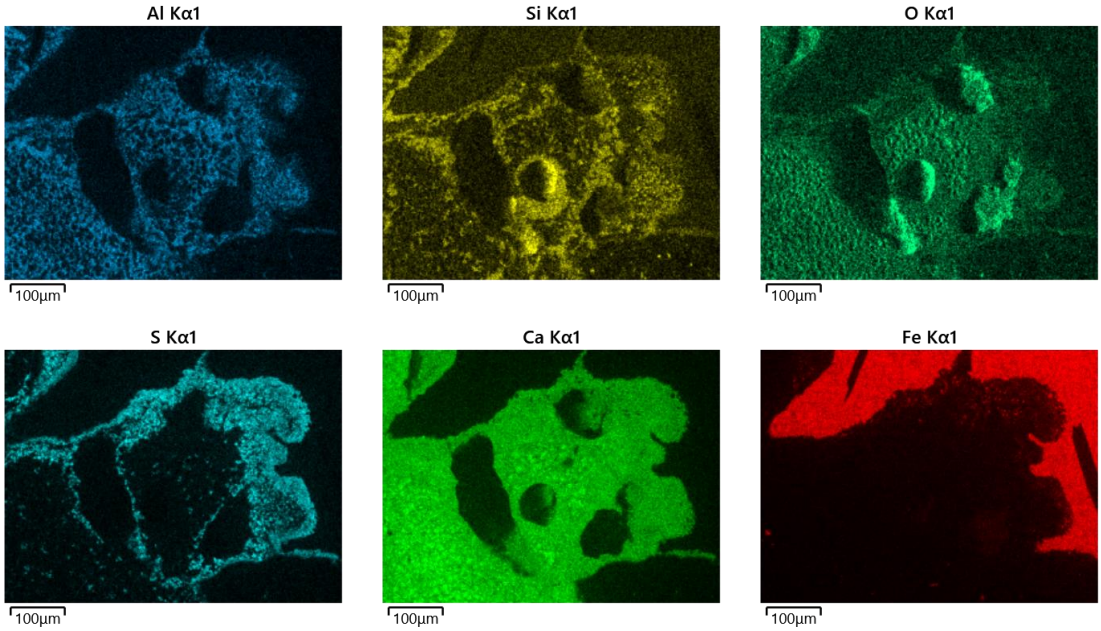

Figure 5.3. Element mapping result of the reaction layer captured in **Figure 5.2**.

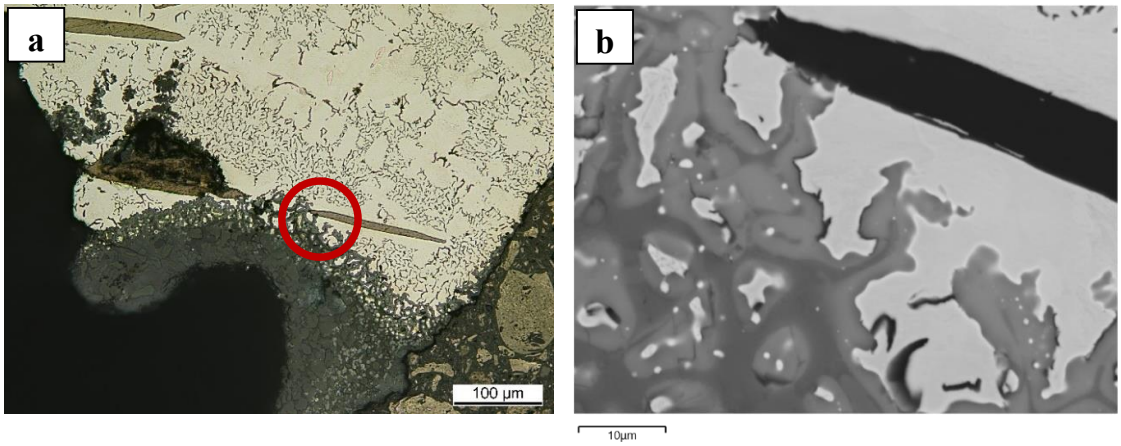

Figure 5.4. Sample of reaction layer under (**a**) light microscope and detailed (red circle) under (**b**) SEM observation concentrated to the slag/iron interface**.**

In addition to initial identification, further analysis focused on the interface between the indication of the CaS system and cast iron was also carried out, as provided in **Figure 5.4**. Based on the respective element mapping supplied in **Figure 5.5**, it is shown that besides being attached to the cast iron (Fe), the indication of CaS in **Figure 5.4b** (lighter grey in the lower left) is associated with a possible slag system containing complex oxide Ca-Al-Si-Fe

(darker grey). Since the experiment used a pure graphite crucible in an inert atmosphere, the detected Al and O should only originate from the cast iron and lime particle system. Furthermore, given the irregular morphology and the appearance of iron segregation engulfed in this specific structure, it is shown that the CaS system could also be presumed to exist in a liquid phase during the desulfurization process associated with the possible existence of liquid slag, whose composition and configuration will be provided in the next section.

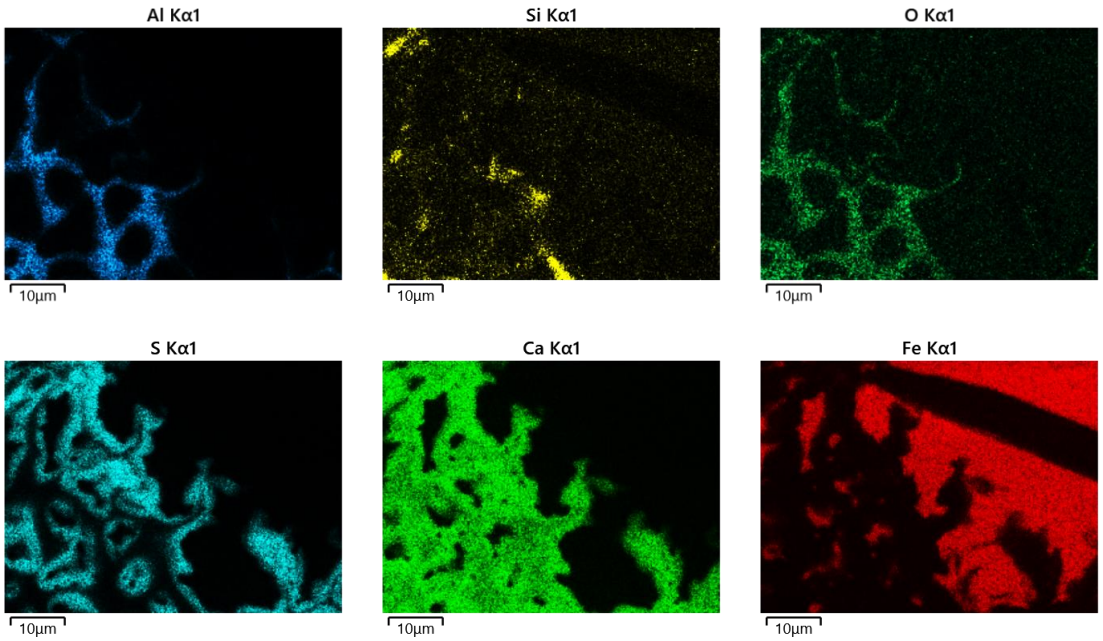

Figure 5.5. Elemental mapping result of red-circled area (interface) in **Figure 5.4**.

5.2.2. ON-AD: Observation of the Desulfurization in Open Atmosphere

Following the initial identification in an inert atmosphere, further exploration regarding the chemical composition of each configuration transition on the reaction layer between lime and cast iron was conducted in practical circumstances (atmospheric conditions). Since the BO-AD trials provide a qualitative reference for an optimal expected reaction layer, the results from ON-AD trials were first compared to the BO-AD to justify their soundness before being utilized to explore and explain the whole reaction sequence of lime-based desulfurization.

Accordingly, the first examined region was the transition between the possible rest lime and the segregation of the slag system, as captured in **Figure 5.6a**. It is essential to mention that this region is contextually comparable to the boundary between the segregation of rest lime (green dashed-circle) and segregation of specific slag (yellow solid-circle) system indicated in **Figure 5.2**. The observation focused on the marked red circle employing the SEM/EDS method provided in **Figure 5.6b** coupled with the chemical analysis in **Table 5.2**, where the remaining lime is clustered on the left side (measurement points in green) and the slag system on the right side (detection points in yellow). According to this analysis result, it is measured that the cluster marked with A (possible rest of CaO) consisted mainly of high concentrations of calcium and oxygen; meanwhile, its matrix (marked with B) is enriched with aluminum.

Such an aluminum enrichment is also detected on the matrix of the slag system on the right side (marked with C) but not at the measurement points D, where silicon enrichment was detected instead of aluminum, indicating a possible different phase.

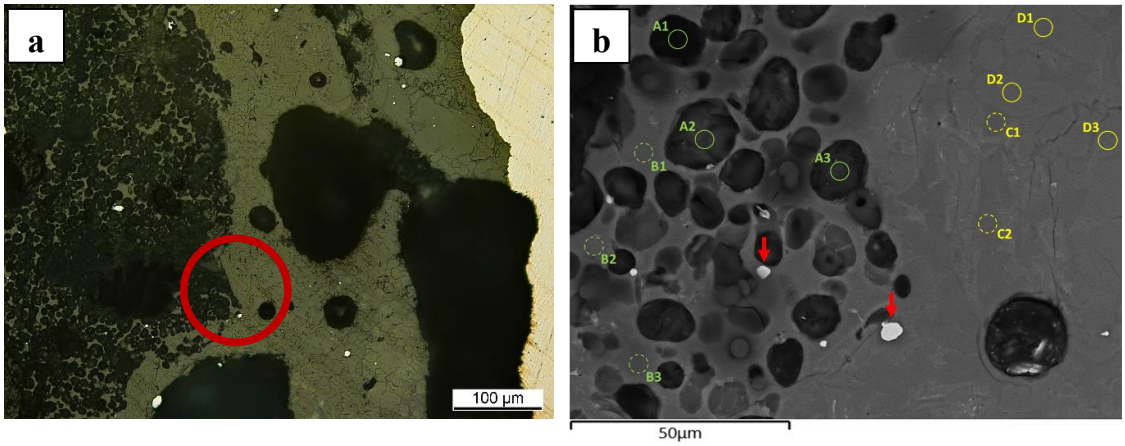

Figure 5.6. Sample of transition on reaction layer under (**a**) light microscope and detailed (red circle) under (**b**) SEM observation between rest lime and slag system.

Table 5.2. Chemical composition (wt.%) of analysis points indicated in **Figure 5.6b**.

No.	Ca	O	S	Si	Al	Mn	Fe
A1	34.99	43.02	0.51	4.75	4.53	0.71	11.48
A2	45.07	40.50	0.37	2.79	2.68	0.36	8.22
A3	39.00	43.87	0.50	3.84	3.19	0.66	8.95
B1	40.84	33.33	1.62	4.86	11.04	1.00	7.31
B2	39.29	33.10	1.98	5.29	11.16	1.30	7.90
B3	41.16	37.81	0.94	4.01	7.34	1.16	7.59
C1	39.72	32.64	0.39	6.27	12.11	0.82	8.05
C2	39.04	31.84	0.45	5.05	14.08	1.15	8.40
D1	42.14	33.19	0.35	13.61	2.55	0.43	7.73
D2	42.13	32.68	0.35	13.59	2.73	0.54	7.99
D3	41.70	32.37	0.38	13.90	2.68	0.43	8.54

The subsequent analysis was focused on the transition between the indication of the slag system and CaS as a direct reaction product, as shown in **Figure 5.7a**. In this instance, this region is circumstantially comparable to the boundary region between the segregation of specific slag (yellow dashed circle) and the segregation of CaS (red dashed circle) indicated in **Figure 5.2**. The detailed analyses took place on the marked red circle in **Figure 5.7b**, supplemented by the chemical analysis in **Table 5.3**, where the slag is on the left side (measurement points in yellow) and the indication of CaS (detection points in red) on the right side attached with the cast iron. Accordingly, it is detected that the matrix of the slag system considered in **Figure 5.7b** (marked with C) was enriched by Al, Si, and a notable content of Fe. The lighter grey islands of possible different phases in this slag system (marked with D) revealed a relatively similar composition to its counterpart in **Figure 5.6b,** except for the iron content. Moreover, the highest sulfur is detected in the CaS region, represented by high sulfur percentages followed by calcium (measurement points E). This structure is

attached to an approximate slag system (marked with G), whose component is comparable to the measurement points in C in **Figure 5.7b**.

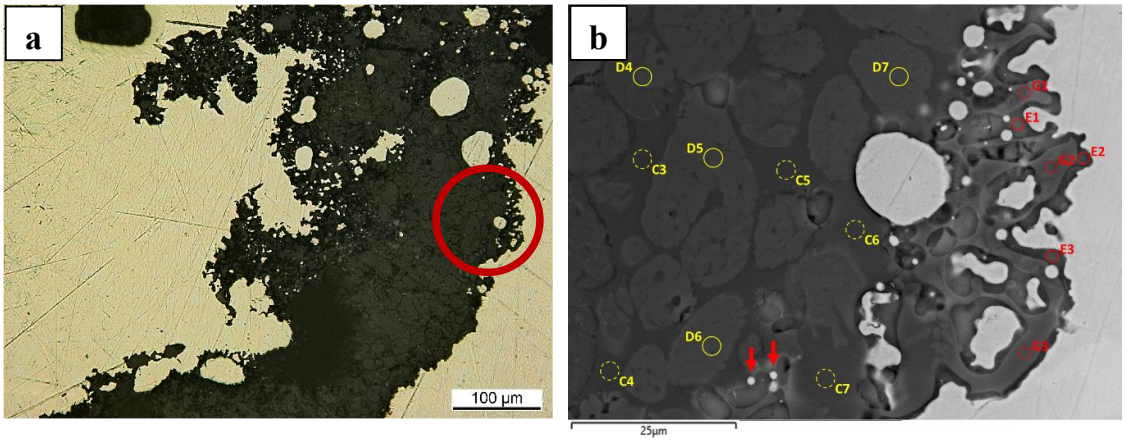

Figure 5.7. Sample of transition on reaction layer under (**a**) light microscope and detailed (red circle) in (**b**) SEM observation between indication of CaS and slag system.

Table 5.3. Chemical composition (wt.%) of analysis points indicated in **Figure 5.7b**.

No.	Ca	O	S	Si	Al	Mn	Fe
C3	29.52	27.42	2.05	14.44	7.60	0.55	18.42
C4	30.21	27.58	1.92	14.28	6.64	0.47	18.90
C5	28.31	26.17	2.05	14.39	7.61	0.65	20.82
C6	27.12	24.93	2.10	13.99	7.86	0.68	23.32
C7	26.75	24.54	2.27	13.93	7.52	0.63	24.37
D4	37.28	26.00	1.33	14.88	1.47	0.32	18.73
D5	36.84	26.14	1.20	14.77	1.20	0.33	19.52
D6	36.48	25.10	1.43	14.59	1.16	0.36	20.90
D7	35.59	24.24	1.37	14.42	1.16	0.37	22.85
E1	33.55	10.15	21.94	3.45	0.97	0.39	29.55
E2	29.54	10.97	13.47	5.79	2.36	0.86	37.01
E3	28.04	12.99	15.91	4.32	0.97	0.71	37.06
G1	27.82	20.58	9.84	9.14	4.31	0.54	27.77
G2	29.02	21.98	2.24	12.85	4.05	0.54	29.32
G3	23.62	20.31	4.65	11.41	6.23	0.91	32.87

5.2.3. Involvement Indication of MnS and FeS during Desulfurization

In addition to previous analysis results, certain occasions of the reaction layer also revealed an indication of other sulfide segregations besides the direct reaction product of the CaS system. The first conceivable sulfide segregation involves manganese enrichment, as captured on the reaction layer in **Figure 5.8**, supported by the elemental mapping analysis in **Figure 5.9**. Based on this analysis, the typical component of the reaction layer made of the Ca-Si-Al-Fe oxides system was revealed, except a high content of Mn was also detected attached to the segregation of CaS at the interface to the cast iron.

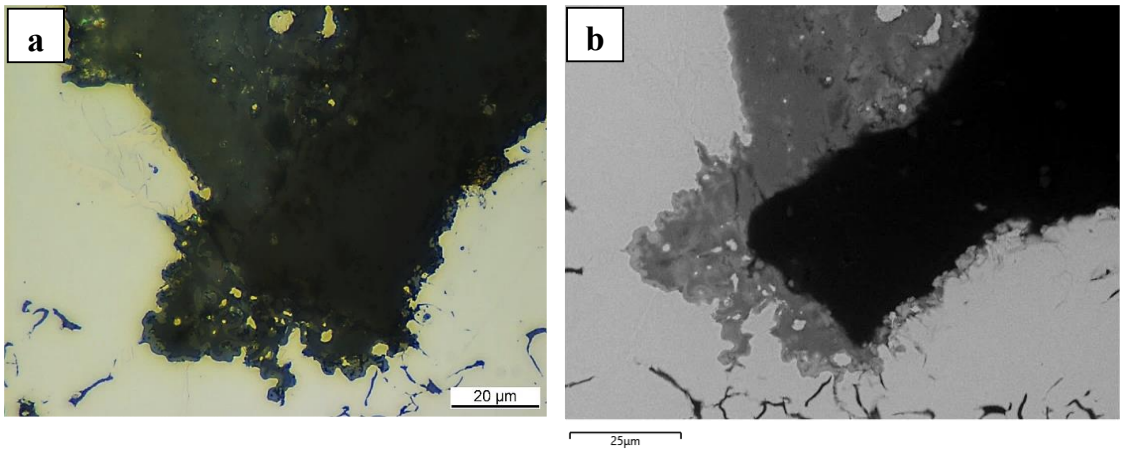

Figure 5.8. Sample of reaction layer under (**a**) light microscope and (**b**) SEM observation involving detection of possible manganese-sulfide segregation.

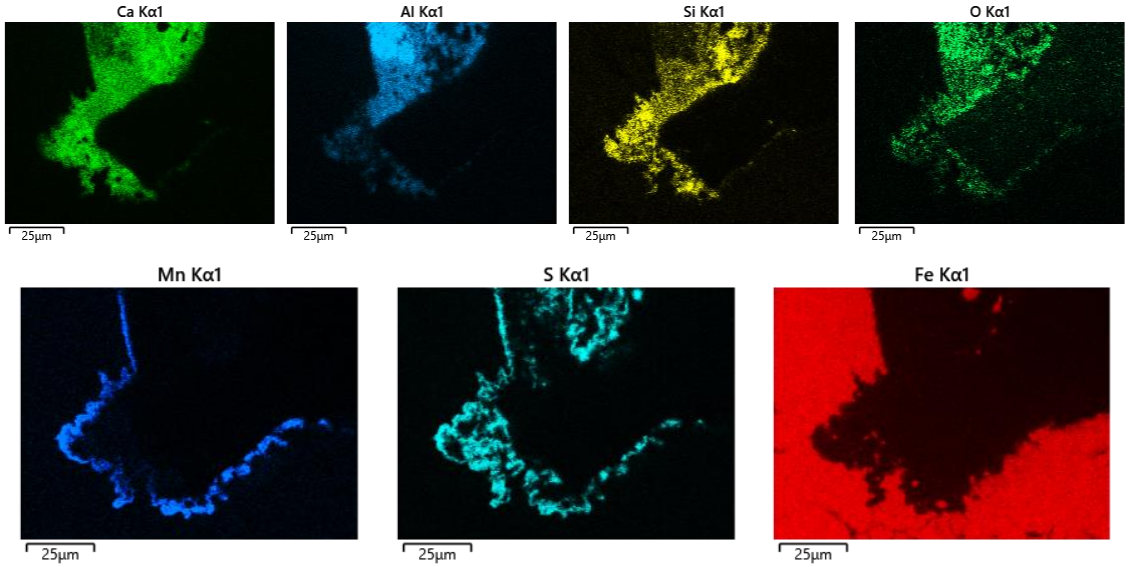

Figure 5.9. The elemental mapping result of the reaction Layer in **Figure 5.8**.

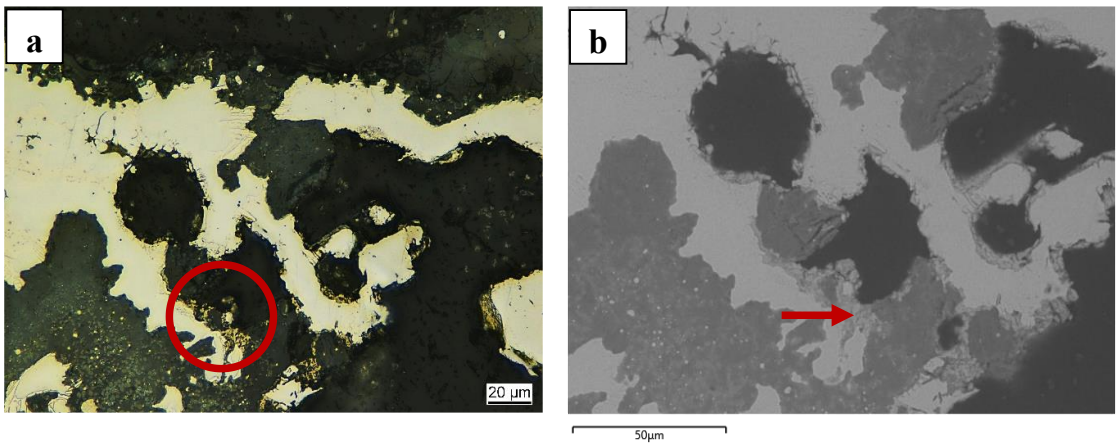

Figure 5.10. Sample of reaction layer under (**a**) light microscope and (**b**) SEM observation involving detection of possible iron-sulfide segregation (red circle and arrow).

Complementary to detecting the possible MnS system, another sulfide involving iron was also captured, as shown in **Figure 5.10**, followed by the chemical analysis in **Figure 5.11**. A typical component was also recorded except on the area specifically marked with a red circle in **Figure 5.10a**. Especially in this area (marked with a red arrow in **Figure 5.10b**), including all yellowish-brown phases under a light microscope, a lighter contrast of iron with high sulfur intensity suggested a possible FeS system. Furthermore, it is worth noting that minor manganese was also captured, as indicated in dark blue in **Figure 5.11**, representing a feasible interplay between these distinct sulfide formations comprising CaS-FeS-MnS.

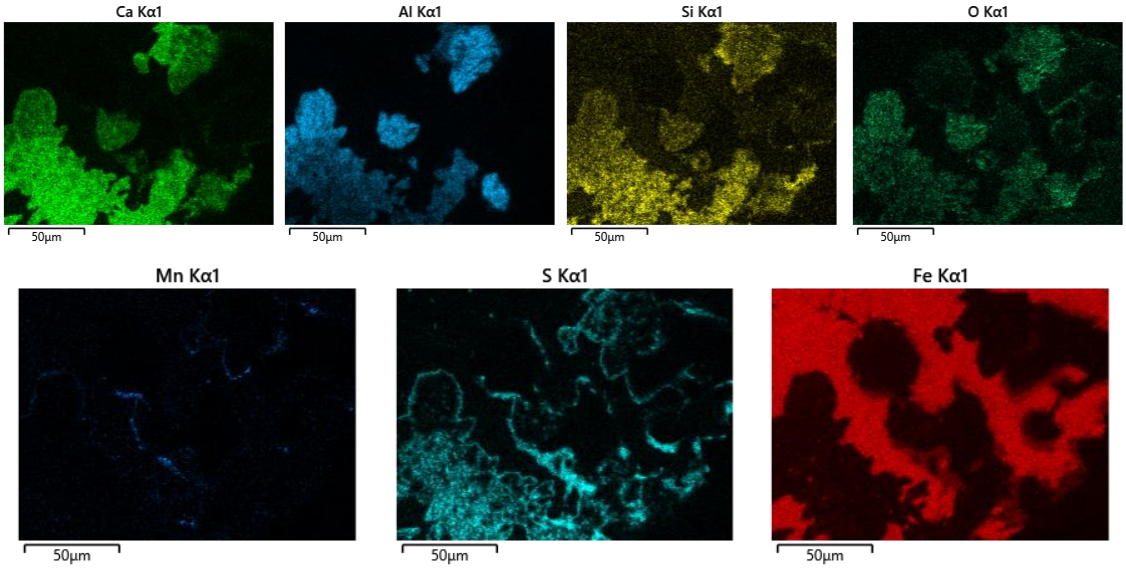

Figure 5.11. The elemental mapping result of the reaction layer in **Figure 5.10**.

5.2.4. Analysis of Reaction Mechanism during Cast Iron Desulfurization

According to the metallography observations and chemical composition analysis of all the detected phase transitions, the general morphology of the reaction layer between lime and cast iron can be illustrated in **Figure 5.12**. In general, four different phase configurations are identified in this examination between the CaO and molten cast iron during the lime-based desulfurization process. First are layers A and B, corresponding to the chemical analysis in **Figure 5.6** and **Table 5.2**. Meanwhile, layers C and D represent the observation in **Figure 5.7** and **Table 5.3**, including the indication of other formations of the sulfide system in **Figure 5.9** and **Figure 5.11**.

Align with several previous reports on steel industries, the role of aluminum addition in enhancing the result of lime-based desulfurization in cast iron can also be observed in this chapter. Based on the chemical analysis results on layer A in **Figure 5.12**, it is suggested that when the lime was in contact with molten cast iron, the desulfurization process ran complementarily with a deoxidation involving aluminum. This circumstance is supported by the fact that a gradient in aluminum concentration can be observed across layer D to layer A, where the proportion changes from around 4.9±1.2 wt.% into 9.8±2.2 wt.%. Since precipitation of Al_2O_3 was unlikely to be detected on layer A, a calcium aluminate formation is instead expected based on the results in **Table 5.2**, where $Ca_3Al_2O_6$ (C3A) should be preferable as a calcium-rich configuration. However, no exact sole indication of calcium

aluminate precipitation was found either, but an indication of a liquid Ca-Al-O slag system was captured instead. Based on the ternary diagram in **Figure 5.13**, this existence of liquid slag is related to SiO_2. Precisely, instead of establishing the CaO + C3A, the SiO_2 shifts the equilibrium to the CaO + slag liquid II system (marked qualitatively by No.1), which then represents the configuration in layer A, concluding the existence of partially reacted lime and Ca-Al-O slag system A.

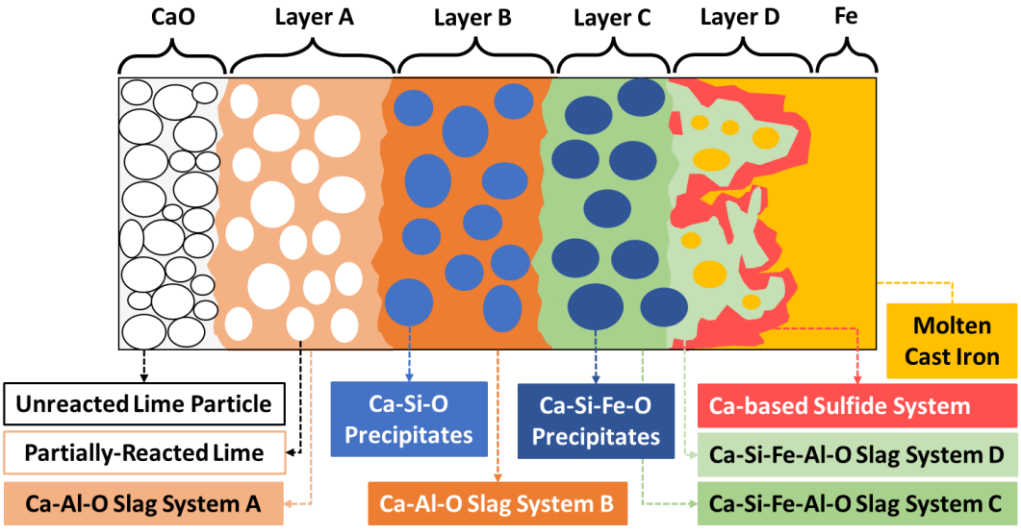

Figure 5.12. General morphology of reaction layer between lime powder and molten cast iron during desulfurization.

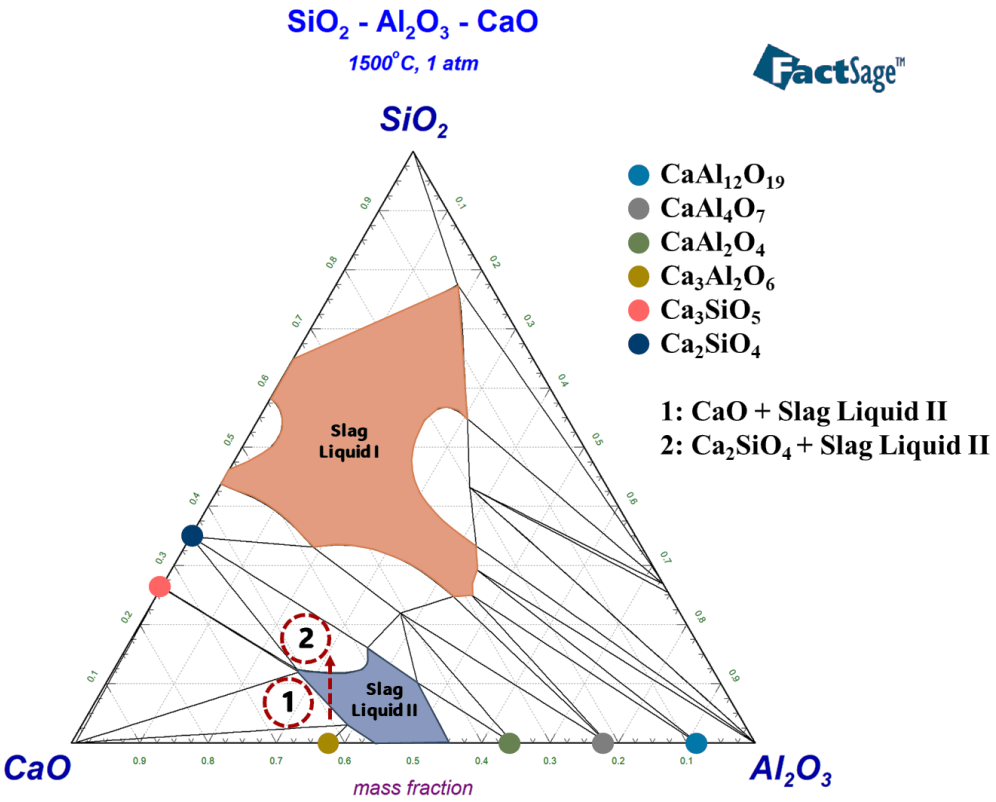

Figure 5.13. Isothermal ternary phase diagram SiO_2-Al_2O_3-CaO calculated on FactSage.

Following the description above, the dissolved silicon is expected to complementarily start taking over the deoxidation, responding to desulfurization upon a certain lower aluminum content. As the process continues, all available lime supplies will be dissolved, and the proportion of SiO_2 in liquid slag will increase. This elevated concentration of SiO_2 component in the slag system changed the equilibrium even further until surpassing the solubility limit. Consequently, as presented in **Figure 5.13** as a red arrow, Ca_2SiO_4 (C2S) precipitation will occur, and a C2S + slag liquid II (marked qualitatively by No.2) system will be established. This configuration represents layer B comprising Ca-Si-O precipitates and Ca-Al-O slag system B. This formation of C2S is also confirmed by the chemical analysis in **Table 5.2** in study points D, where the mass proportion of its main component (Ca-Si-O) stoichiometrically matches the proportion of C2S. Furthermore, despite possessing a similar system of slag liquid II (**Figure 5.13**), the designation of slag systems A and B in **Figure 5.12** aimed to cover possible distinct proportions of their components, especially the minor elements.

Given the equilibrium in **Figure 5.13**, it can be identified that an uncontrolled increasing proportion of SiO_2 leads to a significant decrease in slag liquid II, which eventually retards the further CaO availability, sulfur diffusion, and eventually the whole desulfurization process. This critical role of liquid slag is also elucidated in this chapter. It is supported by the measured concentration gradient of Ca and S, notably along the path of liquid slag from layer D to A. In this context, a decreasing tendency can be observed for sulfur, where around 5.6±3.9 wt.% was measured in layer D (**Table 5.3** detection points G), changing to only 1.5±0.5 wt.% in layer A (**Table 5.2** measurement points B). These observations suggest that the desulfurization process took place in the liquid slag system, involving the supply of CaO and diffusion of sulfur into the slag system, which aligns well with the previous finding provided in [53].

Interestingly, such a passive layer made of solid C2S on the surface of CaO was not directly detected in the boundary of this chapter. Either way, the closure of the diffusion path due to excessive growth of C2S precipitation was also not captured, or at least the process was not immediate under the parameter applied in this trial. One possible explanation related to this phenomenon is the involvement of FeO, which could explain the detection value of Fe in **Table 5.2** and clearly in **Table 5.3**. This distinguishable measured iron between layers A-B and C-D indicated that the involvement of iron followed the prior behavior between Al and Si but later in the sequence and upon a specific thermodynamic and kinetic order. Nevertheless, it is worth mentioning that the implication of increasing FeO content might be favorable. As indicated in **Figure 5.14**, adding FeO as the third component to the binary SiO_2-CaO will expand the range of configurations involving the existence of liquid slag III. A similar effect is also expected in the ternary system FeO-CaO-Al_2O_3 as once reported by Wrampelmeyer et al. [142], particularly considering the binary effect of FeO to the CaO, SiO_2, or Al_2O_3 [143], where particular arrangement possesses a liquidus temperature lower than 1500°C. In this instance, a counterproductive effect of FeO on the slag liquid II in **Figure 5.13** should be less anticipated or at least balanced in a comparable configuration of C2S + liquid slag system as suggested by Kalmanovitch and Williamson [144] for CaO-SiO_2-Al_2O_3 system with various addition of FeO.

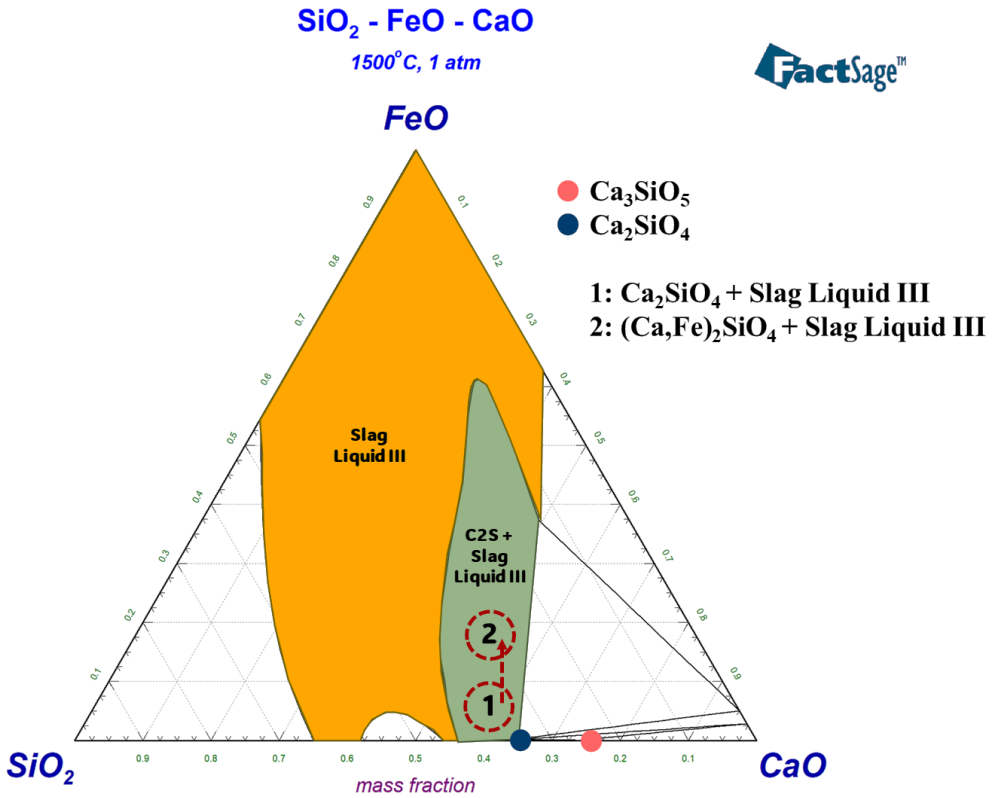

Figure 5.14. Isothermal ternary phase diagram of SiO_2-FeO-CaO calculated on FactSage.

The enhancing effect of FeO is elucidated by the fact that no other remarkable additional precipitation was detected between layer B and layer C in **Figure 5.12**, as also indicated in the ternary diagram in **Figure 5.14**. In addition, it is also suggested that the stability of Ca_3SiO_5 (C3S) is significantly narrowed, which could explain why no C3S was detected on the reaction layer. Conversely, the chemical analysis results proposed only a modification of C2S and the liquid slag are revealed. In the liquid slag system case, an iron enrichment was measured in **Table 5.3** detection points C, where FeO addition might increase the solubility limit of SiO_2 before C2S starts to precipitate compared to its direct counterpart in **Table 5.2**. On the other hand, the composition of C2S-based precipitations in **Table 5.3** detection points D revealed a higher Fe content than the comparable structure in layer B (**Table 5.2** analysis points D).

However, such a compositional change for the C2S-based precipitation mentioned earlier is not represented in **Figure 5.14**, as qualitatively marked by No.1 and No.2 for layers B and C, respectively. Based on the diagram, both compositions are located on the C2S + slag liquid III system upon increasing the portion of FeO content in the ternary system. Accordingly, it is suggested that to modify the C2S configuration as expected in layer C, the involvement of FeO should not be considered solely as monoxide but rather in a system of Fe_2SiO_4. In this case, once the solubility limit has been surpassed, the precipitation step of C2S follows a different behavior before eventually reaching the configuration in layer C. According to Selleby [145] and Hidayat et al. [146], two different C2S modifications are considered in this case: α-phase as C2S and α´-phase as $(Ca,Fe)_2SiO_4$ or a solid solution between Ca_2SiO_4 and Fe_2SiO_4.

Table 5.4. Phase configuration along the increasing ratio of Fe_2SiO_4 to Ca_2SiO_4.

Isothermal Transformation at 1500°C	Ref.
$C2S + (Ca, Fe)_2SiO_4 \rightarrow^1 (Ca, Fe)_2SiO_4 \rightarrow^2 (Ca, Fe)_2SiO_4 + \text{Slag Liquid}$	[145]
$C2S + Fe_{Liq} \rightarrow^1 C2S + (Ca, Fe)_2SiO_4 + Fe_{Solid} \rightarrow \Delta$ $\Delta \rightarrow^2 (Ca, Fe)_2SiO_4 + Fe_{Solid} \rightarrow^3 (Ca, Fe)_2SiO_4 + Fe_{Solid} + \text{Slag Liquid}$	[146]

The change in phase configuration correlated with increasing content of Fe_2SiO_4 at 1500°C is listed in **Table 5.4**. In general, both studies suggested that along with the increasing content of Fe_2SiO_4 associated with the desulfurization reaction, the precipitation of C2S will approach the configuration in layer B once the solubility limit is exceeded. As the reaction progresses, the elevated concentration of Fe_2SiO_4 modifies the C2S, as it will be dissolved in the C2S and construct the α´-phase. Eventually, the solubility of Fe_2SiO_4 in C2S will arrive at its limit upon further addition, thus forming a slag liquid (system C) + α´-phase (Ca-Si-Fe-O) system as described in layer C.

Supplementarily, unlike Selleby [145], the calculation result proposed by Hidayat et al. [146] includes the existence of liquid iron (Fe) during the initial involvement of Fe_2SiO_4. As the transformation continues, this liquid iron solidifies parallel to the gradual transformation of C2S into α´-phase. That suggested behavior of iron could be related to the observation result in this chapter, where several iron droplets (detected with around 40 to 65 wt.% Fe masked by high CaO concentration from the slag system) are engulfed in layers B and C, as captured in **Figure 5.6b** and **Figure 5.7b** marked explicitly by red arrows. Those droplets are distinguishable compared to the iron segregation on layer D, which is predominantly caused by a physical mixture. Given their morphology attached to the indication of a liquid slag system, those particles could be associated with a liquid that solidifies following a transformation, as listed in **Table 5.4**.

The fact that iron participated in the lime-based desulfurization could be a reason related to the applicability of this approach even though no addition of aluminum was carried out into the molten cast iron, as was conducted in BO-AD trials in this chapter. This development is beneficial due to the limited aluminum content (up to 0.1 wt.% [140]) allowed in cast iron to avoid unnecessary casting defects. As a matter of fact, it is publicly reported that a CaO-SiO_2-based system has been practiced as a configuration to sustain lime-based desulfurization. However, it might be limited by the CaO/SiO_2 ratio and their proportion compared to the C2S, as investigated in [136, 137]. Their observation results are also strengthened in this chapter, even though the positive effect related to the involvement of iron in modifying the solid C2S was driven and limited by the equilibrium that took place during the desulfurization process. It is based on the fact that the C2S-based precipitates are always observable along the reaction layers B and C, which should not be the case with further addition of FeO or Fe_2SiO_4 is possible, as provided in [145, 146] and **Figure 5.14**.

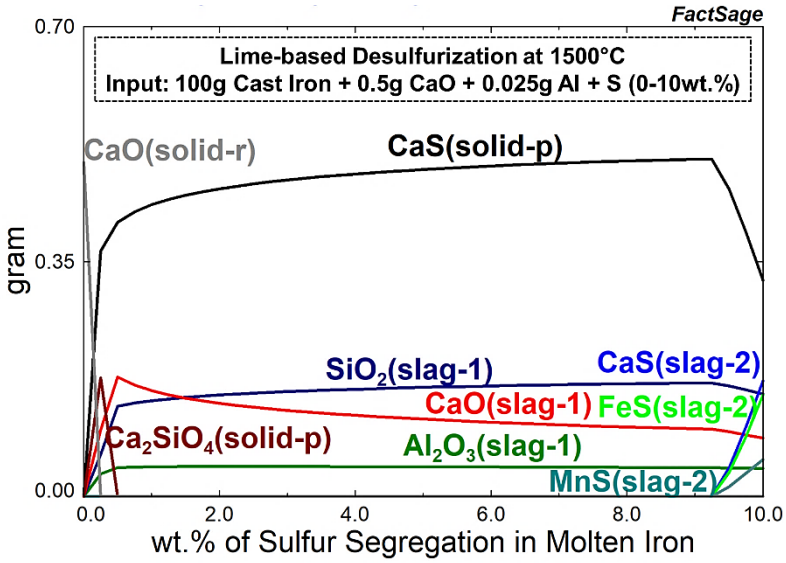

Figure 5.15. Phase development correlated with sulfur segregation at the interface calculated on FactSage.

In addition to the configuration in layer A, the absence of C2S-based precipitates can only be observed in layer D, which is directly located on the interface to the molten iron. Compared to layers B and C, this layer possesses an exceptionally high concentration of sulfur, as provided in **Table 5.3** measurement points E and G, thus indicating the segregation of CaS as a reaction product. Complementarily, the concentrated sulfur content in a general context should also be expected at this layer and associated with its distinct structure. Supported by the thermodynamic calculation provided in **Figure 5.15** for a hypothetic approach to describe the anticipated circumstances at the interface, it is suggested that a particular phase transformation should be foreseen upon a certain level of sulfur segregation that could also be observed in this chapter.

The configuration in layer D could be explored by considering the basic concept of CaS formation, in particular, the framework of sulfide capacity for lime-based liquid slag. As reported by Fincham and Richardson [147] for the binary of $CaO\text{-}Al_2O_3$ [139, 148] and ternary of $CaO\text{-}Al_2O_3\text{-}SiO_2$ [136, 138], the sulfide capacity of lime-based molten slag is positively correlated with the CaO content in liquid slag up to the solubility limit of CaS. In this case, according to Hino et al. [138], a C2S-saturated lime-based liquid slag will have already exhibited lower sulfide capacity, which is the case considered in layers B and C. Complementary to the reducing sulfide capacity, the growth of solid C2S-based precipitates as the reaction progress further will also eventually reduce the proportion of liquid phase, decelerate the supply of CaO and consequently retard the desulfurization process.

Since the diffusion process to sustain the reaction encounters a hindrance, the availability of CaO in the liquid slag to react with dissolved sulfur becomes gradually limited. Nearing the interface, the CaO would be proportionally consumed, followed by the formation of C2S and CaS. As provided in **Figure 5.15**, if no sufficient supply of CaO is available yet segregation of sulfur is expected, the C2S will redissolve and form a configuration of solid CaS and liquid slag. Given the sulfide capacity and solubility limit of the liquid slag that has

been nearing the composition of slag system D, this solid CaS formation is also expected to proceed through precipitation, as comparatively reported by Ban-Ya et al. [139] for the CaO-Al_2O_3 slag system. However, given the irregular morphology observed in the indication of CaS segregation both at layer D and highlighted in **Figure 5.4b**, it is hardly convincing that a solid CaS solely constructed the reaction product structure.

$$CaO + [S] \quad \leftrightarrow \quad CaS + [O] \tag{11}$$

According to the lime-based desulfurization reaction in **Equation (11)**, sulfur segregation (high sulfur activity at the interface) is necessary to sustain the stability of CaS, even more so in case the supply of CaO is limited. This build-up in sulfur concentration is expected to induce the formation of the FeS system with a lower liquidus temperature [149] and provide an ideal circumstance for MnS formation, as described by Tanaka et al. [107]. This possibility is also predicted by the calculation in **Figure 5.15** at elevated sulfur segregation, where a second slag system involving sulfide components should be expected. Correspondingly, this present chapter also elucidated the mentioned phenomena, as the involvement of MnS and FeS during the process was appreciably detected in **Figure 5.9** and **Figure 5.11**, respectively. This interplay between the existence of another possible slag system induced by the interchange of sulfide compounds rationalizes the appearance of CaS segregation as a covering-region layer separating the liquid slag (system D) and the iron at the interface.

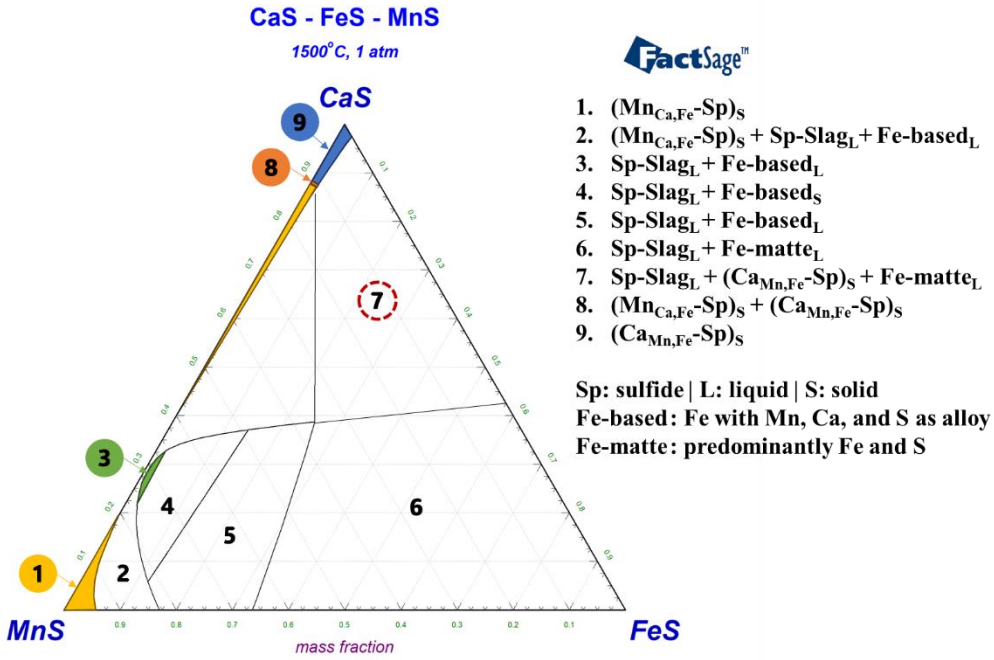

Figure 5.16. Isothermal ternary phase diagram of CaS-FeS-MnS calculated on FactSage.

Considering the behavior of MnS in compounding sulfide with CaS, the existence of MnS could be correlated with the availability of sulfur segregation, as it induces the diffusion of dissolved manganese toward the interface as contextually described by Liu and Webler [150] through (Ca,Mn)S-inclusion investigation. Depending on the composition, a liquid Ca-Mn-S system might be achieved at a temperature of 1500°C. This composition is homogeneous

before disassociating as Ca_{Mn}-S and Mn_{Ca}-S at temperatures below 1150°C [151, 152]. Furthermore, in the case of FeS involved in the system, the FeS phase will be hardly distinguishable since MnS can dissolve the FeS at a notable proportion [153, 154].

However, the possibility mentioned above of MnS in forming a low melting point sulfide composition with CaS and dissolving a notable amount of FeS is thermodynamically foreseen only in the MnS-rich region, as indicated in **Figure 5.16**. This dominance of MnS is appraised as unlikely, given the studied sample's chemical composition and the reaction layer's dynamic. On the contrary, the CaS-rich region should be considered, as predicted in **Figure 5.15**. Based on this calculation, the increasing sulfur segregation will decrease the proportion of solid CaS and elevate the sulfide slag component, which is well represented by the region marked by No.7 in **Figure 5.16**, comprising liquid sulfide slag, CaS solid, and liquid Fe matte. Accordingly, it is also reasonable to anticipate that the existence of FeS more influenced the formation of liquid sulfide slag than MnS. This perspective amplifies the binary behavior of the FeS-CaS system, which can possess a low eutectic temperature of 1100°C [155, 156].

In addition, it is further expected that the proportion of solid CaS could completely vanish by excessive sulfur segregation at the interface, as indicated in **Figure 5.15**. That mechanism can also be observed by shifting the slag composition in **Figure 5.16** from No.7 to No.6. Despite a change in proportions, both compositions still consist of liquid sulfide slag and liquid Fe matte. To this extent, it is also interestingly revealed that the liquid sulfide slag could accommodate a notable amount of MnS as its component, thus amplifying the formation of Ca-Fe-Mn-S liquid slag. This formation of liquid CaS-based slag represents the involvement of FeS and MnS during this present chapter, which also explains the irregular morphology of CaS segregation captured in **Figure 5.8**. On the other hand, the predicted incorporation of liquid Fe matte could also be related to detecting the iron-sulfur-rich region marked in **Figure 5.10**.

Eventually, since the liquid slag system also arises in direct contact with molten cast iron, the mixing possibility as one plausible reason for iron segregation in layer D is increased. As briefly mentioned in the previous explanation addressing the iron droplet indication in layers B and C, which are predominantly chemically driven, iron segregation in layer D should be related to sulfur concentration. Since the significant sulfur content at the interface between layer D and molten iron is considered combined with the characteristic of sulfur as a surface active element, this segregation will reduce the surface tension [157, 158] and enhance the possibility of physical slag-metal mixing [159, 160]. This approach, combined with previous explanations regarding CaS formation, will deliver the construction of layer D comprising CaS-based sulfide slag solution, Ca-Si-Fe-Al slag system, and molten iron segregation.

5.3. Summary of Lime-based Desulfurization Mechanism

Following the experiment results and thermodynamic calculations, the proposed reaction mechanism between lime and molten cast iron during the desulfurization process could be described as follows:

(1) As the lime powder and cast iron interacted, the desulfurization process will be initiated, coupled with the aluminum oxidation process. This reaction established the

reaction product of CaS and a calcium aluminate slag system. Since the availability of aluminum in cast iron was limited, the silicon took over the deoxidation process, thus increasing the silicon proportion in the slag system and creating a liquid slag system. In this case, considering the low sulfur amount that could penetrate the CaO-particle and diffuse into the liquid slag system combined with high CaO concentration, the sulfide capacity was expected to be high enough to prevent the precipitation of CaS.

(2) As the lime-based desulfurization reaction progressed, the concentration of SiO_2 in liquid slag increased. Eventually, the solubility of SiO_2 in the slag system is exceeded, initiating the precipitation of Ca_2SiO_4 (C2S), thus forming the interference for desulfurization as this growth of C2S will reduce the liquid slag proportion and induce lower sulfide capacity. Driven by the circumstances during the desulfurization, iron was expected to contribute as a Fe_2SiO_4 compound. It modified the precipitation of C2S into α'-phase $(Ca,Fe)_2SiO_4$ coupled with increasing Fe content in liquid slag.

(3) Once the development of solid C2S-precipitates becomes significant, the further supply of CaO becomes limited; meanwhile, the sulfur concentration was significantly high, particularly in the vicinity of the interface. Given this inhibition, the solubility limit of CaS was approached and eventually surpassed. Concurrently, sulfur segregation at the interface was established, inducing the formation of other sulfides: MnS and FeS. The interplay between those sulfides modified the proportion of solid CaS as a reaction product into a liquid sulfide slag system beside the oxide slag system.

Chapter 6

Ecotechnological Study on Lime-based Desulfurization

After assessing the lime applicability and its reaction mechanism during the desulfurization process on a laboratory scale, this chapter comprehensively explores the ecotechnological consideration and perspective of implementing a lime-based desulfurization process in the cast iron industry to partially replace the utilization of magnesium. By adopting an injection process to introduce the lime powder into molten cast iron, this chapter elucidated that the new alternative concept can be integrated with daily operations without any disparities in cast iron quality, as proved by the production of compacted graphite cast iron.

Publication Note:
During the manuscript preparation until the final submission of this dissertation, this chapter is a part of a published research article in the Journal of Sustainable Metallurgy [141].

6.1. Materials and Methods

6.1.1. Technological Trial in Industrial Lime-based Desulfurization

The operation analyzed in this chapter involves a newly developed injection process in the cast iron foundry in Germany. The technological concept was based on positive results on a laboratory scale provided in different studies and previous chapters. This alternative process involves an introduction of a lime powder desulfurization agent into 2.5-ton molten cast iron by employing inert nitrogen gas as a transport medium through a refractory coated lance. The construction of the injection machine is provided in **Figure 6.1**.

Table 6.1. Initial chemical composition (wt.%) of cast iron before desulfurization.

C	Si	S	P	Mn	Fe
3.4 – 3.5	1.6 – 1.7	0.08 – 0.13	0.06 – 0.07	0.5 – 0.6	93 – 94

Considering the future coupled integration defined by working synchronously in one integrated industrial cast iron production system, the injection machine was designed to be operatively comparable to the magnesium-based desulfurization process. In this regard, the lime injection operation should also be conducted using a batch ladle-based approach, starting by tapping one ladle of molten cast iron from a cupola furnace, which has a typical composition provided in **Table 6.1**. The molten iron would subsequently be transported to the injection station and desulfurized at a starting temperature of around 1500°C for five to seven minutes. Furthermore, the slag skimming process is carried out, followed by chemical composition analysis and temperature measurement, before being transferred to the further production sequence of the compacted graphite cast iron (CGI) manufacturing process following the routine standard operational procedures in the foundry involved in this study.

Following the establishment of the lime injection desulfurization process, the development encompassed three sequential phases. The first step was the experimenting stage, which involved a set of trials for different mixtures of lime-based desulfurization agents and lance

designs to identify the optimal process. Two distinct designs of refractory-coated lance were assessed: one (In-Tip) and two (To-Tip) holes in the nozzle of the injection lance. In addition, the desulfurization ability of four mixtures was also examined, namely CaO-Na_2CO_3-CaF_2 (KNF), CaO-Na_2CO_3 (KN), CaO-C-Na_2CO_3 (KCN), and CaO-C (KC) including an essential evaluation to the generated slag for respective mixtures through a leaching test.

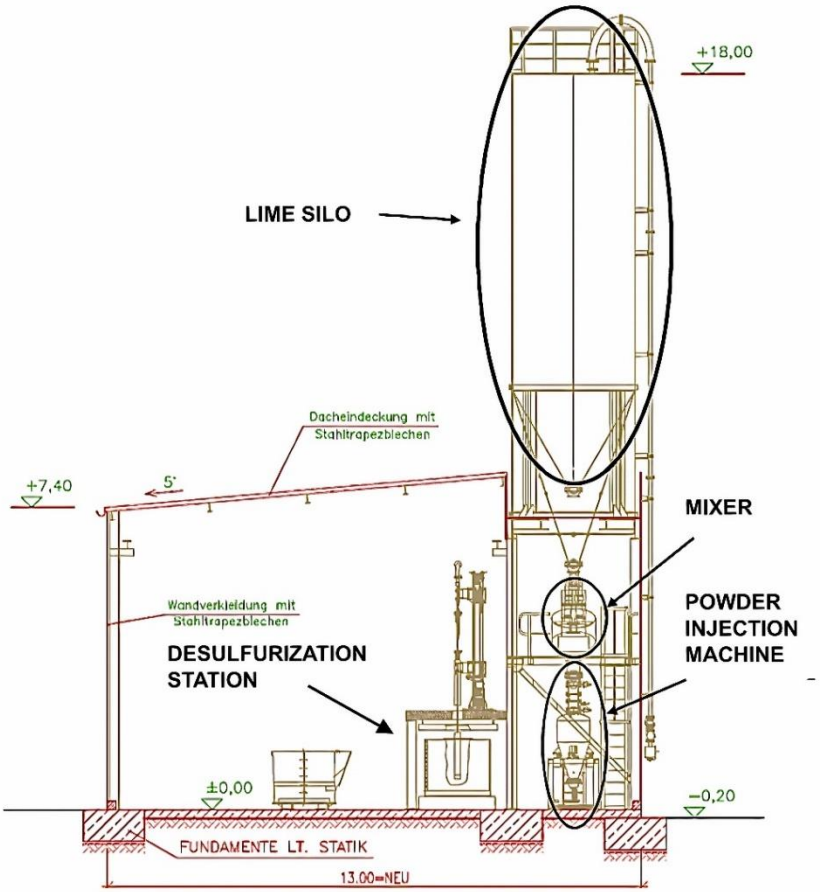

Figure 6.1. Construction of an automatic injection machine for lime-based desulfurization of cast iron [129, 161].

Subsequently, the second sequence was the injection optimization phase, which explored different configurations of injection parameters and utilized a coarser lime particle size of around <2 mm compared to <100 μm during the previous stage. Conclusively, the final leap was the integration process, where the optimum result from the preceding phases was employed to integrate the injection method for desulfurizing the molten cast iron into the operating production system in the cast iron foundry.

6.1.2. Ecological Examination in Industrial Lime-based Desulfurization

Supplementary to the technical analysis, a straightforward life cycle study was conducted following the general framework provided in DIN EN ISO 14040 [162]. This section analyzes the expected environmental benefits of substituting the magnesium-based operation with the lime-based desulfurization process. By referring to a set of primary industrial data, the evaluation of possible emission reduction during the desulfurization of 1 kg cast iron was carried out and subsequently used as the functional unit. However, the

analysis provided in this ecological approach involves only a direct juxtaposition by considering solely the desulfurization operation. Hence, the process sequences before and after the desulfurization operation are settled to be identical, which is also required to support the concept of coupled integration mentioned earlier.

The study will be carried out under a cradle-to-gate approach based on contextual scenarios in the foundry that participated in this study. Considering only the final development phase (integration process) of lime injection technology, the material and energy balance both for magnesium-based designated as treatment 1 (current) and lime-based desulfurization indicated as treatment 2 (alternative) are respectively provided in **Figure 6.2** and **Figure 6.3**. It is worth noting that some prior limiting circumstances should be considered to refine the subject of this comparative study.

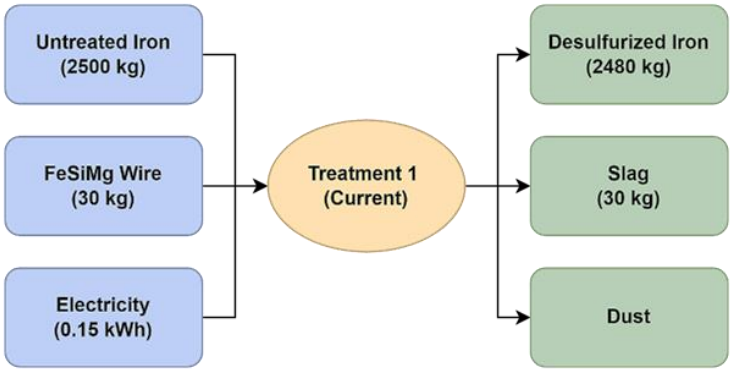

Figure 6.2. Material flow diagrams of the current magnesium-based desulfurization.

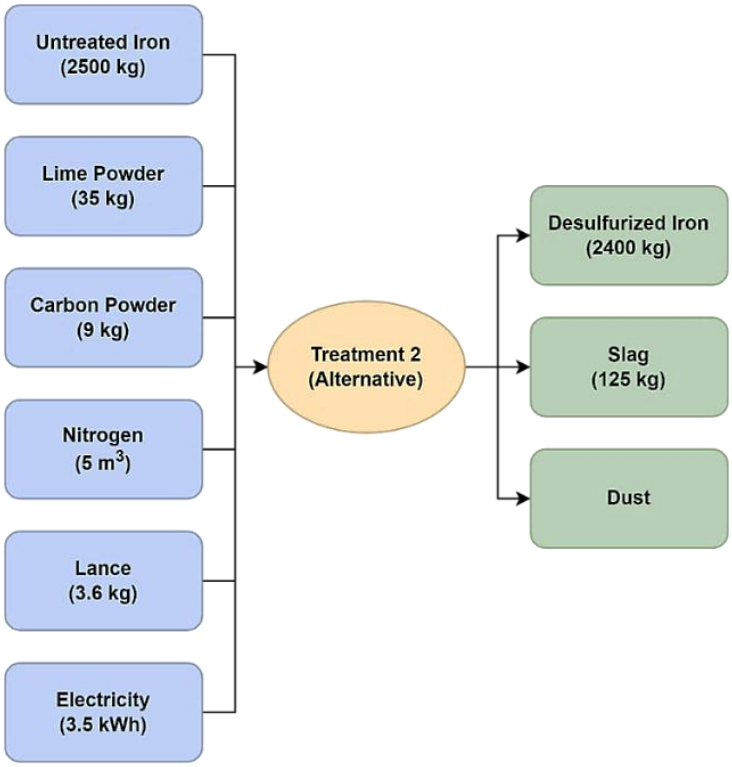

Figure 6.3. Material flow diagrams of the alternative lime-based desulfurization.

By starting from the perspective of emitted emission for both process options, the air contamination in the form of gas, fume, and dust is hypothesized to be resultantly comparable. Therefore, they are not considered in the life cycle inventory. A similar approach was also adopted to exclude the slag discharge since the slag from the lime-based process could be recycled back into the cupola furnace instead of landfilled [163]. This interchange between slag amount and recyclability is expected to neutralize their contribution from the perspective of a comparative study. Despite this limitation, the result of this study should be negligibly affected since forthcoming results will elucidate that the indirect emissions representing scope III emission [164] considered during the calculation contribute enormously dominant than these direct emissions (Scope I) components.

Table 6.2. List of estimated specific emissions for utilized materials in magnesium-based desulfurization process.

Materials		Specific Emission Range		Emission Unit	Note
Entities	**Segments**	**Minimum**	**Maximum**	**CO_2eq/Material**	**References**
FeSiMg-Wire	FeSi	2920	7850	kg/ton	[165, 166, 167]
	Mg	13800	37000	kg/ton	[168, 169, 170]
	Steel	540	2300	kg/ton	[171, 172, 173]
Transport		235	580	g/ton.km	[174]
Electricity		485		g/kWh	[175]

Table 6.3. List of estimated specific emissions for utilized materials in lime-based desulfurization process.

Materials		Specific Emission Range		Emission Unit	Note
Entities	**Segments**	**Minimum**	**Maximum**	**CO_2eq/Material**	**References**
CaO-Powder Blend	CaO	987	1975	kg/ton	[176, 177, 178]
	Carbon	1040	2300	kg/ton	[179, 180, 181]
	Nitrogen[1)]	85	136	kg/ton	[182]
Injection Lance	$ZrSiO_4$	320		kg/ton	[183]
	Al_2SiO_5	145		kg/ton	[184]
	Al_2O_3	400	830	kg/ton	[185, 186]
	SiO_2	33	75	kg/ton	[187]
	$CaAl_2O_4$	310	1060	kg/ton	[188, 189]
	SiC	2910	4200	kg/ton	[190, 191, 192]
	Fe_2O_3	9	13	kg/ton	[193, 194]
	Steel	540	2300	kg/ton	[171, 172, 173]
	Fabricate[2)]	361	771	kg/ton	[195, 196]
Transport		235	580	g/ton.km	[174]
Electricity		485		g/kWh	[175]

NOTE:

1) It was estimated from specific energy consumption of 175 – 280 kWh/t sourced from electricity.
2) It was estimated that the specific energy consumption of 5105 – 8850 kJ/kg as oil and electricity.

Regarding energy consumption, electricity is considered the primary energy source supplied by the industrial power mix in Germany unless explicitly mentioned. Furthermore, regarding the input materials, all consumables are considered qualitatively pure or available in one component system except for the FeSiMg-wire and injection lance. Consequently, the life cycle inventory for FeSiMg-wire and injection lance would comprehensively include a separate consideration for each building component and proportionally calculated based on their partial contribution. Given the restriction of publishing internal company data, the composition in this regard will not be explicitly revealed, though it could be traced through the calculation process.

Considering all the predefined boundaries, the life cycle inventory in terms of specific emission ranges is provided in **Table 6.2** and **Table 6.3**. The data was mainly gathered from secondary sources, such as peer-reviewed literature studies and official reports, followed by necessary calculations. The involvement of range values instead of one single number as the calculation approach is appraised to be beneficial since it could represent a holistic comparative CO_2eq. Practically, by using minimum and maximum emissions, the calculation results can accommodate sensitivity associated with the technology alternatives and energy source combinations, which depend highly on the supplier's circumstances.

6.2. Results and Discussion

6.2.1. Lime-based Desulfurization Results by Injection Process

The change in chemical composition following the desulfurization process was recorded and analyzed in every development phase, as recorded in **Figure 6.4**. It is observable that the first two development phases exhibited high fluctuation in end sulfur content due to the experimentation of different lime-based desulfurization mixtures as well as possible parameter combinations. In contrast, the integration process showcased stable and consistently good-quality desulfurization treatment where the end sulfur contents are mainly lower than 0.015 wt.% as required.

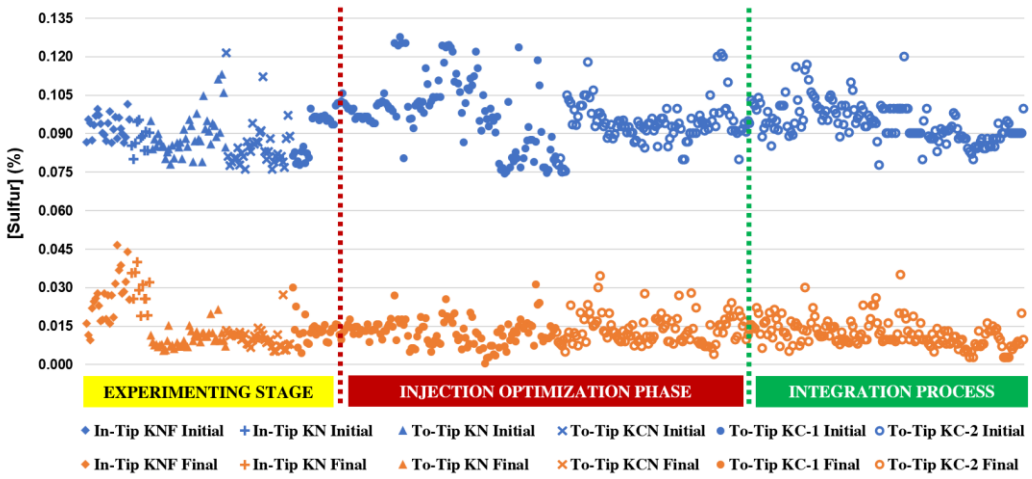

Figure 6.4. Sulfur content before (initial) and after (final) desulfurization process.

Supplementary to the results summarized in **Figure 6.4**, details of final sulfur concentration during the first two development phases are comparatively provided in **Figure 6.5**, where

the To-Tip KC comprised both KC-1 and KC-2 (lime particle size of <100 µm and <2 mm, respectively). Accordingly, it is elucidated that the To-Tip lance design is better than the In-Tip in terms of desulfurization degree. It is also suggested that introducing the CaF_2 and Na_2CO_3 into the lime-based desulfurization mixture could improve the desulfurization process, as represented by a lower final sulfur content than the KC (without CaF_2 and Na_2CO_3). In the distinct case of KC, the results in **Figure 6.4** indicate that a comparable desulfurization degree could also be achieved using a coarser lime particle.

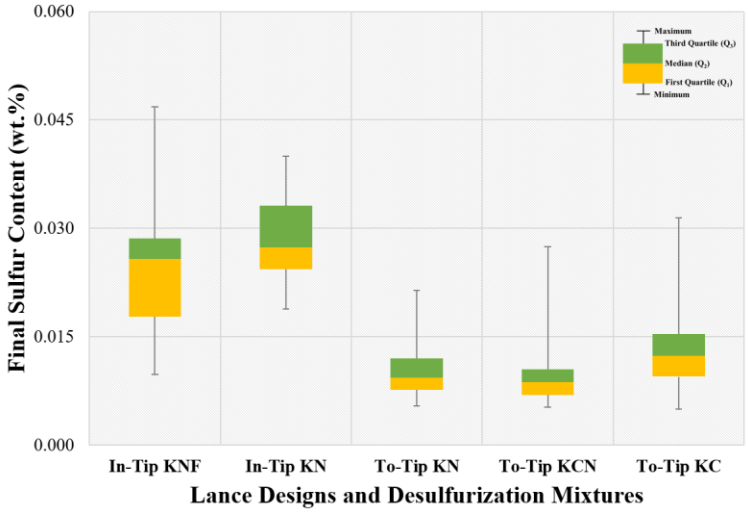

Figure 6.5. Effect of different lance design and desulfurization mixtures on the final sulfur content.

Table 6.4. Effect of different desulfurization agent mixtures on the landfill classes of the desulfurization slag.

		FeSiMg	KNF	KN	KCN	KC
pH		10.9	11.9 – 12.7	12.4 – 12.9	12.6 – 12.7	12.5 – 12.7
Sb	µg/l	<5.0	0.9 – 18.0	0.2 – 7.4	0.3 – 0.4	0.1 – 0.4
As	µg/l	<5.0	0.1 – 7.7	1.0 – 12.3	0.1 – 0.2	0.1 – 0.3
Ba	µg/l	30	9.3 – 23.2	0.4 – 2.0	6.8 – 38.4	18.8 – 81.3
Mo	µg/l	<10.0	19.3 – 80.7	5.3 – 90.7	40.8 – 92.1	5.5 – 58.1
Ni	µg/l	<7.0	1.6 – 34.0	4.8 – 20.2	0.5 – 0.6	0.7 – 2.5
Zn	µg/l	<50.0	6.1 – 26.3	<5.0	<5.0	<5.0
Cl^-	mg/l	7	1.6 – 6.6	<1.0	<1.0	<1.0
F^-	mg/l	0.7	19 – 337	<0.4	<0.4	<0.4
SO_4^{2-}	mg/l	23	60 – 754	399 – 843	12 – 303	4 – 30
Landfill Classes [197]			**Underground**	**DK 1**	**DK 1**	**DK 0**

Considering the better performance of the desulfurization agent containing CaF_2 and Na_2CO_3, the slag analysis indicated a counterbalancing effect. According to the leaching test of desulfurization slags in **Table 6.4**, the operation involving CaF_2 is expected to be hard to take care of due to its contamination and requires an underground landfill. Improvement in landfill classes to DK 1 is observed in cases where no CaF_2 was incorporated in the mixture, which practically means it is less hazardous. Furthermore, the mixture that was utterly free

from CaF_2 and Na_2CO_3 can even reach the DK 0, which indicates high stability, less contaminant, and higher recyclability, as well as possesses comparable quality to the slag from the magnesium-based (FeSiMg) process.

Table 6.5. Average mechanical properties of CGI products made from magnesium- and lime-based desulfurized cast iron.

CGI Products	Tensile Strength (MPa)	Yield Strength (MPa)	Elongation (%)
Cylinder Head – FeSiMg	498	364	2.0
Cylinder Head – Lime	496	373	1.9
Cylinder Block – FeSiMg	502	378	1.7
Cylinder Block – Lime	497	384	1.6

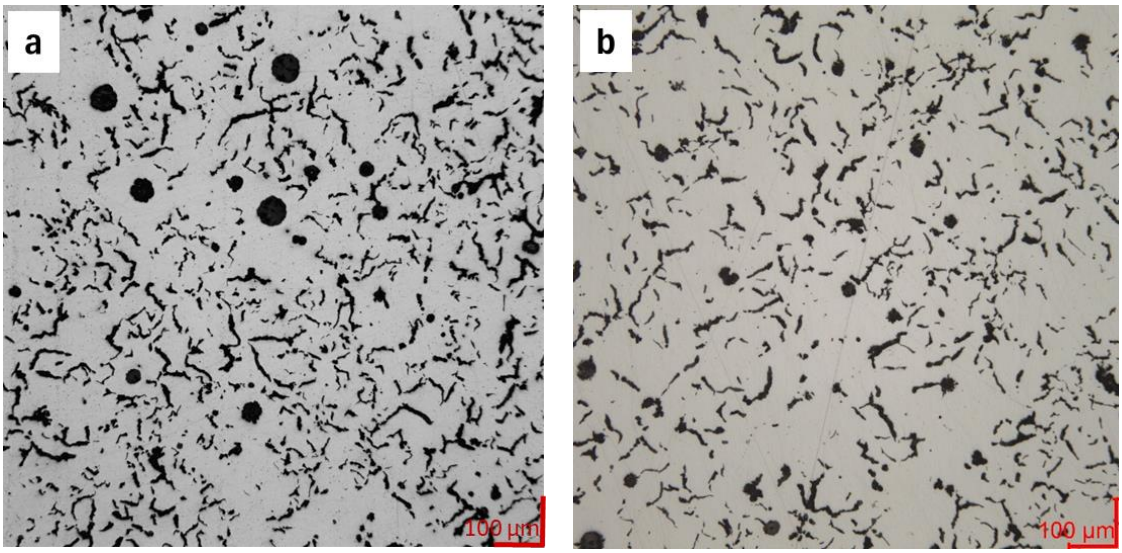

Figure 6.6. Graphite structure of CGI products made from (**a**) magnesium- and (**b**) lime-based desulfurized cast iron.

Besides exploring the process development and parameter configuration, the iron desulfurized using optimum parameters (**Figure 6.3** using To-Tip KC-2) was subsequently utilized to produce industrial cast iron products during the last development phase. Following the positive results in chemical composition, specifically final sulfur content, the lime-based desulfurized cast iron was transferred to the post-desulfurization process, including examination sequences following the standard operational procedures. **Table 6.5** and **Figure 6.6** show that the CGI produced from lime-based desulfurized cast iron exhibited comparable mechanical properties and desirable graphite morphology, suggesting no disparity in achieving comparable material characteristics.

6.2.2. Ecological Impact Assessment in Comparative CO_2eq

As previously indicated, an essential ecological analysis complemented the perspective after exploring the technological feasibility. **Table 6.6** presents the results of the estimated CO_2eq emission comparison between the FeSiMg-wire desulfurization process and the lime-

based operation according to the respective mass and energy balance provided in **Figure 6.2** and **Figure 6.3** both for one treatment as well as for the designated functional unit.

Table 6.6. Comparative impact assessment (estimated CO_2eq) for desulfurization process of cast iron.

Impact Assessment CO_2eq		g CO_2eq for 1 Treatment Ladle		g CO_2eq for 1 kg Cast Iron	
Process	**Materials**	**Minimum**	**Maximum**	**Minimum**	**Maximum**
FeSiMg Process	FeSiMg-Wire[1)]	171651	537794	68.66	215.12
	Transport[2)]	18350	51197	7.34	20.48
	Electricity	51	77	0.02	0.09
TOTAL Current Process		**190052**	**589068**	**76.02**	**235.69**
Lime Powder Process	Lime Blend	44481	90746	17.79	36.30
	Lance[3)]	2961	6014	1.18	2.41
	Transport[2)]	3176	7839	1.27	3.14
	Electricity	1364	2046	0.55	0.82
TOTAL Alternative Process		**51982**	**106645**	**20.79**	**42.67**

NOTE:

1) It was estimated from FeSi, magnesium, and steel emission accumulation based on the SAF-based manufacturing process of FeSiMg-Wire. The mass proportion of each component refers to the respective supplier data.
2) Transportation calculation covers only the transfer from supplier and company site, where the desulfurization process occurs, and does not consider the transportation during raw material preparation (mining, manufacturing, etc.).
3) It was estimated from emission accumulation from all refractory materials listed in **Table 6.3**, including the necessary fabrication process. The mass proportion of each component refers to the respective supplier information.

The calculations reveal that, depending on the technology employed in the manufacturing process of raw materials, the expected CO_2eq emissions for treating one ladle of molten iron range from 190 to almost 590 kg (total current process) for the FeSiMg-wire process. In contrast, the lime-based process demonstrates significantly lower estimated emissions ranging from 52 to 107 kg (total alternative process) for the same quantity of molten cast iron. It is also indicated from this calculation result that the raw materials play a significantly critical role, considering their massive contribution to the whole life cycle of emission regardless of the process alternative. **Table 6.6** also suggests that the manufacturing process of raw materials accounts for approximately 90% of the total emission.

Complementary to the ecological advantage explored earlier, technological acquisition could also provide a capital gain. As indicated in **Table 6.7**, a certain saving amount should also be expected for one treatment process upon employing a lime-based desulfurization process. It is worth mentioning that this saving, which could range from 10-50 € for one treatment, should first cover the initial investment cost of around 1.5 Mio. € before delivering an actual profit. Considering a linear breakeven point (BEP), the number of treatments in one year and the price fluctuation of raw materials would highly determine the extent of BEP.

Table 6.7. Cost estimation for the desulfurization process of cast iron (including possible slag disposal).

Rough Cost Estimation			Price (€) per Unit Material		Price (€) for 1 Treatment Ladle	
Process	**Materials**	**Unit**	**Minimum**	**Maximum**	**Minimum**	**Maximum**
FeSiMg Process[1)]	FeSiMg-Wire	ton	1500	2500	45.00	75.00
	Electricity	MWh	150	200	0.02	0.03
	Slag Disposal	ton	40	75	1.20	2.25
TOTAL Cost of Current Process for 1 Ladle (2500 kg)					**46.22**	**77.28**
Lime Powder Process[1,2)]	Lime Blend	ton	800	950	13.90	18.60
	Lance	unit	300	400	6.00	8.00
	Electricity	MWh	150	200	0.53	0.70
	Slag Disposal	ton	40	75	5.00	9.38
TOTAL Cost of Alternative Process for 1 Ladle (2500 kg)					**25.43**	**36.68**

NOTE:

1) A rough estimation of the price range was contextually provided by the cast iron foundry involved in this study.
2) Prices apply to batch procurement during the development phase and are expected to be reduced upon higher order quantity.

6.2.3. Comparative Discussion on Ecotechnological Advantages

As summarized in **Figure 6.4**, a distinct behavior in terms of significant fluctuation in desulfurization performance is recorded, highlighting the challenges faced during the first two development phases. During these periods, some prospective mixtures were examined, including introducing additives to control dissolved oxygen levels [48] and enhance the proportion of liquid slag on the surface of lime particles [46]. This course of action was aimed to drive the process towards the highest desulfurization degree possible coupled with an optimum level of lime utilization to counterbalance the desulfurization duration of five to seven minutes, which lags the magnesium-based operation (three to five minutes).

Adding aluminum to control the dissolved oxygen based on the investigation results from Matousek [135] was one of the first considerations during the optimization phase. However, given the critical limit of 1000 ppm [140] to avoid any undesired casting defects, intentionally bringing the aluminum into molten cast iron was considered a long-term strategy. On the other hand, as indicated in **Figure 6.5**, increasing the proportion of liquid slag by utilizing Na_2CO_3 and CaF_2 proved effective and comparable to previous studies provided in [51]. Unfortunately, the slag leaching test results in **Table 6.4** suggest that these modifications lead to highly contaminated slags, which is potentially counterproductive. In addition, violent reactions followed by intensive fume generation were observed during the desulfurization process involving Na_2CO_3. Amplifying the consideration of safety procedure, uncontrolled turbulence in molten metal is also not preferable as it can reduce the refractory lifespan both on the process ladle and the injection lance.

Interesting to observe is the utilization of KC as a desulfurization agent, where comparable desulfurization performance is surprisingly observed. This introduction of carbon was

initially aimed to compensate for the depletion in dissolved carbon following the intensive atmospheric high-temperature treatment. According to the correlation proposed by Orths and Weis [105, 114] and recently supported by Grachev [106], this discrepancy is chemically related to the dissolved oxygen level. Considering the treatment temperature of 1500°C and the chemical composition of the molten cast iron, carbothermic reduction of oxidized dissolved silicon is favorable, thus inducing a decrease in carbon content.

The effect of involving carbon is seemingly not just limited to the alloying process but, to a certain extent, eases the desulfurization process, as once also explored by Boyd et al. [42], Fruehan [43], and Turkdogan and Martonik [133]. Their correlation is circumstantially rational since a higher carbon content will influence the dissolved oxygen level [131] in molten iron, which eventually will positively facilitate the reaction between lime and dissolved sulfur. Furthermore, complementary to its effectiveness in reducing the sulfur content, utilization of KC is followed by less contamination on the desulfurization slag until it is comparable to the magnesium-based process provided in **Table 6.4**. This favorable combination is the main reason for selecting KC as the standard desulfurization agent considered during the integration process and the life cycle assessment.

It is worth noting that the comparable desulfurization degree without incorporating fluxes, as mentioned earlier, was theoretically appraised as an anomaly. Contrary to the numerous investigation results, liquid slag is expected to deliver a better desulfurization degree since it is crucial to facilitate sulfur diffusion, particularly if forming a solid reaction product due to high silicon content is anticipated. One plausible explanation associated with this phenomenon is the dynamic resultant from the kinetic perspective. Given the size of the ladle in a cast iron foundry, which is one hundred times smaller than in the iron and steel industry, the available upward transport period of lime to the surface of molten metal is significantly narrowed. Even though the desulfurization process could continue at the slag-metal interface on the top surface of molten cast iron, the observations indicate that the desulfurization reaction was surficial and limited to the pure lime particle.

In other words, the further diffusion of sulfur through desulfurization product on the surface of reacted lime is limited because of its lower rate compared to the floating duration and additional availability of fresh lime due to the continuous injection process. This dynamic can also explain the occurrence observed in the boundary of this chapter that using finer particles (KC-1) is not necessarily better than coarser lime (KC-2) since a comparable final sulfur content was measured, as provided in **Figure 6.4**. This limitation is yet wholly acceptable from an industrial perspective due to other technical considerations, including material handling, stable injection rate, desulfurization batch duration, reliability of final sulfur content, and slag mineralogy. Accordingly, as shown in **Figure 6.4**, desulfurization employing To-Tip KC-2 is considered optimum results for the integration process.

Additional crucial enhancing factors can also be generated from the perspective of ecological advantages. According to the calculation carried out in this chapter, considering the whole life cycle as summarized in **Figure 6.7**, the result indicates that the lime-based desulfurization alternative offers less carbon footprint operation than the magnesium-based process.

Specifically, the calculation demonstrated that the least environmental-friendly technology currently available for the lime-based approach (43 g CO_2eq) could still deliver more sustainable operation compared to the cleanest (76 g CO_2eq) accessible technology required to desulfurize one-kilogram molten cast iron using FeSiMg-wire.

As mentioned previously, the production process of raw materials (FeSiMg and lime) contributes significantly to the total reported emissions. In addition, the results in **Table 6.6** suggest that the transportation emission associated with the FeSiMg process is up to six times higher than the lime-based alternative. This disparity represents that the required materials for the lime-based desulfurization process are readily available domestically, indicating a plausible opportunity to reduce dependency on the global supply chain or high-risk monopolistic market situation. However, it is essential to note on the other side that the injection machine for the lime-desulfurization process consumes more energy, although its contribution to the overall emissions is considered negligible.

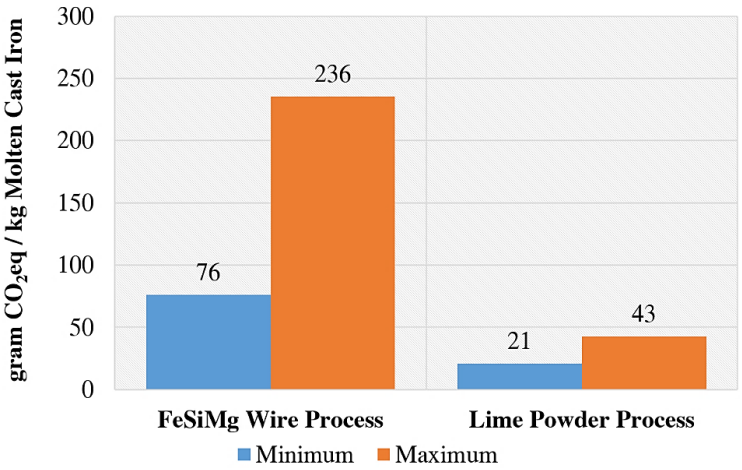

Figure 6.7. Summary of comparative carbon footprint potential (CO_2eq) for magnesium-based and lime-based desulfurization process in cast iron.

Another challenge in implementing the lime-based desulfurization process is the significant amount of slag generated, which is also associated with higher expected metal loss. This occurrence results from high molten bad turbulence during the injection process, including the molten metal trapped in lime particles due to agglomeration (sintered) mechanism or pore penetration. The disadvantage of this high slag volume can also be observed in the cost estimation in **Table 6.7**, which shows that the slag disposal could account for up to 25% of the total treatment cost and thus reduce the promising capital gain of the lime-based desulfurization process.

In response to the abovementioned challenge, a recycling practice was taken as an alternative to overcome this challenge. Specifically, the foundry in this study charged back the lime-based desulfurization slag into the cupola furnace for the lamellar cast iron (LGI) production process, where the sulfur should not be a concern, and the rest of the iron could be recovered. Nonetheless, it is crucial to consider that this action depends entirely on slag

disposal and energy price fluctuation. Hence, it is extensively contextual to each iron foundry, which always holds distinct circumstances.

6.3. Summary of Industrial Lime-based Desulfurization

Based on the experimental results conducted on industrial scales coupled with an ecological consideration, the following findings could be extracted from this chapter:

(1) Lime-based desulfurization through injection mechanism in the cast iron industry can be successfully implemented, as proven by the reproducible final sulfur content lower than 0.015 wt.%, followed by the comparable quality of the final product.

(2) Given the technological consideration of adopting the lime powder injection approach, it offers additional opportunities for further improvement, including an extended alloying function for fine alloying materials, which is challenging in foundry practice.

(3) The ecological impact assessment indicates that the lime-based desulfurization process holds significantly lower theoretical CO_2eq (43 g/kg cast iron) than its counterpart (76 g/kg cast iron), mainly associated with raw materials production.

(4) The substitution of magnesium with lime reduces the dependency and consumption of an expensive resource since the magnesium can no longer be economically recycled from sulfide or oxide form in the slag once utilized in the desulfurization process.

(5) The adaptation of lime as a desulfurization agent in cast iron enhances a secure supply chain, higher market competitiveness, and sustainable economic advantages due to lower desulfurization costs.

PART IV
Nodularization

Chapter 7

Graphite Nucleation during Recycling of Ductile Iron

Following the identification in the earlier chapter regarding the role of magnesium during nodularization, assessing any possibility of producing nodular graphite without any addition of magnesium should be started by exploring the recycling process of ductile iron. Therefore, this chapter systematically analyzed the impact of the ductile iron remelting process on graphite nucleation. Based on observation results, different graphite structures nucleate in cast iron in response to the recasting process. Specifically, the formation of vermicular and potentially chunky graphite structures can be observed, thus providing further insight into their relation to the nodular graphite in the ductile cast iron production process.

7.1. Materials and Methods

7.1.1. Cooling Curve Analysis

The first experimental set involved cooling curve analysis employing a commercial closed double-chamber AccuVo-Cup® crucible [198] for thermal analysis. In these trials, approximately 500 g of a cast iron sample was melted under various superheating conditions, including 1300°C, 1400°C, and 1500°C. In this instance, two distinct cast iron samples with different compositions, as delineated in **Table 7.1**, were considered in this chapter. As a reference, the first sample (HS-CI) comprised the base cast iron produced by the cupola furnace. In contrast, the second sample (LS-CI) contained ductile iron returns.

Table 7.1. Initial chemical composition (wt.%) of cast iron samples.

	C	Si	S	P	Mn	Mg	Fe
HS-CI	3.4 – 3.5	1.6 – 1.7	0.10 – 0.12	0.06 – 0.07	0.5 – 0.6	< 0.005	93 – 94
LS-CI	3.4 – 3.6	2.2 – 2.3	< 0.005	0.02 – 0.03	0.10 – 0.15	0.03 – 0.04	93 – 94

The cooling curve analysis was conducted by melting the respective cast iron sample in a clay–graphite crucible using an induction furnace. Upon reaching the designated superheating temperature, the molten metal was swiftly poured into the empty crucible, and the temperature profile during the cooling process was digitally recorded. No additional materials other than the cast iron itself were introduced during this process. After cooling, the samples were removed from the crucible and prepared for further metallography analysis under a light microscope.

7.1.2. Copper Mold Chill Casting

The second investigation utilized a chill casting approach, where the molten cast iron was cast into a copper mold upon remelting at a superheating temperature equivalent to the cooling curve analysis. As illustrated in **Figure 7.1**, the chill casting setup encompasses two components: the melting and casting sections. The melting section is designed to prepare approximately 200 g of molten iron in **Table 7.1** in a clay–graphite crucible. In this case, the crucible is equipped with a base opening yet previously secured by a refractory-based stopper during the melting process. This stopper will be retracted once the designated superheating

is attained. This mechanism allows the molten iron to immediately flow through the opening and cast into the copper mold (inner diameter of 25 mm) at the casting section. After cooling, the samples were extracted and subjected to the sample preparation indicated in **Figure 7.1** before being analyzed employing light microscopy and scanning electron microscopy with energy-dispersive X-ray spectroscopy (SEM/EDS).

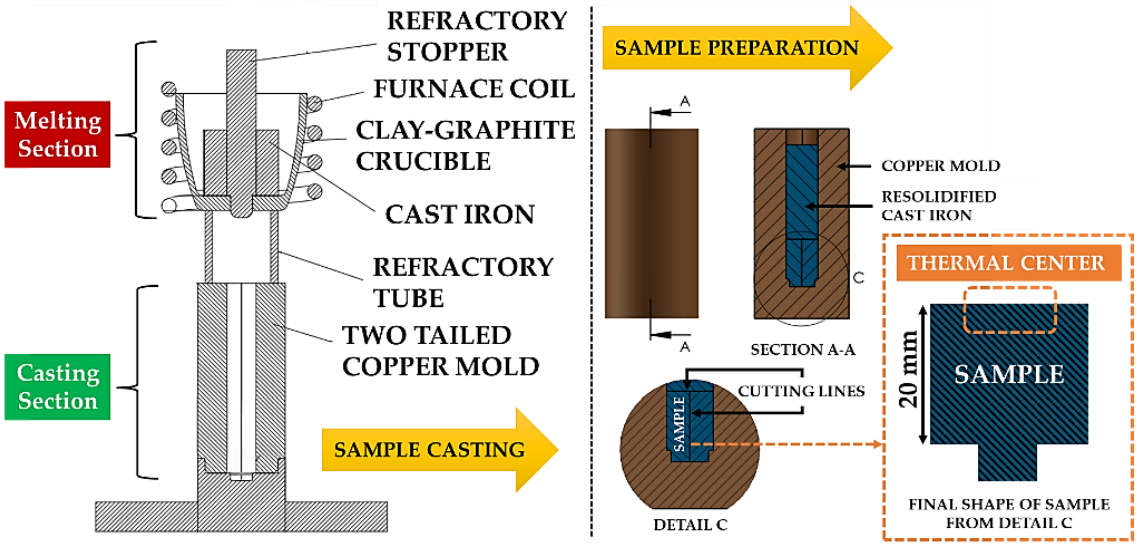

Figure 7.1. Experimental setup and sample preparation for the chill casting experiment.

7.1.3. Extended Cooling Curve Analysis and Chill Casting Experiments

Supplementary to the above experimental designs, an extended set of three-minute holding trials was also conducted as a variance for the cooling curve analysis and chill casting trials but only for the LS-CI, given its development in the forthcoming research outcomes. Specifically, instead of being directly cast into the crucible or mold, samples were held for three minutes at similar superheating temperatures to enhance spheroidal graphite dissolution while minimizing the change in chemical composition. Moreover, adding 0.5 wt.% aluminum to the chill casting with superheating at 1500°C was explored to observe the dynamic effect on carbon solubility.

7.2. Experimental Results

7.2.1. Temperature Profile during Cooling Curve Analysis without Holding

Employing the correlation proposed by Humphreys [199] in **Equation (12)**, the calculated average carbon equivalent liquidus values (CELs) are expected to be approximately 3.90 and 4.08 for HS-CI and LS-CI, respectively. Considering those CELs to be approached further by the correlation developed by Sillén [200] and subsequently industrially proven by Van der Perre [201] as written in **Equation (13)**, the HS-CI and LS-CI are attributed to liquidus temperatures of approximately 1186°C and 1166°C, respectively. These calculated projections are also substantiated by the results of the cooling curve analysis, as indicated by the first thermal event in **Figure 7.2**.

$$\text{Carbon Eq. Liquidus (CEL)} = \%C + 0.25 \times \%Si + 0.5 \times \%P \quad \textbf{(12)}$$

$$\text{Carbon Eq. Liquidus (CEL)} = 14.45 - 0.0089 \times \text{Liquidus Temperature} \quad \textbf{(13)}$$

Furthermore, as indicated in the further thermal event in **Figure 7.2**, elevated superheating correlates with a longer cooling duration and increasing undercooling. Although there are fewer distinctions in undercooling, the recalescence, representing the distance between the lower and upper eutectic temperatures, decreases with increasing superheating for LS-CI (**Figure 7.2b**). These results are also substantiated in **Figure 7.3** as a metallography analysis result of solidified LS-CI removed from the double-chamber crucible.

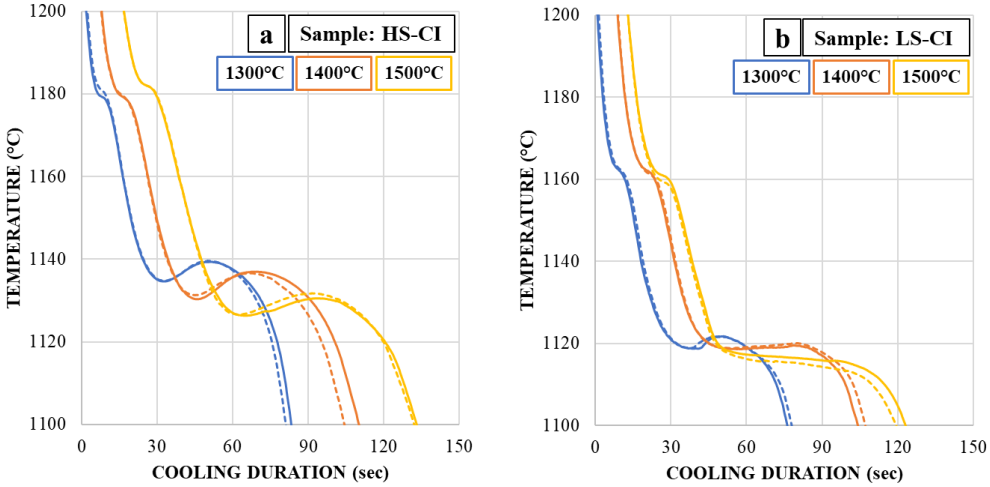

Figure 7.2. Cooling curves analysis results of (**a**) HS-CI and (**b**) LS-CI with different superheating temperatures.

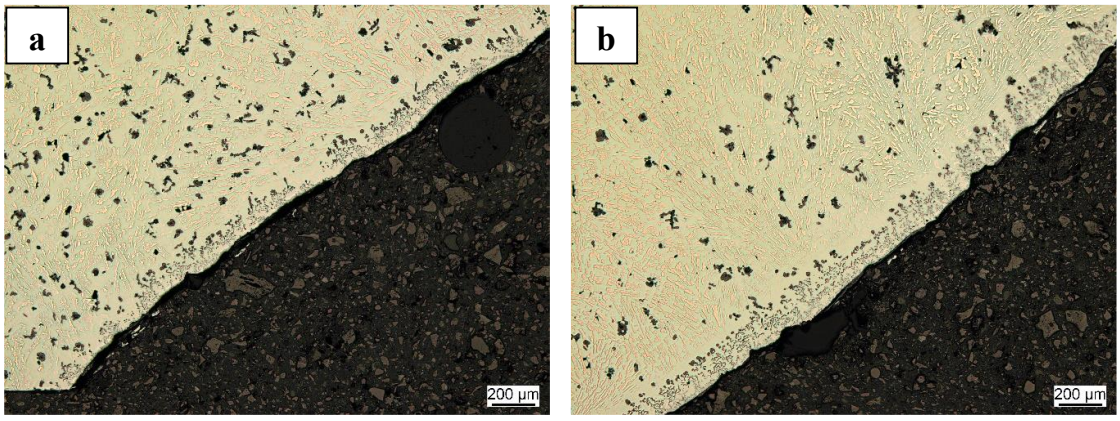

Figure 7.3. The microstructure of the solidified cast iron sample removed from the double-chamber crucible for the cooling curve analysis experiment for the LS-CI sample at (**a**) 1300°C and (**b**) 1400°C.

In this instance, the result in **Figure 7.3** indicates that the LS-CI removed from the crucible of the cooling curve analysis shows a decreasing count of the graphite structure as the superheating temperature increases from 1300°C (**Figure 7.3a**) to 1400°C (**Figure 7.3b**). As generally associated with a high chilling tendency, a predominant ledeburite structure is depicted in **Figure 7.4b**, followed by certain distinguishable graphite segregations. Specifically, the vermicular-like structure detailed in **Figure 7.4a**, which was the molten metal that solidified directly on the crucible wall, appeared on the edge of the metal sample.

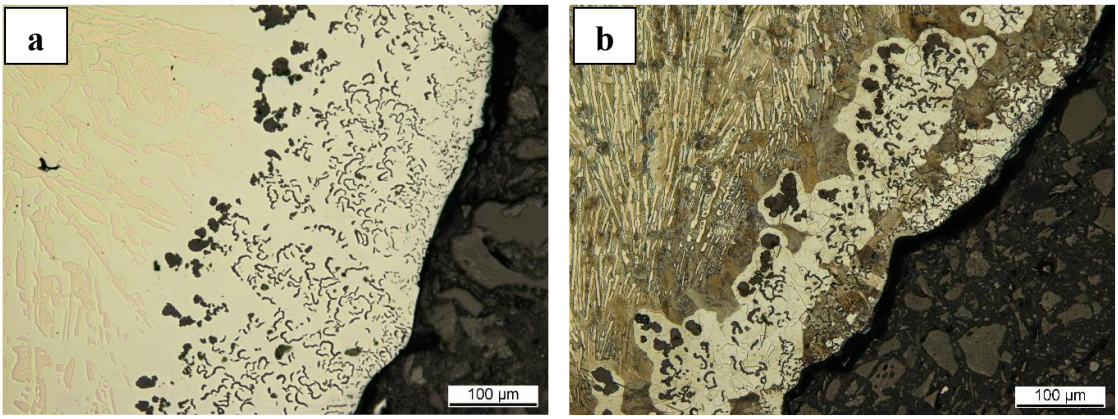

Figure 7.4. Detailed microstructure on the sample in **Figure 7.3b** (LS-CI at 1400°C without holding) at the interface to the crucible indicating (**a**) vermicular structure and (**b**) ledeburite matrix after Nital-etching

7.2.2. Microstructure Development due to Chill Casting without Holding

In addition to the cooling curve analysis, the characteristics of HS-CI and LS-CI as molten metals, including any possible justification of their homogeneity, were investigated using the chill casting approach.

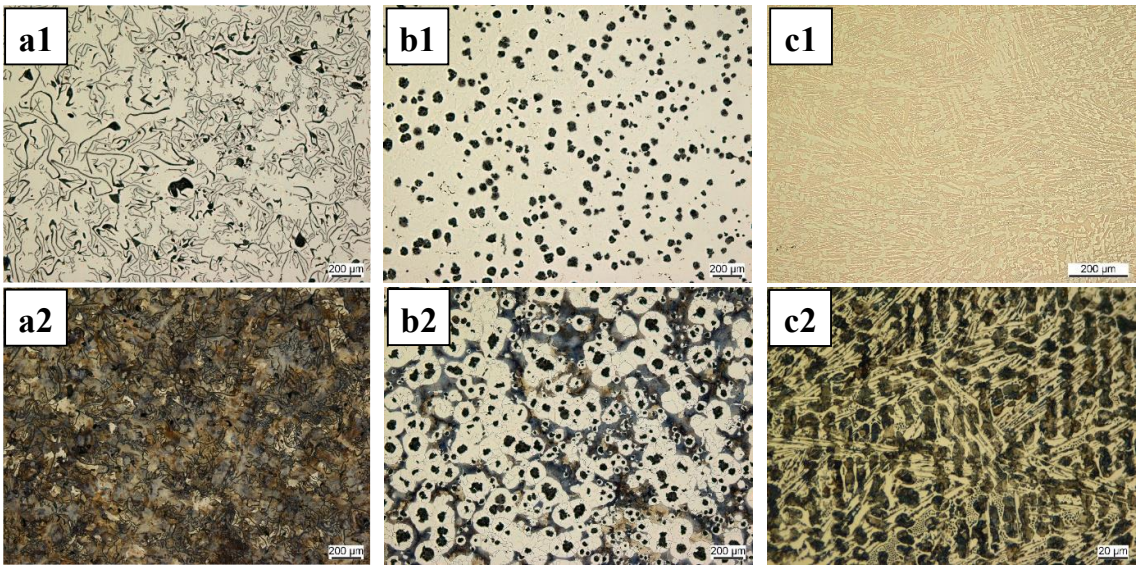

Figure 7.5. Microstructure of as-polished (**a1**, **b1**, and **c1**) and Nital-etched (**a2**, **b2**, and **c2**) of cast iron samples before chill casting for HS-CI (**a1** and **a2**) and LS-CI (**b1** and **b2**) compared with the typical microstructure after chill casting (**c1** and **c2**) – microstructure after the chill casting experiments is essentially similar for both HS-CI and LS-CI regardless of the superheating temperatures.

The as-received HS-CI and LS-CI were reviewed to determine the starting point. According to the result, the HS-CI exhibits a lamellar graphite structure in the pearlite matrix, as documented in **Figure 7.5a1** and **Figure 7.5a2**. On the other hand, the as-received LS-CI displays a spheroidal graphite structure in a pearlite-ferrite matrix, as shown in **Figure 7.5b1** and **Figure 7.5b2**. Following the as-received identification, a microstructure transformation

after chill casting was also observed. Both HS-CI and LS-CI exhibited a ledeburite configuration at all the studied superheating temperatures, as shown in **Figure 7.5c1** and **Figure 7.5c2**. This phase comprises former primary austenite dendrites, eutectic cementite, and former eutectic austenite. All the former austenite structures transformed into a pearlite configuration through a eutectoid reaction, as revealed after etching by Nital.

Despite the observation results showing a structure aligned with nearly 100% white iron formation after chill casting, a deeper search revealed some nonmetallic particles emerging within the matrix, as shown in **Figure 7.6**. Supported by the chemical analysis (EDX method) in **Table 7.2**, Mn-S-enriched inclusions were detected in **Figure 7.6a** for the HS-CI samples. In this instance, the possible formation of MnS particles can be anticipated and detected at all superheating temperatures after chill casting. In contrast, a possible trace of the remaining spheroidal graphite was discovered in the LS-CI sample after comparable trials instead of apparent nonmetallic inclusions, as shown in **Figure 7.6b**. Notably, this trace of preserved graphite was commonly found at low superheating temperatures, including 1300°C and 1400°C. In addition to the high carbon content representing a graphite structure, the chemical analysis in **Table 7.2** also suggested that the graphite nodule in **Figure 7.6b** (chill casting result at 1400°C) might contain Mg-S-enriched nuclei.

Table 7.2. Chemical composition (wt.%) of nonmetallic inclusions detected after chill casting as provided in **Figure 7.6**.

	C	Si	S	Mn	Mg	Fe
No.1: Mn-S Particle	12.94	1.01	6.31	11.73	-	68.01
No.2: Matrix of HS-CI	12.35	1.36	-	-	-	86.29
No.3: Rest Graphite	60.77	0.75	0.06	-	0.15	38.27
No.4: Matrix of LS-CI	12.66	1.82	-	-	-	85.24

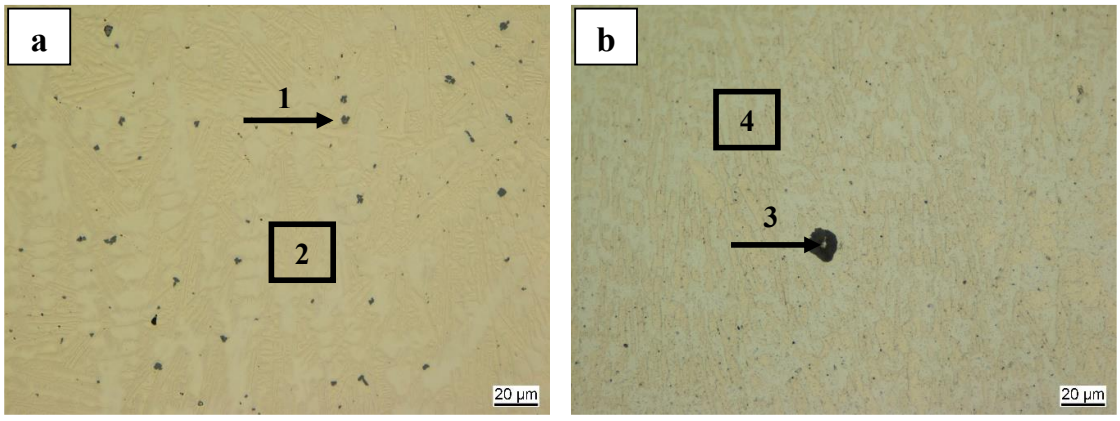

Figure 7.6. Sample of (**a**) Mn-S-enriched inclusions in chill-casted HS-CI (found at all studied temperatures) and (**b**) rest graphite in chill-casted LS-CI (detected at low superheating of 1300°C and 1400°C).

7.2.3. Formation of Graphite Cluster at the Thermal Center after Chill Casting

In addition to the nonmetallic inclusion found after chill casting, the metallography analysis revealed a distinct graphite cluster at the thermal center (**Figure 7.1**) at specific times and trial configurations. In the case of the reference sample of HS-CI in **Figure 7.7a**,

graphite clusters adopting a type-D (undercooled) graphite structure were detected. The cluster is mainly identified as a nearly round structure with a pearlite matrix yet is engulfed in a generally ledeburite configuration (**Figure 7.7b**).

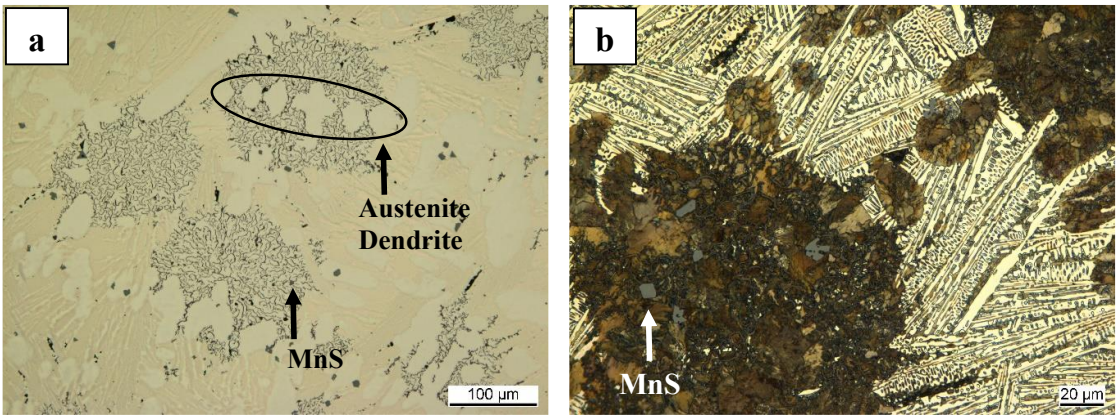

Figure 7.7. Typical representation of graphite cluster structure captured at the thermal center of chill-casted HS-CI in (**a**) as-polished and (b) Nital-etched conditions.

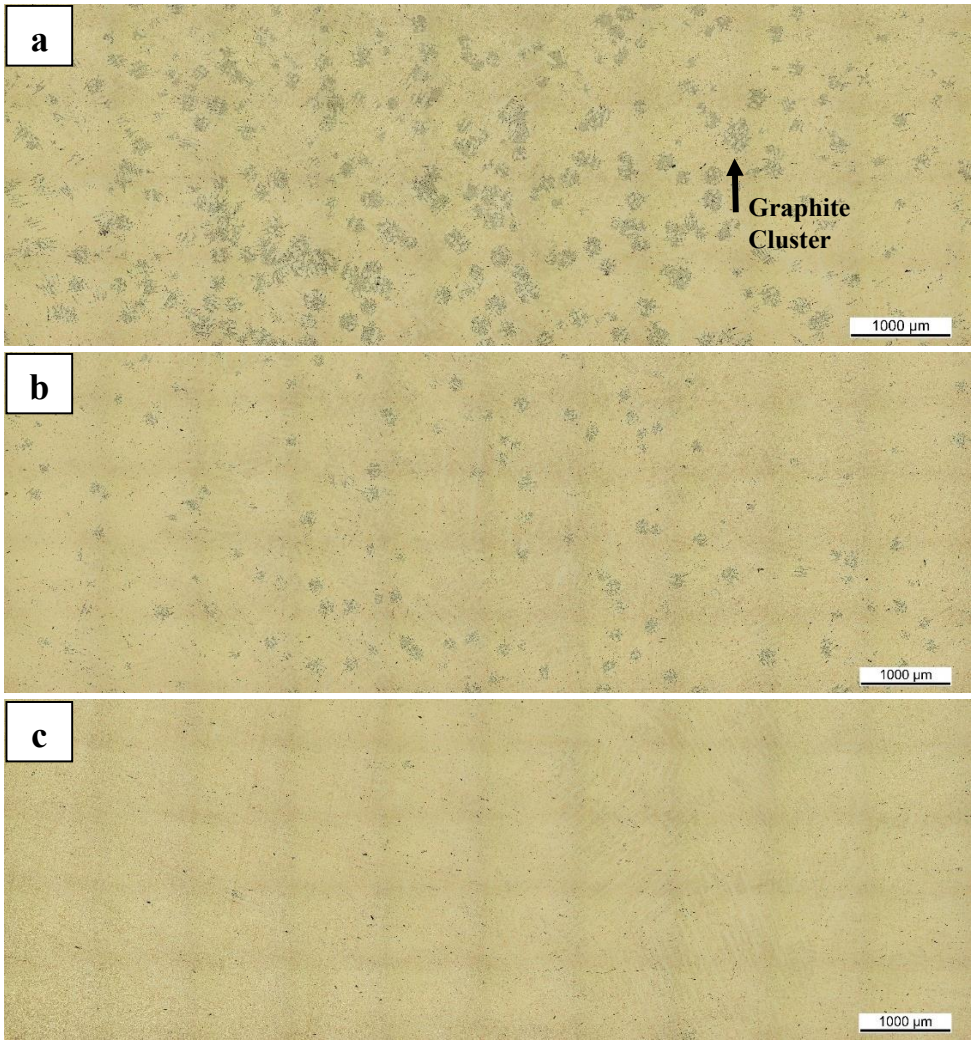

Figure 7.8. Graphite cluster in HS-CI sample after chill casting at (**a**) 1300°C, (**b**) 1400°C, and (**c**) 1500°C.

Furthermore, some MnS particles are detected inside the graphite cluster, whose nucleation occurs near or between the dendrite arms of the former primary austenite (**Figure 7.7a**). The number of graphite clusters in the HS-CI sample also correlates with the superheating temperature. As substantiated in **Figure 7.8** as a stitching image (a combined 50 images emerging as a pixelated figure) along the whole thermal center zone, it is suggested that the number of graphite clusters decreases if the superheating temperature increases.

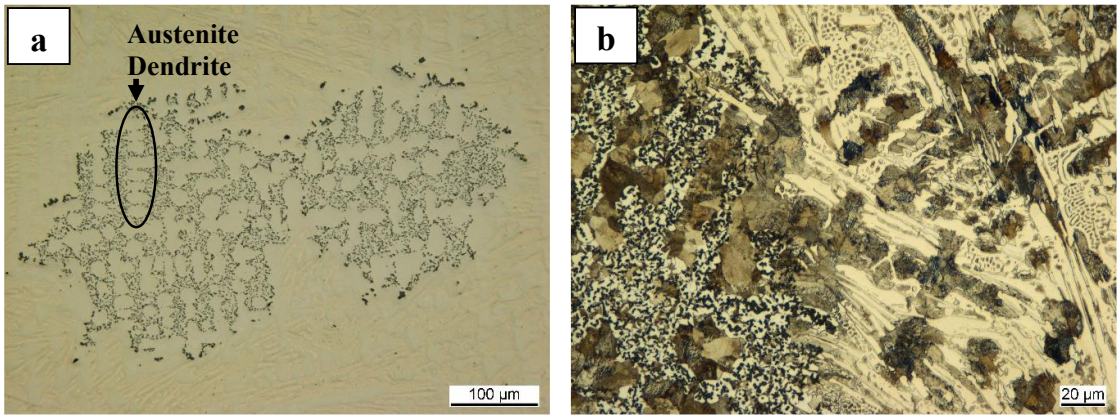

Figure 7.9. Typical representation of graphite cluster structure captured at the thermal center of chill-casted LS-CI in (**a**) as-polished and (**b**) Nital-etched conditions.

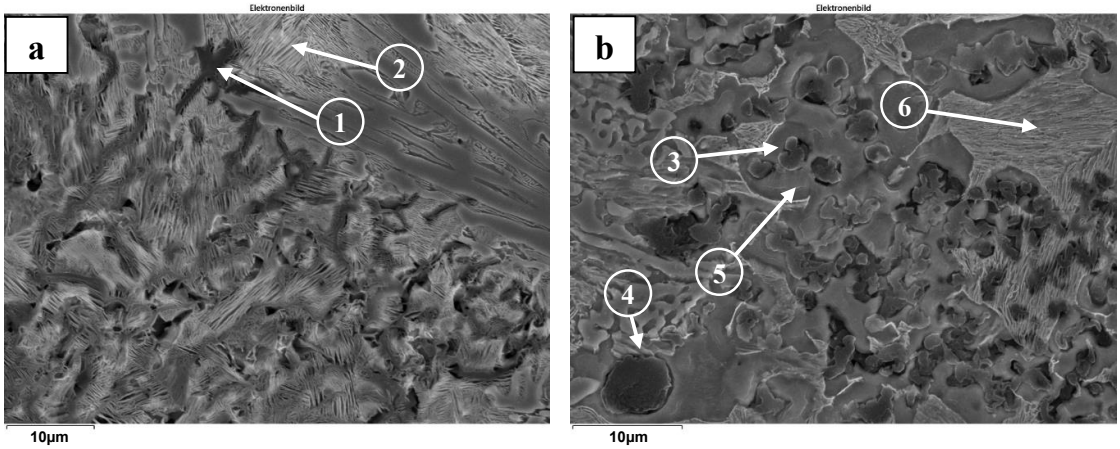

Figure 7.10. Graphite cluster morphology in chill-casted (**a**) HS-CI and (**b**) LS-CI observed under SEM after deep-etching process: (**1**) lamellar graphite, (**2**) pearlite matrix in HS-CI, (**3**) vermicular graphite, (**4**) spheroidal graphite, (**5**) ferrite matrix in LS-CI, and (**6**) pearlite matrix in LS-CI.

The LS-CI sample after chill casting also substantiates a comparable graphite cluster at the thermal center, as shown in **Figure 7.9**. This graphite cluster is also indicated to nucleate near or between the dendrite arms of the former primary austenite structure (**Figure 7.9b**). Nevertheless, in contrast to the cluster detected in the reference sample, the graphite clusters in the LS-CI are almost always round in morphology and constructed of fine graphite (vermicular-like graphite) structures near the center and several small spheroidal graphites on the edge of the cluster configuration (**Figure 7.9a**). Furthermore, unlike in HS-CI, the

cluster in LS-CI was found within a predominantly ferritic matrix engulfed by a typical ledeburite configuration.

Table 7.3. Chemical composition (wt.%) of LS-CI after chill casting without and with three-minute holding.

	C	Si	S	Mn	Mg
1300-0Min	3.51	2.28	0.002	0.14	0.017
1300-3Min	3.48	2.22	0.004	0.13	0.003
1400-0Min	3.53	2.27	0.003	0.15	0.010
1400-3Min	3.44	2.21	0.004	0.15	0.002
1500-0Min	3.56	2.24	0.004	0.14	0.003
1500-3Min	3.41	2.21	0.004	0.15	0.001

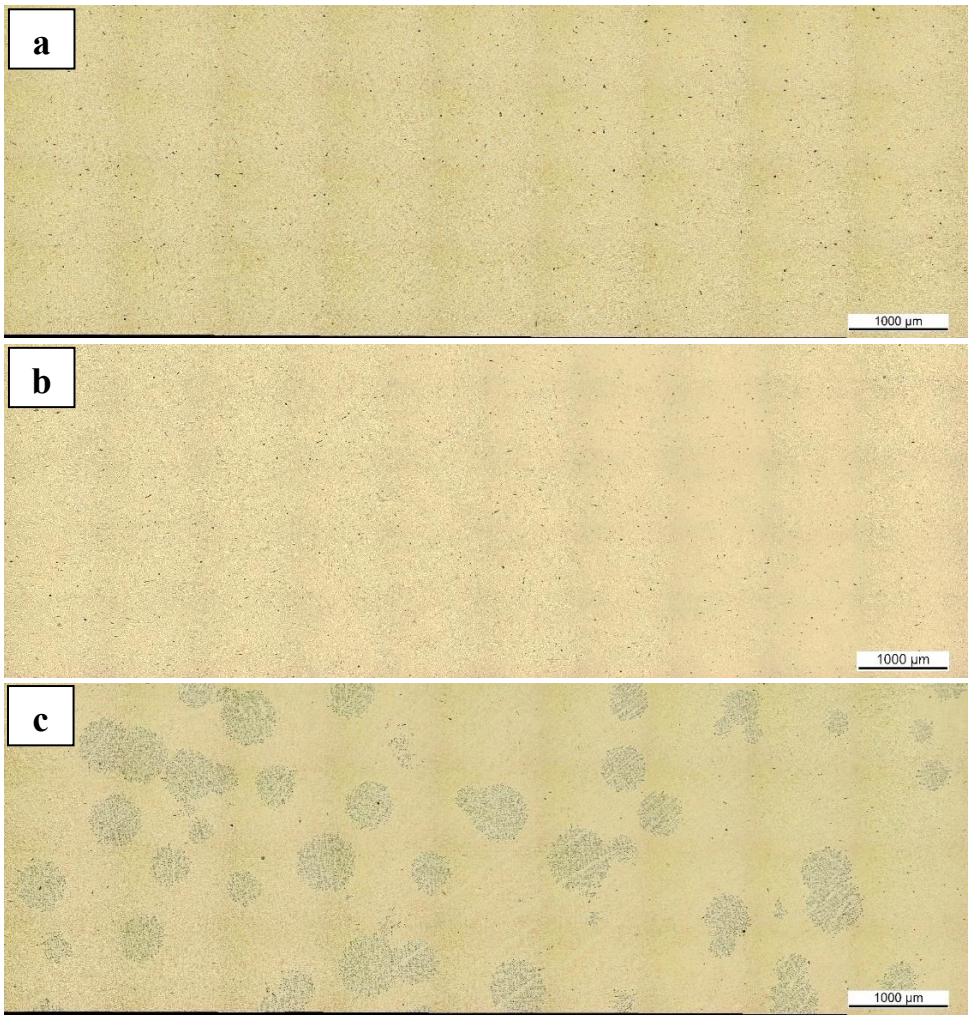

Figure 7.11. Graphite cluster in LS-CI sample after chill casting at (**a**) 1300°C, (**b**) 1400°C, and (**c**) 1500°C without a holding procedure.

The distinction between the graphite clusters in HS-CI and LS-CI is more evident after deep etching is conducted and subsequently observed under SEM, as shown in **Figure 7.10**. **Figure 7.10a** shows that the graphite clusters in HS-CI are composed of fine lamellar graphite structure (1) almost embedded in the lamellar configuration of the pearlite matrix

(2). On the other hand, **Figure 7.10b** proposed that the counterpart in LS-CI is composed of radially spreading vermicular-like graphite (3) and edged by spheroidal graphite structure (4) immersed in a ferritic matrix (5) with some pearlite system (6).

However, in contrast to the observed tendency in the HS-CI sample, the formation of graphite clusters in the LS-CI sample might not be due only to the superheating temperature, as highlighted in **Figure 7.11**. In this case, residual magnesium is another identified parameter that changes and might correlate with superheating. According to the chemical analysis in **Table 7.3**, the remainder of the magnesium can still be expected during chill casting if the cast iron is immediately poured (without holding). Accordingly, this magnesium content is anticipated to decrease significantly without any notable change in other major alloying elements if the molten iron has been held at the superheating temperature for 3 minutes.

The correlations among the graphite clusters in LS-CI, the superheating temperature, and the holding procedure are represented in **Figure 7.11**. Based on this metallography analysis, if no three-minute holding was considered, it is suggested that the graphite cluster was formed only at the highest superheating temperature of 1500°C. On the other hand, at a lower temperature of 1400°C, a comparable graphite cluster can only be observed once the molten iron was held for three minutes before being cast, as shown in **Figure 7.12b**. However, this three-minute holding effect was not necessarily manifested at the lowest considered superheating of 1300°C since no graphite cluster can be detected, as highlighted in **Figure 7.12a**.

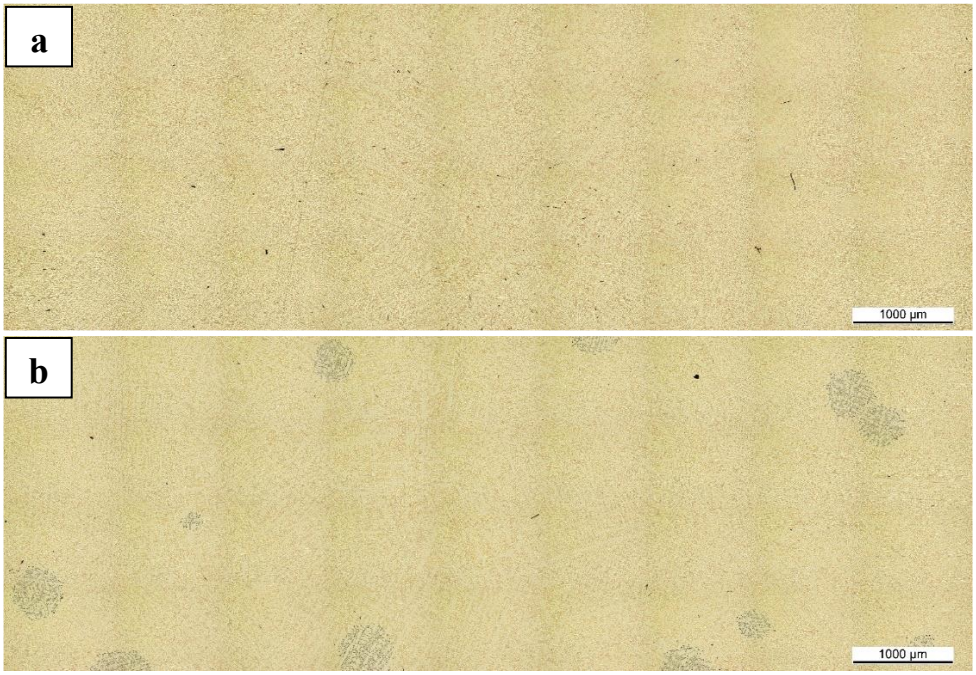

Figure 7.12. Graphite cluster in LS-CI after chill casting at (**a**) 1300°C and (**b**) 1400°C with a three-minute holding procedure.

Given the different behaviors at the temperature of 1400°C, the effect of three-minute holding at this respective superheating was explored using the crucible associated with the

cooling curve analysis. Specifically, metallography analysis was conducted on solidified LS-CI removed from the double-chamber crucible. As substantiated in **Figure 7.13a**, a distinct graphite structure was suggested to have nucleated, comprising a mixture of different classes of lamellar graphite. In addition, **Figure 7.13b** reveals that the matrix is composed predominantly of a ferrite phase with minor indications of the pearlite configuration.

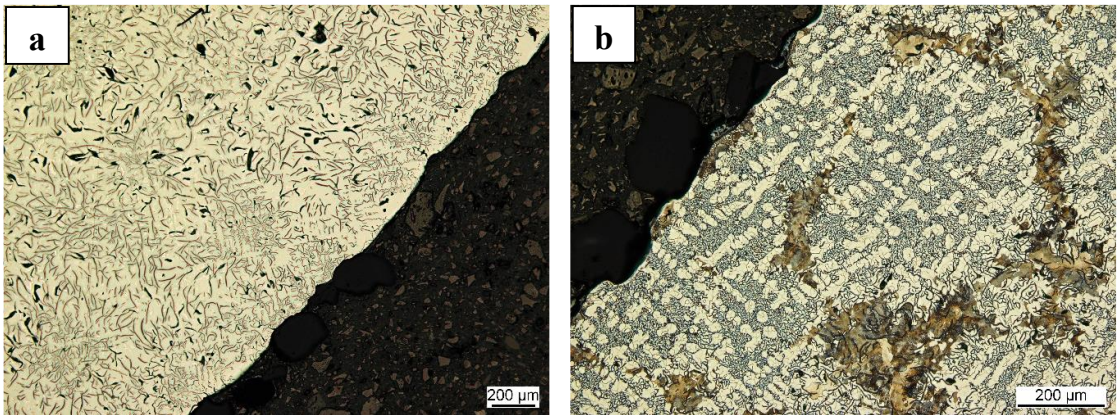

Figure 7.13. The microstructure of the solidified LS-CI removed from the double-chamber crucible for cooling curve analysis involving the three-minute holding procedure at 1400°C in (**a**) as-polished and (**b**) Nital-etched conditions.

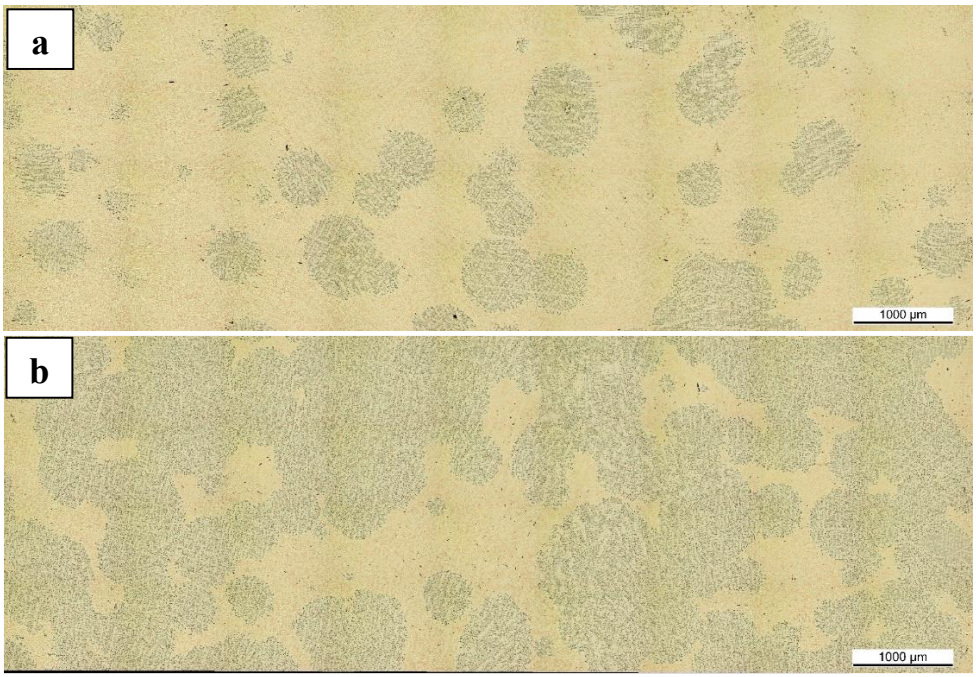

Figure 7.14. Graphite cluster in LS-CI after chill casting involving the three-minute holding procedure at 1500°C (**a**) without and (**b**) with the addition of aluminum metal.

An additional intriguing observation was also revealed when the incorporation of aluminum metal in the system was considered. Specifically, aluminum was introduced through a surface addition method shortly before casting. As shown in **Figure 7.14a**, if a three-minute holding procedure was used, the morphology of the graphite cluster detected at the thermal center in LS-CI increased in size. This effect was enhanced, as represented by an increasing tendency

in size and the number of graphite clusters following the addition of aluminum metal, as elucidated in **Figure 7.14b**.

7.3. Analysis and Discussion

7.3.1. Effect of Superheating on the Solidification of Cast Iron upon Remelting

In the case of HS-CI, the chill casting results in **Figure 7.8** suggest that increasing the superheating temperature reduces the number of graphite clusters detected at the thermal center (**Figure 7.1**). Considering the nearly spherical shape (**Figure 7.7a**) of fine type-D (undercooled) lamellar graphite and their nucleation sites being located in the vicinity of the austenite dendrite structures (**Figure 7.7b**), it is convincingly rational to associate those graphite clusters with the representation of eutectic cell solidification, as also described previously [202, 203]. In this instance, the indication of type-D graphite constructing the graphite cluster in the HS-CI sample can also be related to the rapid cooling approach as an implication of casting in the copper mold, which is unfavorable for type-A graphite due to significant undercooling [204, 205].

Since the nucleation of primary austenite thermodynamically correlates with rejecting a certain amount of carbon into the molten cast iron due to decreasing carbon solubility, a locally high concentration (segregation) of carbon surrounding the austenite dendrite is consequently anticipated. This carbon segregation reduces the local melting temperature, which explains the spherical structure of the graphite cluster. On the other hand, as documented in **Figure 7.2a**, the cooling curve analysis results indicate that an increase in the superheating temperature correlates with the degree of undercooling, which aligns well with the findings in [206, 207, 208]. To this extent, compounding with the results of chill casting experiments, the increasing undercooling driven by elevated superheating correlates with the decreasing tendency of the number of eutectic cells, representing a lower nucleation potential despite the presence of MnS particles in the cast iron matrix, as captured in **Figure 7.6a**. Notably, as the graphite clusters are hardly identifiable at the highest studied superheating of 1500°C, as indicated in **Figure 7.8c**, all the graphite structures were anticipated to be entirely dissolved. As a result, the potential nucleation effect driven by residual effective nuclei is wiped out, which is not the case for lower superheating temperatures.

In contrast to the HS-CI results, despite a similar correlation between the superheating temperature and degree of undercooling, the temperature profile during the cooling curve analysis of the LS-CI suggested a different solidification pattern, as shown in **Figure 7.2b**. By adopting the correlation from Kanno et al. [209, 210] in terms of graphite (TEG) and carbide (TEC) eutectic temperature estimation, it can be projected that the HS-CI will exhibit a TEG of 1152°C and a TEC of 1122°C. On the other hand, the LS-CI records TEG and TEC values at approximately 1158°C and 1116°C, respectively. Accordingly, based on the cooling curve analysis in **Figure 7.2**, a greater chill tendency can be concluded for LS-CI, where its eutectic solidification occurred at notably lower temperatures and even near its TEC.

The potential reasons correlated with the greater chill tendency in the LS-CI could be the disparity in chemical composition, inadequate inoculation, and superheating practices. As

provided in a substantial review by Fras et al. [211], those three basic parameters are valued as pivotal factors in governing the chill tendency. Bringing the approach into context, based on the perspective of chemical composition, the remelted LS-CI could also be considered a low-sulfur HS-CI. This argument can be circumstantially substantiated, given that lamellar structure formation is based upon the remelting process of LS-CI, as shown in **Figure 7.13**. Consequently, despite the counterbalancing availability of higher carbon and silicon concentrations in LS-CI, prior investigations [212, 213, 214] reported that lower manganese and sulfur contents correlate with a greater chill tendency and undercooling degree.

Furthermore, from the viewpoint of the inoculation practice, the approaching tendency toward the TEC recorded in **Figure 7.2b** represents a possible increasing proportion of carbide formation. As contrasted by the highest examined temperature of 1500°C, the cooling curve analysis result indicates a collinear line following the TEC, corresponding to the uninoculated ductile cast iron melt behavior suggested in [215, 216]. Based on those results, the elevated superheating temperature reduces the graphite nucleation potential, as previously reported for the decreasing number of graphite clusters in the HS-CI sample. Moreover, since increasing superheating promotes the establishment of uninoculated ductile cast iron, the decreasing graphite nucleation capability is potentially related to the fading of the formerly available inoculant due to the remelting process.

The notable chill tendency observed in **Figure 7.2b** for the LS-CI sample is further supported by the ledeburite matrix in the solidified cast iron removed from the double-chamber crucible of cooling curve analysis, as indicated in **Figure 7.3** and **Figure 7.4**. Nonetheless, it is also worth mentioning that despite the white iron matrix structure, some graphite solidification can still be observed in an inverse chill configuration. In this context, in addition to being associated with an increasing cooling rate, such an inverse chill structure can also indicate a reduction in the nucleation and growth rate of the graphite eutectic [217]. Hence, as provided in **Figure 7.3**, it is once again suggested that increasing superheating for the LS-CI lessens the nucleation potential represented by a reduction in the number of renucleated graphites.

Conclusively, as briefly indicated previously, a correlation between superheating and the reduction of graphite nucleation in LS-CI has been practically known in the foundry practice of SGI production as the fading effect. However, previously published investigations describing this effect [88, 218, 219] focused solely on post-magnesium treatment and melt inoculation instead of the remelting process of recycled SGI. Therefore, based on the findings generated from this chapter, the transformation in the physicochemical state of LS-CI due to the remelting process can be described by considering the interplay of the following phenomena:

(1) Diminishing formerly available inoculants and the nodulizer
The identification in **Figure 7.4b** revealed that an inverse chill structure was established. Consistent with the observations of Abdolhossein and Ahmadabadi [218], such an inverse structure in SGI is related to a lowering nucleation potential due to the fading effect of the inoculant. Furthermore, Michels et al. [88] also revealed a

comparable configuration in magnesium-treated but uninoculated ductile iron. Since no inoculation process was introduced during the remelting process in this chapter, the establishment of the inverse chill structure, the reduction in graphite count in **Figure 7.3**, and the cooling behavior indicated in **Figure 7.2b** should be related to the decrease in formerly available inoculants in LS-CI induced by superheating during the remelting process.

Nonetheless, a different mechanism should be considered to address the nucleation of vermicular graphite on the edge of the LS-CI sample in **Figure 7.4a**. In this case, nucleation is expected to be enhanced by a heterogeneous mechanism, considering a chilled zone adjacent to the crucible wall. In addition, the post-remelting chemical analysis in **Table 7.3** measured an average residual magnesium of 0.01 wt.%, which is within the typical magnesium concentration required for CGI production [219, 220]. This residual magnesium explains the establishment of a vermicular structure, which is anticipated in LS-CI remelting, as reported in [219, 221] for the high-temperature holding of SGI. Based on this change in nodularity, a certain degree of nodulizer fading has subsequently occurred.

(2) Dissolution degree of formerly available spheroidal graphite
The results of the metallography analysis in **Figure 7.3** indicate that increasing the superheating temperature reduces the number of graphite structures. On the other hand, based on the results from chill casting in **Figure 7.6b**, incomplete dissolution of spheroidal graphite is detectable at lower superheating. To this extent, however, a discrepancy in the density of the graphite structure between the chill casting and cooling curve analyses implies that the graphites in **Figure 7.3** are not residual graphite but renucleated or regrown graphite structures. Since remelting is the only operation considered, the graphite nucleation in **Figure 7.3** (except adjacent to the crucible wall) is predominantly induced by the incomplete or partial dissolution of the inoculant, nodulizer, and former graphite structures, as also seen as a possibility by previous investigations [202, 222].

7.3.2. Solidification of Deteriorated Graphite upon Remelting of LS-CI

In the specific case of magnesium fading as a nodulizer, the reduction in its concentration in **Table 7.3** substantiates that the fading process during the remelting operation is also associated with prolonged holding at high temperatures. As briefly mentioned in the previous section, the effect of magnesium fading was also captured by metallography analysis of the solidified metal from the cooling curve analysis sample. Instead of the inverse chill structure documented in **Figure 7.4** (1400°C without holding), a mixture of lamellar graphite structures coupled with a predominant ferritic matrix can be observed in **Figure 7.13** (1400°C with three-minute holding). This comparison circumstantially represents a complete fading effect of dissolved magnesium, as listed in **Table 7.3**, which aligns well with the investigation results provided in [88, 222]. Particularly in these trials, the residual concentrations are 100 ppm for trials without holding and 20 ppm for trials with a three-minute holding at 1400°C. In this context, it is also important to mention that at high

temperatures and slower solidification, a continuous decrease in the magnesium content reduces the surface tension and promotes the growth of lamellar graphite.

Furthermore, this residual magnesium could be an additional factor influencing the establishment of graphite clusters at the thermal center of LS-CI. This finding is supported by the evidence that an apparent tendency in the number of graphite clusters cannot be observed in **Figure 7.11** compared with the HS-CI in **Figure 7.8**. In this case, despite constructing a similar nearly round morphology, suggesting a relatively equivalent formation mechanism involving carbon segregation surrounding austenite dendrites (**Figure 7.9**), the graphite cluster formation in LS-CI might not be affected only by the superheating temperature. Specifically, as shown in **Figure 7.11**, no graphite clusters can be identified in the LS-CI samples after remelting at 1300°C and 1400°C. Once superheating at 1500°C (without holding) was applied, clusters were observed, followed by a significantly lower residual magnesium concentration of 30 ppm (**Table 7.3**) compared to 170 and 100 ppm at 1300°C and 1400°C, respectively.

Fascinating insight was revealed as the three-minute holding samples were cast into a copper mold, where it was assumed that low residual magnesium guaranteed the formation of graphite clusters. However, as shown in **Figure 7.12**, despite possessing low magnesium contents of 30 ppm and 20 ppm for superheating temperatures of 1300°C and 1400°C, respectively, the graphite clusters were only formed at 1400°C (**Figure 7.12b**). Based on these results, a particular degree of combination between the superheating temperature and residual magnesium concentration is necessary to establish the graphite cluster in the LS-CI sample. In this context, a specific prolonged cooling duration is needed. Since a similar copper mold was employed, the lower pouring temperature should be associated with a shorter cooling duration since less heat should be released [223], as also substantiated in **Figure 7.2b**.

As mentioned, the graphite clusters are induced by late and slow solidification related to carbon segregation, thus creating a local high carbon equivalent and suggesting eutectic cell formation. Considering this perspective, aluminum was introduced into dedicated samples in chill casting at 1500°C with three minutes of holding exactly before casting. Compared with silicon, aluminum is recognized to have a similar effect on increasing the eutectic cell count by reducing carbon solubility [224, 225]. As compared in **Figure 7.14**, it is evident that an increase in the number of graphite clusters was noticeable. This increase indicates enhanced supersaturation and a greater driving force, thus allowing a smaller critical radius of nuclei to grow instead of being redissolved, as postulated in the classical nucleation theory (CNT) reviewed in [226, 227]. In this instance, introducing aluminum can extend the reduction in the dissolved oxygen content [135] and potentially provide some micro inclusions that sustain graphite nucleation [228]. Moreover, given another effect of aluminum in increasing stable and metastable eutectic temperatures, its addition essentially correlates with a decreasing chill tendency and the undercooling degree [229] of the cast iron.

Finally, compounding all the above findings, at least three identified factors might explain the morphological disparity between the graphite clusters at the thermal center of both

studied samples, as shown in **Figure 7.10**. These factors include prolonged cooling duration, low residual magnesium concentration, and reduced carbon solubility. Furthermore, as explicitly highlighted in **Figure 7.10b**, the identified graphite cluster in LS-CI potentially indicates chunky graphite formation, as it is typically marked by a spherical region where small nodules can be observed at the edge of the structure [230]. This morphology plausibly strengthens the insights provided in [231, 232] concerning chunky graphite formation involving the establishment of eutectic cells. In this instance, the matrix of each graphite cluster matches the matrix of the as-received configuration provided in **Figure 7.5**, suggesting that the clusters circumstantially represent the building blocks of the entire structure.

Accordingly, at the boundary of this chapter, it is suggested that the chill casting results could offer several enhanced supplementary perspectives to the previously published findings related to the formation of chunky graphite structures in ductile cast iron. As mentioned earlier regarding the correlation between chunky graphite structure and eutectic cells, the establishment of chunky graphite is relatively early during the solidification process, as indicated in [230, 232]. This early solidification perspective is supported in **Figure 7.9**, where chunky graphite formation was related to the nucleation sequence surrounding the primary austenite dendrites, which was also reported in [231, 233].

Furthermore, comparing the chill casting results between both studied samples, although possibly induced by distinct circumstances, it is convincing to propose that chunky graphite might conditionally be comparable to the formation of undercooled graphite. The formation of chunky graphite in this chapter can only be detected in chill casting trials, which represent a high cooling rate, and not in the thermal analysis, which uses a double-chamber AccuVo-Cup crucible (**Figure 7.13**) with a slower cooling rate and different nucleation conditions, where distinct lamellar graphite structures crystallize instead. These findings suggest that the rate of chunky graphite nucleation should be faster than that of lamellar graphite, as once contextually reported by Källbom et al. [230].

It is also evident that the formation of chunky graphite in the LS-CI correlates with the complete fading of magnesium and residual inoculant, as substantiated in **Figure 7.11** and **Figure 7.12**, aligning well with the results proposed in [230, 234]. Similarly, it should be noted that the reduced surface tension of residual molten iron with decreasing magnesium concentration promoted graphite growth toward a lamellar structure. Hence, it is suggested that the fading of magnesium and the inoculant alone cannot ultimately ensure the formation of chunky graphite, as also contrasted in **Figure 7.12**. In this context, it is proposed that a prolonged cooling duration is necessary, amplifying the investigation results provided by Prinz et al. [235]. As a consequence, as indicated in **Figure 7.9** and **Figure 7.14**, the establishment of chunky graphite should involve the promoted carbon saturation level driven by decreasing carbon solubility, enhancing the results provided by Gagne and Argo [236].

7.4. Summary of Graphite Structure upon Ductile Iron Recycling

This chapter demonstrated the dissolution of the graphite structure during the remelting process of lamellar graphite (HS-CI) and spheroidal graphite (LS-CI) cast iron, as

well as the subsequent renucleation of the graphite structure due to the slow and rapid solidification rate without any additional melt treatments or inoculation. Based on the investigation outcomes, the following findings can be drawn:

(1) The thermal analysis revealed that increasing the degree of superheating from 1300°C to 1500°C in HS-CI correlates with an increasing degree of undercooling during eutectic solidification. However, regardless of the superheating temperature, MnS particles are still observable after the chill casting in a copper mold.
(2) Graphite clusters were formed during the chill casting trials of HS-CI at a temperature of 1300°C. These clusters are lamellar undercooled graphite structures that tend toward eutectic cell formation. Fewer graphite clusters can be observed at higher superheating temperatures until they are difficult to identify at 1500°C. Based on this fact, residual nuclei (e.g., small undissolved graphite particles) that still have nucleating effects at lower temperatures but no longer exist at 1500°C can be anticipated.
(3) In the case of the remelting process of LS-CI without any additional melt treatment or inoculation, graphite clusters are also observable upon chill casting trials. Interestingly, these clusters manifest the typical morphology and arrangement of chunky graphite. However, in contrast to HS-CI, the graphite cluster in LS-CI is detected only at 1500°C and not at 1300°C or 1400°C without a three-minute hold.
(4) In addition to the chill casting trials, the thermal analysis of the LS-CI data indicated that no recalescence was recorded during eutectic solidification at 1500°C and that eutectic solidification was significantly prolonged.
(5) Based on the disparity in the formation of graphite clusters in HS-CI and LS-CI, an interplay of other factors should be taken into account during the potential formation of chunky graphite, which includes the following:
    a. A high superheating temperature is needed to completely dissolve the former spheroidal graphite structure, residual magnesium, and preexisting inoculant.
    b. Higher superheating also leads to a slower (prolonged) cooling and solidification rate, yet it should be faster than the crystallization rate of lamellar graphite.
    c. Carbon supersaturation is established by decreasing carbon solubility related to the nucleation of primary austenite dendrites.

Since the molten iron was not treated and inoculated before chill casting in a copper mold, the possible nucleating effect from the mold could be neglected. Therefore, the interplay between magnesium and the inoculant fading process, the distinct cooling rate, and carbon solubility drive the formation of chunky graphite.

Chapter 8

Dissolution Behavior of Spheroidal Graphite

Following the examination results on the nucleation of various graphite structures during a recycling approach of ductile iron, this chapter comprehensively examines the dissolution mechanism of nodular graphite structure at the early phase of the remelting process. It is substantiated that the dissolution of nodular graphite does not occur primarily in the liquid state but has already started during the austenitization. Based on this dissolution behavior, this chapter also represents an alternative method for observing the core of nodular graphite by intentionally partially dissolving the graphite structure.

Publication Note:
During the manuscript preparation until the final submission of this dissertation, this chapter is part of a published research article in Metals [237].

8.1. Materials and Methods

8.1.1. MH-Exp: High-Temperature Molten Metal Holding Trials

The cast iron specimens considered in this chapter are recycled ductile iron (coded as LS-CI), with the chemical composition delineated in **Table 8.1**. Furthermore, an additional specimen (designated HS-CI) comprising the cast iron produced by the cupola furnace (traditional input for ductile cast iron production) is also included as a comparative reference, and its chemical composition is also listed in **Table 8.1**.

Table 8.1. Initial chemical composition (wt.%) of cast iron samples.

	C	Si	S	P	Mn	Fe
LS-CI	3.4–3.6	2.2–2.3	< 0.005	0.02–0.03	0.10–0.15	93–94
HS-CI	3.4–3.5	1.6–1.7	0.10–0.12	0.06–0.07	0.5–0.6	93–94

The experimental procedure (coded as MH-Exp) involves subjecting the respective cast iron sample to elevated temperatures within a 30-minute holding duration to discern potential changes in its chemical composition. Approximately 1 kg of cast iron was melted using an induction furnace in a clay-graphite crucible under an atmospheric condition until the prescribed holding temperature was reached. Three different holding temperatures were investigated: 1300°C, 1400°C, and 1500°C. Following the melting process, molten metal was periodically extracted using a metal cap sampler at 5-minute intervals throughout a cumulative experimental duration of 30 min. The collected samples subsequently underwent chemical analysis comprising optical emission spectroscopy (OES) and combustion carbon-sulfur (CS) analysis to determine the precise carbon content.

8.1.2. ET-Exp: Dissolution Behavior of Nodular Graphite Experiments

The dissolution behavior of nodular graphite (coded as ET-Exp) was investigated by subjecting a cubic sample of LS-CI with dimensions of 20 × 20 × 20 mm^3 to elevated temperatures approximating the eutectic temperature: 1100°C, 1200°C, and 1300°C. The

heating process was conducted in a muffled furnace for different holding durations: 5, 10, and 15 min. The procedure started by heating the furnace until the designated temperatures were reached before the samples (contained in an alumina-based boat crucible) were inserted. In this instance, the holding duration is the total range since the samples enter the muffle furnace until they are removed and immediately cooled using a water-quenching technique. After cooling, all the samples were halved and metallographically prepared for further analysis using a light microscope. In addition to metallography, scanning electron microscopy with energy-dispersive X-ray spectroscopy (SEM/EDS) was also used to observe the residual graphite structures, particularly their nonmetallic core.

8.2. Experimental Results

8.2.1. Changes in Concentration of Carbon and Silicon during MH-Exp

An interchange in the chemical composition development of carbon and silicon is observed during MH-Exp, where their behavior correlates with the melting temperature profile and the holding duration. Specifically, as shown in **Figure 8.1**, changes in the carbon concentration in both the HS-CI and LS-CI samples positively correlate with increasing melting temperatures during the 30-minute high-temperature holding process.

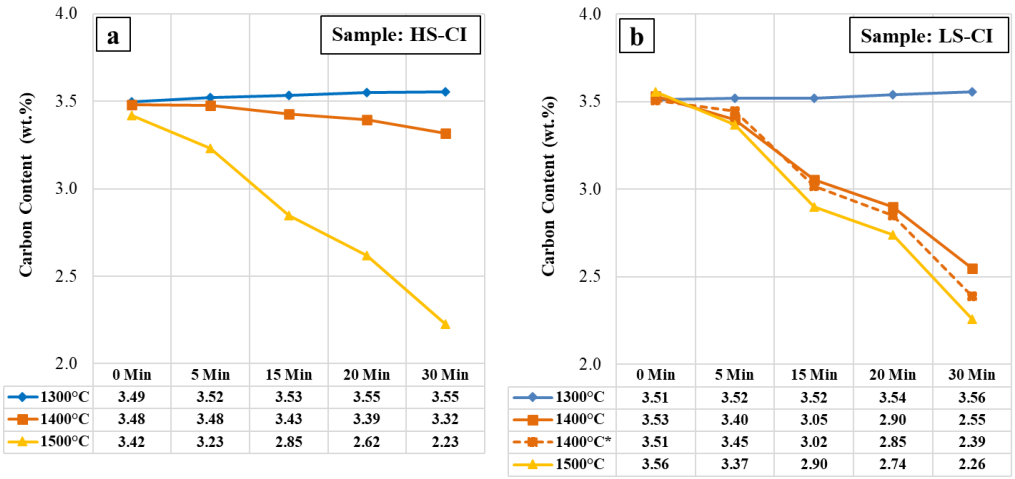

	0 Min	5 Min	15 Min	20 Min	30 Min
1300°C	3.49	3.52	3.53	3.55	3.55
1400°C	3.48	3.48	3.43	3.39	3.32
1500°C	3.42	3.23	2.85	2.62	2.23

	0 Min	5 Min	15 Min	20 Min	30 Min
1300°C	3.51	3.52	3.52	3.54	3.56
1400°C	3.53	3.40	3.05	2.90	2.55
1400°C*	3.51	3.45	3.02	2.85	2.39
1500°C	3.56	3.37	2.90	2.74	2.26

Figure 8.1. The average change in the carbon content during the high-temperature holding of (**a**) HS-CI and (**b**) LS-CI – additional sample LS-CI 1400°C* was melted in an alumina-based crucible.

The results in **Figure 8.1** also indicate that both studied samples manifested a reduction in carbon content from approximately 3.5 wt.% to as low as 2.2 wt.% at a temperature of 1500°C within 30 min. A comparable decreasing tendency was also detected at 1400°C, despite the LS-CI indicating a higher degree of carbon reduction than the HS-CI, measured at approximately 2.5 wt.% and 3.3 wt.%, respectively. An additional LS-CI sample melted in an alumina-based crucible at 1400°C indicated a similar tendency of carbon reduction, as shown in **Figure 8.1b**. In contrast to those decreasing trends, a constant concentration of carbon was observed at 1300°C for both samples during the 30-minute holding process.

Nonetheless, although a constant carbon content was recorded during high-temperature holding at 1300°C for both LS-CI and HS-CI samples, a disparity in silicon concentration

was detected instead. The interplay is related to the temperature, yet in a counter way compared with the carbon content, as provided in **Figure 8.2**. These results indicate that the silicon content decreases with increasing holding time at 1300°C. Comparatively, this decreasing tendency of silicon was not observed at 1500°C, where the highest degree of carbon reduction was recorded instead, as substantiated in **Figure 8.3**.

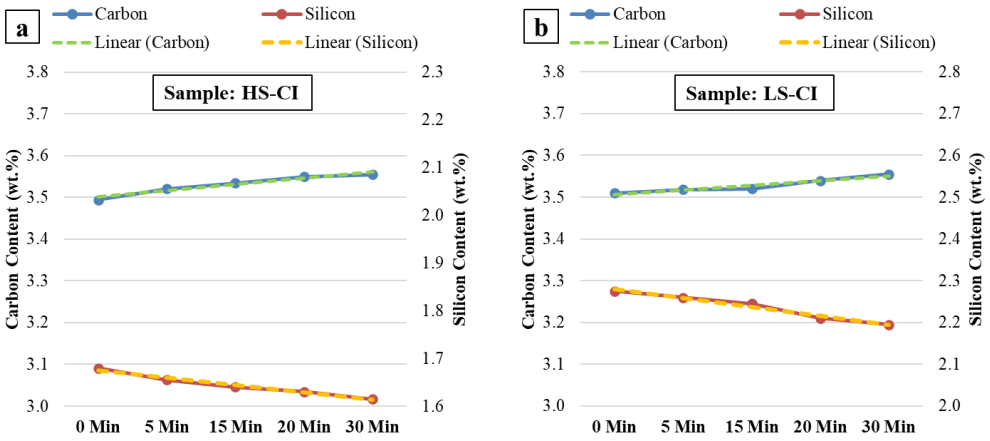

Figure 8.2. The average development in the carbon and silicon contents in (**a**) HS-CI and (**b**) LS-CI during holding at a temperature of 1300°C.

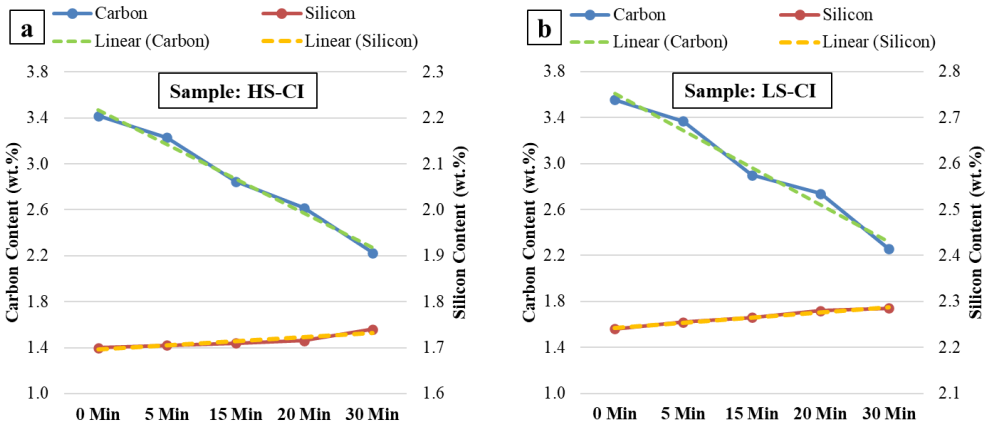

Figure 8.3. The average development in the carbon and silicon contents in (**a**) HS-CI and (**b**) LS-CI during holding at a temperature of 1500°C.

8.2.2. Matrix Development and Graphite Structure after ET-Exp

In contrast to the previous section, the following two sections consider only nodular graphite from LS-CI as the subject of study. The focus of this section is based on the last chapter indicating that the dissolution rate of nodular graphite in SGI is slower than that of lamellar graphite in gray cast iron (LGI); however, understanding the mechanism could be contextually adopted to explain the similar dissolution process in HS-CI. Moreover, given the forthcoming results, the dissolution of nodular graphite provides additional insight into its heterogeneous nucleation sequence, which is more unsettled than its counterpart.

Figure 8.4 shows the microstructure of the LS-CI sample before and after the heating trials ET-Exp. As indicated in **Figure 8.4a**, the as-received LS-CI with a pearlite-ferrite matrix

was transformed after 10 min of holding at 1200°C into a ledeburite-martensite system coupled with residual graphite structures, as represented in **Figure 8.4b**. Furthermore, the density of martensite surrounding the residual graphite is greater than that of the former austenite matrix system, which was also transformed into martensite eventually upon water quenching. Considering this former austenite, a denser martensite structure is also observed on the edge of its grains, where the ledeburite structure is anticipated to develop.

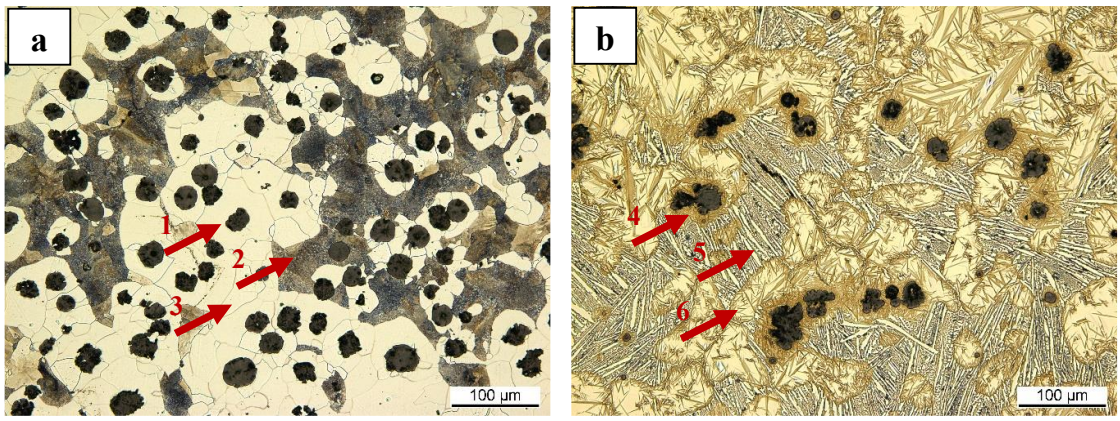

Figure 8.4. Microstructure of Nital-etched LS-CI (**a**) before and (**b**) after ET-Exp (1200°C for 10 min) – transforming (**1**) nodular graphite in a matrix system of (**2**) pearlite and (**3**) ferrite into (**4**) residual graphite in a matrix system of (**5**) ledeburite and (**6**) martensite.

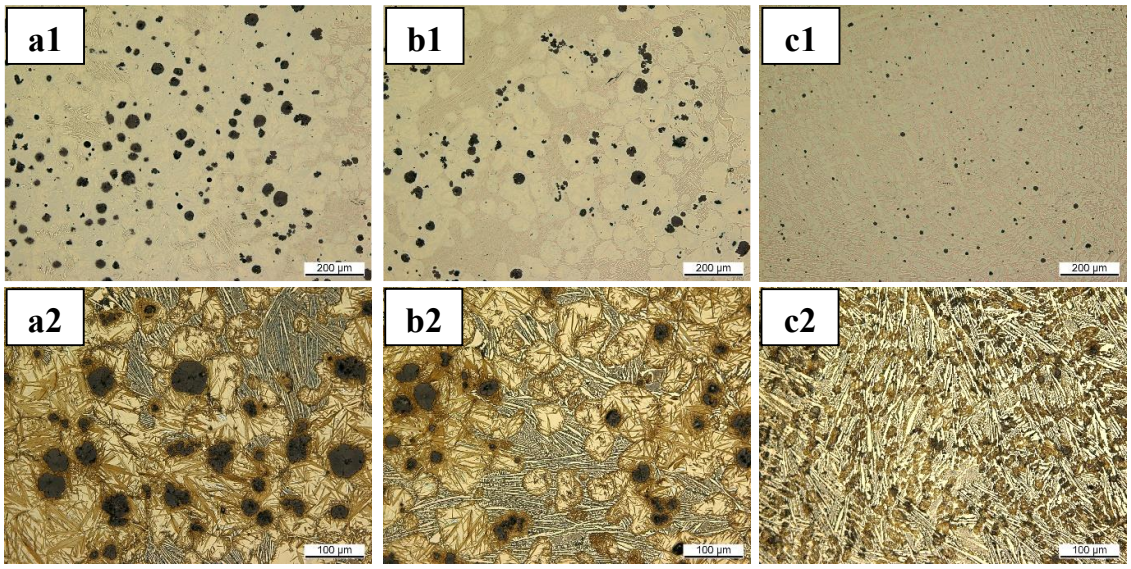

Figure 8.5. Microstructure development LS-CI after being held at 1200°C followed by water quenching for (**a1**) 5, (**b1**) 10, and (**c1**) 15 min in as-polished condition as well as for (**a2**) 5, (**b2**) 10, and (**c2**) 15 min in Nital-etched condition.

Furthermore, it is also documented that the count of residual nodular graphite after the experiment correlates with the holding duration and temperature. As shown in **Figure 8.5**, panels a1 to c1, a decreasing tendency in the nodular graphite count is substantiated following a holding duration from 5 to 15 min. Concurrently, as depicted in panels a2 to c2, a change in the matrix microstructure related to increasing holding duration is also apparent. These

findings indicate that the zone surrounding the graphite transformed into martensite, whereas the remaining matrix region began to exhibit a ledeburite structure. Prolonged holding durations corresponded to an increasing ledeburite proportion and a reduction in the graphite nodule count and size before complete dissolution within a predominant ledeburite matrix, as indicated in **Figure 8.5c2**. Notably, even until nearly complete melting, the coverage of the martensite layer encapsulating the rest of the graphite nodule remained detected, as contrasted in **Figure 8.6**.

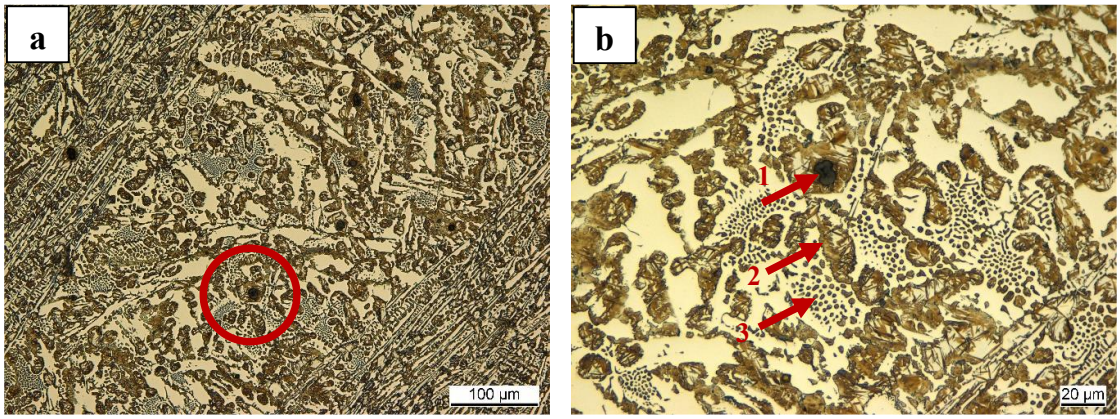

Figure 8.6. Microstructure of the Nital-etched LS-CI after 15 min of holding at 1200°C followed by water quenching indicating (**a**) residual graphite in red circle detailed in (**b**): (**1**) graphite, (**2**) martensite, and (**3**) ledeburite.

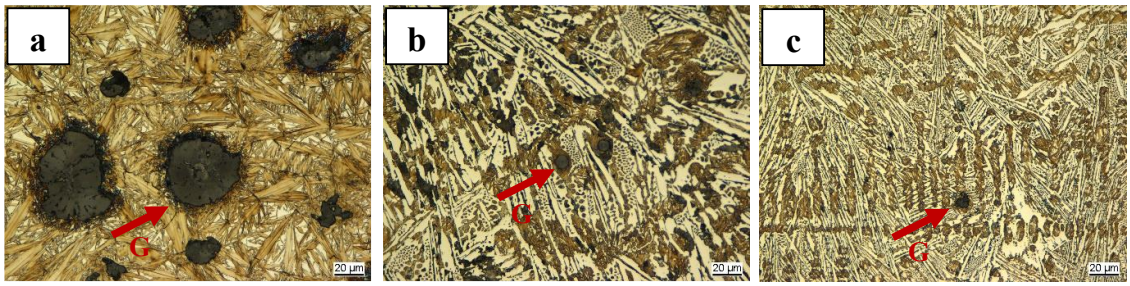

Figure 8.7. Microstructure of the Nital-etched LS-CI after 15 min of holding at (**a**) 1100°C, (**b**) 1200°C, and (**c**) 1300°C followed by water quenching – the detailed red arrow of G pointing at residual graphite.

Moreover, the proportion of graphite–martensite–ledeburite during the holding process also correlates with temperature. As captured in **Figure 8.7a**, even with a 15-minute holding duration at a lower temperature of 1100°C, the dominant process was matrix austenitization, represented by a complete martensite structure surrounding the residual graphite nodules (size of around 20 to 40 µm). In contrast, as explored earlier for a holding temperature of 1200°C, a ledeburite structure is evident in **Figure 8.7b**, accompanied by a smaller dimension of graphite nodules (size of <10 µm) yet still engulfed by the martensite phase. This development becomes particularly pronounced at the highest trial temperature of 1300°C, where the cast iron transforms into an utterly ledeburite structure with the appearance of a primary dendrite constructed by martensite originating from a formerly primary austenite phase. This matrix structure is coupled with the unobvious observable existence of the remaining nodular graphite, indicating complete melting, as represented in **Figure 8.7c**.

8.2.3. Observation of the Residual Graphite Structure after ET-Exp

Interestingly, the availability of residual graphite during the ET-Exp experiments provided an additional opportunity to observe the nodular graphite structure. Specifically, since the graphite structures were only partially dissolved, where a surficial reaction mainly governed dissolution, their core was almost perfectly preserved. Therefore, since the size of graphite nodules in some instances is optimally tiny, it increases the likelihood of revealing their core during sample preparation and accelerates the analysis.

Table 8.2. The chemical composition (wt.%) of the nonmetallic graphite nucleus provided in **Figure 8.8b**.

	C	Si	Mg	N	Al	Fe
Nucleus	11 – 17	36 – 37	24 – 25	34 – 38	1.0 – 1.5	1.0 – 3.0

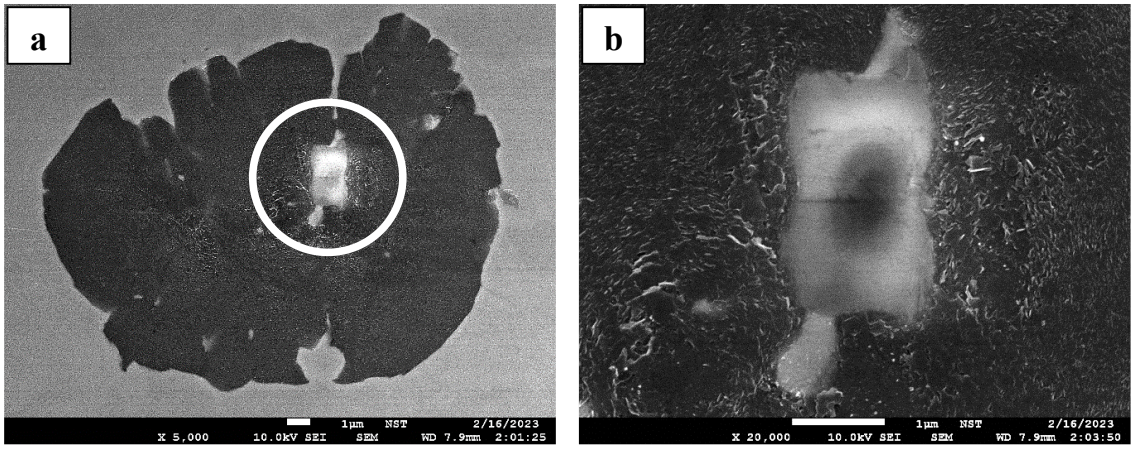

Figure 8.8. Structure of (**a**) residual nodular graphite and (**b**) detail of its nonmetallic nucleus in the LS-CI sample.

Accordingly, numerous graphite nodules from various treatment temperatures during ET-Exp were subsequently observed using the SEM/EDS. A representative sample from this approach and the most prevalent nonmetallic inclusion configuration found inside a graphite structure during the analysis is depicted in **Figure 8.8**. This figure shows a residual graphite nodule with its nucleus exposed. The core was subsequently subjected to chemical analysis, with the results provided in **Table 8.2**. This analysis suggests that the nucleus is a nitride particle composed mainly of silicon and magnesium with a slight aluminum trace.

8.3. Analysis and Discussion

8.3.1. Discussion on Carbon and Silicon Depletions during MH-Exp

According to the results recorded in **Figure 8.1**, **Figure 8.2**, and **Figure 8.3**, a tendency emerges where either dissolved carbon or silicon in cast iron experiences a concentration change during the holding process and correlates to melting temperatures. As shown in **Figure 8.2**, the carbon content slightly increased at 1300°C, which could be associated with the effect of the clay–graphite crucible used. Conversely, at higher temperatures of 1400°C and 1500°C, a decrease in carbon content followed by an insignificant increase in silicon concentration is observed in both samples, as contrasted in

Figure 8.3. It could be explained by considering the compositional constraint effect, given the notable loss in carbon content, as documented in **Figure 8.1**.

Furthermore, the decreasing carbon content for HS-CI and LS-CI at the highest studied temperature of 1500°C can be associated with the oxidation reaction. It is worth mentioning that the effect of the clay-graphite crucible could not even balance the kinetic in carbon reduction, indicated by the comparable decreasing tendency of the LS-CI sample melted at 1400°C in **Figure 8.1b**. In this instance, at high temperatures, the dissolved carbon reacts with the oxygen in the atmosphere, generating CO gas and escaping to the atmosphere. In contrast, at the lowest observed temperature of 1300°C, the silicon concentration decreased instead of the carbon content in HS-CI and LS-CI. In this case, the oxygen reacted with the dissolved silicon and formed SiO_2. However, the reduction in silicon concentration is more moderate than the degree of carbon depletion. This divergence arises from the differing natures of their reaction products. Instead of yielding a gaseous phase (CO), silicon oxidation leads to forming a slag layer (SiO_2) covering the surface of molten cast iron, thus preventing further oxidation reactions.

Considering the atmospheric oxygen influx, this interplay in oxidation dynamics during the cast iron melting could also be approached circumstantially by an equilibrium carbothermic reduction reaction of SiO_2 known in the foundry industry as the crucible reaction [105, 106]. According to this approach, if the temperature of molten cast iron is lower than the equilibrium temperature of the crucible reaction, SiO_2 is stable. In another case, carbon will reduce the amount of SiO_2 formed, and carbon depletion is expected. Furthermore, since it involves a carbothermic reaction, the equilibrium temperature is correlated with the carbon and silicon concentration of the studied cast iron. Concerning the chemical compositions of LS-CI and HS-CI, the equilibrium temperatures were 1420°C and 1410°C, respectively. Therefore, at 1500°C, the carbon decreases over time during high-temperature holding.

However, emphasis is required to describe the outcomes at 1400°C since the results do not support the mentioned theory. Accordingly, considering the dynamics at the equilibrium temperature, a set of thermodynamic calculations by FactSage was conducted, and the results are compiled in **Figure 8.9**. According to the calculation outcomes, comparable results were obtained where silicon dioxide formed at 1300°C, and the dissolved carbon content decreased at 1500°C. Employing the approach for a temperature of 1400°C, the calculation results align with the experimental observation that carbon depletion is expected.

The mismatch between the equilibrium temperature based on [105, 106] and the thermodynamic calculation can be explained by their different approaches during the oxidation process. In the crucible reaction, oxidation generally involves the formation of SiO_2 before it is subjected to temperature-dependent interactions with dissolved carbon. Nevertheless, oxygen dissolution during melting to form SiO_2 did not necessarily occur, as a direct surface reaction upon oxygen influx should be considered; thus, thermodynamic calculations should be more representative. Furthermore, **Figure 8.1** also reported that at 1400°C, there was a disparity in the degree of carbon reduction between HS-CI and LS-CI. This phenomenon can be associated with the higher silicon content in LS-CI. Despite the

oxygen solubility in cast iron reaching its peak at low superheating [114], the higher silicon content in LS-CI limits oxygen solubility but increases carbon activity. Consequently, the perpetuation of oxidation reactions that balance the oxygen influx is preferable, leading to more significant carbon depletion.

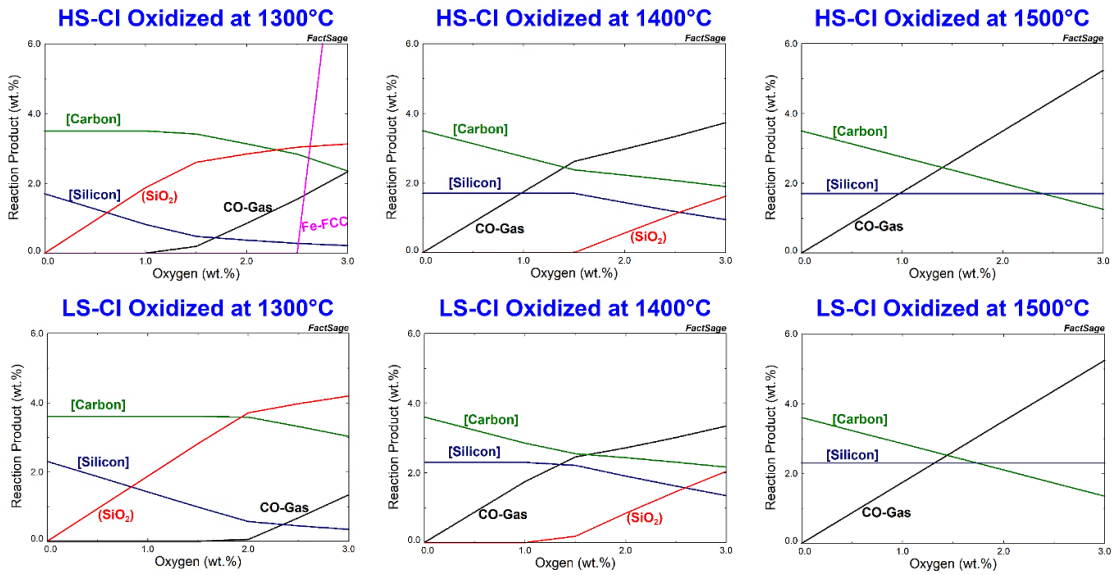

Figure 8.9. FactSage calculation results for HS-CI and LS-CI oxidation processes at all explored temperatures.

8.3.2. Description of Nodular Graphite Dissolution Mechanism

Although rarely systematically explored, the concern of remaining graphite dissolution when circulated cast iron is used as a graphite-containing charge material is not entirely novel in foundry practice [62, 238]. Under these circumstances, particular care should be taken during the melting operation if recycled SGI is considered the input material because of the late dissolution of nodular graphite compared with its counterpart in LGI. Specifically, because of the morphological disadvantage of the nodular structure in terms of a lower effective surface area, its dissolution rate is potentially slower than that of lamellar graphite during the remelting process. Moreover, despite the unsettled debate, the main consensus argues that the nodular graphite exhibits a thickening on the basal plane [239, 240, 241], where the carbon dissolution is expected to be slower than in the prismatic plane [242, 243]. Correspondingly, the significance of the effective surface area is amplified by the results of **Figure 8.5**, **Figure 8.6**, and **Figure 8.7**, which also indicate that the surficial reaction governs the dissolution of nodular graphite. Hence, it is proposed that the initial microstructure of the charged material is a critical factor, especially during the starting sequence of the melting process, in addition to the temperature and heating rate.

According to Wade and Ueda [244], an intermediate austenitization rate is expected in the LS-CI sample because of the initial ferrite–pearlite matrix, as highlighted in **Figure 8.4a**. To this extent, as the temperature starts to increase, pearlite dissolution is anticipated to occur primarily at a lower temperature [245] and faster than carbon diffusion from graphite nodules into the ferrite matrix to transform it into austenite. Nonetheless, as the temperature further elevated, the volume diffusion of carbon from the graphite nodule into the surrounding

ferrite structure is enhanced. This diffusion is followed by the nucleation of austenite cells on the ferrite grain boundaries and eventually at the graphite/ferrite interface, as suggested in [246, 247]. Finally, the mechanism results in a complete austenitic matrix at 1100°C, accommodating high carbon solubility and transforming into martensite upon water quenching. Nevertheless, it is worth mentioning that establishing austenite does not necessarily consume all the graphite structure since (hence) residual graphite nodules are still observable in **Figure 8.7a**.

A significant decrease in the count and size of nodular graphite is eventually detected once a temperature of 1200°C is considered. As the temperature exceeds the eutectic temperature, the melting process starts concurrently with rejecting dissolved carbon from austenite into the molten phase. As indicated in **Figure 8.4b**, the nucleation of the liquid phase began, and the phase grew at the grain boundaries. Interestingly, no liquid phase (indicated as ledeburite) is detected around the graphite, as shown in **Figure 8.6b** and **Figure 8.7b**. This result suggests that the carbon enrichment at the graphite/austenite interface might be lower than that at the austenite grain boundaries and should be associated with a difference in the melting point. In other words, the diffusion rate of carbon from graphite into the iron matrix is notably slower than intergranular or intragranular diffusion through the austenite grains. Circumstantially, this disparity in rate could also be associated with the heterogeneity at the graphite/austenite interface, which has been reported to be susceptible to debonding due to thermal and mechanical loading [248, 249].

In the case of intragranular diffusion, a carbon concentration gradient is anticipated. In this case, it is suspected that the lowest carbon concentration is in the center of the austenite grains due to the denser martensite structure surrounding the graphite and on the edge of the austenite grains. Consequently, uphill diffusion should be foreseen. Primarily proposed by Darken [250], such uphill carbon diffusion is plausible since a Fe–C–Si system is considered in this case. Given the initial microstructure of LS-CI and silicon characteristics in iron, including its inverse segregation behavior and role as a ferrite stabilizer [251, 252], an enrichment of silicon is expected in the ferrite structure [253] surrounding the graphite, thus reducing carbon solubility [120]. Chou et al. [247] suggested this interchange approach to describe carbon enrichment at grain boundaries during the austenitization of ferritic cast iron, which was further elucidated by Domeij and Dioszegi [254].

Since graphite is the only carbon source in the studied system, its dissolution is associated with the solubility dynamic in the austenite phase before and after forming a liquid state, which sequentially reduces the nodule size, as depicted in **Figure 8.5**. As the temperature increases to nearly 1300°C, an exponential rise in the liquid fraction is eventually anticipated. It is driven by the substantial ability of liquid iron to dissolve a notable amount of carbon as molten metal and the decreased amount of dissolved carbon required at austenite/melt equilibrium. In the case of complete melting, depending on the initial size of the graphite nodules and pearlite-ferrite matrix proportion, some graphite can persist in molten cast iron and follow the well-established dissolution mechanism. Based on findings in [255, 256], the dissolution of graphite-containing materials in molten iron is determined by the sequence of graphite dissociation followed by a mass transfer of carbon into the bulk of liquid iron. It

was also elucidated that mass transfer is the controlling rate; thus, an interfacial layer and local carbon saturation are expected [257].

8.3.3. Correlation of Homogenization and Oxidation to Fading

The exploration of graphite dissolution reveals that a solid austenite layer surrounding the graphite nodules can still be detected even near the complete melt condition, as documented in **Figure 8.6b** and **Figure 8.7c**. This investigation suggests that sufficiently high-temperature exposure is necessary during the melting process using recycled SGI since residual graphite can be anticipated if a low melting temperature is applied. Furthermore, this graphite dissolution is considered surficial since iron penetration was unlikely except through any morphological defect, as supported by [257]. No direct oxidation has been reported, but an endothermic reaction was measured during graphite dissolution [242]. Consequently, since the graphite nodule could be protected during the melting process, it is rational to expect their nucleus to be preserved, as depicted in **Figure 8.8**.

According to the chemical composition analysis in **Table 8.2**, nitride nuclei in graphite stoichiometrically tend to form a phase of $MgSiN_2$ that aligns well with Mercier et al. [258]. A comparable nitride compound is also suggested in [81, 83, 84], including the coexistence of aluminum. However, the trace amount of aluminum detected in the present chapter resonates better with that reported by Alonso et al. [259]. Considering these results, the partial dissolution approach to the nodular graphite structure could reliably deliver results similar to the direct observation of graphite nodules and interrupted ductile cast iron solidification process.

The existence of $MgSiN_2$ as a heterogeneous nucleus for nodular graphite can be associated with the magnesium treatment process employing FeSiMg. Since the solubility of magnesium in molten iron is almost negligible [121, 122], the Mg in FeSiMg compounds an intermetallic phase of Mg_2Si in a matrix of FeSi. This Mg_2Si phase is expected to transform into a nitride during the cooling process as it approaches the liquidus temperature [82]. This argument is amplified by Uchida et al. [260]. Based on their observation, the nitridation of Mg_2Si starts at 800°C (stable until ca. 1400°C), which accords well with the practical circumstances during the nodulizing process (magnesium treatment) immediately before the casting step.

In the context of foundry practice, nitridation could also be favored by decreasing the solubility of nitrogen in molten iron. It has also been reported that reducing nitrogen solubility in liquid Fe-C-Si correlates with increasing carbon and silicon [261, 262] contents and elevated temperatures [263]. Since the formation of $MgSiN_2$ occurred in the liquid state, high activities of carbon and silicon are necessary, which can be achieved only by segregation associated with the early-stage dissolution of FeSiMg, as contextually demonstrated in [264]. Based on this perspective, an enriched silicon zone related to the FeSi is anticipated at the dissolution of treatment agents. This process increases both silicon and carbon activities, thus decreasing nitrogen solubility and favoring the nitridation of Mg_2Si.

Moreover, since Mg_2Si is stable under atmospheric pressure and inert conditions [265], the dissociation of Mg_2Si is less probable under the circumstances of the magnesium treatment,

except through Mg_2Si dissolution in molten cast iron, which also increases the magnesium content in molten iron during this process sequence. Assuming a low concentration of sulfur and oxygen that could be controlled by the magnesium supplied from Mg_2Si, silicon segregation can also be established during the early stage of Mg_2Si dissolution. This highly localized silicon content could increase the nitrogen and carbon activity, thus promoting the formation of $MgSiN_2$ and potentially the nucleation of the graphite structure.

Nevertheless, in the case of prolonged holding and remelting processes, this segregation tends to disperse into the bulk of iron. Consequently, a reduced driving force of nucleation related to local segregation is anticipated because the $MgSiN_2$ solidifies later near the liquidus, and the graphite even requires eutectic undercooling. Therefore, this reduced nucleation potential associated with homogenization might be one determining cause of the fading process coupled with the evaporation susceptibility of dissolved magnesium. Notably, silicon segregation alone cannot ensure the nucleation of nodular graphite [80, 229]; instead, a certain amount of dissolved magnesium coupled with this segregation is crucial.

Another fading mechanism could be explained by considering the oxidation process during prolonged holding and remelting processes, as demonstrated earlier in this chapter. As mentioned, low oxygen activity is required to facilitate direct nitridation; otherwise, the oxidation of Mg_2Si is favored [266, 267]. Depending on the dissolved oxygen level, the oxidation products of Mg_2Si extend between the MgO + Si and $MgO.SiO_2$. Interestingly, the complex formation of $MgO.SiO_2$ could also be expected to be an oxidation product of $MgSiN_2$ at temperatures from 1040°C to 1400°C [260]. Following Skaland et al. [79], this $MgO.SiO_2$ possesses a relatively large lattice disregistry to nodular graphite structure and unfavorably acts as a nucleation site. Consequently, this oxidation process can reduce the nucleation potential and should be related to another possible fading mechanism.

8.4. Summary of Graphite Dissolution in Ductile Cast Iron

Based on the investigation results comprised in this present chapter, the following findings could be extracted:

(1) Sufficient exposure to high temperatures is necessary to ensure the homogeneity of molten cast iron during the recycling process. However, care must be taken since chemical composition fluctuations are expected due to the reaction with atmospheric oxygen. Specifically, the interplay between dissolved carbon and silicon concentration changes could be anticipated during the remelting process and prolonged holding of molten cast iron, which depends on the operating temperature.

(2) The inhomogeneity in molten iron using SGI recycled materials originated from the former graphite structure, which could persist despite already surpassing the eutectic temperature. These findings indicate that the dissolution process is surficial because of the formation of austenite surrounding layer, which can be identified after rapid solidification as a martensite layer covering graphite nodules. Although it starts as early as the austenitization process at low temperatures, the carbon diffusion from the graphite into the matrix is slower than from the austenite into the bulk of the iron.

(3) Since the liquid phase starts to nucleate at the grain boundaries of the austenite structure and not at the graphite/austenite interface, partial dissolution of the nodular

graphite structure can be achieved with well-preserved nonmetallic nuclei. One of the most commonly detected cores is a nitride particle of $MgSiN_2$, related to the Mg_2Si in the FeSiMg treatment agent. Examining the behavior of this $MgSiN_2$ formation and dissolution in molten metal makes it possible to offer an alternative perspective to the fading mechanism, which could be related to the homogenization and oxidation process upon prolonged high-temperature holding and remelting processes.

Chapter 9

Relation of Magnesium and Heterogeneous Nucleation

According to the results from previous chapters, a particular concentration of magnesium is necessary to ensure the nucleation and growth of nodular graphite. Nonetheless, besides reacting with oxygen and sulfur, the primary role of magnesium during heterogeneous nucleation of nodular graphite has not been deeply explored. Therefore, this chapter introduces an innovative method developed in the previous chapter to revisit heterogeneous nucleation in the formation of spheroidal graphite during the production of ductile cast iron. The findings revealed that the graphite nucleus comprises oxides, sulfides, carbides, nitrides, and carbo-nitrides. In addition, the research underscores the role of magnesium during the nodular graphite nucleation through a mechanism involving segregation and solubility dynamics, desulfurization and deoxidation, and inclusions as nucleation sites.

9.1. Materials and Methods

9.1.1. Observation of the Nuclei of Nodular Graphite (Controlled Melting)

As part of the preliminary investigation, a reassessment of the nodular graphite nuclei was conducted. Cast iron samples coded as LS-CI were employed in this section, representing a circulated SGI material with chemical composition as delineated in **Table 9.1**.

Table 9.1. Initial chemical composition (wt.%) of cast iron samples.

	C	Si	S	P	Mn	Fe
LS-CI	3.4 – 3.6	2.1 – 2.3	< 0.005	0.02 – 0.03	0.1 – 0.2	93 – 94
HS-CI	3.3 – 3.6	2.2 – 2.5	< 0.004	0.04 – 0.06	0.5 – 0.6	93 – 94
AS-CI	3.5 – 3.6	2.0 – 2.2	< 0.009	0.01 – 0.02	0.05 – 0.1	93 – 94

This experiment involved approximately 100 g of LS-CI, which was melted in a clay-graphite crucible using an induction furnace. This crucible was equipped with a base opening yet secured by a ceramic filter. As the temperature increased and the liquid phase began to establish, molten LS-CI flowed through the filter channels and dripped into a copper mold under the melting system. Controlled by a type-S thermocouple, the temperature was limited to 1200°C to increase the number of residual graphite. The produced samples were subsequently prepared for metallography analysis employing a light microscope coupled with a scanning electron microscope with X-ray dispersive spectroscopy (SEM/EDS). Residual graphites from another dissolution method [237] were also investigated to increase the number of samples.

9.1.2. Effect of Treatment Agents on Graphite Nucleation (In-mold Treatment)

In addition to LS-CI, this section incorporates two additional cast iron samples to explore the effects of different treatment agents on graphite nucleation. The second sample (HS-CI) is cast iron produced using a cupola furnace and subjected to lime-based desulfurization, which is varied to achieve distinct sulfur concentrations. The details of the applicability of this alternative desulfurization operation are provided in the previous chapter.

Furthermore, the third cast iron sample (AS-CI) is an alloyed cast iron sample created by remelting ARMCO pure iron, FeSi75, and graphite in proportional quantities to achieve a chemical composition comparable to SGI. Together with LS-CI, the chemical compositions of HS-CI (full desulfurized) and AS-CI are also available in **Table 9.1**.

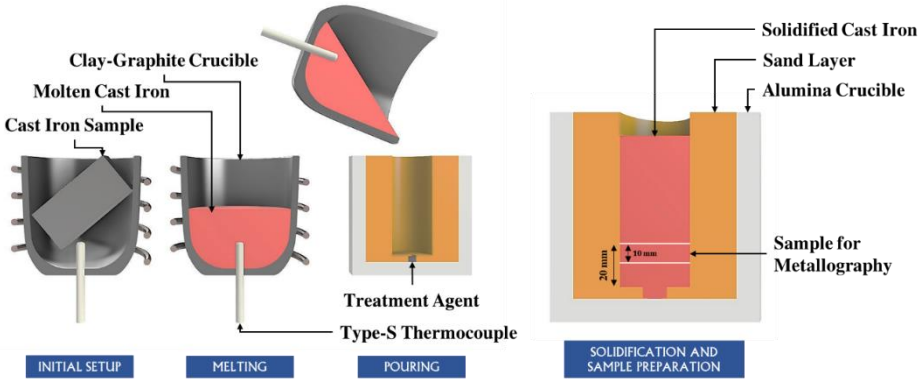

Figure 9.1. Experimental setup of in-mold treatment of molten cast iron.

As shown in **Figure 9.1**, 400 g of the cast iron samples were melted in a clay–graphite crucible using an induction furnace. Immediately after reaching the designated pouring temperature, the molten cast iron was poured into a cylindrical cast cavity (diameter of 25 mm) in a double-layered mold comprising a sand-layered alumina crucible. The explored melting-pouring temperature was 1500°C. In addition, FeSiMg6, FeSi75, FeSi-CeLa, SiC, Ca, CaSi, CaC_2, Mg-AlSn, and NiMg15 were utilized as treatment agents positioned at the bottom of the mold to address the effects of variables, including sulfur and magnesium, on nodular graphite nucleation. In this case, metallography observations of the graphite structures were conducted on the sectioned sample from the solidified cast iron, as indicated in **Figure 9.1**.

9.2. Experimental Results

9.2.1. Chemical Composition of the Nuclei in the Residual Graphite Structure

As documented in **Figure 9.2**, the as-received LS-CI exhibited a spheroidal graphite structure with an average diameter of approximately 20 µm surrounded by an iron matrix comprising a pearlite-ferrite configuration.

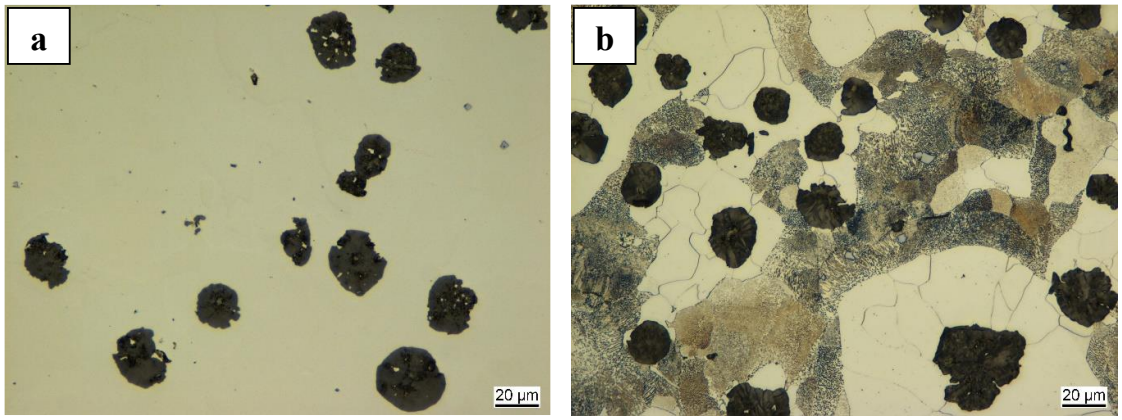

Figure 9.2. As-received microstructure of LS-CI in (**a**) as-polished and (**b**) Nital-etched conditions.

Following the controlled melting process at 1200°C, a reduction in nodule size was observed, as depicted in **Figure 9.3**. Their dimensions range from 10 µm to fine nodules less than 500 nm in diameter. Nonetheless, because of specific technical considerations, graphite larger than 5 µm was preferred, already reaching a substantial 75% reduction in diameter. One reason is the considered investigation approach, which starts with cursory elemental mapping before delving into the chemical analysis of the nuclei.

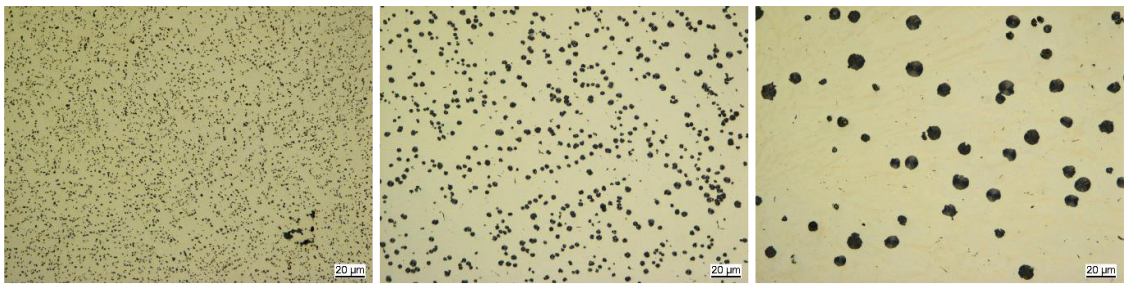

Figure 9.3. Spectrum of graphite nodules in different regions in LS-CI after controlled melting at <1200°C.

Several nonmetallic inclusions have been exposed based on the preparatory observation of partially dissolved residual nodular graphite. According to the chemical analysis in **Table 9.2** corresponding to the measurement points in **Figure 9.4**, the inclusions consisted of oxides, sulfides, or (carbo-) nitrides. Moreover, in addition to Fe, C, and Si, which are the primary alloying elements of LS-CI, other components could also be detected in the inclusion. These elements, including Mg, Al, Ca, P, Ce, and La, are available as commercial treatment agents for casting ductile cast iron (FeSiMg6), as shown in **Figure 9.5**. Based on this initial positive result, subsequent data enrichment of graphite nuclei from controlled melting trials and graphite dissolution studies was conducted. Accordingly, the inclusions can be categorized into oxy-sulfide, carbo-nitride, or complex-compound configurations.

Table 9.2. Chemical composition (wt.%) of inclusions in residual graphite structures pointed out in **Figure 9.4**.

Nr.	C	O	N	S	Mg	P	Fe	Si	Al	Ca	Ce	La
a1	55.9	-	-	0.26	16.1	-	10.0	16.8	0.96	0.11	-	-
a2	47.3	-	20.8	0.16	13.0	-	5.1	12.9	0.76	0.07	-	-
b3	65.4	-	-	0.05	3.6	-	26.8	4.0	0.17	-	-	-
b4	37.8	-	-	-	5.9	-	50.4	5.7	0.30	-	-	-
b5	54.9	-	23.7	0.10	8.1	-	5.2	7.7	0.32	-	-	-
c6	58.8	10.8	-	-	-	0.23	3.2	0.2	-	-	26.8	-
c7	63.0	8.1	-	-	-	0.40	2.5	0.1	-	-	25.5	0.48

The chemical analysis of various oxy-sulfide configurations found within or affixed to residual graphite is summarized in **Table 9.3**. As depicted in **Figure 9.6**, a well-preserved spheroid containing a predominant Mg-O system has been identified, coupled with a minor detection of Si and Al. A comparable system can also be implicated in concurrently identifying increasing sulfur concentrations, as documented in **Figure 9.7**. Furthermore, a higher sulfur content can also be detected in the center of the distorted graphite, as Ca, Ce,

and La were measured in the respective structures, as provided in **Figure 9.8a**. In another case, a certain level of Ti can also be perceived following a notable amount of N, as substantiated in **Figure 9.8b**.

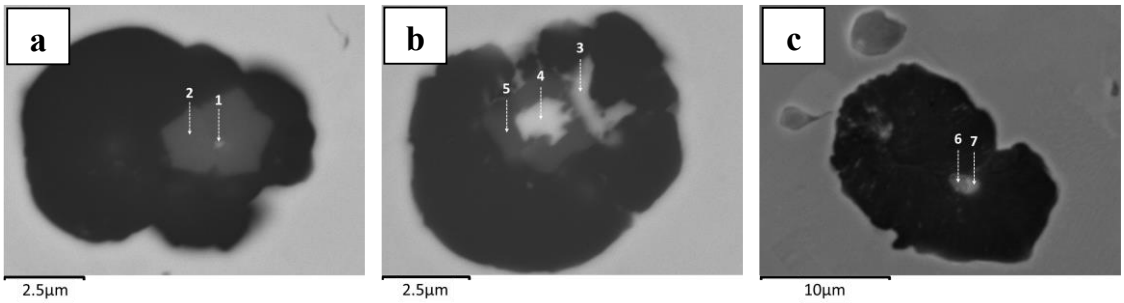

Figure 9.4. Nonmetallic inclusion detected within residual nodular graphites after a controlled melting trial.

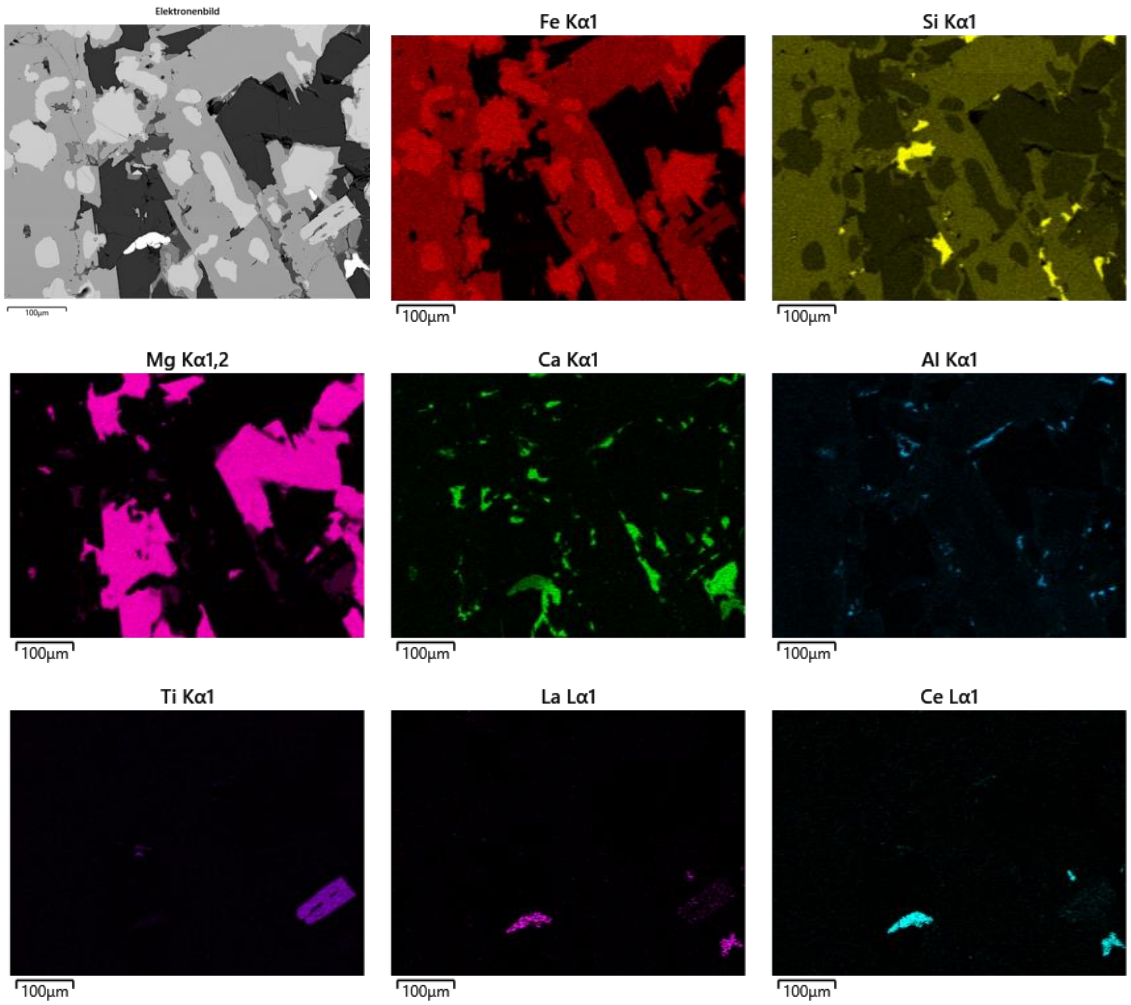

Figure 9.5. Elemental mapping result of the commercial treatment agent FeSiMg6 in cast iron production.

Table 9.3. Chemical composition (wt.%) of oxy-sulfide-based nuclei in residual graphite structures.

Nuclei	C	O	N	S	Mg	Ti	Fe	Si	Al	Ca	Ce	La
Figure 9.6b	49.3	20.4	-	-	20.1	2.2	6.4	1.5	0.2	-	-	-
Figure 9.7a 1	31.4	22.9	-	2.5	12.8	-	30.3	-	-	-	-	-
Figure 9.7a 2	13.4	10.3	-	3.4	6.5	-	66.4	-	-	-	-	-
Figure 9.7b 1	34.9	25.4	-	6.5	18.1	-	15.1	-	-	-	-	-
Figure 9.7b 2	32.8	14.9	-	9.4	10.1	-	30.8	1.3	0.9	-	-	-
Figure 9.8a 1	37.0	19.4	2.3	1.1	27.7	4.7	6.8	1.2	-	-	-	-
Figure 9.8a 2	32.4	26.3	-	8.4	24.5	-	2.7	4.3	0.7	0.6	-	-
Figure 9.8a 3	38.5	5.2	-	13.6	4.3	-	6.4	0.4	1.4	2.3	12.1	15.7
Figure 9.8b 1	58.3	17.4	-	0.7	14.5	5.0	3.4	-	0.8	-	-	-
Figure 9.8b 2	53.3	11.2	7.9	0.2	7.7	14.0	5.2	0.2	0.3	-	-	-

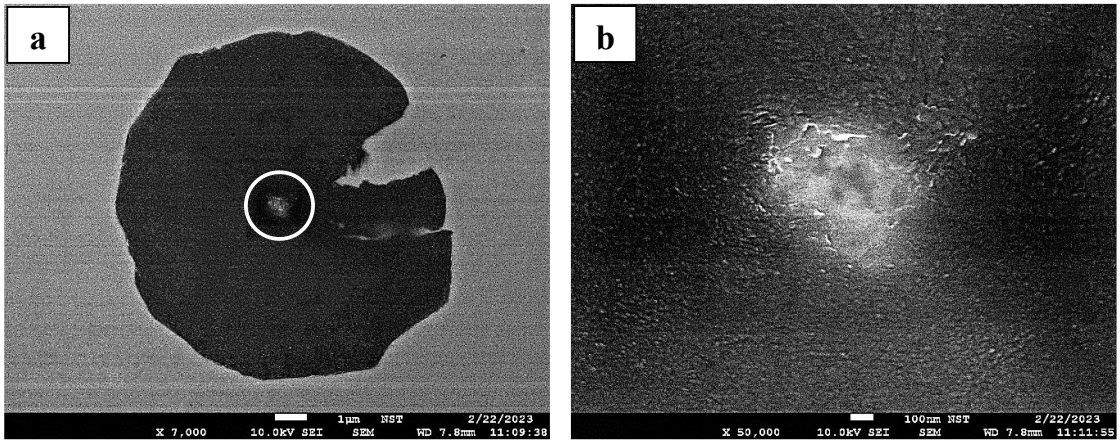

Figure 9.6. Structure of (**a**) residual graphite nodule with a trace of (**b**) oxide nucleus.

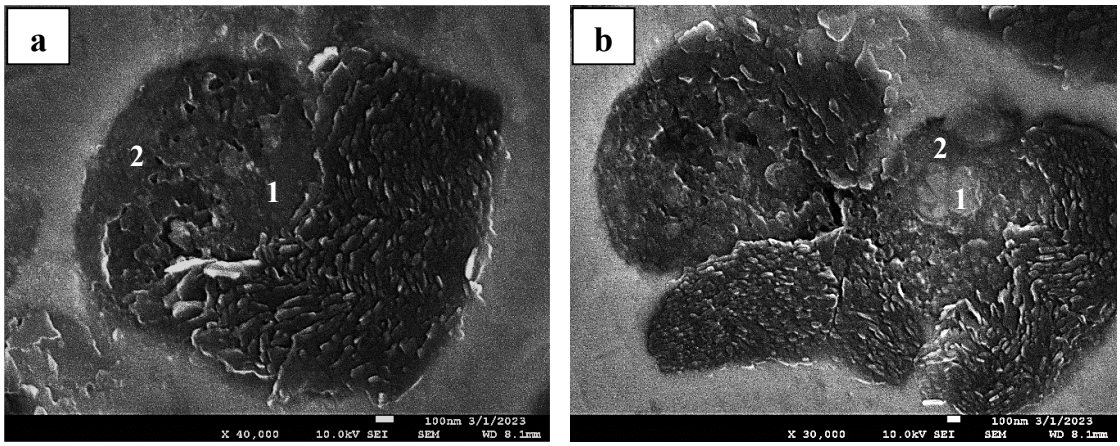

Figure 9.7. Structure of residual graphite with a trace of oxy-sulfide nuclei.

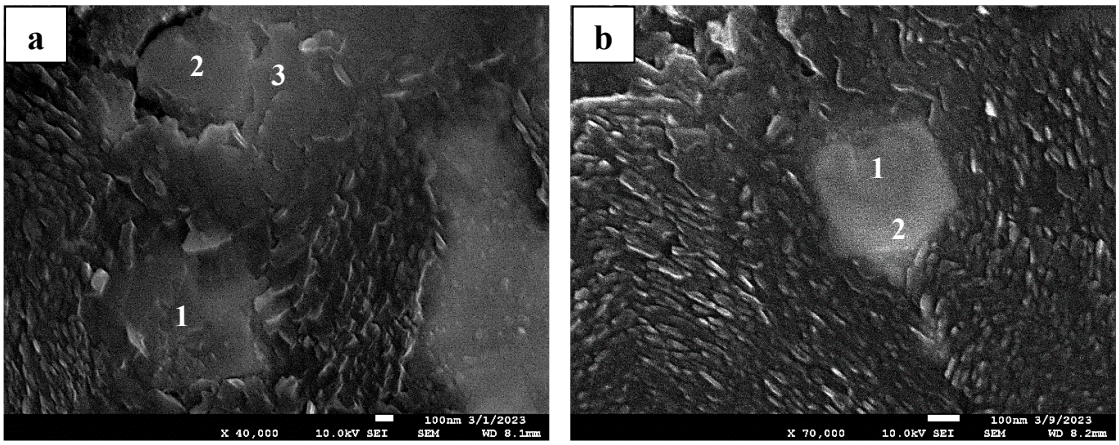

Figure 9.8. Structure of residual graphite with a trace of oxy-sulfide nuclei coexisting with (carbo-) nitride.

The establishment of carbides and nitrides as inclusions found in residual nodular graphite is also detected in simple configurations or complex compounds, as they coexist with the oxy-sulfide system. **Table 9.4** indicates a possible Si-C system to construct a nucleus in the residual graphite nodule documented in **Figure 9.9a**. Furthermore, a simple nitride compound is also substantiated in **Figure 9.9b**, which is also the most frequent configuration found in the boundary of this chapter. As detailed in **Figure 9.10**, this nitride structure located in the center of the graphite nodule is attached to the residual graphite structure, and it is expected to contain an Mg-Si-N configuration with a minor of Al, as listed in **Table 9.4**.

Table 9.4. Chemical composition (wt.%) of carbide- and nitride-based nuclei in residual graphite structures.

Nuclei	C	O	N	S	Mg	Ti	Fe	Si	Al
Figure 9.9a	32.1	0.4	-	-	-	-	0.9	66.6	-
Figure 9.9b	21.7	-	28.3	0.06	22.6	0.17	1.6	24.2	1.3
Figure 9.10b 1	11.4	-	31.2	-	22.1	-	1.2	33.1	1.0
Figure 9.10b 2	16.9	-	30.6	-	20.1	-	2.2	29.3	0.9

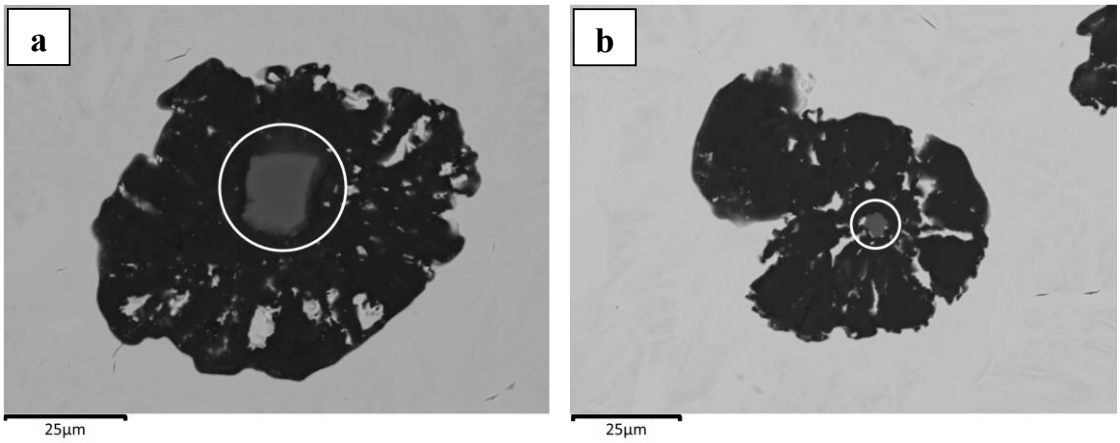

Figure 9.9. Structure of residual graphite nodules with a trace of (**a**) carbide and (**b**) nitride nuclei.

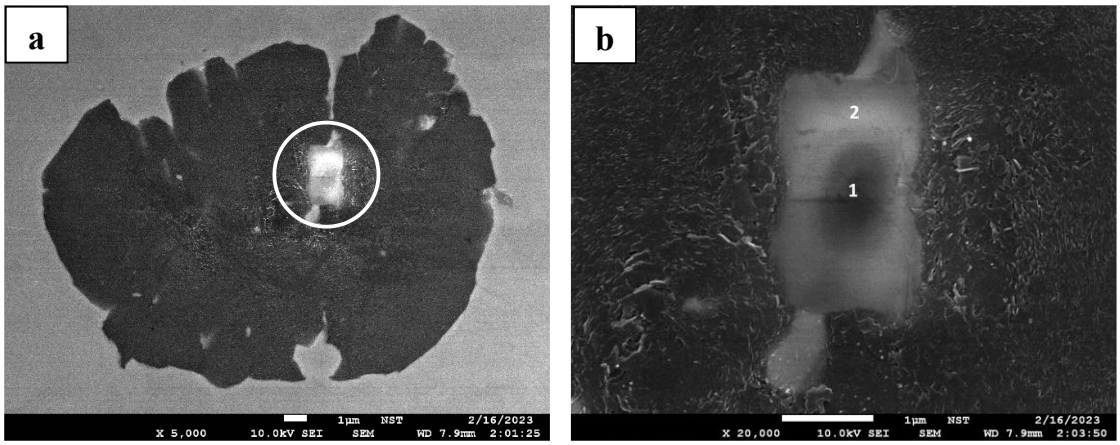

Figure 9.10. Structure of (**a**) residual graphite nodule with a trace of (**b**) nitride nucleus [237].

In addition to simple carbide and nitride inclusions, complex compounds were also detected in the middle of the residual graphite. **Table 9.5** indicated that the oxy-sulfide could coexist with the carbo-nitride configuration. As representatively provided in **Figure 9.11**, a staged nuclei system is substantiated. Chemical analysis revealed that an oxide with Ti-N configuration constructs the core, where an oxy-sulfide and Mg-Si-N system acts as a covering system before the graphite structure grows on it.

In another case documented in **Figure 9.12**, a complex compounding system is proposed based on several oxy-sulfide and carbo-nitride systems. Listed in **Table 9.5**, considering the measurement point, especially **Figure 9.12b** 1 and 2, a trace of possible oxides and oxy-sulfides involving Mg could be expected to coexist with nitride and carbo-nitride associated with Ti. Furthermore, an increasing proportion of the oxy-sulfide system can be observed as the measurement point moves toward the center (**Figure 9.12b** 3 to 6). Particularly indicated in **Figure 9.12b** 5 and 7, notable concentrations of Al and Ti are measured, indicating the possible complex formation of Al-O and Ti-C, respectively. Notably, it is worth mentioning that the graphite structure grows on those inclusions regardless of their different chemical compositions.

Table 9.5. Chemical composition (wt.%) of the compounding nuclei in the residual graphite structures.

Nuclei	C	O	N	S	Mg	Ti	Fe	Si	Al
Figure 9.11b 1	29.3	9.4	7.2	-	4.8	5.5	34.4	6.1	3.3
Figure 9.11b 2	28.4	12.3	8.6	-	7.2	13.0	16.6	8.7	5.2
Figure 9.11b 3	36.0	15.4	9.4	0.24	8.4	-	6.2	16.8	7.4
Figure 9.11b 4	51.7	2.2	21.1	0.18	9.0	-	1.8	13.1	1.0
Figure 9.12b 1	39.5	11.8	13.9	-	5.0	26.9	2.6	-	0.3
Figure 9.12b 2	41.0	25.9	3.5	0.50	16.4	10.3	1.5	0.3	0.6
Figure 9.12b 3	51.3	24.9	-	1.57	4.3	1.8	7.1	1.5	7.5
Figure 9.12b 4	64.9	15.7	1.3	1.20	6.6	1.3	7.3	0.6	1.3
Figure 9.12b 5	27.7	32.9	-	1.65	16.4	-	9.9	1.2	10.3
Figure 9.12b 6	49.4	25.6	-	1.66	16.7	-	4.5	0.7	1.6
Figure 9.12b 7	66.7	9.7	1.0	0.39	6.4	12.3	3.0	-	0.6

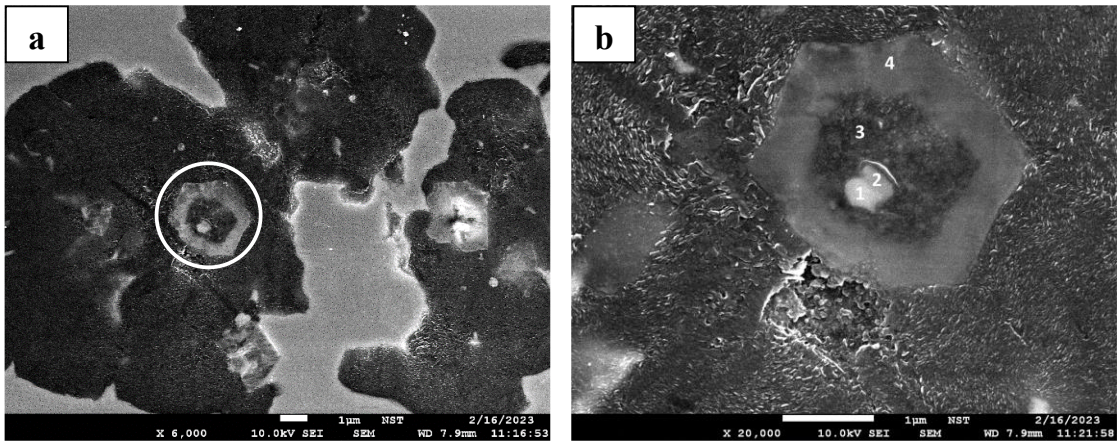

Figure 9.11. Structure of (**a**) residual graphite nodules with a trace of (**b**) staged nucleus.

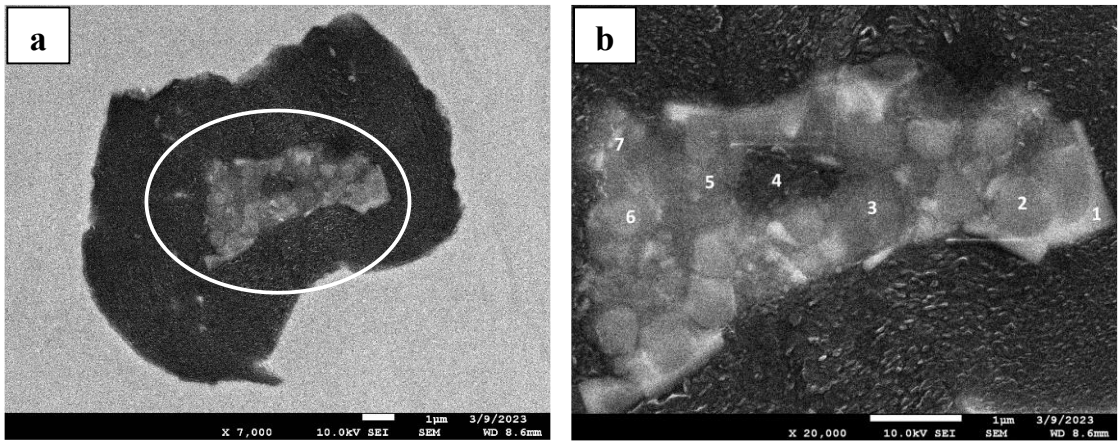

Figure 9.12. Structure of (**a**) residual graphite nodule with a trace of (**b**) complex nucleus.

9.2.2. Effect of the In-mold Treatment Agent on Graphite Nucleation

Following the setup illustrated in **Figure 9.1**, an initial identification was carried out where no treatment agent was placed on the base of the crucible. As shown in **Figure 9.13**, all the samples melted and cast at 1500°C have no nodular graphite structure and instead exhibit predominantly undercooled lamellar graphite. This reference is essential considering the original structure and characteristics of LS-CI, HS-CI, and AS-CI.

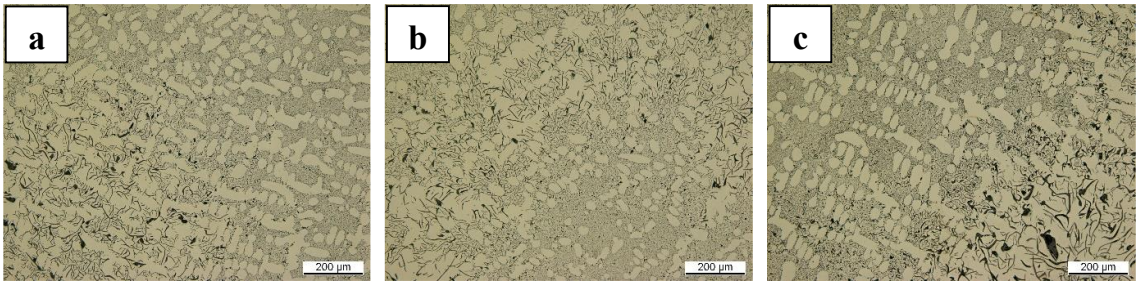

Figure 9.13. Graphite structures of (**a**) LS-CI, (**b**) HS-CI, and (**c**) AS-CI without involving treatment agents.

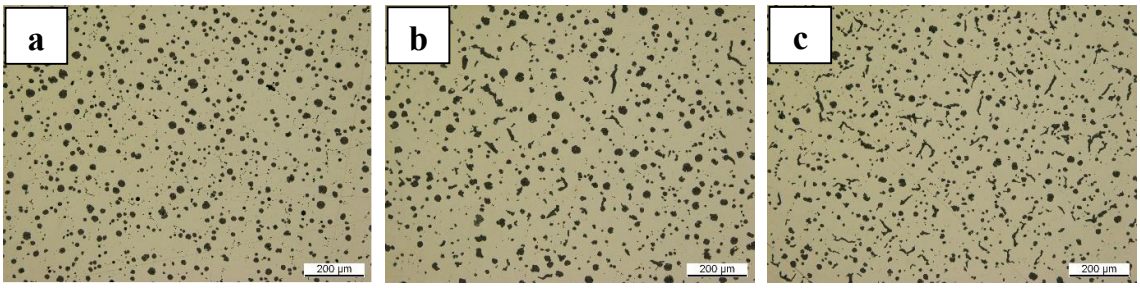

Figure 9.14. Graphite structures of LS-CI with (**a**) 10, (**b**) 5, and (**c**) 2.5 g FeSiMg6 as the treatment agent.

Nodular graphite can eventually be observed in the cast iron samples once 10 g of FeSiMg6 is used as an in-mold treatment agent. Specifically, as documented in **Figure 9.14a** and **Figure 9.15a**, both LS-CI and HS-CI possess 100% spheroidal graphite, although their nodule sizes are not uniform. Furthermore, based on the observation in **Figure 9.14**, the graphite nodularity decreases with the reduction amount of FeSiMg6 introduced during the in-mold treatment. A similar effect could also be observed in **Figure 9.15** for increasing the remaining sulfur content. It is indicated that the count of spheroidal graphite decreases, followed by the formation of vermicular and, eventually, lamellar graphites.

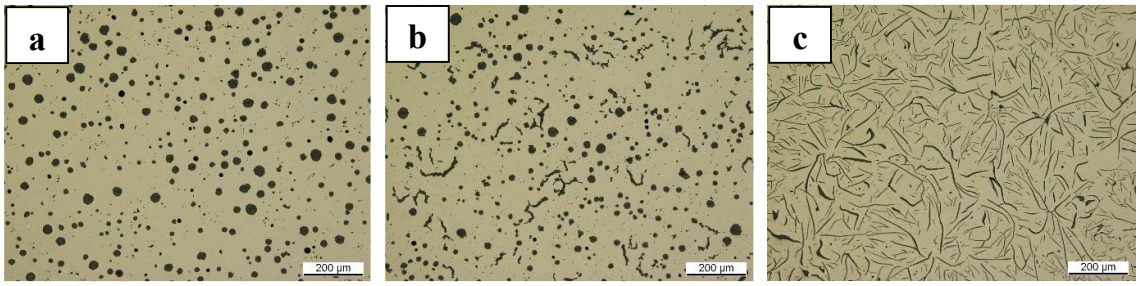

Figure 9.15. Graphite structures of HS-CI containing (**a**) 0.002, (**b**) 0.04, and (**c**) 0.1 wt.% S with 10 g FeSiMg6 as the treatment agent.

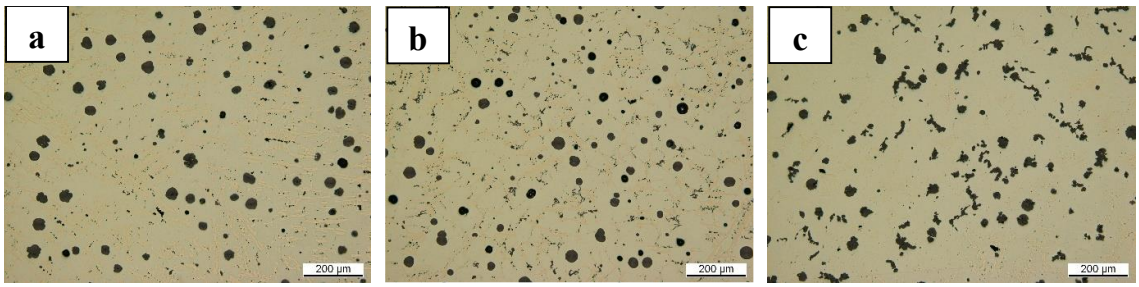

Figure 9.16. Graphite structures of AS-CI with 5 g (**a**) Mg-AlSn, (**b**) NiMg15, and (**c**) FeSi-CeLa as treatment agents.

A certain degree of graphite nodularity could also be observed if Mg-bearing materials and FeSi-CeLa were used as in-mold treatment agents. As shown in **Figure 9.16**, round spheroidal graphite solidified, mainly if 5 g of Mg-AlSn or NiMg15 was used. Although some nodules were documented as 5 g of FeSi-CeLa was utilized, vermicular graphite structures were also established. Additionally, in contrast to the results for FeSiMg6, the cast iron matrix depicted in **Figure 9.16** indicates the formation of a white iron (carbide) structure.

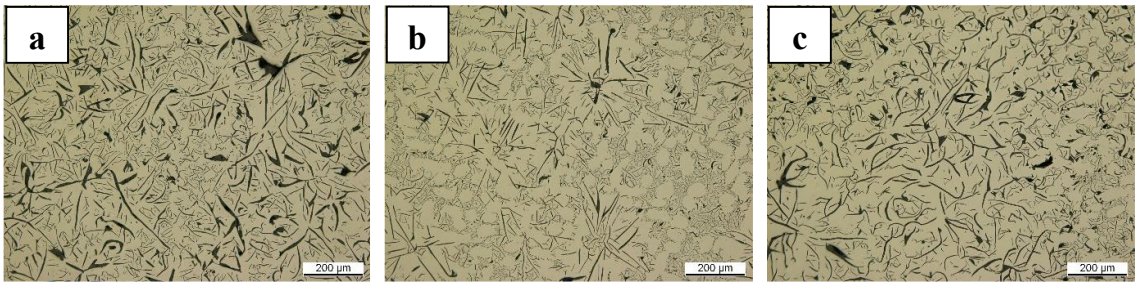

Figure 9.17. Graphite structures of (**a**) LS-CI, (**b**) HS-CI, and (**c**) AS-CI with 5 g CaSi as the treatment agent.

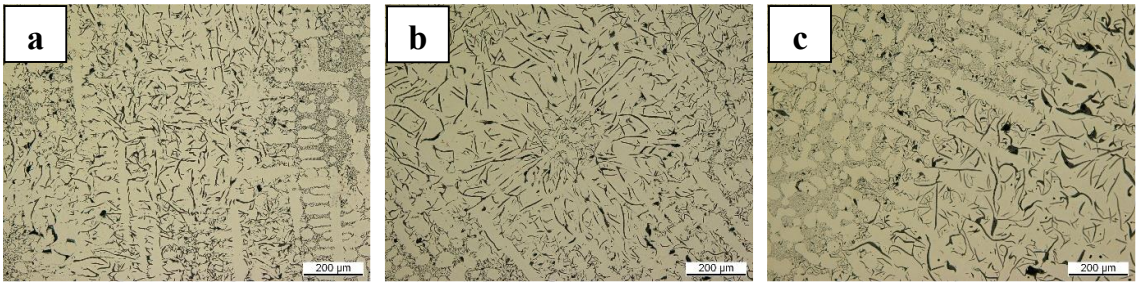

Figure 9.18. Graphite structures of (**a**) LS-CI, (**b**) HS-CI, and (**c**) AS-CI with 10 g FeSi75 as the treatment agent.

Based on the observation results in **Figure 9.15**, which indicate the effect of the remaining sulfur content, Ca-bearing materials were utilized as in-mold treatment agents. However, as documented in **Figure 9.17**, no nodular graphite can be identified after using 5 g of CaSi as an in-mold treatment agent. Comparable behavior was also recognized in other experiments that used 5 g of Ca or CaC_2 as treatment agents for all samples. Like CaSi, using another silicon-bearing material (10 g of FeSi75) as an in-mold treatment agent also delivered no nodulizing effect, as indicated in **Figure 9.18**. A similar result of predominantly lamellar graphite formation was also shown if 10 g of SiC was utilized as an in-mold treatment agent within the boundary of a similar experimental setup in **Figure 9.1**.

9.2.3. Effect of Nonmetallic Inclusion on the Graphite Structure

In addition to the microstructure analysis of the graphite morphology related to the treatment agents, the behavior of graphite nucleation on nonmetallic inclusions was also revealed. As shown in **Figure 9.19 a** and **b** as detailed observations of LS-CI in **Figure 9.13a** and HS-CI in **Figure 9.15c,** respectively, lamellar graphite heterogeneously grows on inclusions with the chemical compositions listed in **Table 9.6** and **Table 9.7**, respectively.

Table 9.6. Chemical composition (wt.%) of Mg-modified nitride as a nucleation site for lamellar graphite.

Nuclei	C	O	N	S	Mg	Ti	Fe	Mn	Si	Al	Ca	Ce
Figure 9.19a 1	-	20.4	6.7	3.0	13.9	45.8	5.1	0.4	-	-	0.5	1.6
Figure 9.19a 2	3.3	-	8.9	7.1	8.6	60.0	7.2	1.1	-	0.4	0.9	-
Figure 9.19a 3	4.6	-	12.1	4.8	4.2	58.7	5.9	0.3	0.3	0.6	0.8	3.8
Figure 9.19a 4	-	-	16.8	0.2	0.4	65.3	12.6	-	0.3	-	-	-
Figure 9.19a 5	54.5	-	-	-	-	0.4	44.8	-	0.3	-	-	-

Table 9.7. Chemical composition (wt.%) of Mg-modified sulfide as a nucleation site for lamellar graphite.

Nuclei	C	O	S	Mg	Fe	Mn	Si	Al	Ca	Ce	La
Figure 9.19b 1	11.8	-	36.4	17.3	3.6	27.3	-	-	-	2.5	1.2
Figure 9.19b 2	9.8	-	36.0	17.8	8.9	27.8	-	-	-	-	-
Figure 9.19b 3	6.8	-	17.8	12.3	43.7	9.9	0.8	-	0.1	3.3	5.3
Figure 9.19b 4	5.6	3.4	14.1	9.5	43.4	6.5	0.7	4.0	0.1	4.5	8.1
Figure 9.19b 5	80.2	-	0.1	-	19.1	0.2	0.5	-	-	-	-

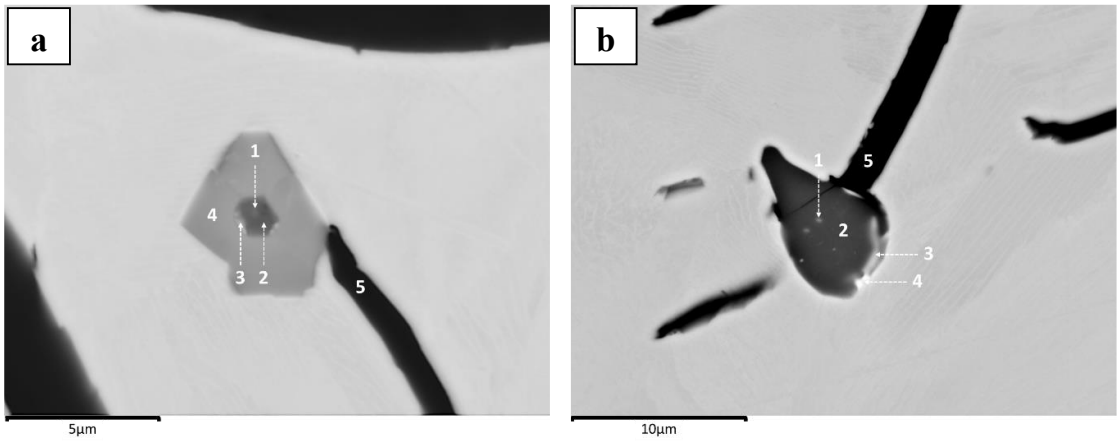

Figure 9.19. Mg-modified inclusions as heterogeneous nucleation sites for lamellar graphite structures captured in (**a**) untreated LS-CI in **Figure 9.13a** and (**b**) HS-CI with 0.1 wt.% S in **Figure 9.15c**.

Table 9.8. Chemical composition (wt.%) of Mg-containing nuclei in graphite nodules pointed out in **Figure 9.20**.

Nr.	C	O	S	Mg	Fe	Si	Al	Ca
a1	65.8	12.4	1.8	2.5	10.1	0.3	7.1	-
b2	79.1	-	8.8	6.4	5.5	0.1	-	0.2
c3	75.6	-	0.4	8.6	3.2	9.4	2.8	-

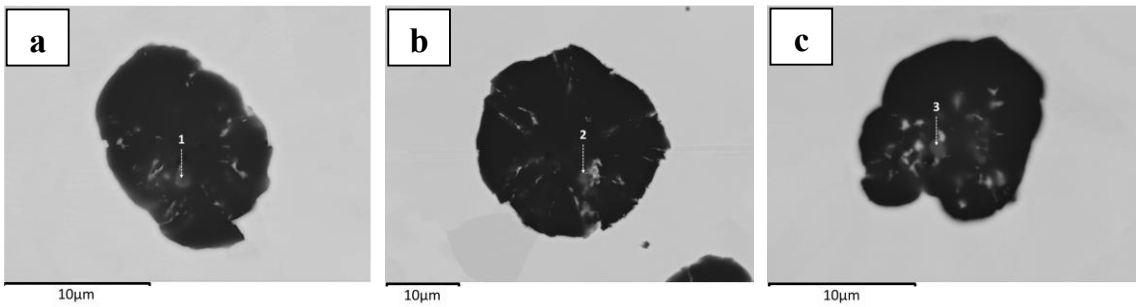

Figure 9.20. Mg-containing inclusions in the center of graphite nodules in HS-CI with 0.04 wt.% S in **Figure 9.15b**.

Based on the analysis in **Table 9.6**, a possible configuration of the Mg-O-S core covered with a Ti-N configuration is suggested. In another case, **Table 9.7** shows a mixture of Mn-S and Mg-S inclusion systems where minor sulfides of Ce and La were also detected. Notably,

the origin of Mg in both samples is distinguishable (as residual compared to an addition). Yet, both were insufficient to induce nodular graphite formation.

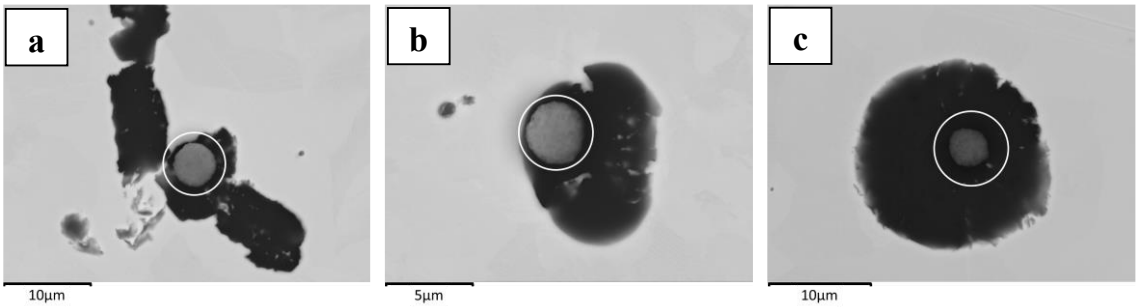

Figure 9.21. Al-containing oxide inclusions as possible heterogeneous nuclei of graphite structures in HS-CI with 0.04 wt.% S in **Figure 9.15b**.

In the case of varying the sulfur content provided in **Figure 9.15**, the number of graphite nodules increases with decreasing sulfur content. This change in the sulfur content was also observed to influence the chemical composition of the inclusion, where no significant involvement of manganese was detected. As summarized in **Table 9.8**, based on detailed observations of nodular graphite nucleated on the HS-CI in **Figure 9.15b**, distinct configurations of Mg-containing inclusions were revealed, as depicted in **Figure 9.20**. In addition to those Mg-bearing inclusions, several Al-containing oxides were also captured, which were also associated with the nucleation of the graphite structure. As documented in **Figure 9.21**, despite having an identical morphology with an approximately Al-O composition, the graphite structures that grow on those inclusions do not necessarily follow similar behaviors.

9.3. Analysis and Discussion

9.3.1. The Interplay between Inclusions, Composition, and Graphite Structure

As shown in **Figure 9.6**, detecting an Mg-O-based system in the center of a well-preserved graphite nodule suggests that this nodular graphite nucleated heterogeneously. However, this establishment of Mg-O alone does not guarantee that the nucleated graphite grows as nodular graphite. As captured in **Figure 9.8b** and **Figure 9.19a**, distinct graphite morphologies of nodular and lamellar graphite are captured, respectively, despite possessing a comparable composition of nonmetallic compounds as their heterogeneous nucleation sites by exhibiting a certain extent of Mg-O and Ti-N configurations. In this context, despite originating from a similar LS-CI sample, the examination in **Figure 9.19a** resulted from the remelting process at 1500°C (in **Figure 9.13a**) instead of at 1200°C for controlled dissolution (as in **Figure 9.8b)**; hence, significant fading of the remaining magnesium (measured at less than 30 ppm) is highly anticipated. Based on these findings, it is suggested that graphite nucleation should not always immediately start with the availability of the Mg-O nonmetallic system since it can also provide a nucleation site for another compound before (or parallel with) graphite nucleation.

Moreover, although nonmetallic inclusions might induce or trigger graphite nucleation, the abovementioned results reaffirm that the concentration of magnesium in molten iron has a

more pivotal role in determining the nucleation and growth of nodular graphite, as further amplified in **Figure 9.14**, which aligns well with [219, 268]. On the other hand, it is also essential to note that the residual dissolved magnesium concentration is related to the dissolved oxygen content in molten cast iron [269]; thus, the presence of Mg-O should be attributed to the oxidation of magnesium. This formation is crucial because only the Mg-O system established during the process can preferably serve as an effective graphite nucleation site since the direct addition of MgO particles has been proven to be a disadvantage [270].

The residual sulfur concentration could also influence the remaining dissolved magnesium in molten cast iron [271]. However, it is worth noting that the desulfurization reaction to MgS can proceed just after a specific low level of dissolved oxygen has been attained [32]. In the context of nucleation, this reaction will produce the Mg-S inclusion system, which could serve as an effective nucleation site for graphite as either a relatively dominant compound (**Figure 9.20b**) or coexist with Mg-O (**Figure 9.7**). As already explored in the Mg-O system, solely establishing the Mg-S inclusion system could not determine whether the graphite would nucleate on its surface. Concurrently, assuming that graphite nucleation has started, it does not necessarily mean that a nodular graphite will develop, as shown in **Figure 9.19b**, where a lamellar graphite structure grows instead.

Given the circumstances of the abovementioned observed sample (HS-CI with 0.1 wt.% S with 10 g of FeSiMg6 as an in-mold treatment agent captured in **Figure 9.15c**), the formation of the Mg-S system is expected to occur early during solidification [272]. However, no graphite nucleation was directly started, and sulfide formation consisting of Mg-Mn was preferred because of the limited amount of magnesium compared to sulfur content. This sulfide facilitates the nucleation and growth of lamellar graphite, amplifying the results documented in [273]. Furthermore, this sulfide system also provides a nucleation site for an oxy-sulfide containing Ce and La originating from FeSiMg6, as suggested in [74]. Hence, as depicted in **Figure 9.15**, enhancing the previous results in [274, 275], achieving certain low levels of sulfur and oxygen is crucial for promoting the growth of nodular graphite.

Despite the anticipated low solubility limit in molten cast iron [121, 122], the introduction of magnesium-bearing materials should be followed by a dissolution process if the dissolved oxygen and sulfur concentrations are maintained at lower levels than the critical thresholds. Considering that FeSiMg6 was utilized, the introduction of Mg involves the dissolution of Mg_2Si, which has a melting point of ca. 1100°C [276]. In this instance, the graphite is expected to be able to start its nucleation at an early stage of dissolution, as indicated in **Figure 9.20c**, where high Mg and Si contents are detected.

On the other hand, this inhomogeneous dispersion could also induce nitridation of Mg_2Si, producing the core structure shown in **Figure 9.4b**. This nitrogen interaction arises from the decreasing solubility with increasing concentrations of carbon and silicon [261, 262], which could be triggered by segregation associated with FeSi dissolution. Moreover, since the silicon content increases, the solubility of carbon decreases [120] and might be, to a certain extent, favorable for graphite nucleation on $MgSiN_2$, forming the structure depicted in **Figure 9.10**. Similarly, since FeSi has no direct nodularization effect, as substantiated in

Figure 9.18, which strengthens previous findings in [80, 229], the nucleated graphite could only eventually develop into a nodular structure because of the low oxygen and sulfur concentrations coupled with a sufficient dissolved magnesium concentration in cast iron.

9.3.2. The Importance of Inclusion and Magnesium to the Nodular Graphite

Since the composition of inclusions varies despite originating from one iron sample, it is suggested that no definite format is required for graphite nucleation. This case is supported by the fact that the graphite structure can nucleate on a single system based on magnesium (**Figure 9.6**), silicon (**Figure 9.9a**), and cerium (**Figure 9.4c**), as well as start congruently with the nucleation chain as in staged (**Figure 9.11**), compound (**Figure 9.8a**) and complex (**Figure 9.12**) configurations. The formation of this variance also suggests that either inhomogeneity or segregation was involved in inclusion formation, as supported by the results of **Figure 9.20**. In this case, three different inclusions were found in one similar sample of HS-CI in **Figure 9.15b**. These chemical compositions should be thermodynamically chronological (A1: Mg-O system first – then B2: Mg-S format – and eventually C3: Mg-Si) yet detected as a coexistence.

The findings of this chapter also substantiate that there is no direct relationship between the composition or morphology of inclusions and the growth of nodular graphite. In addition to the case explored earlier, despite being revealed as a nucleus in **Figure 9.9a**, the utilization of SiC as an in-mold treatment agent showed no nodularization effect, which is analogous to the direct involvement of MgO. In the case of morphology, as highlighted in **Figure 9.21**, despite the similar nucleus shape as a predominant Al-O system was established, the associated graphite developed toward a different structure (coexists in one similar HS-CI in **Figure 9.15b**). Accordingly, it is suggested that the (local) liquid composition plays a pivotal role in the nucleation and growth of nodular graphite, which might be associated with the availability of dissolved magnesium, sulfur, and oxygen.

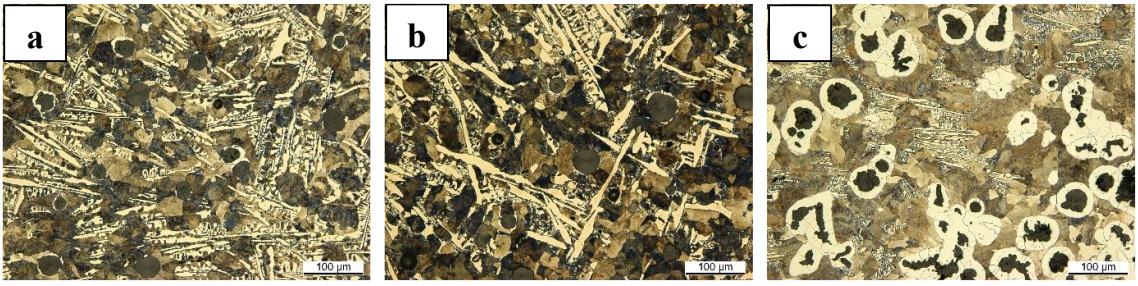

Figure 9.22. Matrix configuration in Nital-etched conditions of AS-CI with 5 g of (**a**) Mg-AlSn, (**b**) NiMg15, and (**c**) FeSi-CeLa as treatment agents.

The role of magnesium in promoting the nucleation and growth of nodular graphite can also be observed as other Mg-bearing materials have been utilized. As indicated in **Figure 9.16a** and **Figure 9.16b**, where Mg-AlSn and NiMg15 were employed, respectively, nodular graphite was established despite having a white iron matrix structure, as documented in **Figure 9.22 a** and **b**. This carbide formation could be associated with Mg-overtreatment, as demonstrated in [277]. In this case, it is induced by either excessive addition or more efficient dissolution than FeSiMg6, as delineated in [278]. However, magnesium is not the only

alternative to produce nodular graphite, as revealed in **Figure 9.16c**. In this case, FeSi-CeLa (ca. 17 wt.% Ce and 14 wt.% La) was utilized as an in-mold treatment agent without magnesium. Compared with Mg-AlSn and NiMg15, the cast iron matrix also indicates a carbide system, as depicted in **Figure 9.22c**. These instances are congruently related to the possible excessive addition of Ce and La, which is also reported to be responsible for the observed deteriorated graphite structures, as provided in [279].

Calcium is also assumed as an element that promotes the nodularization of graphite in cast iron. Compared with magnesium, calcium has a high affinity for oxygen and sulfur and is thus commonly employed in deep desulfurization in the iron industry [280, 281, 282]. The solubilities of both magnesium and calcium in iron at 1600°C are significantly low, ranging from 0.023 to 0.059 wt.% [121, 122] and 0.024 to 0.046 wt.% [283, 284, 285], respectively. However, despite the resemblance in characteristics, no convincing nodularization effect can be observed, as shown in **Figure 9.17**, including by employing Ca and CaC_2 in a similar trial setup (melting at 1500°C and an in-mold treatment).

In fact, there are only two published reports related to the nodularization process of SGI using CaSi [286, 287] and one for Ca [288]. Based on the reported utilization of CaSi, a certain amount of Mg was measured in the CaSi employed in the studies; thus, distinguishing the effects of Mg or Ca given the total amount of approximately 5 to 10 wt.% introduced into the molten iron is unclear. Considering only the Ca-metal reported in [288], the expected quality of graphite nodularity was proven unattained. Moreover, the charge materials used during the investigation were pure Fe, metallic Si, and graphite, thus questioning the role of Ca since a similar approach was able to produce a treatment-free nodular graphite structure in cast iron [289], which will be explored in the next section.

9.3.3. Theoretical Dynamics in the Nucleation and Growth of Nodular Graphites

Based on the current results, two prerequisites are needed to produce commercial SGI: a low concentration of sulfur and oxygen coupled with the addition of magnesium or cerium-lanthanum. Since Mg, Ce, and La react with sulfur and oxygen during the treatment process, it is relatively easy to conclude that these metals act only as scavengers of surface-active elements, as proposed by Jung et al. [290]. In this context, the results of the present chapter suggest that they might not be utterly true since the use of Ca-bearing materials did not result in positive nodularity. Accordingly, a direct role of Mg, Ce, and La should also be expected during the growth of nodular graphite. Notably, heterogeneous nucleation cannot be perceived as indirect, as once proven by Dhindaw and Verhoeven [68] in the vacuum melting of synthetic Fe-C-Si alloys. Based on their report, nodular graphite can form at a specific cooling rate if high-purity iron is used, but it is not the case if ultrahigh-purity iron is utilized.

Consequently, it is convincing that the cause of nodular graphite establishment in synthetic Fe-C-Si alloys is, to a certain extent, comparable with that in commercial SGI, as revealed in the present chapter, particularly in explaining the role of Mg, Ce, and La. As key findings provided in [68, 289, 290], a high cooling rate and superheating are necessary to ensure the formation of nodular graphite in a carbide-containing cast iron matrix. These two factors are also known in foundry practice to be correlated with high undercooling, thus increasing the

chill tendency, carbide formation, and supersaturation degree of molten iron [291, 292]. This factor of supersaturation as a determining factor in the growth of nodular graphite, as reported in [293], could be the intersection between synthetic and commercial SGI. As indicated in **Figure 9.22**, spheroidal graphite within a carbide-containing matrix associated with an excessive introduction of Mg, Ce, and La is also identified. It is correlated with the characteristics of those elements as carbide former, and their addition increases the degree of undercooling [277, 294], contrasting with Ca, which tends to act as a graphitizer [288]. Accordingly, the supplementary role of Mg, Ca, and La in commercial SGI might be associated with increasing supersaturation coupled with low sulfur and oxygen content.

Despite the rational resonance between both phenomena in synthetic and commercial SGI regarding supersaturation, further empirical investigations are necessary to describe precisely the mechanism of this complex and dynamic interaction. The hypothetical explanation might be related to the carbon solubility and activity since those factors are correlated with the dissolved sulfur and oxygen concentrations [131, 295]. Furthermore, since carbide formation is involved, it is also conventionally known that the carbide stabilizers reduce the activity of carbon [296] as well as carbon equivalent (CE) [117] in molten iron, which might not be the case for Mg, Ce, and La. Specifically for Mg, the shift in the CE value and saturation degree is substantiated by a review of several experimental results provided in [127], which suggests that adding Mg during the treatment of molten iron displaces the liquidus line to the left. This shift would change the measured liquidus temperature, which is typically associated with an increasing CE. Since the solubility of Mg in austenite is negligible, the lowering liquidus temperature at the hypoeutectic composition indicates that the bulk of molten cast iron solidifies in supercooled circumstances, known as constitutional undercooling.

9.4. Summary of Relation between Magnesium and Nodular Graphite

Based on the results revealed in the present chapter, the following findings could be drawn related to the nucleation and growth of nodular graphite in cast iron:

(1) The alternative experimental approaches employed in this chapter are reliable for observing the nonmetallic nuclei of the graphite structure and effectively observing the established graphite structure related to variations in the treatment agents.
(2) The graphite structure nucleates heterogeneously, but no such definite system of nonmetallic structure is required. In commercial SGI, the nucleus can be an oxy-sulfide, a carbo-nitride, or a complex compound between the two.
(3) There is no direct correlation between the chemical composition or morphology of nonmetallic inclusions and the growth of the graphite structure. It is also indicated that graphite development is highly dependent on the chemical composition of molten iron, especially the establishment of any local segregation.
(4) Low sulfur and oxygen concentrations are undoubtedly necessary, but the involvement of magnesium is not always obligatory in establishing nodular graphite. Nonetheless, it does not mean and is proven that the role of magnesium is not limited to being only a scavenger of those surface-active elements.
(5) Another possible pivotal role of magnesium, including cerium and lanthanum, could be related to its distinct behavior as a carbide stabilizer for enhancing supersaturation in molten iron, thus increasing the driving force of nodular graphite formation.

PART V
Denouement

Chapter 10
Conclusion and Outlook

10.1. Conclusion

Based on the observation, investigation, and experimental outcomes, in addition to supplementary thermodynamic, ecological, and economic calculations provided in previous chapters in this dissertation, the following conclusions could be extracted:

(1) Rapid dissolution, deoxidation, and desulfurization are expected during the high-temperature interactions between magnesium and molten cast iron. Those sequential physical and chemical interactions involve the establishment of liquid magnesium and are detected to be complete before a significant boiling process begins. Further heat transfer supplemented by exothermic reactions (MgO and MgS formations) will induce a superheating condition at the interface as the reaction progresses. Depending on the superheating degree, a distinct boiling mechanism is anticipated, resulting in further physical-chemical reaction sequences or liquid fragmentation.

(2) Based on the further understanding of the interaction between magnesium and molten cast iron during the desulfurization process, the applicability of lime as its sustainable substitute was evaluated and proven to be a reliable alternative. The interplay between the low level of dissolved oxygen and the existence of liquid slag proportion is detrimental to sustaining the lime-based desulfurization process. In this case, aluminum, silicon, and iron are detected to be involved in the sequential approach by establishing a specific liquid slag configuration followed by the development of solid precipitations that eventually retard the desulfurization operation. However, despite these limitations, the concept can be industrially implemented. It is supported by technical performance in delivering comparable quality levels of CGI-based products and advantages from prospective economic and ecological perspectives.

(3) According to the possible influence of magnesium on the behavior of dissolved carbon in molten cast iron, the irreplaceable role of magnesium was explored, especially during the heterogeneous nucleation of nodular graphite. It is confirmed that low oxygen and sulfur concentration levels coupled with adequate dissolved magnesium content are required to ensure the nucleation and growth of nodular graphite. The argument is amplified by the observation of deteriorated graphite structure during the recycling of ductile iron. Despite still possessing nucleation potential due to the low dissolution rate of nodular graphite, no favorable structure could be detected due to magnesium fading. On the other hand, further results indicate that the role of magnesium is not limited to the scavenger of surface-active elements since the use of calcium could not establish ductile iron. Therefore, it is suggested that magnesium has a critical role in influencing solidification behavior by enhancing carbon supersaturation.

10.2. Outlook

Considering the unavoidable limitations in the boundary of all considered approaches in this dissertation, including analysis method availability and wide-spectrum coverage of

materials involved in the production of ductile cast iron, the following studies could be intriguing to explore in the near future:

(1) The high-temperature interaction between various magnesium-bearing materials and molten cast iron could be enriching since it should provide additional insight into the complete reaction mechanism involving magnesium introduction. By extending the possibility to the inoculation process, the interaction mechanism of several inoculation agents could also be explored to carefully describe their dissolution and effect in the molten cast iron as well as their interplay with magnesium-containing nodulizer.

(2) The utilization of lime during the desulfurization process of molten cast iron might circumstantially already be industrially practicable. Nonetheless, the post-effect of lime introduction during the desulfurization to the nucleation process at further process chain during the CGI and SGI manufacturing process is relatively wide open and needs to be explored. As revealed in this study, Ca-containing nonmetallic inclusions could act as effective nucleation sites for nodular graphite and should be a starting argument for further comprehensive research.

(3) Considering the apparent change in graphite precipitation and matrix solidification behavior related to the dissolved magnesium content, further exploration is needed. The primary concentration could be aimed at the role of magnesium on the carbon equivalent and supersaturation since no empirical evidence comprising a reliable interaction factor currently arrives at a consensus.

Bibliography

[1] The European Foundry Association, "The European Foundry Industry 2021," CAEF, Düsseldorf, 2022.

[2] World Foundry Organisation, "Census of World Casting Production in Modern Casting," World Foundry Organisation, United Kingdom, 2017.

[3] Umweltbundesamt, "Emissionen aus Betrieben der Metallindustrie," The Federal Republic of Germany - Ministry for the Environment, Nature Conservation, Nuclear Safety and Consumer Protection (BMUV), 08 02 2023. [Online]. Available: https://www.umweltbundesamt.de/daten/umwelt-wirtschaft/industrie/emissionen-aus-betrieben-der-metallindustrie#umweltbelastende-emissionen-aus-der-metallindustrie-. [Accessed 08 09 2023].

[4] A. Trianni, E. Cagno, P. Thollander and S. Backlund, "Barriers to Industrial Energy Efficiency in Foundries: A European Comparison," *Journal of Cleaner Production,* vol. 40, pp. 161-176, 2013.

[5] Y. Zhu, G. A. Keoleian and D. R. Cooper, "A Parametric Life Cycle Assessment Model for Ductile Cast Iron Components," *Resources, Conservation, and Recycling,* vol. 189, p. 106729, 2023.

[6] K. Salonitis, M. Jolly, E. Pagone and M. Papanikolaou, "Life-Cycle and Energy Assessment of Automotive Component Manufacturing: The Dilemma between Aluminum and Cast Iron," *Energies,* vol. 12, no. 13, p. 2557, 2019.

[7] K. Jhaveri, G. M. Lewis, J. L. Sullivan and G. A. Keoleoan, "Life Cycle Assessment of Thin-Wall Ductile Cast Iron for Automotive Lightweighting Applications," *Sustainable Materials and Technologies,* vol. 15, pp. 1-8, 2018.

[8] A. Abdelshafy, D. Franzen, A. Mohaupt, J. Schüssler, A. Bührig-Polaczek and G. Walther, "A Feasibility Study to Minimize the Carbon Footprint of Cast Iron Production while Maintaining the Technical Requirements," *Journal of Sustainable Metallurgy,* vol. 9, pp. 249-265, 2023.

[9] J. Mitterpach, E. Hroncova, J. Ladomersky and K. Balco, "Environmental Evaluation of Grey Cast Iron via Life Cycle Assessment," *Journal of Cleaner Production,* vol. 148, pp. 324-335, 2017.

[10] L. Finkewirth, A. Abdelshafy and G. Walther, "A Comparative Environmental Assessment of the Cast Iron and Steel Melting Technologies in Germany," *Energy Proceedings,* vol. 29, pp. 1-9, 2022.

[11] O. Yilmaz, A. Anctil and T. Karanfil, "LCA as a Decision Support Tool for Evaluation of Best Available Techniques (BATs) for Cleaner Production of Iron Casting," *Journal of Cleaner Production,* vol. 105, pp. 337-347, 2015.

[12] R. M. Torielli, F. S. Cannon, R. C. Voigt, T. J. Considine, J. C. Furness, J. T. Fox, J. E. Goundzwaard and H. Huang, "The Environmental Performance and Cost of

Innovative Technologies for Ductile Cast Iron Foundry Production," *International Journal of Metal Casting,* vol. 8, no. 1, pp. 37-48, 2014.

[13] D. Joshi, Y. Modi and B. Ravi, "Evaluating Environmental Impacts of Sand Cast Products using Life Cycle Assessment," *ICORD11: Proceedings of the 3rd International Conference on Research into Design Engineering,* pp. 551-558, 2011.

[14] F. N. H. Scharma, E. M. Beunder, B. van den Berg, Y. Yang and R. Boom, "Sulphur Removal in Ironmaking and Oxygen Steelmaking," *Iron & Steelmaking,* vol. 44, no. 5, pp. 333-343, 2017.

[15] T. Emi, "Steelmaking Technology for the Last 100 Years: Toward Highly Efficient Mass Production Systems for High Quality Steels," *ISIJ International,* vol. 55, no. 1, pp. 36-66, 2015.

[16] C. Adey, "Verfahren zur Herstellung von Grauguss höherer Festigkeit". Germany Patent DRP Aktz. G98 710 VI/18b, 18 9 1939.

[17] H. Morrogh, "Nodular Cast Iron and the Manufacture Thereof". United States Patent US2488511A, 15 11 1949.

[18] K. D. Millis, A. P. Gagnebin and N. B. Pilling, "Cast Ferrous Alloy". United States Patent US2485760A, 25 10 1949.

[19] S. Ehrenberger, "Carbon Footprint of Magnesium Production and its Use in Transport Applications," German Aerospace Center e.V., Stuttgart, Germany, 2020.

[20] F. Cherubini, M. Raugei and S. Ulgiati, "LCA of Magnesium Production Technological Overview and Worldwide Estimation of Environmental Burdens," *Resources, Conservation and Recycling,* vol. 52, pp. 1093-1100, 2008.

[21] M. Schmitz, "Rohstoffrisikobewertung - Magnesium (Metall)," DERA Rohstoffinformationen, Berlin, 2019.

[22] R. Deike, I. Adhiwiguna and M. Walz, "Die Substitution von Magnesium zur Entschwefelung von Gusseisen: Ein Weg globale Abhängigkeiten in der Eisengussindustrie zu verringern," *Gießerei Rundschau,* vol. 70, no. 4, pp. 12-18, 2023.

[23] G. A. Irons and R. I. L. Guthrie, "The Kinetics of Magnesium Vapour Dissolution into Pig Iron," *Canadian Metallurgical Quarterly,* vol. 15, no. 4, pp. 325-332, 1976.

[24] G. A. Irons and R. I. L. Guthrie, "The Kinetics of Molten Iron Desulfurization using Magnesium Vapor," *Metallurgical Transactions B,* vol. 12B, pp. 755-767, 1981.

[25] G. A. Irons and R. I. L. Guthrie, "The Role of an Interfacial Product Layer in Magnesium Desulphurization of Molten Iron," *Canadian Metallurgical Quarterly,* vol. 21, no. 4, pp. 429-443, 1982.

[26] D. Lindström, P. Nortier and D. Sichen, "Functions of Mg and Mg-CaO Mixtures in Hot Metal Desulfurization," *Steel Research International,* vol. 85, no. 1, pp. 76-88, 2014.

[27] J. Yang, K. Okumura, M. Kuwabara and M. Sano, "Desulfurization of Molten Iron with Magnesium Vapor Produced In-Situ by Aluminothermic Reduction of Magnesium Oxide," *ISIJ International,* vol. 41, no. 9, pp. 965-973, 2001.

[28] J. Yang, K. Okumura, M. Kuwabara and M. Sano, "Behaviour of Magnesium in the Desulfurization Process of Molten Iron with Magnesium Vapor Produced In-situ by

Aluminothermic Reduction of Magnesium Oxide," *ISIJ International,* vol. 42, no. 7, pp. 685-693, 2002.

[29] J. Yang, S. Ozaki, R. Kakimoto, K. Okumura, M. Kuwabara and M. Sano, "Desulfurization of Molten Iron with Magnesium Vapor Produced In-Situ by Carbothermic Reduction of Magnesium Oxide," *ISIJ International,* vol. 41, no. 9, pp. 945-954, 2001.

[30] J.-m. Su, Z.-h. Dou, T.-a. Zhang and Y. Liu, "Effect of Magnesium Injection Process on Hot Metal Desulfurization," *Journal of Iron and Steel Research International,* vol. 27, pp. 1391-1399, 2020.

[31] J.-m. Su, Z.-h. Dou, T.-a. Zhang and Y. Liu, "Utilization Rate of Magnesium in Hot Metal Desulfurization by Magnesium Vapor Injection," *ISIJ International,* vol. 60, no. 5, pp. 915-921, 2020.

[32] J. Yang, M. Kuwabara, T. Sakai, N. Uchida, Z. Liu and M. Sano, "Simultaneous Desulfurization and Deoxidation of Molten Steel with in Situ Produced Magnesium Vapor," *ISIJ International,* vol. 47, no. 3, pp. 418-426, 2007.

[33] H. Sun, Y.-C. Liu and M.-J. Lu, "Behaviour of Ar-1%Mg Bubbles in Desulfurization of Hot Metal by Magnesium Injection," *Steel Research International,* vol. 80, pp. 209-217, 2009.

[34] R. Deike, B. Smaha and S. Maqbool, "Was macht Magnesium bei der Magnesiumbehandlung?," *Giesserei,* vol. 108, no. 9, pp. 33-39, 2021.

[35] H.-J. Visser and R. Boom, "Advanced Process Modelling of Hot Metal Desulphurization by Injection of Mg and CaO," *ISIJ International,* vol. 46, no. 12, pp. 1771-1777, 2006.

[36] J. Yang, M. Kuwabara, T. Teshigawara and M. Sano, "Mechanism of Resulfurization in Magnesium Desulfurization Process of Molten Iron," *ISIJ International,* vol. 45, no. 11, pp. 1607-1615, 2005.

[37] E. Moosavi-Khoonsari, M.-A. Van Ende and I.-H. Jung, "Kinetic Simulation of Hot Metal Pretreatment: Desulfurization using Powder Injection," *Metallurgical and Materials Transactions B,* vol. 53, pp. 981-998, 2022.

[38] I. A. Manachin and A. F. Shevchenko, "Desulfurization of Hot Metal by the Injection of High-Quality Lime Powder," *Steel in Translation,* vol. 48, no. 8, pp. 204-522, 2018.

[39] F. Oeters, P. Strohmenger and W. Pluschkell, "Kinetik der Entschwefelung von Roheisenschmelzen mit Kalk und Erdgas," *Arch. Eisenhüttenwes.,* vol. 10, pp. 727-733, 1973.

[40] Y. Kawai, K. Mori and Y. San-Nomiya, "Fundamental Study on the Rate of Desulphurization of Pig Iron by Solid Lime," *Tetsu-to-Hagane,* vol. 61, no. 1, pp. 29-35, 1975.

[41] S. Lee and D. J. Min, "A Study on the Formation Mechanism of the Interfacial Layer between Solid CaO and Molten Iron Alloys," *Metals and Materials International,* vol. 25, pp. 248-256, 2019.

[42] D. C. Boyd, W. C. Phelps and M. T. Hepworth, "Desulfurizing Iron-Carbon Melts with Lime under Reduced Pressures," *Metallurgical Transactions B,* vol. 6, pp. 87-93, 1975.

[43] R. J. Fruehan, "Desulfurization of Liquid Steel Containing Aluminum or Silicon with Lime," *Metallurgical Transactions B,* vol. 9B, pp. 287-292, 1978.

[44] D. Lindström and D. Sichen, "Study on Desulfurization Abilities of Some Commonly Used Desulfurization Agents," *Steel Research International,* vol. 86, no. 1, pp. 73-83, 2015.

[45] J. C. Niedringhaus and R. J. Fruehan, "Reaction Mechanism for the CaO-Al and CaO-CaF_2 Desulfurization of Carbon-Saturated Iron," *Metallurgical Transactions B,* vol. 19B, pp. 261-268, 1988.

[46] E. Oktay and R. J. Fruehan, "On the Hot Metal Desulfurization," *Steel Research,* vol. 66, no. 3, pp. 93-95, 1995.

[47] Y. Nakai, N. Kikuchi, Y. Miki, Y. Kishimoto, T. Isawa and T. Kawashima, "Hot Metal Desulfurization Behavior with Dolomite Flux," *ISIJ International,* vol. 53, no. 6, pp. 1020-1027, 2013.

[48] T. Mitsuo, T. Shoji, Y. Hatta, H. Ono, H. Mori and T. Kai, "Improvement of Desulfurization by Addition of Aluminium to Hot Metal in the Lime Injection Process," *Transactions of the Japan Institute of Metals,* vol. 23, no. 12, pp. 768-779, 1982.

[49] R. Inoue and H. Suito, "Calcium Desulfurization Equilibrium in Liquid Iron," *Steel Research,* vol. 65, no. 10, pp. 403-409, 1994.

[50] M. Vargas-Ramirez, A. Romero-Serrano, R. Morales, M. Angeles-Hernandez, F. Chaves-Alcala and J. Castro-Arellano, "Hot Metal Pretreatment by Powder Injection of Lime-based Reagents," *Steel Research,* vol. 72, no. 5, pp. 173-181, 2001.

[51] W. H. Van Niekerk and R. J. Dippenaar, "Thermodynamic Aspects of Na_2O and CaF_2 Containing Lime-based Slags used for the Desulfurization of Hot Metal," *ISIJ International,* vol. 33, no. 1, pp. 59-65, 1993.

[52] J.-Y. Choi, D.-J. Kim and H.-G. Lee, "Reaction Kinetics of Desulfurization of Molten Pig Iron using CaO-SiO_2-Al_2O_3-Na_2O Slag System," *ISIJ International,* vol. 41, no. 3, pp. 216-224, 2001.

[53] K. Takahashi, K. Utagawa, H. Shibata, S.-y. Kitamura, N. Kikuchi and Y. Kishimoto, "Influence of Solid CaO and Liquid Slag on Hot Metal Desulfurization," *ISIJ International,* vol. 52, no. 1, pp. 10-17, 2012.

[54] T. Tanaka, Y. Ogiso, M. Ueda and J. Lee, "Trial on the Application of Capillary Phenomenon of Solid CaO to Desulfurization of Liquid Fe," *ISIJ International,* vol. 50, no. 8, pp. 1071-1077, 2010.

[55] M. Volmer and A. Weber, "Keimbildung in übersättigten Gebilden," *Zeitschrift für physikalische Chemie,* vol. 119, no. 1, pp. 277-301, 1926.

[56] M. Volmer, "Über Keimbildung und Keimwirkung als spezialfälle der heterogenen Katalyse," *Zeitschrift für Elektrochemie und angewandte physikalische Chemie,* vol. 35, no. 9, pp. 555-561, 1929.

[57] J. H. Hollomon and D. Turnbull, "Nucleation," *Progress in Metal Physics,* vol. 4, pp. 333-388, 1953.

[58] D. M. Stefanescu, "Cast Iron," in *ASM Handbook Volume 15: Casting*, United States, ASM International, 1988, pp. 168-181.

[59] I. Riposan, M. Chisamera and S. Stan, "Enhanced Quality in Electric Melt Grey Cast Irons," *ISIJ International,* vol. 53, no. 10, pp. 1683-1695, 2013.

[60] W. Krieger and H. Trenkler, "Die Deutung der Schmelzstrukturen von Eisen-Kohlenstoff- und Eisen-Nickel-Legierungen aus dem Viskositätsverhalten," *Archiv für das Eisenhüttenwesen,* vol. 42, no. 3, pp. 175-184, 1971.

[61] C. R. Loper Jr, S. Shirvani and T. H. Witter, "Graphite Inoculants for Gray Cast Iron," *MRS Online Proceedings Library,* vol. 34, pp. 89-98, 1984.

[62] J. M. Frost and D. M. Stefanescu, "Melt Quality Assessment of SG Iron through Computer-Aided Cooling Curve Analysis," *AFS Transactions,* vol. 100, pp. 189-199, 1992.

[63] D. M. Stefanescu, G. Alonso, P. Larranaga and R. Suarez, "On the Stable Eutectic Solidification of Iron-Carbon-Silicon Alloys," *Acta Materialia,* vol. 103, pp. 103-114, 2016.

[64] H. Fredriksson, "Inoculation of Iron-base Alloys," *Materials Science and Engineering,* vol. 65, pp. 137-144, 1984.

[65] T. Semleit, I. Adhiwiguna, J. Wijaya and R. Deike, "Investigation of Silicon Carbide Dissolution Behavior in Molten Cast Iron under Specific Consideration of the Formation of Reaction Layers," *Giesserei Special,* vol. 1, pp. 46-53, 2021.

[66] T. Hara, T. Kitagawa, K. Kuroki, S. Saikawa, K. Terayama, S. Ikeno and K. Matsuda, "Morphologies of Some Graphites in Ductile Cast Irons," *Materials Transactions,* vol. 55, no. 9, pp. 1500-1505, 2014.

[67] B. Dhindaw and J. D. Verhoeven, "Inverse Chill and Nodular Graphite Formation in Synthetic Cast Irons Melted and Cast under Vacuum," *Transactions of the Japan Institute of Metals,* vol. 24, no. 2, pp. 71-80, 1983.

[68] B. Dhindaw and J. D. Verhoeven, "Nodular Graphite Formation in Vacuum Melted High Purity Fe-C-Si Alloys," *Metallurgical Transactions A,* vol. 11, pp. 1049-1057, 1980.

[69] S. Yamamoto, B. Chang, Y. Kawano, R. Ozaki and Y. Murakami, "Mechanism of Nodularization of Graphite in Cast Irons Treated with Magnesium," *Metal Science,* vol. 12, no. 5, pp. 239-246, 1978.

[70] H. Itofuji, "Study of Voids in Chilled Samples of Magnesium Treated Irons," *International Journal of Cast Metals Research,* vol. 17, no. 4, pp. 220-228, 2004.

[71] G. Alonso, P. Larranaga, E. De la Fuente, D. M. Stefanescu, A. Natxiondo and R. Suarez, "Kinetic of Nucleation and Growth of Graphite at Different Stages of Solidification for Spheroidal Graphite Iron," *International Journal of Metal Casting,* vol. 11, no. 1, pp. 14-26, 2017.

[72] M. H. Jacobs, T. J. Law, D. A. Melford and M. J. Stowell, "Basic Process Controlling the Nucleation of Graphite Nodules in Chill Casting Iron," *Metals Technology,* vol. 1, no. 1, pp. 490-500, 1974.

[73] B. Francis, "Heterogeneous Nuclei and Graphite Chemistry in Flake and Nodular Cast Irons," *Metallurgical Transactions A,* vol. 10, pp. 21-31, 1979.

[74] H. Nakae and Y. Igarashi, "Influence of Sulfur on Heterogeneous Nucleus of Spheroidal Graphite," *Materials Transactions,* vol. 43, no. 11, pp. 2826-2831, 2002.

[75] J. Tartera, N. Llorca-Lsern, M. Marsal, M. Puig and M. Espanol, "Confocal Microscope Observation of Graphite Morphology," *International Journal of Cast Metals Research,* vol. 11, no. 6, pp. 459-464, 1999.

[76] D. M. Stefanescu, A. Crisan, G. Alonso, P. Larranaga and R. Suarez, "Growth of Spheroidal Graphite on Nitride Nuclei: Disregistry and Crystallinity During Early Growth," *Metallurgical and Materials Transactions A,* vol. 50, pp. 1763-1772, 2019.

[77] M. M. Celis, B. Domenges, E. Hug and J. Lacaze, "Analysis of Nuclei in a Heavy-Section Nodular Iron Casting," *Material Science Forum,* vol. 925, pp. 173-180, 2018.

[78] M. H. Jacobs, T. J. Law, D. A. Melford and M. J. Stowell, "Identification of Heterogeneous Nuclei for Graphite Spheroids in Chill-Cast Iron," *Metal Technology,* pp. 98-107, 1976.

[79] T. Skaland, Ø. Grong and T. Grong, "A Model for the Graphite Formation in Ductile Cast Iron: Part I. Inoculation Mechanisms," *Metallurgical Transactions A,* vol. 24, pp. 2321-2345, 1993.

[80] V. Cochard, R. A. Harding, J. Campbell and R. Herold, "Inoculation of Spheroidal Graphite Cast Iron," *Advanced Materials Research,* Vols. 4-5, pp. 277-284, 1997.

[81] Y. Igarashi and S. Okada, "Observation and Analysis of the Nucleus of Spheroidal Graphite in Magnesium-treated Ductile Iron," *International Journal of Cast Metals Research,* vol. 11, no. 2, pp. 83-88, 1998.

[82] J. Qing, S. Lekakh, M. Xu and D. Field, "Formation of Complex Nuclei in Graphite Nodules of Cast Iron," *Carbon,* vol. 171, pp. 276-288, 2021.

[83] J. K. Solberg and M. I. Onsøien, "Nucleus for Heterogeneous Formation of Graphite Spheroids in Ductile Cast Iron," *Material Science and Technology,* vol. 17, no. 10, pp. 1238-12242, 2001.

[84] L. Laffont, A. Pugliara, T. Hungria and J. Lacaze, "STEM Observation of a Multiphase Nucleus of Spheroidal Graphite," *Journal of Materials Research and Technology,* vol. 9, no. 3, pp. 4665-4671, 2020.

[85] L. Michels, B. Cygan, M. Pawlyta, J. Jezierski, A. Götz and J. Akola, "Graphite Nucleation on (Al,Si,Mg)-Nitrides: Elucidating the Chemical Interactions and Turbostratic Structures in Spheroidal Graphite Cast Irons," *Carbon,* p. 118484, 2024.

[86] G. Alonso, D. M. Stefanescu, P. Larranaga, E. De la Fuente, E. Aguado and R. Suarez, "Solidification of Superfine Graphite Iron Revealed by Interrupted Solidification Experiments," *International Journal of Cast Metals Research,* pp. 1-8, 2016.

[87] D. M. Stefanescu, G. Alonso, P. Larranaga, E. De la Fuente and R. Suarez, "Reexamination of Crystal Growth Theory of Graphite in Iron-Carbon Alloys," *Acta Materialia,* vol. 139, pp. 109-121, 2017.

[88] L. Michels, A. J. F. Pires, C. A. S. Ribeiro, B. Kroka, E. G. Hoel, E. Ott and C. Hartung, "Effect of Holding Time on Populations of Microparticles in Spheroidal Graphite Irons," *Metallurgical and Materials Transactions B,* vol. 53, pp. 836-847, 2022.

[89] S. J. Splinter, N. S. McIntyre, W. N. Lennard, K. Griffiths and G. Palumbo, "An AES and XPS Study on the Initial Oxidation of Polycrystalline Magnesium with Water Vapour at Room Temperature," *Surface Science,* vol. 292, pp. 130-144, 1993.

[90] M. S. Cohen, "Oxidation of Evaporated Magnesium Films," *Acta Metallurgica,* vol. 8, pp. 356-361, 1960.

[91] Y. Wang, M. Li, Y. Yang, X. Zhao, E. Ma and Z. Shan, "In-situ Surface Transformation of Magnesium to Protect Against Oxidation at Elevated Temperature," *Journal of Materials Science & Technology,* vol. 44, pp. 48-53, 2020.

[92] E. A. Gulbransen, "The Oxidation and Evaporation of Magnesium at Temperatures from 400° to 500°C," *Transactions of the Electrochemical Society,* vol. 87, no. 1, pp. 589-599, 1945.

[93] T.-S. Shih, J.-B. Liu and P.-S. Wei, "Oxide Films on Magnesium and Magnesium Alloys," *Materials Chemistry and Physics,* vol. 104, pp. 497-504, 2007.

[94] N. B. Pilling and R. E. Bedworth, "The Oxidation of Metals at High Temperatures," *Journal of the Institute of Metals,* vol. 29, pp. 529-591, 1923.

[95] Z. Zhang, X. Fu, M. Mao, Q. Yu, S. X. Mao, J. Li and Z. Zhang, "In Situ Observation of Sublimation-Enhanced Magnesium Oxidation at Elevated Temperature," *Nano Research,* vol. 9, no. 9, pp. 2796-2802, 2016.

[96] F. Czerwinski, "The Early Stage Oxidation and Evaporation of Mg-9%Al-1%Zn Alloy," *Corrosion Science,* vol. 46, pp. 377-386, 2004.

[97] A. A. Nayeb-Hashemi, J. B. Clark and L. J. Swartzendruber, "The Fe-Mg (Iron-Magnesium) System," *Bulletin of Alloy Phase Diagrams,* vol. 6, no. 3, pp. 235-238, 1985.

[98] A. Abbud-Madrid, M. C. Branch and J. W. Daily, "Ignition and Combustion of Bulk Titanium and Magnesium at Normal and Reduced Gravity," *Symposium (International) on Combustion,* vol. 26, no. 2, pp. 1929-1936, 1996.

[99] T. Takeno and S. Yuasa, "Ignition of Magnesium and Magnesium-Aluminum Alloy by Impinging Hot-Air Stream," *Combustion Science and Technology,* vol. 21, no. 3, pp. 109-121, 1980.

[100] S. Nukiyama, "The Maximum and Minimum Values of the Heat Q Transmitted from Metal to Boiling Water under Atmospheric Pressure," *International Journal of Heat and Mass Transfer,* vol. 9, no. 12, pp. 1419-1433, 1966.

[101] N. Xiong, Y. Tian, B. Yang, B.-Q. Xu and D.-C. Liu, "Volatilization and Condensation Behaviours of Mg Under Vacuum," *Vacuum,* vol. 156, pp. 463-468, 2018.

[102] A. Simons, I. Bellemans, T. Crivits and K. Verbeken, "Heat Transfer Considerations on the Spontaneous Triggering of Vapor Explosions - A Review," *Metals,* vol. 11, no. 55, pp. 1-36, 2021.

[103] N. Kouraytem, E. Q. Li and S. T. Thoroddsen, "Formation of Microbeads during Vapor Explosions of Field's Metal in Water," *Physical Review E,* vol. 93, p. 063108, 2016.

[104] L. C. Witte, J. E. Cox and J. E. Bouvier, "The Vapor Explosion," *Journal of Metals,* vol. 22, pp. 39-44, 1970.

[105] K. Orths and W. Weis, "Bedeutung and Beeinflussung des Kieselsäuregehaltes von Gußeisen," *Giessereiforschung,* vol. 25, no. 1, pp. 1-10, 1973.

[106] V. A. Grachev, "Thermodynamics and Mechanism of Silicon Reduction by Carbon in a Crucible Reaction," *Oriental Journal of Chemistry,* vol. 32, no. 6, pp. 2929-2937, 2016.

[107] Y. Tanaka, F. Pahlevani, S.-C. Moon, R. Dippenaar and V. Sahajwalla, "In Situ Characterisation of MnS Precipitation in High Carbon Steel," *Scientific Reports,* vol. 9, p. 10096, 2019.

[108] J. Fu, Y. Yu, A. Wang and B. Chen, "Inclusion Modification with Mg Treatment for 35CrNi3MoV Steel," *Journal of Material Science and Technology,* vol. 14, pp. 53-56, 1998.

[109] L. K. Bigelow and M. C. Flemings, "Sulfide Inclusions in Steel," *Metallurgical Transactions B,* vol. 6, pp. 275-283, 1975.

[110] K. Oikawa, H. Ohtani, K. Ishida and T. Nishizawa, "The Control of the Morphology of MnS Inclusions in Steel during Solidification," *ISIJ International,* vol. 35, no. 4, pp. 402-408, 1995.

[111] C. E. Sims and F. B. Dahle, "Effect of Aluminium on the Properties of Medium Carbon Cast Steel," *Transaction American Foundrymen Society,* vol. 46, pp. 65-132, 1938.

[112] B. J. Skinner and F. D. Luce, "Solid Solutions of the Type (Ca, Mg, Mn, Fe)S and Their Use as Geothermometers for the Enstatite Chondrites," *The American Mineralogist,* vol. 56, pp. 1269-1296, 1971.

[113] D. Dilner, "Thermodynamic Description of the Fe-Mn-Ca-Mg-S System," *CALPHAD: Computer Coupling of Phase Diagrams and Thermochemistry,* vol. 53, pp. 55-61, 2016.

[114] K. Orths and W. Weis, "Die Beeinflussung des Kieselsäuregehaltes von Gußeisen durch die Schmelztechnik," *Gießereiforschung,* vol. 25, no. 1, pp. 9-19, 1973.

[115] D. Moszynski, H. J. Grabke and A. Schneider, "Effect of Sulphur on the Formation of Graphite at the Surface of Carburized Iron," *Surface and Interface Analysis,* vol. 34, pp. 380-383, 2002.

[116] F. N. H. Schrama, E. M. Beunder, H.-J. Visser, J. Sietsma, R. Boom and Y. Yang, "The Hampering Effect of Precipitated Carbon on Hot Metal Desulfurization with Magnesium," *Steel Research International,* vol. 91, p. 1900441, 2020.

[117] F. Neumann, H. Schenck and W. Patterson, Einfluss der Eisenbegleiter auf Kohlenstofflöslichkeit, Kohlenstoffaktivität und Sättigungsgrad im Gusseisen, Köln und Opladen: Westdeutscher, 1966.

[118] H. Ohtani and T. Nishizawa, "Calculation of Fe-C-S Ternary Phase Diagram," *Transactions ISIJ,* vol. 26, pp. 655-663, 1986.

[119] V. Sahajwalla and R. Khanna, "Influence of Sulfur on the Solubility of Graphite in Fe-C-S Melts: Optimization of Interaction Parameters," *Acta Materialia,* vol. 50, pp. 663-671, 2022.

[120] S. H. Ahn, Y. H. Kim, J.-P. Shin and Y. E. Lee, "Thermodynamic Assessment of Liquid Fe-Si-C System by Unified Interaction Parameter Model," *ISIJ International,* vol. 54, no. 4, pp. 750-755, 2014.

[121] X. Zhang, Q. Han and D. Chen, "Dissolution Equilibrium of Magnesium Vapor in Liquid Iron," *Metallurgical Transactions B,* vol. 22B, pp. 918-921, 1991.

[122] G. G. Mikhailov, O. V. Samoilova, L. A. Makrovets and L. A. Smirnov, "Thermodynamic Modeling of Isotherms of Oxygen Solubility in Liquid Metal of the Fe-Mg-Al-O System," *Steel in Translation,* vol. 49, no. 8, pp. 522-527, 2019.

[123] P. K. Trojan and R. A. Flinn, "Fundamentals of Magnesium Addition to Ductile Iron," *SAE Transactions,* vol. 73, pp. 265-271, 294, 1965.

[124] E. Scheil, "Bemerkungen zur Schichtkristallbildung," *Zeitschrift für Metallkunde,* vol. 23, pp. 237-239, 1931.

[125] P. K. Basutkar, R. W. Heine and C. R. Loper, "Effect of Magnesium and Cerium Addition on the Fe-C-Si Diagram," *AFS Transaction,* vol. 81, pp. 336-340, 1973.

[126] K. Yamane, H. Yasuda, A. Sugiyama, T. Nagira, M. Yoshiya, K. Morishita, K. Uesugi, A. Takeuchi and Y. Suzuki, "Influence of Mg on Solidification of Hypereutectic Cast Iron: X-ray Radiography Study," *Metallurgical and Materials Transactions A,* vol. 46, pp. 4937-4946, 2015.

[127] D. M. Stefanescu, "Analysis of the Rationale and Accuracy of the Use of Carbon Equivalent and Thermal Analysis in the Quality Control of Cast Iron," *International Journal of Metal Casting,* vol. 16, no. 3, pp. 1057-1078, 2022.

[128] I. B. G. S. Adhiwiguna, G. Karagülmez, O. Keskin and R. Deike, "Investigation on Applicability of Lime as Desulfurization Agent for Molten Cast Iron," *Steel Research International,* p. 2400416, 2024.

[129] Y. Tekneci, M. Walz, O. Keskin, I. Adhiwiguna, B. Vennemann, M. Großarth, R. Deike and D. Algermissen, "Automatisierte Einblasanlage zur kalkbasierten Entschwefelung und Legierungseinstellung von Gusseisen (EKALGU): Abschlussbericht zum r+Impuls-Verbundvorhaben," Fritz Winter Eisengießerei GmbH und Co. KG, Stadtallendorf, 2021.

[130] D. M. Stefanescu, "Thermodynamics Principles as Applied to Cast Iron," in *ASM Handbook Volume 1A Cast Iron Science and Technology*, ASM International, 2017, pp. 31-45.

[131] S. Ban-Ya and S. Matoba, "Activity of Carbon and Oxygen in Liquid Iron," *Tetsu-to-Hagane,* vol. 48, no. 8, pp. 925-932, 1962.

[132] E. T. Turkdogan, L. E. Leake and C. R. Masson, "Thermodynamic of Iron-Carbon Melts," *Acta Metallurgica,* vol. 4, pp. 396-406, 1956.

[133] E. T. Turkdogan and L. J. Martonik, "Sulfur Solubility in Iron-Carbon Melts Coexistent with Solid CaO and CaS," *Transactions ISIJ,* vol. 23, pp. 1038-1044, 1983.

[134] S. S. Shibaev, P. V. Krasovskii and K. V. Grigorovitch, "Solubility of Oxygen in Iron-Silicon Melts in Equilibrium with Silica at 1873K," *ISIJ International,* vol. 45, no. 9, pp. 1243-1247, 2005.

[135] J. W. Matousek, "Oxygen in Molten Iron: Deoxidation with Silicon and Aluminum," *The Minerals, Metals & Materials Society JOM,* vol. 67, no. 5, pp. 1216-1222, 2015.

[136] C. Allertz and D. Sichen, "Sulfide Capacity in Ladle Slag at Steelmaking Temperatures," *Metallurgical and Materials Transaction B,* vol. 46, pp. 2609-2615, 2015.

[137] X. He, S. Ma, L. Wang, H. Dong and K. Chou, "Comparison of Desulfurization Mechanism in Liquid $CaO-SiO_2$ and $MnO-SiO_2$: An ab initio Molecular Dynamic Simulation," *Journal of Alloys and Compounds,* vol. 896, p. 163009, 2022.

[138] M. Hino, S. Kitagawa and S. Ban-Ya, "Sulphide Capacities of $CaO-Al_2O_3-MgO$ and $CaO-Al_2O_3-SiO_2$ Slags," *ISIJ International,* vol. 33, no. 1, pp. 36-42, 1993.

[139] S. Ban-Ya, M. Hobo, T. Kaji, T. Itoh and M. Hino, "Sulphide Capacity and Sulfur Solubility in $CaO-Al_2O_3$ and $CaO-Al_2O_3-CaF_2$ Slags," *ISIJ International,* vol. 44, no. 11, pp. 1810-1816, 2004.

[140] T. Elbel and J. Hampl, "Influence of Al and Ti on Microstructure and Quality of Compacted Graphite Iron Castings," *Metalugija,* vol. 48, no. 4, pp. 243-247, 2009.

[141] I. Adhiwiguna, K. Vellayadevan, Y. Tekneci, M. Walz, D. Algermissen and R. Deike, "Industrial Ecotechnological Assessment of Lime as a Sustainable Substitute for Desulfurization of Cast Iron," *Journal of Sustainable Metallurgy,* vol. 10, no. 2, pp. 797-809, 2024.

[142] J.-C. Wrampelmeyer, S. Dimitrov and D. Janke, "Dephosphorization Equilibria between Pure Molten Iron and CaO-saturated $FeO_n-CaO-SiO_2$ and $FeO_n-CaO-Al_2O_3$ Slags," *Steel Research,* vol. 60, no. 12, pp. 539-549, 1989.

[143] L. Dreval, T. Zienert and O. Fabrichnaya, "Calculated Phase Diagram and Thermodynamic Properties of the $Al_2O_3-Fe_2O_3-FeO$ System," *Journal of Alloys and Compounds,* vol. 657, pp. 192-214, 2016.

[144] D. P. Kalmanovitch and J. Williamson, "Crystallization of Coal Ash Melts," *Mineral Matter and Ash in Coal,* pp. 234-255, 1986.

[145] M. Selleby, "An Assessment of the Ca-Fe-O-Si System," *Metallurgical and Material Transactions B,* vol. 28, pp. 577-596, 1997.

[146] T. Hidayat, D. Shishin, S. A. Decterov and E. Jak, "Critical Thermodynamic Re-evaluation and Re-optimization of the $CaO-FeO-Fe_2O_3-SiO_2$ System," *CALPHAD: Computer Coupling of Phase Diagrams and Thermochemistry,* vol. 56, pp. 58-71, 2017.

[147] C. J. B. Fincham and F. D. Richardson, "The Behaviour of Sulfur in Silicate and Aluminate Melts," *Proceedings of the Royal Society A,* vol. 223, pp. 40-62, 1954.

[148] D.-H. Kim, S.-Y. Won, J.-S. Han, H.-S. Nam and J.-J. Pak, "Thermodynamics of Sulfur in Carbon Saturated Liquid Ferro-alloys Containing Ni, Mo and V at 1873K," *ISIJ International,* vol. 58, no. 3, pp. 408-414, 2018.

[149] P. Waldner and A. D. Pelton, "Thermodynamic Modeling of the Fe-S System," *Journal of Phase Equilibria and Diffusion,* vol. 26, no. 1, pp. 23-38, 2005.

[150] C. Liu and B. Webler, "Evolution of Non-Metallic Inclusion during Heat Treatment," *Metallurgical Research and Technology,* vol. 117, no. 4, p. 408, 2020.

[151] C.-H. Leung and L. H. Van Vlack, "Solubility Limits in Binary (Ca,Mn) Chalcogenides," *Journal of the American Ceramic Society,* vol. 62, no. 11-12, pp. 613-616, 1979.

[152] R. Piao, H.-G. Lee and Y.-B. Kang, "Activity Measurement of the CaS-MnS Sulfide Solid Solution and Thermodynamic Modeling of the CaO-MnO-Al_2O_3-CaS-MnS-Al_2S_3 System," *ISIJ International,* vol. 53, no. 12, pp. 2132-2141, 2013.

[153] H. Ohtani, K. Oikawa and K. Ishida, "Optimization of the Fe-Rich Fe-Mn-S Ternary Phase Diagram," *High Temperature Materials and Processes,* vol. 19, no. 3-4, pp. 197-210, 2000.

[154] D. Dilner, H. Mao and M. Selleby, "Thermodynamic Assessment of the Mn-S and Fe-Mn-S System," *CALPHAD: Computer Coupling of Phase Diagrams and Thermochemistry,* vol. 48, pp. 95-105, 2015.

[155] T. Heumann, "Die Löslichkeit von Eisensulfid in Kalziumsulfid bei der Eutektischen Temperature," *Archiv für das Eisenhüttenwesen,* vol. 15, no. 12, pp. 557-558, 1942.

[156] D. Dilner, L. Kjellqvist and M. Selleby, "Thermodynamic Assessment of the Fe-Ca-S, Fe-Mg-O, and Fe-Mg-S System," *Journal of Phase Equilibria and Diffusion,* vol. 37, no. 3, pp. 277-292, 2016.

[157] K. Ogino, K. Nogi and C. Hosoi, "Surface Tension of Molten Fe-O-S Alloy," *Tetsu-to-Hagane,* vol. 69, no. 16, pp. 1989-1994, 1983.

[158] M. Suzuki, M. Nakamoto, T. Tanaka, Y. Tsukaguchi, K. Mishima and M. Hanao, "Effect of Sulfur in Slag on Dynamic Change Behavior of Liquid Iron/Molten Slag Interfacial Tension," *ISIJ International,* vol. 60, no. 11, pp. 2332-2338, 2020.

[159] T. Tanaka, H. Goto, M. Nakamoto, M. Suzuki, M. Hanao, M. Zeze, H. Yamamura and T. Yoshikawa, "Dynamic Changes in Interfacial Tension between Liquid Fe Alloy and Molten Slag Induced by Chemical Reaction," *ISIJ International,* vol. 56, no. 6, pp. 944-952, 2016.

[160] R. Zhang, Z. Wang, Y. Meng, S. Jiao, J. Jia, Y. Min and C. Liu, "Structural Analysis and Evaluation of Surface Tension of Silicate Melts Containing CaO and Fe_xO," *Chemical Engineering Science,* vol. 245, p. 116870, 2021.

[161] Velco, "Product Innovation: Lime-based Desulfurization in an Iron Foundry," Velco Gesellschaft für Förder-, Spritz- und Silo-Anlagen mbH, 23 02 2023. [Online]. Available: https://www.velco.de/en/news/product-innovation-lime-based-desulfurization-in-an-iron-foundry/. [Accessed 04 07 2023].

[162] DIN EN ISO 14040, *Umweltmanagement - Ökobilanz - Grundsätze und Rahmenbedingungen EN ISO 14040:2006 + A1:2020,* Beuth Verlag GmbH, 2021.

[163] R. Deike, A. Kahrl and A. Brümmer, "Verbundvorhaben SubMag: Entwicklung eines alternativen Entschwefelungsverfahrens in der Gießereiindustrie zur nachhaltigen Substitution von Magnesium - Schlussbericht BMBF-Forschungsvorhaben," Universität Duisburg Essen, Essen, 2016.

[164] "Annex III - Regulation (EU) 2016/1011 of the European Parliament and of the Council on indices used as benchmarks in financial instruments and financial contracts or to measure the performance of investment funds and amending Directives 2008/48/EC and 201," European Union (EU), Brussels, Belgium, 2016.

[165] G. Cusano, M. Rodrigo Gonzalo, M. Farrell, R. Remus, S. Roudier and L. Delgado Sancho, "Best Available Techniques (BAT) Reference Document for the Non-Ferrous Metals Industries. Industrial Emissions Directive 2010/75/EU (Integrated Pollution Prevention and Control)," Publications Office of the European Union, Luxembourg, 2017.

[166] N. Haque and T. Norgate, "Estimation of Greenhouse Gas Emissions from Ferroalloy Production using Life Cycle Assessment with Particular Reference to Australia," *Journal of Cleaner Production,* vol. 39, pp. 220-230, 2013.

[167] L. Holappa, "Towards Sustainability in Ferroalloy Production," *The Journal of The Southern African Institute of Mining and Metallurgy,* vol. 110, pp. 703-710, 2010.

[168] H. Li, W. Zhang, Q. Li and B. Chen, "Updated CO_2 Emission from Mg Production by Pidgeon Process: Implications for Automotive Application Life Cycle," *Resources, Conservation and Recycling,* vol. 100, pp. 41-48, 2015.

[169] S. Ramakrishnan and P. Koltun, "A Comparison of the Greenhouse Impacts of Magnesium Produced by Electrolytic and Pidgeon Processes," in *Essential Readings in Magnesium Technology*, Springer, Cham, 2016, pp. 169-174.

[170] D. D'Errico, G. Perricone and R. Oppio, "A New Integrated Lean Manufacturing Model for Magnesium Products," *The Journal of The Minerals, Metals & Materials Society,* vol. 61, pp. 14-18, 2009.

[171] World Steel Association, "Life Cycle Inventory Study Report 2020," Brussels Belgium, 2021.

[172] S. Grimes, J. Donaldson and G. C. Gomez, "Report on the Environmental Benefits of Recycling," Imperial College London, 2008.

[173] Wirtschaftsvereinigung Stahl, "Fakten zur Stahlindustrie 2022," Wirtschaftsvereinigung Stahl, Berlin, 2022.

[174] M. Allekotte, F. Bergk, K. Biemann, C. Deregowski, W. Knörr, H. Jörg-Althaus, D. Sutter and T. Bergmann, "Ökologische Bewertung von Verkehrsarten," Umweltbundesamt, 2020.

[175] P. Icha, T. Lauf and G. Kuhs, "Entwicklung der spezifischen Kohlendioxid - Emissionen des deutschen Strommix in den Jahren 1990 - 2020," Umweltbundesamt, 2021.

[176] F. Schrocht, I. Kourti, B. M. Scalet, S. Roudier and L. D. Sancho, "Best Available Techniques (BAT) Reference Document for the Production of Cement, Lime and Magnesium Oxide," Publications Office of the European Union, Luxembourg, 2013.

[177] L. Hanle, P. Maldonado, E. Onuma, M. Tichy and H. G. van Oss, "Industrial Processes and Product Use," in *2006 IPCC Guidelines for National Greenhouse Gas Inventories*, Intergovernmental Panel on Climate Change (IPCC), 2006, pp. 3.1-3.110.

[178] M. Stork, W. Meindertsma, M. Overgaag and M. Neelis, "A Competitive and Efficient Lime Industry Cornerstone for a Sustainable Europe," The European Lime Association, 2014.

[179] J. Zhang, C. Liang and J. B. Dunn, "Graphite Flows in the U.S.: Insights into a Key Ingredient of Energy Transition," *Environmental Science and Technology,* vol. 57, pp. 3402-3414, 2023.

[180] D. Surovtseva, E. Crossin, R. Pell and L. Stamford, "Toward a Life Cycle Inventory for Graphite Production," *Journal of Industrial Ecology,* vol. 26, no. 3, pp. 667-1154, 2022.

[181] S. W. Gao, X. Z. Gong, Y. Liu and Q. Q. Zhang, "Energy Consumption and Carbon Emission Analysis of Natural Graphite Anode Material for Lithium Batteries," *Material Science Forum,* vol. 913, pp. 985-990, 2018.

[182] Air Liquide Engineering & Construction, "Technology Handbook," Air Liquide Engineering & Construction, 2021.

[183] J. Gediga, A. Morfino, M. Finkbeiner, M. Schulz and K. Harlow, "Life Cycle Assessment of Zircon Sand," *The International Journal of Life Cycle Assessment,* vol. 24, pp. 1976-1984, 2019.

[184] D. Frulli, D. Heever, F. Ahouanto and C. Parr, "Andalusite Based Raw Materials for Refractory Castable: Properties and Application," Imerys Refractory, 2018.

[185] Ecofys, Fraunhofer Institute and Öko-Institut, "Sector Report for the Aluminium Industry," European Commission, 2009.

[186] G. Saevarsdottir, H. Kvande and B. J. Welch, "Aluminum Production in the Times of Climate Change: The Global Challenge to Reduce the Carbon Footprint and Prevent Carbon Leakage," *The Journal of The Minerals, Metals & Materials Society,* vol. 72, pp. 296-308, 2020.

[187] A. Grbeš, "A Life Cycle Assessment of Silica Sand: Comparing the Beneficiation Processes," *Sustainability,* vol. 8, no. 11, 2016.

[188] D. Fernández-González, J. Prazuch, I. Ruiz-Bustinza, C. González-Gasca, J. Piñuela-Noval and L. F. Verdeja, "Solar Synthesis of Calcium Aluminates," *Solar Energy,* vol. 171, pp. 658-666, 2018.

[189] E. Henry-Lanier, M. Szepizdyn, C. Wöhrmeyer and C. Parr, "Optimisation of the Environmental Footprint of Calcium-Aluminate-Cement Containing Castables," *Refractory Worldforum,* vol. 8, pp. 81-86, 2016.

[190] Fraunhofer Institut for Ceramic Technology, "Energy-efficient and Low in Emissions — Silicon Carbide Recycling with RECOSiC©," Fraunhofer, Dresden, 2023.

[191] P. V. Kumar and G. S. Gupta, "Study of Formation of Silicon Carbide in the Acheson Process," *Steel Research,* vol. 73, no. 2, pp. 31-38, 2016.

[192] US Environmental Protection Agency, "Inventory of U.S. Greenhouse Gas Emissions and Sinks 1990 - 2018," US EPA, 2020.

[193] T. Norgate and N. Haque, "Energy and Greenhouse Gas Impacts of Mining and Mineral Processing Operations," *Journal of Cleaner Production,* vol. 18, no. 3, pp. 266-274, 2010.

[194] M. Tost, B. Bayer, M. Hitch, S. Lutter, P. Moser and S. Feiel, "Metal Mining's Environmental Pressures: A Review and Updated Estimates on CO_2 Emissions, Water Use, and Land Requirements," *Sustainability,* vol. 10, no. 8, 2018.

[195] European IPPC Bureau, "Reference Document on Best Available Techniques in the Ceramic Manufacturing Industry," European Commission, 2007.

[196] K. Juhrich, "CO_2-Emissionsfaktoren für fossile Brennstoffe," Umweltbundesamt, 2022.

[197] "Anhang 3 DepV – Zulässigkeits- und Zuordnungskriterien," in *Verordnung über Deponien und Langzeitlager (Deponieverordnung - DepV)*, Bundesrepublik Deutschland, Bundesrecht, 2009, p. 5.

[198] Technical Service Kuehn GmbH, "Giesserei Technik Kuehn - Product," Technical Service Kuehn GmbH, [Online]. Available: https://tsk-web.eu/en/products/sensors/article-thermoanalysis-sensor-accuvo-cup.html. [Accessed 01 12 2023].

[199] J. G. Humphreys, "Effect of Composition on the Liquidus and Eutectic Temperatures and on the Eutectic Point of Cast Irons," *BCIRA Journal,* vol. 9, no. 5, pp. 609-621, 1961.

[200] R. Sillén, "Finding the True Eutectic Point - An Essential Task for Efficient Process," in *Keith Millis Symposium on Ductile Cast Iron - AFS Ductile Iron Society*, Strongsville Ohio, 2008.

[201] W. Van der Perre, "Thermal Analysis Principles and Applications," [Online]. Available: https://www.heraeus.com/media/media/hen/media_hen/products_hen/iron/thermal_analysis_of_cast_iron.pdf. [Accessed 10 08 2023].

[202] E. Fras and H. Lopez, "Eutectic Cells and Nodule Count - An Index of Molten Iron Quality," *International Journal of Metal Casting,* vol. 10, pp. 35-61, 2010.

[203] W. Oldfield, "The Solidification of Hypo-Eutectic Grey Cast Iron," *BCIRA Journal,* vol. 8, no. 2, pp. 177-192, 1960.

[204] J. S. Park and J. D. Verhoeven, "Transition between Type A Flake, Type D Flake, and Coral Graphite Eutectic Structures in Cast Irons," *Metallurgical and Materials Transaction A,* vol. 27, pp. 2740-2753, 1996.

[205] T. Tsuchiya, K. Sigeno, H. Kawashima and M. Morinaka, "Formation of D-Type Graphite at Center of Cast Iron," *Journal of Japan Foundry Engineering Society,* vol. 88, no. 10, pp. 624-630, 2016.

[206] W. Patterson and D. Ammann, "Solidification of Flake Iron-Graphite Eutectic in Gray Iron," *Giesserei Techn.-Wissen,* vol. 23, p. 1247, 1959.

[207] K. Edalati, F. Akhlaghi and M. Nili-Ahmadabadi, "Influence of SiC and FeSi Addition on the Characteristic of Gray Cast Iron Melts Poured at Different Temperature," *Journal of Materials Processing Technology,* vol. 160, pp. 183-187, 2005.

[208] I. Riposan, M. Chisamera, S. Stan and M. Barstow, "Identifying Chill Tendency of Cast Iron Melts by Thermal Analysis," *International Journal of Cast Metals Research,* vol. 26, no. 3, pp. 152-159, 2013.

[209] T. Kanno, I. Kang, T. Mizuki and H. Nakae, "Effects of S, Mn and RE on Eutectic Temperature of Cast Iron," *Journal of Japan Foundry Engineer Society,* vol. 73, no. 7, pp. 441-446, 2001.

[210] T. Kanno, Y. Iwami and I. Kang, "Prediction of Graphite Nodule Count and Shrinkage Tendency in Ductile Cast Iron with 1 Cup Therma Analysis," *International Journal of Metalcasting,* vol. 11, no. 1, pp. 94-100, 2017.

[211] E. Fras, M. Gorny and H. F. Lopez, "The Transition from Gray to White Cast Iron during Solidification: Part I. Theoretical Background," *Metallurgical and Materials Transactions A,* vol. 36A, pp. 3075-3082, 2005.

[212] I. Riposan, M. Chisamera, S. Stan and D. White, "Chilling Properties of Ba/Ca/Sr Inoculated Grey Cast Irons," *International Journal of Cast Metal Research,* vol. 20, no. 2, pp. 90-07, 2007.

[213] E. Fras, H. F. Lopez, M. Kawalec and M. Gorny, "Role of Alloying Addition in the Solidification Kinetics and Resultant Chilling Tendency and Chill of Cast Iron," *Metals,* vol. 5, pp. 256-288, 2015.

[214] I. V. Balkn and I. Riposan, "Ce-Bearing FeSi Alloy Inoculation of Electrically Melted, Low Sulphur Grey Cast Irons for Thin Wall Castings," *Metals,* vol. 11, pp. 1-16, 2021.

[215] W. Baumgart, J. Cunha and V. Anjos, "Het enten van gietijzer," *Gietwerk Perspectief Magazine,* vol. 5, pp. 5-12, 2010.

[216] A. Regordosa, U. de la Torre, A. Loizaga and J. Sertucha, "Microstructure Changes during Solidification of Cast Irons: Effect of Chemical Composition and Inoculation on Competitive Spheroidal and Compacted Graphite Growth," *International Journal of Metalcasting,* vol. 14, p. 681–688, 2019.

[217] R. D. Bhavsar, D. Hui and R. W. Smith, "Inverse Chill in Cast Iron," *Transactions of the Japan Institute of Metals,* vol. 28, no. 10, pp. 797-807, 1987.

[218] A. Sheikh Abdolhossein and M. Nili-Ahmadabadi, "Fading Investigation in Ductile Cast Iron aided by Cooling Curve Analysis," *International Journal of Cast Metals Research,* vol. 18, no. 5, pp. 295-299, 2005.

[219] J. C. Hernando, B. Domeij, D. Gonzalez, J. M. Amieva and A. Dioszegi, "New Experimental Technique for Nodularity and Mg Fading Control in Compacted Graphite Iron Production on Laboratory Scale," *Metallurgical and Materials Transactions A,* vol. 48, p. 54325441, 2017.

[220] S. Kim, S. L. Cockcroft and A. M. Omran, "Optimization of the Process Parameters affecting the Microstructures and Properties of Compacted Graphite Iron," *Journal of Alloys and Compounds,* vol. 476, pp. 728-732, 2009.

[221] L. Jinhai, Y. Litao, L. Guolu, L. Changqi, L. Yinguo and Y. Zhaoyu, "Influence of Fading on Characteristics of Thermal Analysis Curve of Compacted Graphite Iron," *China Foundry,* vol. 8, no. 3, pp. 295-299, 2011.

[222] D. M. Stefanescu, "Microstructure Evolution during the Liquid/Solid Transformation in Cast Iron," in *ASM Handbook Volume 1A - Cast Iron Science and Technology*, ASM International, 2016, pp. 59-80.

[223] A. Escobar, D. Celentano, M. Cruchaga and B. Schulz, "On the Effect of Pouring Temperature on Spheroidal Graphite Cast Iron Solidification," *Metals,* vol. 5, pp. 628-647, 2015.

[224] M. Chisamera, I. Riposan, S. Stan, D. White and G. Grasmo, "Graphite Nucleation Control in Grey Cast Iron," *International Journal of Cast metals Research,* vol. 21, pp. 39-44, 2008.

[225] M. S. Soinski, A. Jakubus, P. Kordas and K. Skurka, "The Effect of Aluminium on Graphitization of Cast Iron Treated with Cerium Mixture," *Archive of Foundry Engineering,* vol. 14, no. 2, pp. 95-100, 2014.

[226] J. Zhou, Y. Zhou and W. Tang, "Molecular Mechanism of Organic Crystal Nucleation: A Perspective of Solution Chemistry and Polymorphism," *Crystals,* vol. 12, pp. 1-25, 2022.

[227] R. J. Davey, S. L. M. Schroeder and J. H. ter Horst, "Nucleation of Organic Crystals - A Molecular Perspective," *Angewandte Chemie International Edition,* vol. 52, pp. 2166-2179, 2013.

[228] I. Riposan, M. Chisamera, S. Stan, P. Toboc, C. Ecob and D. White, "Al,Zr-FeSi Preconditioning of Grey Cast Irons," *Material Science and Technology,* vol. 24, no. 5, pp. 579-584, 2008.

[229] E. Fras, H. F. Lopez and C. Podrzucki, "The Influence of Oxygen on the Inoculation Process of Cast Iron," *International Journal of Cast Metals Research,* vol. 13, no. 2, pp. 107-121, 2000.

[230] R. Källbom, K. Hamberg, M. Wessen and L. -E. Björkegren, "On the Solidification Sequence of Ductile Iron Casting Containing Chunky Graphite," *Materials Science and Engineering A,* Vols. 413-414, pp. 346-351, 2005.

[231] J. Zhou, W. Schmitz and S. Engler, "Untersuchung der Gefügebildung von Gußeisen mit Kugelgraphit bei Langsamer Erstarrung," *Giesserei Forschung,* vol. 39, no. 2, pp. 55-71, 1987.

[232] J. Sertucha, R. Suarez, I. Asenjo, P. Larranaga, J. Lacaze, I. Ferrer and S. Armendariz, "Thermal Analysis of the Formation of Chunky Graphite during Solidification of Heavy-section Spheroidal Graphite Iron Parts," *ISIJ International,* vol. 49, no. 2, pp. 220-228, 2009.

[233] J. Sertucha, G. Artola, U. de La Torre and J. Lacaze, "Chunky Graphite in Low and High Silicon Spheroidal Graphite Cast Irons - Occurrence, Control and Effect on Mechanical Properties," *Materials,* vol. 13, no. 23, pp. 1-27, 2020.

[234] M. Gagne and C. Labrecque, "Effect of Wall Thickness on the Graphite Morphology and Properties of D5-S Austenitic Ductile Iron," *AFS Transactions,* vol. 115, pp. 411-421, 2007.

[235] B. Prinz, K. J. Reifferscheid, T. Schulze, R. Döpp and E. Schürmann, "Untersuchung von Ursachen von Graphitentartungen bei Gußeisen mit Kugelgraphit in Form von Chunky-Graphit," *Gießereiforschung,* vol. 43, no. 3, pp. 107-115, 1991.

[236] M. Gagne and D. Argo, "Heavy Section Ductile Iron. II. Formation of Chunk Graphite," *Advanced Casting Technology,* pp. 245-256, 1986.

[237] I. Adhiwiguna, N. Nobakht and R. Deike, "Nodular Graphite Dissolution and Nucleus Observation: High-Temperature Dynamics of Ductile Iron Recycling," *Metals,* vol. 14, no. 8, p. 915, 2024.

[238] S. Stan, I. Riposan, M. Chisamera and M. Barstow, "Undesirable Graphite Morphologies Incidence in Inoculated Grey Irons," *Advanced Material Research,* vol. 23, pp. 307-310, 2007.

[239] D. D. Double and A. Hellawell, "The Nucleation and Growth of Graphite - The Modification of Cast Iron," *Acta Metallurgica et Materialia,* vol. 43, no. 6, pp. 2435-2442, 1995.

[240] S. Amini and R. Abbaschian, "Nucleation and Growth Kinetics of Graphene Layers from a Molten Phase," *Carbon,* vol. 51, pp. 110-123, 2013.

[241] K. Theuwissen, J. Lacaze and L. Laffont, "Structure of Graphite Precipitates in Cast Iron," *Carbon,* vol. 96, pp. 1120-1128, 2016.

[242] V. Sahajwalla and R. Khanna, "A Monte Carlo Simulation Study of Dissolution of Graphite in Iron-Carbon Melts," *Metallurgical and Materials Transaction B,* vol. 31, pp. 1517-1525, 2000.

[243] C. Jiang, J. Zhang, K. Li, W. Liang and Z. Bi, "Influence of Graphite Crystalline Orientation on the Carbon Dissolution Reaction in Liquid Iron: A ReaxFF Molecular Dynamics Simulation Study," *Journal of Molecular Liquids,* vol. 335, p. 115688, 2021.

[244] N. Wade and Y. Ueda, "Isothermal Austenitizing of Spheroidal Graphite Cast Iron," *Transactions ISIJ,* vol. 20, pp. 849-856, 1980.

[245] T. Miki and K. Ishii, "Decomposition Behaviour of Fe_3C under Ar Atmosphere," *ISIJ International,* vol. 54, no. 1, pp. 29-31, 2014.

[246] N. Wade and Y. Ueda, "Continuous Heating Transformation of Spheroidal Graphite Cast Iron," *Transactions ISIJ,* vol. 20, pp. 857-861, 1980.

[247] J.-M. Chou and M.-H. Hon, "The Austenite Transformation in Ferritic Ductile Cast Iron," *Material Science and Engineering,* vol. 158, pp. 241-249, 1992.

[248] E. N. Palkanoglou, K. P. Baxevanakis and V. V. Silberschmidt, "Thermal Debonding of Inclusions in Compacted Graphite Iron: Effect of Matrix Phases," *Engineering Failure Analysis,* vol. 139, no. 106476, pp. 1-13, 2022.

[249] M. Warmuzek and A. Polkowska, "Micromechanism of Damage of the Graphite Spheroid in the Nodular Cast Iron During Static Tensile Test," *Journal of Manufacturing and Material Processing,* vol. 4, no. 22, pp. 1-19, 2020.

[250] L. S. Darken, "Diffusion of Carbon in Austenite with a Discontinuity in Composition," *Metals Technology,* pp. 430-438, 1948.

[251] D. Franzen, P. Weiß, B. Pustal and A. Bührig-Polaczek, "Modification of Silicon Microsegregation in Solid-Solution-Strengthened Ductile Iron by Alloying with Aluminium," *International Journal of Metal Casting,* vol. 14, no. 4, pp. 1105-1114, 2020.

[252] W. Arshad, A. Mehmood, M. F. Hashmi and O. u. Rauf, "The Effect of Increasing Silicon on Mechanical Properties of Ductile Iron," *Journal of Physic IOC Conf. Series,* vol. 1082, pp. 1-6, 2018.

[253] A. Alhussein, M. Risbet, A. Bastien, J. P. Chobaut, D. Balloy and J. Favergeon, "Influence of Silicon and Addition Elements on the Mechanical Behaviour of Ferritic Ductile Cast Iron," *Material Science and Engineering A,* vol. 605, pp. 222-228, 2014.

[254] B. Domeij and A. Dioszegi, "The Distribution of Carbon in Austenite Studied on a Water-Quenched Compacted Graphite Iron using Electron Probe Microanalysis," *International Journal of Metal Casting,* vol. 14, no. 3, pp. 782-793, 2020.

[255] M. Kosaka and S. Minowa, "On the Rate of Dissolution of Carbon into Molten Fe-C Alloy," *Transactions ISIJ,* vol. 8, pp. 392-400, 1968.

[256] H. Sun, "Factor Influencing Dissolution of Carbonaceous Materials in Liquid Iron," *Metallurgical and Materials Transactions B,* vol. 36, pp. 893-894, 2005.

[257] M.-M. Sun, J.-L. Zhang, K.-J. Li, S. Ren, Z.-M. Wang, C.-H. Jiang and H.-T. Li, "Dissolution Behaviours of Various Carbonaceous Materials in Liquid Iron: Interaction between Graphite and Iron," *JOM,* vol. 71, no. 12, pp. 4305-4310, 2019.

[258] J. C. Mercier, R. Paton, J. C. Margerie and C. Mascre, "Inclusions dans les spheroides de graphite," *Fonderie,* vol. 277, pp. 191-200, 1969.

[259] G. Alonso, T. Tokarski, D. M. Stefanescu, M. Gorny, G. Cios and R. Suarez, "On the Crystallography of the Mg-Si-Al Nitride Nuclei and of the Graphite/Nitride Interface in Spheroidal Graphite Iron," *Carbon,* vol. 199, pp. 170-180, 2022.

[260] H. Uchida, K. Itatani, M. Aizawa, F. S. Howell and A. Kishioka, "Synthesis of Magnesium Silicon Nitride by the Nitridation of Powders in the Magnesium-Silicon System," *Journal of the Ceramic Society of Japan,* vol. 105, no. 11, pp. 934-939, 1997.

[261] S. Maekawa and Y. Nakagawa, "Solubility of Nitrogen in Liquid Iron and Effect of Carbon, Silicon and Manganese on the Solubility," *Tetsu-to-Hagane,* vol. 46, pp. 748-753, 1960.

[262] J.-M. Jang, D.-H. Kim, M.-K. Paek and J.-J. Pak, "Nitrogen Solubility in Cast Iron Containing C, Si and Mn," *ISIJ International,* vol. 58, no. 7, pp. 1185-1190, 2018.

[263] M.-K. Paek, J. Jeon and D. Lindberg, "Thermodynamic Behaviour of Nitrogen in the Carbon Saturated Fe-Mn-Si Alloy during Casting," *International Journal of Cast Metals Research,* vol. 33, no. 4-5, pp. 226-232, 2020.

[264] M. T. Prijanovic, P. Mrvar, M. Petric, J. Burja and C. Donik, "Study on Dissolution of Ba-Containing Inoculant in Ductile Cast Iron Melt and Nucleation of Graphite," *International Journal of Metal Casting,* 2023.

[265] S.-M. Hwang, S.-J. Park, G.-T. Kim, H.-N. Kim, J.-W. Ko, Y.-H. Park and D.-W. Lee, "Metallic Silicon Powder Produced by Vacuum Decomposition of Magnesium Silicide Prepared by Magnesiothermic Reduction," *Materials Transactions,* vol. 62, no. 9, pp. 1285-1290, 2021.

[266] D. Stathokostopoulos, D. Chaliampalias, E. Pavlidou, K. M. Paraskevopoulos, K. Chrissafis and G. Vourlias, "Oxidation Resistance of Magnesium Silicide under High Temperature Air Exposure," *Journal of Thermal Analysis and Calorimetry,* vol. 121, pp. 169-175, 2015.

[267] E.-C. Stefanaki, E. Hatzikraniotis, G. Vourlias, K. Chrissafis, G. Kitis, K. M. Paraskevopoulos and G. S. Polymeris, "Thermal Stability Study from Room

Temperature to 1273K (1000°C) in Magnesium Silicide," *Metallurgical and Materials Transactions A,* vol. 47, pp. 5146-5158, 2016.

[268] S. Dawson, "Process Control for the Production of Compacted Graphite Iron," in *106th AFS Casting Congress*, Kansas City, 2002.

[269] F. Mampaey, D. Habets and F. Seutens, "The Use of Oxygen Activity Measurement to Determine Optimal Properties of Ductile Iron during Production," *Giessereiforschung,* vol. 60, no. 1, pp. 2-19, 2008.

[270] D. Sheng, S.-j. Li, Y.-m. Lu, X.-y. Lin and S.-c. Chen, "Critical Content of MgO in Spheroidisers," *Journal of Iron and Steel Research International,* vol. 13, pp. 1-4, 2006.

[271] Q. Han, D. Zhou and C. Xiang, "Determination of Dissolved Sulfur and Mg-S, Mg-O Equilibria in Molten Iron," *Steel Research,* vol. 68, no. 1, pp. 9-14, 1997.

[272] T.-s. Zhang, D.-y. Wang and M.-f. Jiang, "Effect of Magnesium on Evolution of Oxide and Sulphide in Liquid Iron at 1873K," *Journal of Iron and Steel Research International,* vol. 21, no. 12, pp. 1073-1080, 2014.

[273] E. Stefan, M. Chisamera, I. Riposan and S. Stan, "Graphite Nucleation Sites in Commercial Grey Cast Irons," *Materialstoday: Proceedings,* vol. 45, no. 5, pp. 4091-4095, 2021.

[274] O. M. Suarez, R. D. Kendrick and C. R. Loper Jr., "Late Sulfur Inoculation of Spheroidal Graphite Cast Irons," *International Journal of Cast Metals Research,* vol. 16, no. 1-3, pp. 1-6, 2003.

[275] M. Bazdar, H. R. Abbasi, A. H. Yaghtin and J. Rassizadehghani, "Effect of Sulfur on Graphite Aspect Ratio and Tensile Properties in Compacted Graphite Irons," *Journal of Materials Processing Technology,* vol. 209, pp. 1701-1705, 2009.

[276] A. A. Nayeb-Hashemi and J. B. Clark, "The Mg−Si (Magnesium-Silicon) System," *Bulletin of Alloy Phase Diagrams,* vol. 5, no. 6, pp. 584-592, 1984.

[277] R. Suarez, J. Sertucha, P. Larranaga and J. Lacaze, "Active Mg Estimation using Thermal Analysis: A Rapid Method to Control Nodularity in Ductile Cast Iron Production," *Metallurgical and Materials Transactions B,* vol. 47, pp. 2744-2753, 2016.

[278] M. A. Fesenko and A. M. Fesenko, "In-Mould Graphitizing, Spheroidizing, and Carbide Stabilizing Inoculation of Cast Iron Melt," *Progress in Physics of Metals,* vol. 21, no. 1, pp. 83-101, 2020.

[279] D. M. Stefanescu and C. R. Loper Jr, "Effect of Lanthanum and Cerium on the Structure of Eutectic Cast Iron," *American Foundrymen's Society Transactions,* vol. 89, pp. 425-436, 1981.

[280] T. Ototani and Y. Kataura, "Deoxidation and Desulfurization of Liquid Steel with Calcium Complex Alloys," *Transactions ISIJ,* vol. 12, pp. 334-342, 1972.

[281] M. Numata and Y. Higuichi, "Effect of Changes in Sulfur and Oxygen Concentration on Change in Nitrogen Concentration in Liquid Steel during CaO-CaSi Powder Blowing under Reduced Pressure," *ISIJ International,* vol. 52, no. 11, pp. 2019-2025, 2012.

[282] B. Bulko, M. Molnar, P. Demeter, M. Cervenka, G. Trefa, M. Mochnacka, D. Baricova, S. Hubatka, L. Fogaras and V. Sabik, "Deep Steel Desulfurization Practice," *Transactions of the Indian Institute of Metals,* vol. 75, no. 11, pp. 2807-2816, 2022.

[283] T. Ototani, Y. Kataura and T. Degawa, "Calcium Deoxidation and Aluminium Desulphurization of Liquid Iron and Liquid Iron Alloy with a Lime Crucible," *Tetsu-to-Hagane,* vol. 61, no. 9, pp. 2167-2181, 1975.

[284] B. Song and Q. Han, "Equilibrium of Calcium Vapor with Liquid Iron and the Interaction of Third Elements," *Metallurgical and Materials Transactions B,* vol. 29B, pp. 415-420, 1998.

[285] M. Berg, J. Lee and D. Sichen, "Study on the Equilibrium Between Liquid Iron and Calcium Vapor," *Metallurgical and Materials Transactions B,* vol. 48B, pp. 1715-1720, 2017.

[286] T. Kusakawa, "Effects of Calcium Silicide on Cast Iron (I)," *Tetsu-to-Hagane,* vol. 38, no. 6, pp. 376-382, 1952.

[287] B. I. Imasogie, A. A. Afonja and J. A. Ali, "Properties of As-Cast and Heat-Treated Nodular Graphite Cast Irons, Melts Treated with CaSi-CaF_2 Alloy," *Scandinavian Journal of Metallurgy,* vol. 30, pp. 91-102, 2001.

[288] M. Maruyama and H. Chida, "Effects of Calcium on the Cast Iron Molten under Vacuum," *The Journal of the Japan Foundrymen's Society,* vol. 30, no. 11, pp. 880-886, 1958.

[289] M. Doi, S. Nishi and Y. Ueda, "Formation of Inverse Chill and Spheroidal Graphite in High Purity Cast Iron," *The Journal of the Japan Foundrymen's Society,* vol. 45, no. 10, pp. 871-877, 1973.

[290] S. Jung, T. Ishikawa and H. Nakae, "Critical Conditions for Formation of Spheroidal Graphite," *Materials Science and Engineering A,* vol. 476, pp. 350-356, 2008.

[291] E. L. Neacsu, I. Riposan, A. M. Cojocaru, S. Stan and I. Stan, "Carbide to Graphite Transition Control by Thermal Analysis in Grey Cast Irons," *Metals,* vol. 10, no. 8, pp. 933 1-18, 2020.

[292] W. Patterson and D. Ammann, "Beitrag zur Kristallisation des lamellaren Eisen–Graphit–Eutektikume in Gusseisen," *Giesserei Techn.–Wiss. Beih.,* vol. 23, pp. 1245 - 1247, 1959.

[293] S. V. Subramanian and G. R. Purdy, "Graphite Morphology Control in Cast Iron," *Materials Research Society Symposium Proceeding,* vol. 34, pp. 47-56, 1985.

[294] M. I. Onsøien, Ø. Grong, T. Skaland and K. Jørgensen, "Mechanism of Graphite Formation in Ductile Cast Iron Containing Rare Earth Metals," *Material Science and Technology,* vol. 15, pp. 253-259, 1999.

[295] J. P. Morris and R. C. Buehl, "The Effect of Carbon on the Activity of Sulfur in Liquid Iron," *The Journal of The Minerals, Metals & Materials Society,* vol. 2, pp. 317-322, 1950.

[296] A. Kagawa and T. Okamoto, "Coefficients for Equilibrium Partition of a Third Element between Solid and Liquid in Iron-Carbon base Ternary Alloys and Their Relation to Graphitization during Iron-Carbon Eutectic Solidification," *Journal of Materials Science,* vol. 19, pp. 2306-2318, 1984.

Publications

In addition to the thorough citation provided in the bibliography, this dissertation is also based on the results and development steps documented in the following reports:

Research Project

(1) Y. Tekneci, M. Walz, O. Keskin, I. Adhiwiguna, B. Vennemann, M. Großarth, R. Deike, and D. Algermissen, "Automatisierte Einblasanlage zur kalkbasierten Entschwefelung und Legierungseinstellung von Gusseisen (EKALGU 033R183A-C): Abschlussbericht zum r^{+}Impuls-Verbundvorhaben" Fritz Winter Eisengießerei GmbH und Co. KG, Stadtallendorf, Germany, 2021.

Journal Articles

(2) T. Semleit, I. Adhiwiguna, J. Wijaya and R. Deike, "Investigation of Silicon Carbide Dissolution Behavior in Molten Cast Iron under Specific Consideration of the Formation of Reaction Layers," Giesserei Special, vol. 1, pp. 46-53, 2021.

(3) R. Deike, I. Adhiwiguna and M. Walz, "Die Substitution von Magnesium zur Entschwefelung von Gusseisen: Ein Weg globale Abhängigkeiten in der Eisengussindustrie zu verringern," Gießerei Rundschau, vol. 70, no. 4, pp. 12-18, 2023.

(4) I. Adhiwiguna, K. Vellayadevan, Y. Tekneci, M. Walz, D. Algermissen and R. Deike, "Industrial Ecotechnological Assessment of Lime as a Sustainable Substitute for Desulfurization of Cast Iron," Journal of Sustainable Metallurgy, vol. 10, no. 2, pp. 797-809, 2024.

(5) I. Adhiwiguna, N. Nobakht and R. Deike, "Nodular Graphite Dissolution and Nucleus Observation: High-Temperature Dynamics of Ductile Iron Recycling," Metals, vol. 14, no. 8, p. 915, 2024.

(6) I. B. G. S. Adhiwiguna, G. Karagülmez, O. Keskin and R. Deike, "Investigation on Applicability of Lime as Desulfurization Agent for Molten Cast Iron," Steel Research International, p. 2400416, 2024.

Conference Presentations

(7) R. Deike, I. Adhiwiguna, and M. Walz, "Kugelgraphitbildung nur über eine Mg-behandlung?," Gießerei-Symposium – Guss im Wandel der Zeit: Rahmenprogramm GIFA 2023, Düsseldorf, Germany, 16 June 2023.

(8) I. Adhiwiguna, R. Deike, and M. Walz, "Lime Powder as Reliable and Sustainable Substitution of Magnesium for Desulfurization Process in the Cast Iron Industry," FEMS EUROMAT 2023, Frankfurt, Germany, 6 September 2023.

(9) I. Adhiwiguna, R. Deike, and M. Walz, "Reassessing the Role of Magnesium: In Search to a Sustainable Alternative in Cast Iron Production," 63rd IFC Portoroz 2023, Portoroz, Slovenia, 15 September 2023.

Bachelor and Master Theses

(10) G. Karagülmez, "Einflussfaktoren auf die Entschwefelung von Gusseisenschmelzen unter Einsatz einer kalkbasierten Entschwefelungsmischung," Bachelor Thesis, Universität Duisburg-Essen, 2019.

(11) K. D. Vellayadevan, "Ecological and Economical Analysis of Magnesium- and Lime-based Desulfurization in Cast Iron Industry," Bachelor Thesis, Universität Duisburg-Essen, 2022.

(12) H. Böhm, "Bewertung der Bildung von Kugelgraphite in duktilem Gusseisen ohne Magnesium," Master Thesis, Universität Duisburg-Essen, 2023.